

High-Density Excitonic Effects in GaN: Mott-Transition and Polariton Lasing

THÈSE N° 6245 (2014)

PRÉSENTÉE LE 5 SEPTEMBRE 2014

À LA FACULTÉ DES SCIENCES DE BASE

LABORATOIRE EN SEMICONDUCTEURS AVANCÉS POUR LA PHOTONIQUE ET L'ÉLECTRONIQUE

PROGRAMME DOCTORAL EN PHOTONIQUE

ÉCOLE POLYTECHNIQUE FÉDÉRALE DE LAUSANNE

POUR L'OBTENTION DU GRADE DE DOCTEUR ÈS SCIENCES

PAR

Georg ROSSBACH

acceptée sur proposition du jury:

Prof. O. Martin, président du jury
Prof. N. Grandjean, Dr R. Butté, directeurs de thèse
Dr P. Lefebvre, rapporteur
Prof. V. Savona, rapporteur
Prof. L. Viña, rapporteur



ÉCOLE POLYTECHNIQUE
FÉDÉRALE DE LAUSANNE

Suisse
2014

*Wer fertig ist, dem ist nichts recht zu machen.
Ein Werdender wird immer dankbar sein.*

— Johann Wolfgang von Goethe, *Faust* (1808)

gewidmet meinen Eltern und Großeltern,
mit Dank für alles...

Abstract

A major drawback of conventional wide-bandgap semiconductor lasers consists in the generally increased lasing threshold owing to the large effective carrier masses. An elegant solution to this problem could be provided by so-called polariton lasers. They are driven below the population inversion limit and rely on the spontaneous radiative decay of a highly coherent polariton condensate. Cavity-polaritons are admixed particles that result from the strong coupling between an excitonic resonance and a photonic mode in a microcavity. Their energy dispersion exhibits a well-defined ground state with very low effective mass, inherited from the photonic component, that allows condensation at elevated temperatures, given that their bosonic nature is conserved. The latter critically depends on the stability of the excitons. III-nitride based structures provide a sufficient optical quality, highly robust excitons, and a large oscillator strength, i.e. properties that allowed the first observation of polariton condensation at room temperature and beyond. Existing processing infrastructures should facilitate the realization of an eventual polariton laser diode operating under ambient conditions.

This study aims at an in-depth investigation of the optical response of strongly-coupled planar microcavities relying on embedded GaN/AlGaIn quantum wells as active medium. A refined analysis of the linear and non-linear emission properties of polariton condensates under non-resonant optical pumping shall help to deepen the knowledge about the condensate formation at elevated temperatures, including the determination of the carrier injection regime and specificities of polariton relaxation and renormalization. In order to comprehensively address this topic, the present study relies on various optical spectroscopy techniques such as time-resolved and Fourier-space photoluminescence measurements. The manuscript is divided into two main parts.

In the first part the high-carrier density emission properties of high-quality GaN/AlGaIn single and multiple quantum wells are examined. They are of specific interest for understanding the optical response of the eventual microcavity structure and provide furthermore a deeper insight into the operating conditions of III-nitride based laser and light-emitting diodes. These conditions are closely related to the so-called Mott-transition, which describes the injection-induced crossover between an insulating exciton gas and a conductive electron-hole plasma. The Mott-transition is found to be of continuous type, to be connected to a characteristic modification of the emission lineshape and to occur at carrier densities around 10^{12} cm^{-2} , almost independent of temperature.

The second part focuses on the properties of III-nitride based microcavities. The knowledge of the high-injection emission characteristics of the quantum wells facilitated the analysis of the

Abstract

polariton renormalization up to the condensation threshold. It is evidenced to be driven by exciton saturation effects, while the universality of the observations across different material systems suggests a general operation of semiconductor microcavities only one or two orders of magnitude below the Mott-transition. Further experimental studies concerned the relaxation properties along the lower polariton branch toward the condensation threshold. In addition to the thermodynamic and scattering kinetic limitations, two relaxation channels emerging from the quantum well dark exciton and biexciton states could be evidenced, which cause the direct feeding of the polariton ground state population by emission of a longitudinal-optical phonon. Finally, the optical properties of a non-polar microcavity structure are analyzed. The uniaxial symmetry of III-nitrides gives rise to a strongly anisotropic light-matter coupling regime that could be modeled by transfer-matrix simulations and allows different non-linear emission mechanisms along orthogonal polarization planes.

Key words: Gallium nitride, III-nitrides, quantum wells, excitons, biexcitons, electron-hole plasma, Mott-transition, microcavities, exciton-polaritons, polariton condensate, strong coupling regime, polariton lasing, Bose-Einstein condensate, polariton relaxation, polariton renormalization, exciton saturation, exciton oscillator strength, optical anisotropy, non-polar microcavities, anisotropic light-matter coupling

Zusammenfassung

Ein bedeutender Nachteil konventioneller Halbleiterlaser mit großer Bandlücke besteht in der, aufgrund der größeren effektiven Ladungsträgermassen, generell erhöhten Laserschwelle. Eine elegante Lösung dieses Problems könnte durch sogenannte Polariton-Laser erfolgen. Diese basieren auf der spontanen, radiativen Rekombination eines kohärenten Polariton-Kondensats und arbeiten unterhalb der eigentlichen Inversionsbedingung. Exziton-Polaritonen sind Quasipartikel, die durch die starke Kopplung zwischen einem Exziton und einer optischen Mode eines Mikroresonators gebildet werden. Durch die photonische Komponente weist ihre Energiedispersion ein wohldefiniertes Minimum mit sehr geringer effektiver Masse auf, welches unter der Bedingung der Beibehaltung ihrer bosonischen Eigenschaften Kondensation bei hohen Temperaturen ermöglicht. Für die bosonische Natur der Exziton-Polaritonen ist die Stabilität der exzitonischen Komponente entscheidend. Halbleiterstrukturen basierend auf Gruppe-III-Nitriden erreichen eine beachtliche optische Qualität, bieten extrem stabile Exzitonen und eine erhöhte Oszillatorstärke. Dies sind Eigenschaften, die die erste Beobachtung von Polariton-Lasing bei Raumtemperatur und darüber hinaus ermöglichten. Die bereits existente Prozessierungsinfrastruktur sollte die Realisierung einer Polariton-Laserdiode erleichtern.

Diese Arbeit bietet eine umfangreiche Analyse der optischen Eigenschaften stark gekoppelter, planarer Mikroresonatoren, die auf GaN/AlGaIn Quantengraben als aktives Medium beruhen. Eine detaillierte Untersuchung der linearen und nicht-linearen Emissionseigenschaften der Polariton-Kondensate unter nicht-resonanter optischer Anregung gibt Aufschluss über den Prozess der Kondensatbildung bei hohen Temperaturen, sowie über das Ladungsträgerinjektionsniveau und die Eigenschaften der Polariton-Relaxation und Renormalisierung. Um diese Themen angemessen zu bearbeiten, beruht die aktuelle Studie auf verschiedenen optischen Spektroskopiemethoden, wie z.B. zeit- und winkel-aufgelösten Photolumineszenzmessungen. Die Arbeit ist dabei in zwei Hauptteile untergliedert.

Im ersten Teil werden die Emissionseigenschaften einzelner und multipler GaN/AlGaIn Quantengraben hoher Qualität bei hohen Anregungsleistungen diskutiert. Dies ist von spezifischem Interesse für die nachfolgende Diskussion der optischen Eigenschaften der Mikroresonatorstrukturen und bietet weiterhin einen interessanten Einblick in die Betriebsbedingungen von Laser- und Leuchtdioden. Letztere sind eng verbunden mit dem sogenannten Mott-Übergang: Wenn die Ladungsträgerkonzentration immer weiter erhöht wird, findet ab einem kritischen Wert ein Übergang von einem nicht-leitenden Exzitonengas zu einem leitenden Elektron-Loch-Plasma statt. Die Experimente zeigen einen Übergang zweiter Ordnung in GaN/AlGaIn Quantengraben auf, der von einer charakteristischen Veränderung des Emissionsspektrums

begleitet wird und, unabhängig von der Temperatur, bei einer Ladungsträgerdichte von etwa 10^{12} cm^{-2} eintritt.

Der zweite Teil befasst sich mit den Eigenschaften Nitrid-basierter Mikroresonatoren. Das Wissen um die Emissionseigenschaften der Quantengraben bei hoher Injektion erleichtert die Analyse der Polariton-Renormalisierung bis zur Kondensationschwelle. Sie wird durch Sättigungseffekte der Exzitonen dominiert. Die Vergleichbarkeit der experimentellen Beobachtungen in anderen Materialsystemen legt einen generellen Betrieb von Halbleiter-Mikroresonatoren nur ein oder zwei Größenordnungen unterhalb des Mott-Übergangs nahe. Weitere Untersuchungen befassen sich mit den Relaxationseigenschaften entlang der unteren Polariton-Dispersion. Abseits der thermodynamischen und streukinetischen Restriktionen wurden zwei zusätzliche Relaxationspfade entdeckt, die von den dunklen Exziton- und Biexzitonzuständen der Quantengraben ausgehen. Sie bewirken die direkte Zufuhr von Polaritonen zum Grundzustand durch die Emission von longitudinal-optischen Phononen. Im letzten Abschnitt wird eine neu gefertigte, nicht-polare Mikroresonatorstruktur diskutiert. Die uniaxiale Symmetrie der Nitrid-Halbleiter generiert ein stark anisotropes Licht-Materie-Kopplungsregime, welches durch Transfer-Matrix-Simulationen modelliert werden konnte und nicht-lineare Emissionsmechanismen entlang orthogonaler Polarisationssebenen erlaubt.

Stichwörter: Galliumnitrid, Gruppe-III-Nitride, Quantengraben, Exzitonen, Biexzitonen, Elektron-Loch-Plasma, Mott-Übergang, optische Mikroresonatoren, Exziton-Polaritonen, Polariton-Kondensat, Regime der starken Kopplung, Polariton-Lasing, Bose-Einstein Kondensat, Polariton-Relaxation, Polariton-Renormalisierung, Exziton-Sättigung, Exziton-Oszillatorstärke, optische Anisotropie, nicht-polare optische Mikroresonatoren, anisotrope Licht-Materie-Wechselwirkung

Contents

Abstract (English/Deutsch)	v
Table of contents	ix
1 Introduction	1
2 Basics on III-Nitride Semiconductors	5
2.1 Structural Properties	5
2.1.1 Growth: Issues and Techniques	6
2.1.2 Mechanical Properties and Strain	8
2.2 Optical Properties	9
2.2.1 Band Structure	9
2.2.2 Excitons	18
2.2.3 Refractive Index	21
2.3 III-Nitride based Quantum-Wells	22
2.3.1 Quantum Well Confinement	22
2.3.2 Two-dimensional Excitons	24
2.3.3 Polarization Fields	26
2.3.4 Impact of Carrier Density	29
3 Highly-injected GaN Quantum-Wells	31
3.1 Experimental Techniques	31
3.1.1 Photoluminescence, Reflectivity and PLE	31
3.1.2 Time-resolved Photoluminescence	34
3.2 Sample Structures and Basic Optical Properties	35
3.2.1 Single Quantum-Wells	35
3.2.2 Quantum-Well Biexcitons	37
3.2.3 Multiple Quantum-Wells	39
3.3 The Mott-Transition	42
3.3.1 Theoretical Background	42
3.3.2 Low-temperature Mott-transition	48
3.3.3 Temperature Dependence	57
3.3.4 Recombination Dynamics	62
3.4 The Role of Biexcitons	63
3.5 Multiple Quantum-Wells	67
3.5.1 Saturation of Oscillator Strength	69
4 Polariton Condensation in III-nitride based Microcavities	71
4.1 Polaritons in Planar Microcavities	71

Contents

4.1.1	Microcavity Basics	72
4.1.2	Light-Matter Coupling in a Microcavity	77
4.1.3	Polariton Condensation	86
4.2	III-nitride based Structures - Review and Opportunities	90
4.2.1	Polariton Condensation at Room Temperature	91
4.2.2	The Condensation Phase Diagram	92
4.2.3	Toward a Polariton Laser Diode	94
4.3	Experimental Details and Basic Microcavity Properties	98
4.3.1	Fourier-Space Imaging	98
4.3.2	Structural Description of the c -plane Microcavity	100
4.3.3	Basic Optical Properties	101
4.4	Polariton Relaxation: The Impact of Biexcitons	103
4.4.1	Biexcitons in the bare Quantum Wells	105
4.4.2	Cavity Biexcitons	106
4.4.3	Evidences of a Biexciton-mediated Polariton Relaxation	108
4.5	Polariton Renormalization	111
4.5.1	Exciton Saturation in the Coupled-Oscillator Model	112
4.5.2	Experimental Results	115
4.5.3	Impacts of a Saturation-dominated Polariton Renormalization	118
4.6	High-Temperature Polariton Condensates	123
4.6.1	Polariton Condensates emerging in a disordered Landscape	125
4.7	Non-polar III-Nitride based Microcavities	130
4.7.1	Sample Structure	131
4.7.2	Optical Properties of the MQWs: The Impact of Strain	133
4.7.3	Anisotropic Coupling Regime	140
4.7.4	Non-linear Emission Properties	145
5	Conclusion	153
5.1	Summary and Classification of the Results	153
5.2	Perspectives	155
	Appendix	157
A.1	Band-Structure Calculations	157
A.1.1	The k,p -Formalism	157
A.1.2	Schrödinger- k,p Simulations for Quantum-Wells	159
A.1.3	Self-consistent Schrödinger-Poisson Solver	160
A.2	Optical Transfer-Matrix Simulations	162
A.2.1	Isotropic Media	162
A.2.2	Anisotropic Media	163
A.2.3	The Anisotropic Refractive Index of AlGaIn alloys	166
A.2.4	Refractive Index of a Quantum-Well	167
A.3	Recent XRD results on MC-2	168
	Bibliography	171
	List of Acronyms	187
	Acknowledgements	189
	Curriculum Vitae	191

1 Introduction

With an annual market volume that is only surpassed by that of silicon, III-nitrides represent a major family of modern semiconductors. In the thermodynamically stable hexagonal phase, they possess a direct bandgap, that is basically tunable from the infrared (IR) over the entire visible spectrum up to the ultra-violet (UV) range. The dramatic rise of III-nitride semiconductors in the past two decades was initiated by the discovery of an efficient and reliable *p*-type doping [1, 2], and the subsequent fabrication of the first blue light-emitting diodes (LEDs) [3, 4]. Their efficiency and output power have set new standards and led in 1996 to the demonstration of the first edge-emitting laser diodes (LDs) operating in the blue-violet spectral range [5]. Nowadays, III-nitride based LEDs and LDs are produced by leading optoelectronic companies worldwide. White LEDs, based on blue/violet LEDs with phosphor-coated packaging, are used for background illumination of LCD screens¹ and begin to revolutionize the field of general lighting, while blue/violet LDs dominate the field of high-density optical data storage. Moreover, based on their large bandgap and their thermal and chemical robustness, III-nitrides are also successfully used for high-temperature, high-power, and high-frequency electronics, e.g. for high-electron mobility transistors (HEMTs).

Despite the impressive development of III-nitrides in the recent past, some unsolved problems remain to be addressed. One of those is usually referred to as the *green gap*. Indeed, while efficient LEDs and LDs exist for the blue and red spectral region, the green spectral range misses such a solution. Here, the issues for a III-nitride based device consist particularly in the diminishing structural quality of the InGaN alloy when the In-content increases and further in the unknown origin for the commonly observed efficiency droop at high driving currents. The latter is controversially ascribed either to alloy disorder or to the Auger-effect [6, 7]. Eventually, the exact surrounding parameter characteristics in such optoelectronic devices operating at high injection near the Bernard-Duraffourg limit are still matter of debate [8]. They are closely related to the so-called Mott-transition [9, 10], that describes the carrier-injection induced crossover between an insulating exciton² gas and a conductive electron-hole plasma.

Another problem, that concerns wide-bandgap semiconductor based LDs at large, is given by the generally increased lasing threshold densities compared to their low-bandgap counterparts and therefore the increased amount of thermal stress. This issue originates from the large

¹LCD - liquid crystal display

²An exciton is a quasi-particle in a semiconductor that is composed of an electron-hole pair coupled by Coulomb-interaction.

effective carrier masses and the correspondingly delayed Bernard-Duraffourg limit setting the onset of gain [8]. A smart way to overcome this problem could rely on the realization of so-called polariton lasers: Imamoğlu and co-workers proposed those as ultra-low threshold coherent light-emitters [11], following the first observation of exciton-polaritons in a GaAs-based semiconductor microcavity by Weisbuch *et al.* in 1992 [12]. These quasi-particles arise from the strong-coupling between an excitonic resonance in a semiconductor active medium and a photonic mode in an optical microresonator. Considering the simplest case of a planar microcavity, where the photonic component is confined by two plane-parallel distributed Bragg-reflectors, the dispersion curve of exciton-polaritons features a well-defined energy minimum at zero in-plane momentum with very light effective mass. The latter is inherited from the photonic component and lies typically four to five orders of magnitude below the one of the free electron mass. Taking additionally into account the bosonic particle nature, this property should allow the formation of a non-equilibrium polariton condensate at elevated temperatures, ruled by Bose-Einstein statistics [13–15]. Its spontaneous radiative decay should share very similar characteristics with a conventional LD in terms of coherence and non-linear output power scaling, while operating at much lower carrier densities.

Following the first demonstration of polariton-related non-linearities in a strongly-coupled semiconductor microcavity in 1998 [16], it was evidenced in 2006 that a non-equilibrium polariton condensate shares major characteristics with a conventional Bose-Einstein condensate [17]. Since then several experiments have proven the quantum nature of polariton fluids, such as the observation of quantized vortices [18], hints for super-fluidity [19], and Josephson-oscillations [20]. However, the bosonic nature of exciton-polaritons crucially depends on the stability of the excitonic component. Thus, corresponding quantum effects and non-linearities seem to be limited to a material specific cut-off temperature T_{cut} , which is determined by the exciton binding energy E_B [21], i.e. $k_B T_{\text{cut}} \sim E_B$ with k_B denoting the Boltzmann constant. When now targeting the fabrication of a polariton-condensation based device, this requirement should obviously be fulfilled at room temperature. Figure 1.1 displays exciton binding energies of a variety of inorganic bulk semiconductors as a function of their bandgap with a marker corresponding to the thermal energy at room temperature. It is obvious that due to their large effective carrier masses in particular wide-bandgap semiconductor compounds satisfy this condition, among which GaN leads the way due to its mature fabrica-

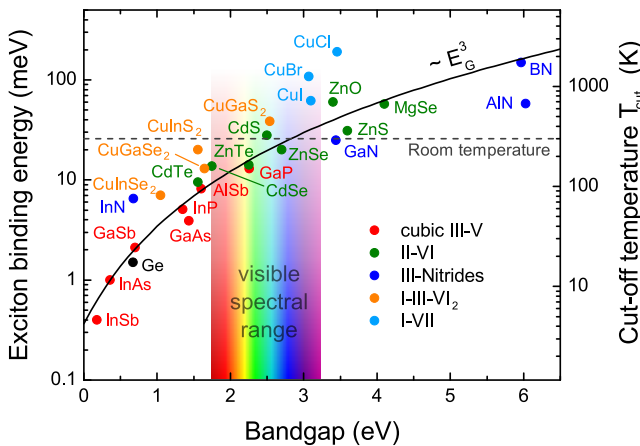


Figure 1.1: Exciton binding energy for various inorganic bulk semiconductors: III-V (red), II-VI (green), I-VII (light blue), chalcopyrites I-III-VI₂ (orange), and III-nitrides (blue). The right hand side axis corresponds to the cut-off temperature T_{cut} of excitons with binding energy E_B . A guide to the eye (black solid line) reproduces the power-law $E_B \propto E_G^3$ and the horizontal dashed line defines the room-temperature limit.

tion technology.³ Driven by this motivation the first demonstration of polariton lasing in GaN bulk and quantum well (QW) based microcavities at $T = 300\text{ K}$ was reported in 2007 and 2008 [22, 23], respectively. Since then the quantum nature of polariton lasing at room temperature was for instance evidenced by the observation of spontaneous symmetry breaking [24], and the demonstration of optimum detuning conditions for condensation different from that of a conventional semiconductor LD [25, 26]. On the other hand, all presently published studies rely on optical excitation: the fabrication of an electrically-injected polariton laser operating at room temperature has not yet been achieved. More information about those issues can be found in Sec. 4.2.

Objectives and Outline

This work aims at addressing the aforementioned issues by a comprehensive study of the high-injection optical properties of GaN-based QWs and by deepening the knowledge about polariton condensation at elevated temperatures in III-nitride based microcavities. More precisely, we will specify the mechanisms driving the condensation threshold, examine the alteration of the polariton properties when the carrier density is raised, and discuss the complex optical characteristics of a newly fabricated anisotropic III-nitride based microcavity. Therefore, the manuscript is organized as follows.

The subsequent chapter provides a consolidated introduction to the specificities of III-nitride semiconductor compounds. Starting from the symmetry characteristics of the wurtzite crystal structure, it will thoroughly describe the electronic and optical properties of bulk III-nitrides and examine the modifications of the latter occurring in QW structures. This discussion provides all necessary information for understanding the experimental part. In view of the latter, it will focus on GaN and Ga-rich AlGaN compounds.

The first part of the experimental investigations in Ch. 3 deals with the optical properties of high-quality GaN/AlGaN single QWs under high non-resonant optical injection. After introducing the experimental setups, this section starts with the description of the investigated sample structures and their low-density absorption and emission properties. Then a brief survey about the Mott-transition and previous experimental results is presented. The subsequent experimental part begins with the presentation and analysis of the low temperature data: the high-carrier density emission properties have been probed by time-resolved and continuous-wave photoluminescence. Afterwards the temperature dependence of the critical density, the impact of biexcitons, and the similarities of the Mott-transition occurring in multiple QWs are discussed. The time-resolved experiments presented in this chapter have been performed in collaboration with G. Jacopin and M. Shahmohammadi (LOEQ-EPFL, group of Prof. B. Deveaud). The discussion is mainly based on two publications, that have been submitted recently:

G. Rossbach, J. Levrat, G. Jacopin, M. Shahmohammadi, J.-F. Carlin, J.-D. Ganière, R. Butté, B. Deveaud, and N. Grandjean, *High-temperature Mott-transition in wide band-gap semiconductor quantum wells*, (submitted).

M. Shahmohammadi, G. Jacopin, G. Rossbach, J. Levrat, J.-F. Carlin, J.-D. Ganière, R.

³At this point, it is worth mentioning that the exciton binding energy can be enhanced by approximately a factor of two in QWs compared to the bulk case. This can partially alter the assortment of eligible compounds in Fig. 1.1.

Chapter 1. Introduction

Butté, N. Grandjean, and B. Deveaud, *Biexcitonic molecules survive excitons at the Mott transition*, (submitted).

Chapter 4 presents the experimental results obtained on III-nitride based microcavity structures. It begins with an introduction to the physics of optical resonators, the basics of the strong-coupling regime, and a brief discussion about the field of polariton-condensation as a whole. Section 4.2 provides a chronological review about III-nitride based microcavities and summarizes selected results of the past years. It further discusses the physical barriers that have to be faced and overcome in order to realize an electrically-pumped polariton LD. Afterwards, the Fourier-space photoluminescence setup, the first sample structure and their basic optical properties are introduced. The experimental part starts with Sec. 4.4 discussing the newly-discovered relaxation efficiency enhancement of lower polaritons due to biexciton states below threshold. Hereafter, the modification of the polariton properties in presence of a finite carrier density are examined. They lead to the commonly observed blueshift of the polariton ground state when approaching the condensation threshold. These two sections are based on the following publications:

P. Corfdir, J. Levrat, G. Rossbach, R. Butté, E. Feltin, J.-F. Carlin, G. Christmann, P. Lefebvre, J.-D. Ganière, N. Grandjean, and B. Deveaud-Plédran, *Impact of biexcitons on the relaxation mechanisms of polaritons in III-nitride based multiple quantum well microcavities*, Physical Review B **85**, 345308 (2012).

G. Rossbach, J. Levrat, E. Feltin, J.-F. Carlin, R. Butté, and N. Grandjean, *Impact of saturation on the polariton renormalization in III-nitride based microcavities*, Physical Review B **88**, 165312 (2013).

They have been worked out in close collaboration with J. Levrat (LASPE-EPFL, thesis 2012), the time-resolved measurements have been performed by P. Corfdir (LOEQ-EPFL, thesis 2011).

The last section of Ch. 4 focuses on the investigation of a newly-fabricated non-polar microcavity. It contains a comprehensive discussion about the optical and excitonic anisotropy of the nitride layer stack, and shows the first evidence for polariton condensation in such a structure. This section is mainly based on two publications, that have been elaborated in cooperation with J. Levrat:

G. Rossbach, J. Levrat, A. Dussaigne, H. Teisseyre, G. Cosendey, M. Glauser, M. Cobet, M. Bockowski, I. Grzegory, T. Suski, R. Butté, and N. Grandjean, *Tailoring the light-matter coupling in anisotropic microcavities: Redistribution of oscillator strength in strained m-plane GaN/AlGaIn quantum wells*, Physical Review B **84**, 115315 (2011).

J. Levrat, G. Rossbach, A. Dussaigne, H. Teisseyre, G. Cosendey, M. Glauser, M. Cobet, M. Bockowski, I. Grzegory, T. Suski, R. Butté, and N. Grandjean, *On the nature of the nonlinear emission properties of an optically anisotropic GaN-based microcavity*, Physical Review B **86**, 165321 (2012).

Our Polish collaborators provided the bulk substrates, A. Dussaigne performed the growth, and G. Cosendey deposited the top Bragg-mirror (both LASPE-EPFL).

Finally, the main results of this work are summarized and classified in Ch. 5. It will further provide a brief outlook to what could follow in the near future. The subsequent appendix introduces the algorithms used for band-structure calculations and optical transfer-matrix simulations.

2 Basics on III-Nitride Semiconductors

III-nitride based devices, such as white LEDs for general lighting or HEMTs suited for high-power and/or high-temperature applications are processed in leading opto- and microelectronic companies worldwide. In each of their applications III-nitride based structures profit (and potentially suffer at the same time) from their unique structural and electronic properties. This chapter provides an overview of the basic properties of III-nitride materials and corresponding heterostructures, building up the basis for understanding the experimental results that are reported and discussed in the subsequent chapters.

2.1 Structural Properties

Fundamental properties of a material can already be inferred from its bare crystal structure and the allowed symmetry operations. Contrary to other III-V compound semiconductors such as GaAs or GaP that crystallize in the cubic zincblende lattice, the thermodynamically stable phase of the conventional III-nitrides (metal atoms Al, Ga and In) is the hexagonal wurtzite structure. Cubic symmetries such as zincblende and rock-salt configurations can also be obtained depending on the substrate choice and the growth conditions. However, they are not subject of this work and will thus not be discussed in the following.

In order to emphasize permutation symmetries, orientations in the hexagonal lattice are,

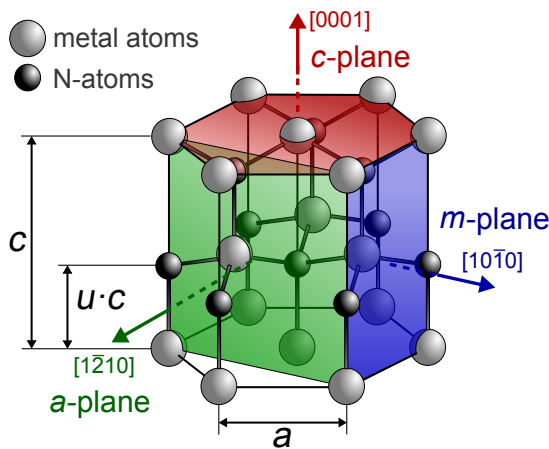


Figure 2.1: Representation of the wurtzite unit cell: metal (gray) and nitrogen (black) atoms, respectively, occupy a hexagonal close-packed sub-lattice. Both are displaced by the u -parameter along the $[0001]$ -direction. Each atom is tetrahedrally surrounded by four atoms of the complementary species. This orientation of the nearest neighbors is caused by the sp^3 -hybridization of the bonding orbitals. The hexagonal lattice constants a and c are indicated and the most-common surface planes are highlighted.

contrary to the cubic case and the corresponding Miller-indices, usually described by four coordinates $[hki\bar{l}]$. The first three define respective axes that are pairwise comprising an angle of 120° and span the hexagonal basal plane of the unit cell. The surface normal to the latter determines the c -axis, which is described by the fourth coordinate. As there are only three degrees of freedom, h, k, i are related via: $-i = h + k$.

The wurtzite structure, which is schematically illustrated in Fig. 2.1, features C_{6v} -symmetry and consists of a hexagonal close-packed lattice with a two-atom basis. In the case of III-nitrides, this basis consists of one metal and one nitrogen atom. Both are separated by $u \cdot c$ along the $[0001]$ -axis. Here, c denotes the lattice constant between equivalent basal planes, while atoms within the latter are separated by the lattice constant a . In an ideal wurtzite crystal, the internal parameter u and the lattice constants satisfy:

$$\frac{c}{a} = \sqrt{\frac{8}{3}} \approx 1.633 \quad \text{and} \quad u = \frac{3}{8} = 0.375. \quad (2.1)$$

The lack of inversion symmetry in the wurtzite lattice and the consequent interactions occurring between second nearest neighbors leads to a displacement of negative and positive charge barycenters in the unit cell along the c -axis, giving rise to an intrinsic polarization vector. This property is usually referred to as pyroelectricity. Its characteristics and related effects emerging in III-nitride based heterostructures will be discussed in more detail in Sec. 2.3.3. On top of this, the pyroelectric character in combination with the polarity of the atomic bonds, due to the different electronegativity values of the involved species, gives rise to a deviation of the equilibrium lattice constants from the above-mentioned ideal values. Table 2.1 summarizes unstrained reference values of the lattice parameters and the electronegativity difference $\Delta\chi$ for the most common binary III-nitride representatives. The stronger polarity of AlN compared to InN and GaN leads to larger deviations of u and c/a from the ideal values and the increasing atom size (in order of increasing atom radius: Al-Ga-In) results in larger lattice constants. Another consequence of the hexagonal crystal symmetry is the intrinsic uniaxial anisotropy of III-nitride materials. Focused on the electronic and optical properties, the latter will be explained in more detail in the forthcoming sections of this chapter.

	GaN	AlN	InN	ideal
c (Å)	5.186	4.981	5.704	
a (Å)	3.189	3.112	3.538	
u	0.379	0.387	0.377	0.375
c/a	1.626	1.601	1.612	1.633
$\Delta\chi$	1.23	1.43	1.26	

Table 2.1: Lattice parameters of the conventional binary III-nitride compounds at room temperature from Refs. [27, 28]. The electronegativity difference between nitrogen and metal atoms $\Delta\chi$ defines the polarity of the bonding (following Pauling [29]).

2.1.1 Growth: Issues and Techniques

The structural and optical quality of semiconductor heterostructures - whatever their eventual appropriation - critically depends on the substrate that is used for the growth. A mismatch in the lattice constants can cause the formation of dangling bonds, dislocations and strain at the substrate interface potentially creating unwanted carrier recombination centers and extended crystal defects, which can detrimentally impact on the device performance. Even larger strain values, that may ultimately lead to a partial surface delamination or the formation

of macroscopic cracks, can be caused by different thermal expansion coefficients between substrate and overgrown layer. Indeed, depending on the deposition technique the growth temperature substantially exceeds the eventual operating temperature of the device. Starting from almost relaxed layers at the growth temperature, the diverging thermal compression when cooling the structure down to ambient conditions may result in large shear stress at the substrate interface. When it comes to devices, certainly additional aspects for the substrate choice have to be considered, such as availability, thermal and electrical conductivity, good cleavability and most-importantly the price. They are often leading to compromises that are not necessarily in favor of the structural quality.

Owing to the lack of reasonably-priced and commercially-available bulk GaN substrates, early III-nitride based structures and devices were usually grown on foreign substrates like sapphire ($\alpha - \text{Al}_2\text{O}_3$), Si, or SiC. Each of those exhibits certain advantages and drawbacks: sapphire features a very low thermal conductivity and a significant lattice mismatch to GaN. Nevertheless, it is today's substrate of choice for the fabrication of white LEDs due to its wide availability and its competitive price. Those advantages are only surpassed by Si-substrates, which further exhibit a superior thermal conductivity.¹ But despite these merits and the huge research efforts that are spent to make Si compatible with III-nitride technology, the optical, structural and electrical quality of layers deposited on silicon remains a major issue of III-nitride heteroepitaxy. This is mainly due to the immense tensile stress that is caused by the low thermal expansion coefficient of Si. For a review of GaN heteroepitaxy the reader is referred to Ref. [30]. Nowadays the situation concerning free-standing and bulk GaN substrates is changing. They become more and more available and their price decreases. Although the latter remains far above the one of sapphire and Si, homoepitaxy of III-nitrides, minimizing the thermal and structural mismatch for Ga-rich layers in absolute favor of the material quality, is rising up and already widely used in research facilities and for the production of laser diodes.

Three different epitaxial growth methods of III-nitrides have been established. They shall briefly be explained hereafter:

Molecular beam epitaxy (MBE): This physical vapor deposition technique requires high or ultra-high vacuum (UHV) conditions and is limited to rather low growth rates ($\sim 1 \mu\text{m/h}$). The bare elements are used as metal precursors, while nitrogen can be supplied either as a plasma or by ammonia. Due to the UHV conditions, the deposition can be monitored *in situ* by RHEED (reflection high-energy electron diffraction) offering an accurate control of the deposited layer thickness and the surface quality.

Metal-organic vapor phase epitaxy (MOVPE): MOVPE is a chemical vapor phase deposition technique that commonly uses ammonia and trimethyl- or triethyl-metal compounds as precursors. Both the growth temperatures and the growth rates are higher than for MBE ($\sim 1000^\circ\text{C}$ and up to $10 \mu\text{m/h}$). In combination with a good reproducibility and scalability, this makes MOVPE the technique of choice for mass-production.

Hydride vapor phase epitaxy (HVPE): Like MOVPE, HVPE is a chemical vapor phase deposition technique. It offers very high growth rates, up to $500 \mu\text{m/h}$, and is commonly used to grow thick epilayers potentially serving as template for other deposition techniques.

¹The balance between the drawbacks and advantages of the different substrates may be modified when considering lift-off processes for the active region. These are frequently used to avoid substrate absorption and to enhance the light-extraction efficiency.

2.1.2 Mechanical Properties and Strain

Owing to the aforementioned growth issues, deposited layers are often subject to a certain degree of strain. In the elastic limit, the latter is deforming the unit cell and thus potentially changing specific properties of the material (e.g. the bandgap energy). Corresponding effects have to be carefully taken into account when it comes to the device design.

In a cartesian basis, defined by the directions x, y, z and the corresponding unit vectors of the lattice \mathbf{e}_j , the deformed lattice vectors \mathbf{e}_i^* are obtained via (using Einstein notation):

$$\mathbf{e}_i^* = I_{ij}\mathbf{e}_j + \epsilon_{ij}\mathbf{e}_j, \quad \text{with} \quad i, j \in x, y, z, \quad (2.2)$$

where I_{ij} and ϵ_{ij} are the elements of the identity matrix and the strain tensor $\boldsymbol{\epsilon}$, respectively. Neglecting any rotation of the whole structure, the tensor elements of $\boldsymbol{\epsilon}$ follow the symmetry $\epsilon_{ij} = \epsilon_{ji}$. While the off-diagonal terms of $\boldsymbol{\epsilon}$ stand for shear strain, the diagonal elements determine a hydrostatic deformation. Positive elements correspond to tensile distortion potentially leading to cracks, whereas negative ones indicate compressive strain.

For elastic deformation, $\boldsymbol{\epsilon}$ and the stress tensor $\boldsymbol{\sigma}$ are connected via Hooke's law:

$$\sigma_{ij} = C_{ijkl}\epsilon_{kl} \quad \text{with} \quad i, j, k, l \in x, y, z, \quad (2.3)$$

where C_{ijkl} denotes the elements of the fourth-ranked elastic modulus \mathbf{C} . By respecting the hexagonal symmetry of the crystal, \mathbf{C} and Eq. (2.3) can be simplified to the form:

$$\begin{pmatrix} \sigma_{xx} \\ \sigma_{yy} \\ \sigma_{zz} \\ \sigma_{yz} \\ \sigma_{xz} \\ \sigma_{xy} \end{pmatrix} = \begin{pmatrix} C_{11} & C_{12} & C_{13} & 0 & 0 & 0 \\ C_{12} & C_{11} & C_{13} & 0 & 0 & 0 \\ C_{13} & C_{13} & C_{33} & 0 & 0 & 0 \\ 0 & 0 & 0 & C_{44} & 0 & 0 \\ 0 & 0 & 0 & 0 & C_{44} & 0 \\ 0 & 0 & 0 & 0 & 0 & C_{66} \end{pmatrix} \begin{pmatrix} \epsilon_{xx} \\ \epsilon_{yy} \\ \epsilon_{zz} \\ 2\epsilon_{yz} \\ 2\epsilon_{zx} \\ 2\epsilon_{xy} \end{pmatrix}. \quad (2.4)$$

Table 2.2: Elements of the elastic modulus \mathbf{C} for III-nitrides [31]. For the element C_{66} holds: $C_{66} = (C_{11} - C_{12})/2$.

	GaN	AlN	InN
C_{11} (GPa)	390	396	223
C_{12} (GPa)	145	137	115
C_{13} (GPa)	106	108	92
C_{33} (GPa)	398	373	224
C_{44} (GPa)	105	116	48

When a layer is grown pseudomorphically on a substrate, i.e. without any plastic strain relaxation, the in-plane lattice parameters are elastically deformed, while the minimization of the elastic energy is leading to a relaxation of the crystal along the growth direction. The latter is mainly determined by the substrate choice and corresponds to the crystal direction that is equivalent to the surface normal of the structure. Without loss of generality, the growth axis shall be lying in the y - z -plane in the following, forming an angle Θ with the c -axis ($\parallel z$). The

elements of the strain tensor are then obtained via [32]:

$$\begin{pmatrix} \epsilon_{xx} \\ \epsilon_{yy} \\ \epsilon_{zz} \\ 2\epsilon_{yz} \\ 2\epsilon_{zx} \\ 2\epsilon_{xy} \end{pmatrix} = \begin{pmatrix} \epsilon_{xx}^* + \epsilon_{xz}^* \frac{\sin\Theta}{\cos\Theta} \\ \epsilon_{xx}^* \\ \epsilon_{zz}^* + \epsilon_{xz}^* \frac{\cos\Theta}{\sin\Theta} \\ 0 \\ 2\epsilon_{xz}^* \\ 0 \end{pmatrix}, \quad (2.5)$$

where the strain components ϵ_{xx}^* and ϵ_{zz}^* are defined by the deformation of the equilibrium lattice parameters a and c to the strained values a^* and c^* , respectively:

$$\epsilon_{xx}^* = \frac{a^* - a}{a} \quad \text{and} \quad \epsilon_{zz}^* = \frac{c^* - c}{c}. \quad (2.6)$$

The off-axis strain ϵ_{xz}^* is given by [32]:

$$\epsilon_{xz}^* = \frac{[(C_{11} + C_{12} + C_{13}\epsilon_{zz}^*/\epsilon_{xx}^*)\sin^2\Theta + (2C_{13} + C_{33}\epsilon_{zz}^*/\epsilon_{xx}^*)\cos^2\Theta]\epsilon_{xx}^*\sin\Theta\cos\Theta}{C_{11}\sin^4\Theta + 2(C_{13} + 2C_{44})\sin^2\Theta\cos^2\Theta + C_{33}\cos^4\Theta}. \quad (2.7)$$

In the following, the two extreme cases for Θ shall be briefly discussed. The major part of III-nitride structures is fabricated with a surface orientation corresponding to one of the main crystal facets highlighted in Fig. 2.1. Among these, c -plane growth corresponding to $\Theta = 0$ is widely preferred due to the superior crystal qualities obtained. Typically, the uniaxial symmetry C_{6v} is maintained in such structures: $\epsilon_{xx} = \epsilon_{yy}$. The condition $\sigma_{zz} = 0$ transforms Eq. (2.4) in this case into:

$$\epsilon_{zz} = -\frac{2C_{13}}{C_{33}}\epsilon_{xx}^*. \quad (2.8)$$

By contrast, growth with a - or m -plane surface orientation corresponding to $\Theta = 90^\circ$ usually breaks the uniaxial symmetry of the crystal. The basal-plane isotropy is lifted ($\epsilon_{xx} \neq \epsilon_{yy}$) and the C_{6v} -symmetry is transformed into a C_{2v} one. The condition $\sigma_{yy} = 0$ leads to:

$$\epsilon_{yy} = -\frac{C_{12}\epsilon_{xx}^* + C_{13}\epsilon_{zz}^*}{C_{11}}. \quad (2.9)$$

2.2 Optical Properties

The interaction between a semiconductor and an electromagnetic light-wave is mainly determined by the electronic properties of the chemical bonds. A detailed knowledge of the optical properties of a material is of essential importance for the operation and the design of corresponding devices.

2.2.1 Band Structure

Once their distance is sufficiently small, two hydrogen atoms in free space bind together and form a molecule. The overlapping valence atom-orbitals interact and split up into bonding and anti-bonding (occupied and unoccupied, respectively) states - the molecular orbitals. Now,

the molecule defines the energetically favorable state - the ground state of the system. This approach can be easily transferred to the solid state. The only difference is that here the huge number of involved atoms creates quasi-continuous energy bands instead of single orbitals. The occupied states build the valence band (VB) and the unoccupied ones the conduction band (CB). In the latter excited electrons are mobile and can freely flow through the crystal, whereas electrons in the VB are rather localized and can only move via hopping processes through a limited number of potentially unoccupied states.² The minimum energy separation in between CB and VB defines the bandgap E_G of the semiconductor.

The band structure of a semiconductor describes the energy eigenvalues of electrons as a function of their momentum. In a perfect crystal it is defined by the Hamiltonian [33]:

$$\begin{aligned} \hat{H} = & \sum_i \frac{\hat{p}_i^2}{2m_i} + \sum_j \frac{\hat{P}_j^2}{2M_j} + \frac{1}{2} \sum_{i \neq i'} \frac{e^2}{|\mathbf{r}_i - \mathbf{r}_{i'}|} - \sum_{i,j} \frac{Z_j e^2}{|\mathbf{r}_i - \mathbf{R}_j|} + \frac{1}{2} \sum_{j \neq j'} \frac{Z_j Z_{j'} e^2}{|\mathbf{R}_j - \mathbf{R}_{j'}|} \\ & + \hat{H}_{\text{so}} + \hat{H}_{\text{ss}} + \hat{H}_{\text{hfs}} + \hat{H}_{\text{ext}} . \end{aligned} \quad (2.10)$$

Electrons are identified by index i , while j corresponds to the nuclei, \mathbf{r} and \mathbf{R} denote their respective coordinates. Z and e are the atomic number and the electron elementary charge, respectively. The first two terms contain the kinetic energy of the electrons and the nuclei, \hat{p} and \hat{P} denote the corresponding momentum operators. The subsequent terms describe the electrostatic electron-electron, electron-nucleus, and nucleus-nucleus interaction, respectively. Further considered are the spin-orbit \hat{H}_{so} , the spin-spin \hat{H}_{ss} , and the hyperfine interaction \hat{H}_{hfs} . Potential external perturbations are taken into account via \hat{H}_{ext} .

A straightforward solution of the multiparticle-Hamiltonian in Eq. (2.10) without any simplification is obviously out of reach. A first one, the adiabatic approximation, succeeds when considering that the nuclei are much more massive than the electrons and that they are thus moving much slower. Indeed, lattice vibrations - so-called phonons - exhibit frequencies around 10^{13} Hz, while electronic excitations in the visible range correspond to frequencies in the range of 10^{15} Hz. Hence, it is reasonable to assume that the electron cloud instantaneously follows the motion of the nucleus and that at the same time, the nuclei only experience a temporal average of the electron fluctuations. Using the mean-field approximation, the problem can be further simplified. Here, the electron-electron interaction term, that is left unchanged in the adiabatic limit, is reduced to the movement of a single electron in the averaged background potential $V(\mathbf{r})$, which comprises the influence of the nuclei and the remaining electron cloud. This leads to the single-electron Schrödinger-equation:

$$\hat{H}_{1e} \phi_q(\mathbf{r}) = \left[\frac{\hat{p}^2}{2m_0} + V(\mathbf{r}) \right] \phi_q(\mathbf{r}) = E_q \phi_q(\mathbf{r}) , \quad (2.11)$$

where m_0 denotes the free electron mass and the index q refers to the various eigenstates. The complexity of this problem can be further reduced by considering the translational symmetry of the crystal lattice and applying Bloch's theorem: here, the band structure of the whole crystal is obtained by solving the Schrödinger-equation within the unit cell of the reciprocal lattice - the so-called Brillouin-zone (BZ). It is obtained by the Fourier-transform of the real

²Unoccupied states in the VB can either be created by an external excitation or by doping of the crystal.

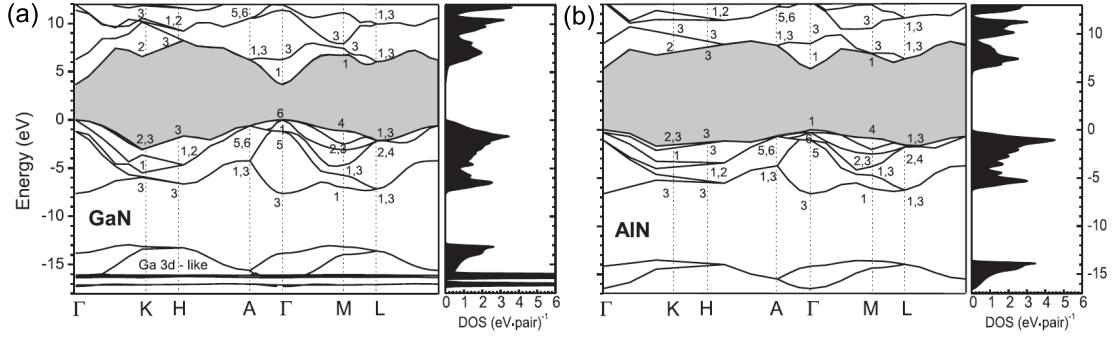


Figure 2.2: Computed band structures of (a) GaN and (b) AlN displayed in the reduced zone scheme around high symmetry points of the first BZ. The forbidden energy band is shaded in gray, its minimum at the Γ -point ($\mathbf{k} = 0$) sets the bandgap energy E_G . The corresponding density of states (DOS) is also shown (adapted from Ref. [35]).

space lattice and also exhibits hexagonal symmetry.³

Calculated band structures of GaN and AlN displayed within the first BZ are shown in Fig. 2.2: CB and VB states are separated by the forbidden gap and both the maximum of the VB and the minimum of the CB are found at the Γ -point, corresponding to zero momentum ($\mathbf{k} = 0$). Such direct bandgap semiconductors are efficient light-absorbers and emitters, since photons possessing a negligible wave-vector can induce a direct transition of electrons at the bandgap.⁴ The lowest CB features s -orbital symmetry and is only spin-degenerated. For small momenta $\mathbf{k} = (k_x, k_y, k_z)$ around the Γ -point, the corresponding energy dispersion of delocalized electrons can be expressed in the parabolic approximation:

$$E_c(\mathbf{k}) = E_c(0) + \frac{\hbar^2 k_x^2}{2m_x^*} + \frac{\hbar^2 k_y^2}{2m_y^*} + \frac{\hbar^2 k_z^2}{2m_z^*} = E_c(0) + \frac{\hbar^2 k_{\perp}^2}{2m_{\perp}^*} + \frac{\hbar^2 k_{\parallel}^2}{2m_{\parallel}^*}, \quad (2.12)$$

where \hbar denotes the reduced Planck-constant. Due to the interaction with the crystal potential the free-space dispersion of the electron $\hbar^2 \mathbf{k}^2 / 2m_0$ is modified, leading to the description of an effective electron mass m^* , which is usually smaller than the free electron mass m_0 [31]. Note that depending on the symmetry of the crystal and thus the potential $V(\mathbf{r})$, m^* can be anisotropic: $\mathbf{m}^* = (m_x^*, m_y^*, m_z^*)$. For wurtzite materials the uniaxial symmetry of the lattice leads to different effective electron masses in the basal plane of the BZ: $k_x^2 + k_y^2 = k_{\perp}^2$ (directions $\Gamma - K$ and $\Gamma - M$ in Fig. 2.2), and the $k_z = k_{\parallel}$ direction ($\Gamma - A$).

The VBs can be described in a similar manner: their concave dispersion can be interpreted either by an electron with negative effective mass or by a positively charged quasi-particle with positive mass - the hole. The latter corresponds to a missing electron in the VB that allows hopping processes of the other VB electrons and thus an effective charge carrier transport. Unoccupied states in the VB can either be created by an external excitation (e.g. light), a finite temperature, or by p -type doping. In the latter case, foreign atoms are inserted into the crystal that feature a lower number of valence electrons than the atom they are replacing. The

³Detailed descriptions of the wurtzite lattice in the real and reciprocal space can e.g. be found in Ref. [34].

⁴An optical transition occurring at an indirect bandgap (e.g. silicon) requires a phonon to fulfill momentum conservation making this process much more unlikely.

missing electron introduces a hole in the VB that becomes mobile with a low activation energy. In III-nitrides Mg-atoms incorporated at the metal sites are used to achieve *p*-type doping. Likewise, *n*-type doping creating free electrons in the CB can be obtained by introducing foreign atoms with a larger number of valence electrons: Si or Ge instead of a metal atom. Note finally that the anisotropy as well as the absolute value of the effective hole masses are usually larger than for the electron in the CB and that owing to the interactions occurring in between the VBs strong non-parabolicity effects in the bands may arise even close to $\mathbf{k} = 0$.

Light-Matter Interaction

The interaction between the electronic states of a medium and the vacuum light-field satisfying Maxwell's equations can be treated by time-dependent perturbation theory. Using the Coulomb-gauge and neglecting quadratic perturbation-terms [33], the Hamiltonian of the system from Eq. (2.11) is complemented by:

$$\hat{H}_{\text{em}} = \frac{e}{m_0 c_0} \mathbf{A} \cdot \hat{\mathbf{p}}, \quad (2.13)$$

where c_0 denotes the vacuum speed of light and \mathbf{A} is the magnetic vector-potential of the electromagnetic perturbation.

Fermi's golden rule determines the absorption probability between the VB Bloch-state $|v\rangle$ (with energy E_v and wave-vector \mathbf{k}_v) and the CB-state $|c\rangle$ (E_c & \mathbf{k}_c) per unit-volume:

$$R(\hbar\omega) = \frac{2\pi}{\hbar} \sum_{\mathbf{k}_c, \mathbf{k}_v} |\langle c | \hat{H}_{\text{em}} | v \rangle|^2 \delta(E_c(\mathbf{k}_c) - E_v(\mathbf{k}_v) - \hbar\omega). \quad (2.14)$$

The δ -function ensures energy conservation and $\hbar\omega$ corresponds to the quantized photon energy. Rewriting \mathbf{A} in terms of the electric-field amplitude $\mathbf{E} = |\mathbf{E}|\mathbf{e}$ of the incoming light-wave, and assuming only vertical transitions in the reciprocal space due to the negligible momentum of the photon ($\mathbf{k} = \mathbf{k}_c = \mathbf{k}_v$), Eq. (2.14) can be transformed into [33]:

$$R(\hbar\omega) = \frac{\pi e^2}{2\hbar m_0^2 \omega^2} |\mathbf{E}|^2 |\mathbf{p}_{cv}|^2 \sum_{\mathbf{k}} \delta(E_c(\mathbf{k}) - E_v(\mathbf{k}) - \hbar\omega). \quad (2.15)$$

Here, $|\mathbf{p}_{cv}|^2$ denotes the transition matrix-element, which can be placed in front of the summation over the reciprocal space when assuming only a small variation for low \mathbf{k} . It is defined by:

$$\mathbf{p}_{cv} = \langle c | \mathbf{e} \cdot \hat{\mathbf{p}} | v \rangle, \quad (2.16)$$

and strongly depends on the polarization of the incoming light via \mathbf{e} . The transition matrix-element further sets the oscillator strength of the corresponding optical transition:

$$f_{cv} = \frac{2 |\mathbf{p}_{cv}|^2}{m_0 \hbar \omega}. \quad (2.17)$$

Considering an infinite number of allowed \mathbf{k} -states in the first BZ, the summation over the

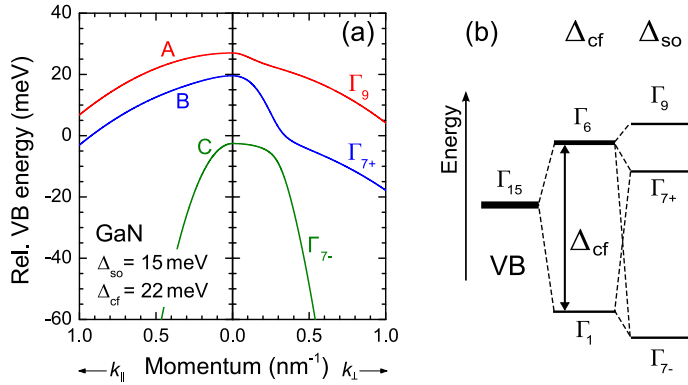


Figure 2.3: Valence bands of GaN at the Γ -point: (a) dispersion of the three uppermost VBs for small wavevectors k_{\parallel} (left) and k_{\perp} (right). (b) Δ_{cf} and Δ_{so} lift the degeneracy of the VBs: the VB-symmetries are indicated in the Rashba-notation [38], the line thickness corresponds to the degeneracy degree.

δ -function in Eq. (2.15) can be rewritten in the form:

$$D_{cv}(\hbar\omega) = \frac{2}{8\pi^3} \int_{BZ} \delta(E_c(\mathbf{k}) - E_v(\mathbf{k}) - \hbar\omega) d^3\mathbf{k}, \quad (2.18)$$

Here, D_{cv} defines the joint-density of states (JDOS), which is mainly depending on the effective carrier masses. Eventually, the transition probability R and the absorption coefficient α of a material are related by the proportionality relationship:

$$\alpha(\hbar\omega) \sim \frac{\hbar\omega}{|\mathbf{E}|^2} R(\hbar\omega) \sim f_{cv} \cdot D_{cv}(\hbar\omega). \quad (2.19)$$

In summary, the light-matter interaction strength depends on the one hand on the bare dispersion of the band structure via D_{cv} , and on the other one on the symmetry of the respective electron and hole-bands via the oscillator strength f_{cv} . This statement is valid when considering coupling to the vacuum light-field. It can be modified in photonic structures by a limited number of allowed photon states (cf. Ch. 4 and Ref. [36]).

Valence-Band Order and Selection Rules

Unlike the s -like CB, the three uppermost VBs in III-nitrides possess p -orbital symmetry. In a cubic system they would be degenerate and isotropic. However, due to the hexagonal symmetry of the wurtzite structure the degeneracy of the p_z -orbital is lifted with respect to the others. The energy splitting, given by the crystal-field energy Δ_{cf} , is closely related to the c/a -ratio (cf. Fig. 2.3(b)). When spin-orbit interaction Δ_{so} comes additionally into play, the degeneracy of the other two p -orbitals is also lifted. The energy splitting of the VBs is further accompanied by a change in symmetry: for positive values of Δ_{so} and Δ_{cf} (GaN-case, cf. Ref. [37]), the VBs exhibit Γ_9 , Γ_{7+} , and Γ_{7-} symmetry in order of decreasing energy [38]. They are often called heavy-hole (hh), light-hole (lh) and split-off (so) bands, their respective optical transitions with the Γ_7 -CB being denoted as A, B, and C in the following.

Figure 2.3(a) shows the VB-dispersion in relaxed bulk GaN around the Γ -point. It has been calculated using the $k \cdot p$ -formalism described in Sec. A.1. The uniaxial anisotropy leading to anisotropic effective masses and the occurrent non-parabolicities due to p -orbital repulsion can be clearly resolved. Strong interaction occurs in particular for the B and C bands in k_{\perp} -direction. The A and B-bands exhibit a typical energy splitting of 8 meV at the Γ -point and

\mathbf{p}_{su}	$\mathbf{u}_1 \mathbf{u}_4$	$\mathbf{u}_2 \mathbf{u}_5$	$\mathbf{u}_3 \mathbf{u}_6$
\mathbf{s}_1	$-\frac{1}{2}P_{\perp}e^{i\phi}\sin\theta$	$-\frac{1}{2}P_{\perp}e^{-i\phi}\sin\theta$	$\mp\frac{i}{\sqrt{2}}P_z\cos\theta$
\mathbf{s}_2	$\mp\frac{1}{2}P_{\perp}e^{-i\phi}\sin\theta$	$\mp\frac{1}{2}P_{\perp}e^{i\phi}\sin\theta$	$\frac{i}{\sqrt{2}}P_z\cos\theta$

Table 2.3: Transition matrix elements \mathbf{p}_{su} between the VB and CB-basis states following Ref. [39]. The polarization vector of light is expressed in spherical coordinates: $\mathbf{e} = (\sin\theta \cos\phi, \sin\theta \sin\phi, \cos\theta)$

feature similar effective masses in k_{\parallel} -direction.

In order to describe the optical selection rules in the BZ-center, the following set of basis-functions shall be introduced [40]:

$$\begin{aligned}
 \text{Conduction Band} \quad \mathbf{s}_1 &= |iS \uparrow\rangle & \mathbf{s}_2 &= |iS \downarrow\rangle \\
 \text{Valence Band} \quad \mathbf{u}_1 &= \left| -\frac{(X+iY)}{\sqrt{2}} \uparrow \right\rangle & \mathbf{u}_2 &= \left| \frac{(X-iY)}{\sqrt{2}} \uparrow \right\rangle & \mathbf{u}_3 &= |Z \uparrow\rangle \\
 & \mathbf{u}_4 = \left| -\frac{(X+iY)}{\sqrt{2}} \downarrow \right\rangle & \mathbf{u}_5 &= \left| \frac{(X-iY)}{\sqrt{2}} \downarrow \right\rangle & \mathbf{u}_6 &= |Z \downarrow\rangle
 \end{aligned} \tag{2.20}$$

Here, the arrows denote the electron spin projection. The orbital basis can be represented by the spherical harmonic functions $\mathbf{Y}_l^m(\theta, \phi)$ of the hydrogen-problem:

$$\begin{aligned}
 |S\rangle &= \mathbf{Y}_0^0(\theta, \phi) = \sqrt{\frac{1}{4\pi}} & |X\rangle &= \mathbf{Y}_1^{-1}(\theta, \phi) = \sqrt{\frac{3}{8\pi}} \sin\theta \exp(-i\phi) \\
 |Y\rangle &= \mathbf{Y}_1^1(\theta, \phi) = -\sqrt{\frac{3}{8\pi}} \sin\theta \exp(i\phi) & |Z\rangle &= \mathbf{Y}_1^0(\theta, \phi) = \sqrt{\frac{3}{4\pi}} \cos\theta,
 \end{aligned} \tag{2.21}$$

where l and m denote the angular and magnetic quantum numbers, respectively. Since the CB exhibits an isotropic s -orbital symmetry,⁵ the transition-matrix elements for the optical transitions A, B, and C are mainly governed by the symmetries of the VB Bloch-states $|v_j\rangle$ (with $j = 1, 2, \dots, 6$ for hh, lh, and so-bands with spin degeneracy). They can be expressed as a superposition of the basis functions:

$$|v_j\rangle = \sum_{i=1}^6 x_{ij} \cdot \mathbf{u}_i \tag{2.22}$$

Correspondingly, the respective transition matrix elements from Eq. (2.16) can be expressed in terms of the transition matrix-elements \mathbf{p}_{su} in between the VB and CB-basis functions (cf. Tab. 2.3), that are related to:

$$P_{\perp} = \langle S | \hat{p}_x | X \rangle \quad \text{and} \quad P_z = \langle S | \hat{p}_z | Z \rangle. \tag{2.23}$$

Here $\hat{p}_{x/z}$ expresses the momentum operator in the x - and z -direction, respectively. In the quasi-cubic approximation, both elements are assumed to be equal: $P_{\perp} = P_z = P$ [39, 41]. Finally, P is related to the Kane-parameter $E_P = 2|P|^2/m_0$, which depends on E_G and the

⁵In the quasi-cubic approximation according to Ref. [41].

effective carrier masses and amounts to 16.9 and 23.8 eV for GaN and AlN, respectively [42].

Eventually, the selection rules of the optical transitions depend on the orientation of the orbital dipole with respect to the electric field amplitude \mathbf{E} of the incoming or emitted light. The uniaxial character of the wurtzite cell results in different oscillator strengths for electric-field polarization perpendicular and parallel to the c -axis - also referred to as the optical axis. The selection rules can be expressed in terms of the relative oscillator strength f_{osc} . The latter corresponds to the squared projection of the Bloch-state $|\nu_j\rangle$ on the VB-basis \mathbf{u}_i and is related to f_{cv} by the Kane-parameter. The relative oscillator strengths can be calculated by $k.p$ -simulations (cf. Sec. A.1) and obey the sum rule: $\sum_{i=A,B,C} f_{\text{osc},i}^{\mathbf{E}\parallel c} = \sum_{i=A,B,C} f_{\text{osc},i}^{\mathbf{E}\perp c} = 1$. Table 2.4 summarizes the symmetry and f_{osc} of the optical transitions at the Γ -point in GaN. The hh-band is exclusively composed of $p_{x/y}$ -orbitals. Therefore, an optical excitation of A is forbidden for light polarization $\mathbf{E}\parallel c$. By contrast, B- and C-transitions are allowed in both polarization directions.

Table 2.4: Symmetries and relative oscillator strengths of the three topmost VBs A, B, and C in unstrained GaN at the Γ -point.

	Symmetry	$f_{\text{osc}}^{\mathbf{E}\perp c}$	$f_{\text{osc}}^{\mathbf{E}\parallel c}$
A	Γ_9	0.5	0
B	Γ_{7+}	0.44	0.12
C	Γ_{7-}	0.06	0.88

While InN exhibits similar selection rules as GaN [31], the VB-order in AlN is reversed [43, 44]: owing to a strongly negative crystal-field energy the uppermost VB has Γ_{7+} symmetry leading to completely different selection rules. Here, the fundamental bandgap is set by the B-transition which is almost exclusively allowed for $\mathbf{E}\parallel c$, whereas A and C are located about 200 meV higher in energy building the bandgap for $\mathbf{E}\perp c$. Finally, it is worth mentioning that the selection rules, as well as the valence band ordering and the transition energies, may be significantly modified by the experienced lattice strain.

Impact of Strain

The influence of strain on the band structure of an epitaxial layer results from the deformation of the lattice and thus the modification of the chemical bondings. In general, compressive strain leads to an increase of the bandgap energy and vice versa for tensile deformation. This can be understood as follows: for compressive strain, the decreased distance in between bonded atoms causes an increased orbital overlap and thus a strengthening of the respective interaction in between them, eventually leading to an enlarged energy separation of bonding and anti-bonding states. Moreover, depending on the nature of the deformation, even the symmetry of the bondings and thus of the unit cell can be modified, which immediately influences the band structure symmetries and thus the selection rules. This becomes in particular important when different surface orientations are considered (cf. Sec. 2.1.2). The modification of the band structure due to strain around the bandgap is determined by the CB and VB deformation potentials [31, 40].

Figure 2.4 shows the dependence of the transition energies and the selection rules on the lattice deformation in bulk GaN. The data have been computed within the bulk $k.p$ -approach of Chuang and Chang [40], which is explained in detail in Sec. A.1. Two different cases are examined: c -plane and m -plane surface orientation. In the first one, the maintained uniaxial

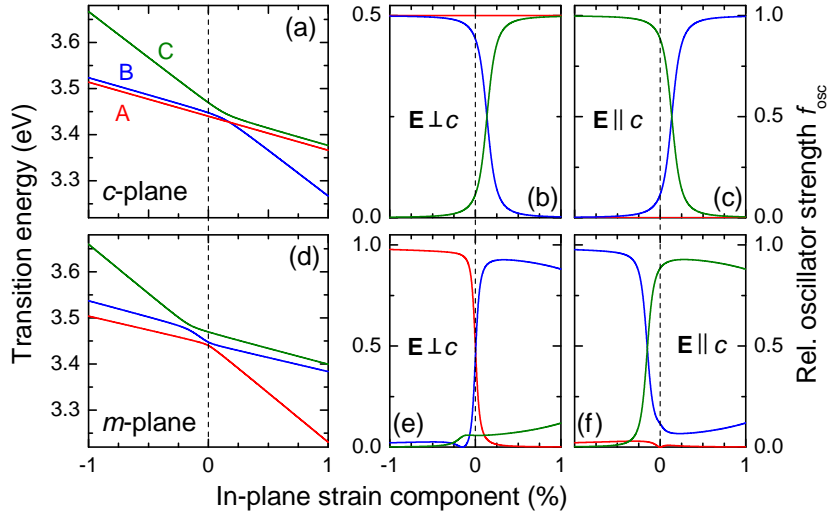


Figure 2.4: The impact of strain on the bandgap in bulk GaN ($\mathbf{k} = 0$): (a) variation of the transition energies of A, B, and C (marked in red, blue, and green color, respectively) for c -plane orientation as a function of the in-plane strain $\epsilon_{xx} = \epsilon_{yy}$, assuming Eq. (2.8). (b,c) Corresponding relative oscillator strengths f_{osc} for light polarization perpendicular and parallel to the optical c -axis. Note that due to the surface orientation the polarization $\mathbf{E} \parallel c$ is widely inapparent. (d-f) Equivalent representation for m -plane orientation assuming the special case $\epsilon_{xx} = \epsilon_{zz}$ and Eq. (2.9). The light polarization parallel to the growth axis has been omitted. The situation for relaxed GaN $\epsilon_{xx} = \epsilon_{yy} = \epsilon_{zz} = 0$ is marked by vertical dashed lines.

symmetry of the crystal ($\epsilon_{xx} = \epsilon_{yy}$) prevents any interaction between the heavy-hole band and the other two VBs. Therefore, the A-transition exhibits the same selection rules as in the relaxed case (cf. Tab. 2.4), whatever the strain value. The situation is different for the B and C-transitions. Here, the strong interaction and the differing deformation potentials lead to an anti-crossing for tensile in-plane strain $\epsilon_{xx} \approx 0.007$. This goes along with a direct exchange in f_{osc} . For planar structures with c -plane orientation, the polarization direction $\mathbf{E} \parallel c$ is of minor importance:⁶ the projection of the electric-field vector onto the c -axis of the transversal light-wave is zero for normal incidence and only becomes partly effective for high angles of incidence. Hence, the optical response of such a structure appears almost isotropic, being governed exclusively by $f_{osc}^{E \perp c}$. For relaxed GaN and compressive strain values, A and B-transitions that are separated by about 8 meV and feature a similar f_{osc} build the fundamental bandgap, while the C-transition is widely absent. This situation changes for larger tensile strain, where the A- and C-transition dominate for $\mathbf{E} \perp c$ and thus govern the optical response, but B marks the ground state.

According to Eq. (2.9) the m -plane surface orientation leaves two degrees of freedom: the in-plane strain components ϵ_{xx} and ϵ_{zz} can vary independently. They are only determined by design and fabrication of the respective structure. However, in order to illustrate the deviating behavior that is common to all biaxially strained structures, the special case $\epsilon_{xx} = \epsilon_{zz}$ shall be explored. Biaxial strain ($\epsilon_{xx} \neq \epsilon_{yy}$) leads to a loss of the basal plane symmetry, i.e. x - and y -direction are no longer equivalent and the uniaxial crystal symmetry is lifted. Now the heavy-

⁶This is not true when the surface symmetry is broken, such as in edge-emitting LDs.

hole band is allowed to interact with the other VBs. This leads to an additional anti-crossing that is occurring between A- and B-bands for zero strain in contrast to the c -plane case, where both simply cross. Moreover, due to the loss of symmetry now three different polarization directions can be distinguished. In Fig. 2.4 the light polarization parallel to the growth axis $\mathbf{E} \parallel y$ has been omitted, since it is only of minor impact in analogy to the $\mathbf{E} \parallel c$ case for a c -plane structure. However, since the optical axis lies within the surface plane, the optical response of such a structure is strongly anisotropic. For compressive strain the ordinary polarization direction, i.e. $\mathbf{E} \perp c$, is dominated by the A-transition, while the extraordinary one ($\mathbf{E} \parallel c$) is ruled by C for small strain values and by B for larger ones. The effect of a correspondingly anisotropic onset of absorption is referred to as dichroism. For a tensile deformation of the lattice, the situation is similar to the c -plane case. Now B- and C-transitions rule the optical response for the accessible polarization directions $\mathbf{E} \perp c$ and $\mathbf{E} \parallel c$, respectively, whereas the fundamental gap set by A is only allowed for polarization parallel to the growth axis and thus has only a marginal impact.

Although the fundamental bandgap features a very low oscillator strength for tensile strain for both surface orientations, luminescence would predominantly emerge from the lowest energy state due to the relaxation of carriers. This situation is very similar to the case of AlN (cf. Fig. 2.5) and might lead to misinterpretations regarding the fundamental bandgap in c -plane layers [44, 45]. Note finally that the strain influence may not be exclusively restricted to the transition energies and oscillator strength, but can also modify the effective carrier masses, in particular in the VB.

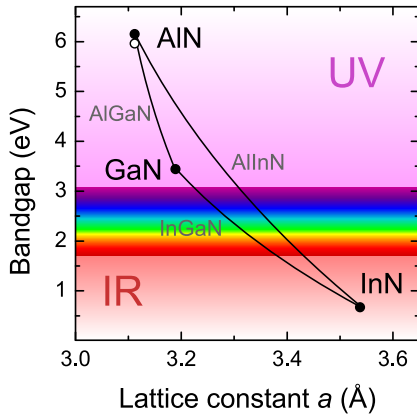


Figure 2.5: Room temperature optical bandgap of III-nitride compounds in the wurtzite configuration versus basal plane lattice constant a : the connecting lines emphasize the possibility of continuously tuning the bandgap via alloying from the ultraviolet (UV) down to the infrared (IR) energy range, while covering the whole visible spectrum. For AlN the bandgaps for both polarizations of light are shown: $\mathbf{E} \parallel c$ (open circle) and $\mathbf{E} \perp c$ (dot) [44].

Bandgap Engineering

GaN and AlN feature a bandgap in the ultraviolet (UV) spectral range, whereas that of InN lies in the infrared (IR). In order to produce devices that emit light in the visible range or to find the right compromise between lattice mismatch and energy barrier height in heterostructures (cf. Sec. 2.3), the bandgap energy E_G has to be tuned. Apart from a deliberate strain management, this can be realized by growing a III-nitride ternary alloy, which is composed out of metal atoms of two different species A and B : $A_xB_{1-x}N$. Figure 2.5 shows the bandgap of the binary III-nitride compounds as a function of their equilibrium lattice constant and highlights the possibility of engineering E_G via alloying. The lattice constants of the ternary alloys InGaIn,

AlGa_xN, and AlIn_xN basically follow Vegard's law:⁷

$$\begin{aligned} a_{A_xB_{1-x}N} &= x \cdot a_{AN} + (1-x) \cdot a_{BN}, \\ c_{A_xB_{1-x}N} &= x \cdot c_{AN} + (1-x) \cdot c_{BN}. \end{aligned} \quad (2.24)$$

By contrast, various other material properties and in particular the bandgap energy are subject to a characteristic bowing:

$$E_{G,A_xB_{1-x}N} = x \cdot E_{G,AN} + (1-x) \cdot E_{G,BN} - x(1-x) \cdot b_{ABN}, \quad (2.25)$$

where b denotes the bowing parameter. Throughout this thesis a value of $b_{\text{AlGaN}} = 0.7 \text{ eV}$ will be used [31, 47].

2.2.2 Excitons

The above-mentioned considerations have been deduced within the single-electron picture. In a more realistic framework, the attraction of free electrons and holes in a semiconductor due to Coulomb interaction should be taken into account, leading occasionally to a strong modification of the band structure [48]. In the vicinity of the bandgap free electrons and holes bind together and form a hydrogen-like quasi-particle - the so-called exciton [9, 49]. It can be described by the following Schrödinger-equation:

$$\left[-\frac{\hbar^2}{2m_e^*} \nabla_{\mathbf{r}_e}^2 - \frac{\hbar^2}{2m_h^*} \nabla_{\mathbf{r}_h}^2 - \frac{e^2}{4\pi\epsilon_0\epsilon_r|\mathbf{r}_e - \mathbf{r}_h|} \right] \psi(\mathbf{r}_e, \mathbf{r}_h) = (E - E_G) \psi(\mathbf{r}_e, \mathbf{r}_h). \quad (2.26)$$

Here, $\mathbf{r}_{e/h}$ denotes the real space coordinates of the electron/hole, ∇^2 corresponds to the Laplacian-operator, ϵ_0 and ϵ_r are the vacuum permittivity and the relative static permittivity of the material, respectively. The first two terms describe the kinetic energy of the electron and hole via their respective effective masses m_e^* and m_h^* . A transformation into center-of-mass and relative coordinates simplifies the problem and eventually leads for a three-dimensional (3D) material to the discrete exciton eigenenergies ($q \in \mathbb{N}$):

$$E_X = E_G + \frac{\hbar^2 \mathbf{k}^2}{2M^*} - \frac{R^*}{q^2}, \quad (2.27)$$

where M^* denotes the exciton mass: $M^* = m_e^* + m_h^*$, and \mathbf{k} corresponds to the sum of electron and hole wave-vectors. The effective Rydberg-energy R^* is also referred to as the exciton binding energy E_B :

$$R^* = E_B = \frac{\mu^* e^4}{2(4\pi\epsilon_0\epsilon_r\hbar)^2} = \frac{\mu^*}{m_0} \frac{1}{\epsilon_r^2} \cdot 13.6 \text{ eV}. \quad (2.28)$$

The reduced mass μ^* of the exciton is obtained by the relation:

$$\mu^* = \frac{m_e^* \cdot m_h^*}{m_e^* + m_h^*}. \quad (2.29)$$

⁷For AlInN, the increased ionicity of the bonding and the strong discrepancy between the metal atom radii might result in slight deviations from Vegard's law [46].

By analogy to the hydrogen atom, an effective exciton Bohr-radius can be defined:

$$a_B = \frac{4\pi\epsilon_0\epsilon_r\hbar^2}{\mu^*e^2} = \frac{m_0}{\mu^*}\epsilon_r \cdot 5.29 \cdot 10^{-11} \text{ m}. \quad (2.30)$$

Table 2.5: Comparison of E_B and a_B for III-nitrides: the effective carrier masses have been adopted from Ref. [31], for the hole they were obtained from the VB-parameters using the procedure described in Ref. [40] at $\mathbf{k} = 0$. Anisotropic parameters have been averaged over the 3D space.

		GaN	AlN	InN
ϵ_r	$\mathbf{E} \perp c$	9.28 [50]	7.76 [51]	13.1 [52]
	$\mathbf{E} \parallel c$	10.1 [50]	9.32 [51]	14.4 [52]
m_e^*/m_0		0.2	0.3	0.07
m_{hh}^*/m_0		0.5	1.13	0.35
E_B (meV)	theo.	21.3	47.4	4.4
a_B (nm)	theo.	3.5	1.8	12.2
E_B (meV)	exp.	25 [53]	56 [44]	-

Table 2.5 summarizes E_B and a_B values for the binary III-nitride compounds. The theoretical values have been obtained using effective masses and static dielectric constants from the literature and Eqs. (2.28) and (2.30). Note that the effective masses stem from *ab initio* calculations and do not necessarily reflect the real values. Nevertheless, the computed E_B values agree quite well with the experimentally observed ones in GaN ($E_B = 25 \text{ meV}$) and AlN ($E_B = 56 \text{ meV}$). The larger E_G for AlN leads to larger effective masses and thus to an increased E_B value compared to GaN.⁸ According to the room temperature thermal energy $k_B T \approx 26 \text{ meV}$ (Boltzmann-constant k_B), III-nitrides, except for InN and In-rich alloys, feature very robust excitons that are even observable under ambient conditions. Note that quantum-confinement in lower dimensional structures can even strengthen E_B (cf. Sec. 2.3). In the following sections certain exciton characteristics shall be highlighted.

Exciton Properties

The optical response of an exciton is characterized by its energy E_X given by Eq. (2.27), its oscillator strength f_X and its linewidth γ_X . The dielectric susceptibility χ for a homogeneously-broadened exciton resonance ($\gamma_X = \gamma_{\text{hom}}$) is given by:

$$\chi(\hbar\omega) \sim \frac{f_X}{\hbar\omega - E_X - i\gamma_X}. \quad (2.31)$$

Each of the three VBs at the Γ -point forms its own exciton with the CB. In the following, these are named A, B, and C-excitons with regard to the VBs they belong to. Their symmetry and thus also the selection rules and oscillator strengths are basically transferred from the corresponding bands [54]. However, note that f_X is only different from zero for *s*-like exciton states and for different quantum numbers q in Eq. (2.27), f_X follows the dependence $f_X \sim 1/q^3$.

Considering an ideal system at zero temperature, the homogeneous natural linewidth γ_{nat} of an exciton is given by the radiative lifetime τ of the initial and final states (indices *i* and *f*,

⁸The opposite applies for InN: its low bandgap causes low effective mass parameters owing to the strong CB-VB interaction and thus a very low E_B value. Excitonic effects in pure InN are correspondingly small and usually hidden by a finite linewidth.

respectively):

$$\gamma_{\text{nat}} = \hbar \left(\frac{1}{\tau_i} + \frac{1}{\tau_f} \right). \quad (2.32)$$

In real structures the total homogeneous linewidth γ_{hom} is subject to additional contributions. For high carrier densities n , collisions occurring in between excitons (elastic or inelastic ones) with a characteristic scattering time $\tau_{\text{col}} = \tau_{\text{col}}(n)$ lead to a contribution $2/\tau_{\text{col}}$ [55]. It has been found to vary linearly with n in GaN epilayers [56]. Moreover, with increasing temperature T the occupancy of acoustic and optical phonon states has to be considered [57]:

$$\gamma_{\text{phon}}(T) = \alpha_{\text{ac}} T + \frac{\alpha_{\text{opt}}}{\exp(E_{\text{LO}}/k_{\text{B}} T) - 1}. \quad (2.33)$$

Here, α_{ac} and α_{opt} are material-dependent proportionality constants, and E_{LO} denotes the longitudinal-optical (LO) phonon energy, which amounts to 92 meV and 110 meV in GaN and AlN [58], respectively.

All the aforementioned mechanisms describe a homogeneous broadening of the transition leading to a Lorentzian lineshape for the excitonic resonance. For low free carrier concentrations, it should ideally converge toward the natural limit based on Eq. (2.32) when T approaches zero. However, due to non-idealities, such as impurities, residual strain variations or alloy composition fluctuations, the lineshape for $T \rightarrow 0$ often converges to a Gaussian of constant linewidth γ_{inh} . This inhomogeneous broadening is very common for III-nitrides: it is not necessarily a signature of a lower crystal quality, but mainly originates from the reduced exciton Bohr-radius which critically increases the sensitivity to lattice imperfections and inhomogeneities. In conclusion, in realistic structures the broadening of an exciton line at finite temperature is usually given by the convolution of a certain homogeneous and inhomogeneous linewidth resulting in a Voigt-profile.

Closely related to the inhomogeneous linewidth, that arises due to fluctuations in the potential landscape, is the effect of carrier localization. It leads to a finite energy difference between the exciton absorption and emission maxima. Indeed, whereas absorption occurs according to the statistic distribution of oscillators and thus the intrinsic material properties, luminescence is always influenced by carrier relaxation. Mobile excitons can relax into the valleys of the potential landscape or can be captured by impurity atoms leading for instance to the emission of localized or bound excitons.

Another characteristic property of excitons is their bosonic nature. Indeed, whereas both electrons and holes obey Fermi-statistics, the excitonic quasi-particle possesses an integer spin. This feature is essential for all effects related to the condensation of cavity-polaritons, which will be discussed in Ch. 4. Moreover, the excitonic properties and even the exciton itself are not invariant with respect to the carrier density. Chapter 3 will discuss the renormalization and the eventual dissociation of excitons in detail. Finally, note that this work mainly focuses on excitons in lower-dimensional structures, i.e. in QWs. Certain properties are modified with regard to the dimensionality. The subsequent Sec. 2.3 will highlight this aspect.

2.2.3 Refractive Index

The linear interaction between light and a medium in terms of absorption, transmission and reflection is described by the complex refractive index of the latter: $n = n_{\text{re}} + i n_{\text{im}}$. It is related to the dielectric function (DF) of the material: $\varepsilon = \varepsilon_1 + i\varepsilon_2 = n^2$. The imaginary part of the latter is linked to the absorption coefficient given by Eq. (2.19) via:

$$\alpha(\hbar\omega) = \frac{\omega}{c_0 n_{\text{re}}(\hbar\omega)} \varepsilon_2(\hbar\omega) . \quad (2.34)$$

Using the intensity of a plane light-wave: $I = 0.5\varepsilon_0 c_0 n_{\text{re}} |\mathbf{E}|^2$, Eq. (2.19) can be rewritten to:

$$\alpha(\hbar\omega) = \frac{\hbar\omega}{I} R(\hbar\omega) , \quad (2.35)$$

which leads to the expression of the imaginary part of the DF via:

$$\varepsilon_2 = \frac{\pi e^2}{m^2 \omega^2 \varepsilon_0} |\mathbf{p}_{\text{cv}}|^2 D_{\text{cv}} . \quad (2.36)$$

Finally, the real and imaginary parts of the refractive index and the DF are not independent of each other. They are linked by the Kramers-Kronig relations:

$$\varepsilon_1(\omega) = 1 + \frac{2}{\pi} \mathcal{P} \int_0^\infty \frac{\omega' \varepsilon_2(\omega')}{\omega'^2 - \omega^2} d\omega' , \quad (2.37)$$

$$\varepsilon_2(\omega) = -\frac{2\omega}{\pi} \mathcal{P} \int_0^\infty \frac{\varepsilon_1(\omega') - \varepsilon_0}{\omega'^2 - \omega^2} d\omega' , \quad (2.38)$$

where \mathcal{P} denotes the Cauchy principal value of the integral.

The scalar notation of the optical constants applies exclusively to isotropic materials. In optically anisotropic media the polarization-dependence of the transition-matrix elements \mathbf{p}_{cv} in Eq. (2.36) requires a tensorial expression:

$$\mathbf{n} = \begin{pmatrix} n_x & 0 & 0 \\ 0 & n_y & 0 \\ 0 & 0 & n_z \end{pmatrix} \quad \text{and} \quad \boldsymbol{\varepsilon} = \begin{pmatrix} \varepsilon_x & 0 & 0 \\ 0 & \varepsilon_y & 0 \\ 0 & 0 & \varepsilon_z \end{pmatrix} . \quad (2.39)$$

Here, light propagation with a certain polarization of \mathbf{E} is described by the projection on the optical axes of the crystal. Recalling the uniaxial anisotropy of III-nitrides with a single optical axis [0001], their optical properties are entirely determined by $n_x = n_y = n_o$ for $\mathbf{E} \perp c$, and $n_z = n_e$ for $\mathbf{E} \parallel c$, likewise for DF.

Figure 2.6 displays the dispersion of the anisotropic complex refractive index of GaN and AlN over a wide range of photon energies, covering both the transparency and the band edge region. The optical constants have been deduced from spectroscopic ellipsometry measurements at room temperature [59, 60]. The transparency regime, defined by $n_{\text{im}} = 0$ for both polarization directions, is governed by birefringence: light propagation is determined by different real parts of \mathbf{n} . Thereby in III-nitrides the inequality $n_e > n_o$ generally holds. This effect is mainly caused by the anisotropy of the high-energy transitions (> 7 eV) of the band structure which are impacting via Eq. (2.37). In the vicinity of the band edge, i.e. around the onset of absorption

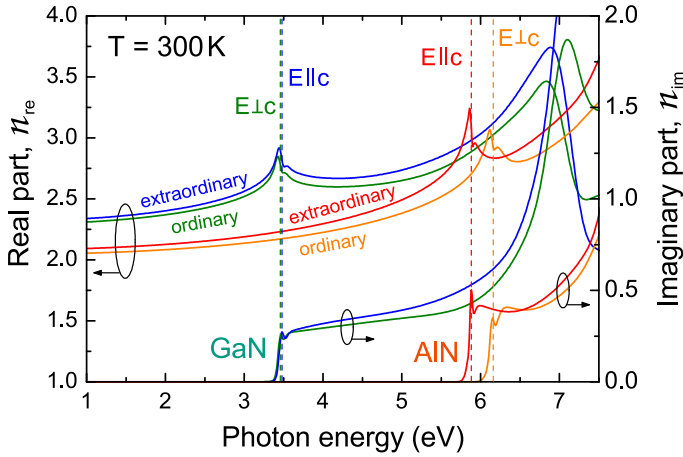


Figure 2.6: Anisotropic dispersion of the complex refractive index for GaN (blue-green) and AlN (red-orange) measured by ellipsometry at room temperature [59, 60]. Note the much lower bandgap for $E \parallel c$ in AlN due to the large negative Δ_{cf} value [44].

in n_{im} , the selection rules for the Γ -point as discussed in Sec. 2.2.1 come into play. This effect exists for GaN, but is much more pronounced for AlN where the large negative Δ_{cf} -energy leads to a much lower bandgap for $E \parallel c$. Note in addition that even for these room temperature data, excitons manifesting themselves as distinct peaks at the band edges are well-resolved owing to the large E_B -values.

2.3 III-Nitride based Quantum-Wells

In the early beginning the active region of optoelectronic semiconductor structures consisted simply of a bulk p - n -junction.⁹ By contrast, the major part of modern semiconductor devices, such as HEMTs, LDs and LEDs, or second generation solar cells, rely on heterostructures, i.e. epitaxial structures that are composed of different materials. In such layer stacks the material properties can be remarkably altered to the benefit of devices: for LEDs and LDs, the enhanced radiative recombination rate due to the confinement of charge carriers in QWs leads to a decrease in the threshold current density for LDs and to a remarkable overall increase of corresponding device efficiencies. Nowadays, QWs are a major building block of optoelectronic and photonic structures. The two-dimensional (2D) particle confinement therein leads to a modification of the electronic material properties that shall be discussed in the following.

2.3.1 Quantum Well Confinement

A semiconductor layer, that features a certain bandgap E_G and that is sandwiched in between two layers with higher bandgap values, represents a potential trap for mobile charge carriers. When the thickness L_{QW} of this layer corresponds to the order of the electron and hole de-Broglie wavelengths or the exciton Bohr-radius, the confinement is determined by quantum-mechanics and the layer defines a QW. Two types of QWs can be distinguished: type-I QWs, which confine both electrons and holes, and type-II QWs that feature a confinement potential for only one of the carrier species. Throughout this work, only type-I QWs will be considered. Here, the increased bandgap energy of the barriers causes a confinement potential that is typically apportioned by a 70 : 30-ratio in between the CB and the VB.

⁹This is still true for conventional first-generation solar cells based on Si.

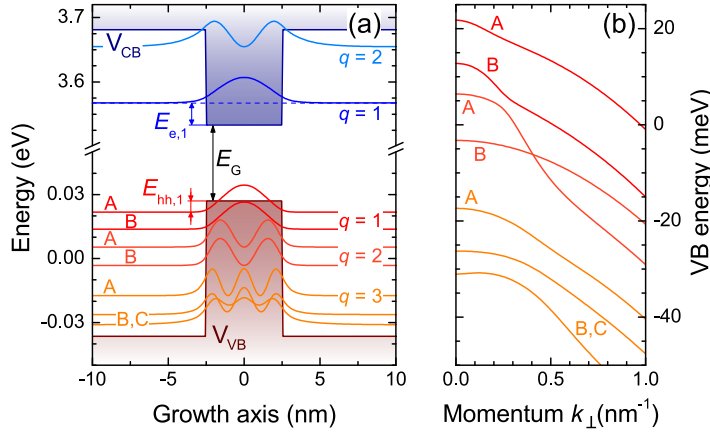


Figure 2.7: Simulation of a fictive 5 nm-thick *c*-plane GaN QW in between Al_{0.1}Ga_{0.9}N barriers without electric field: (a) energy levels and corresponding squared wave-functions. (b) VB dispersion as a function of the in-plane wave-vector.

The confinement-potential V_{QW} along the growth direction z in a QW results in quantized energy levels with quantum numbers $q = 1, 2, \dots$ for both electrons and holes. Their envelope functions Ψ_q and eigenvalues E_q are defined by the Schrödinger-equation [61]:

$$\left[-\frac{\hbar^2}{2m_z^*(z)} \cdot \frac{\partial^2}{\partial z^2} + V_{QW}(z) \right] \Psi_q(z) = E_q \Psi_q(z). \quad (2.40)$$

Figure 2.7(a) shows the eigenenergy spectrum of a field-free (cf. Sec. 2.3.3) 5 nm-thick *c*-plane GaN QW sandwiched in between infinite Al_{0.1}Ga_{0.9}N barriers. It has been calculated by means of the plane-wave Schrödinger- k . p -formalism described in Sec. A.1. For the CB, two levels $q_e = 1, 2$ with respective confinement energies $E_{e,1}$ and $E_{e,2}$ are obtained. By contrast, the VB-structure appears much more complex owing to the three VBs at play. According to Eq. (2.40), the confinement energies are governed by the effective carrier masses along the growth direction. Recalling Fig. 2.3 and the corresponding explanations, A- and B-bands exhibit large almost identical masses along k_{\parallel} . Therefore their energy splitting of about 8 meV in the bulk crystal is maintained for the respective subbands $q_h = 1, 2$. The situation appears different for the C-band which features a very light m_z^* , and thus a larger confinement energy. Moreover its energy position coincides with the B($q_h = 3$) sub-level leading to the formation of two mixed B/C sub-bands. Whereas carrier motion along the growth direction is restricted by the confinement potential, free electrons and holes are allowed to move within the 2D QW-plane. This motion is described by the in-plane band-dispersion $E(\mathbf{k}_{\perp})$, which is exemplified for the valence sub-bands in Fig. 2.7(b). According to the symmetries of the sub-bands, certain bands interact causing an anti-crossing behavior, while others cross. This can lead to a modification of the effective in-plane masses compared to the corresponding directions in the bulk case. Note also that in a QW the JDOS, which was defined for the 3D-case in Eq. (2.18), is modified: for parabolic bands, the 3D-JDOS rises with a square-root dependence from the band edge, while in 2D it corresponds to a step-like function.

The band-to-band transition energy for zero in-plane momentum in a QW is enlarged compared to the bulk bandgap E_G by the confinement energies of the respective electron and hole sub-bands. For a certain QW-level ($q_e \leftrightarrow q_h$) it amounts to (cf. Fig. 2.7(a)):

$$E_{QW}(q_e \leftrightarrow q_h) = E_G + E_{e,q_e} + E_{h,q_h} \quad \text{for } \mathbf{k}_{\perp} = 0. \quad (2.41)$$

The confinement energy of a certain electron or hole sub-level is on the one hand defined by the corresponding effective carrier mass. However, on the other one it also critically depends on the thickness of the QW L_{QW} . For decreasing widths, the confinement energy rises, whereas toward infinite QW widths E_{QW} converges to the bulk bandgap in the field-free case (cf. Fig. 2.8(b)).

Concerning the selection rules of the optical transitions, two additional effects have to be considered in a QW compared to the bulk case: first, the selection rules that exist for the bulk-case due to the polarization dependence of \mathbf{p}_{cv} might be influenced by the confinement potential, e.g. owing to an interaction between different sub-bands and a corresponding exchange of oscillator strength as present in Fig. 2.7(b). And second, the symmetry of the envelope functions of the participating sub-bands has to be taken into account: when \mathbf{p}_{cv} from Eq. (2.16) is adapted to the QW-case, the z -component decouples and transforms into the overlap integral between electron and hole envelope wave-functions [61, 62]:

$$p_{\text{QW}}(q_e \leftrightarrow q_h) = \int_{-\infty}^{+\infty} \Psi_{e,q_e}^*(z) \Psi_{h,q_h}(z) dz. \quad (2.42)$$

Due to this weighting of the oscillator strength, optical transitions between electron and hole sub-bands with $q_e \neq q_h$ are forbidden. This overlap-integral becomes of further importance for the binding energy of excitons in a QW and for the oscillator strength when the QW is subject to an electric field (cf. Secs. 2.3.2 and 2.3.3).

2.3.2 Two-dimensional Excitons

The transformation of the exciton Schrödinger-equation from Eq. (2.26) to a 2D-system, while considering the modified bandgap of a QW according to Eq. (2.41), leads to the eigenenergies of an exciton in an ideal QW defined by [61]:

$$E_X^{\text{QW}} = E_G + E_{e,q_e} + E_{h,q_h} + \frac{\hbar^2 \mathbf{k}_{\perp}^2}{2M^*} - \frac{E_B}{(q - 1/2)^2}. \quad (2.43)$$

Hence, quantum-confinement in a perfect 2D QW ($L_{\text{QW}} \rightarrow 0$) is expected to enhance the 1s exciton binding energy by a factor of four compared to the 3D-case:

$$E_B^{2\text{D}} = E_B^{3\text{D}} / (q - 1/2)^2. \quad (2.44)$$

By analogy, the corresponding 2D Bohr-radius can be deduced. It amounts to one half of the bulk-value [63]. Note however that these are only idealized values: the perfect 2D-case can never be obtained in realistic structures owing to a finite well thickness and barrier height. Moreover, with increasing well thickness $E_B^{2\text{D}}$ has to converge to the 3D-value.

A more realistic picture of QW-excitons has been developed by Leavitt and Little [64]. They treated the 3D Schrödinger-equation given by Eq. (2.26) within a variational approach accounting for the finite QW-width and barrier height, which finally leads to the expression:

$$E_B^{2\text{D}} = E_B^{3\text{D}} \int_{-\infty}^{+\infty} |\Psi_{e,q_e}|^2 |\Psi_{h,q_h}|^2 w[(z_e - z_h)/a_B^{3\text{D}}] dz_e dz_h. \quad (2.45)$$

Here, z_e and z_h represent the respective electron and hole coordinates along the growth axis and w denotes a non-analytical integral-function that can be approximated by a polynomial one. From Eq. (2.45), the eventual value of E_B^{2D} in real QWs critically depends on the compactness and the overlap of the electron and hole envelope functions. It may be enhanced approximately by a factor of two compared to the bulk case. Correspondingly, the Bohr-radius will also feature an intermediate size, ranging in between the bulk and the ideal 2D value. Throughout this thesis it is calculated based on the approach of a fractional-dimensional space introduced by He in Ref. [65].¹⁰ In the following, mainly QW-excitons will be considered: for esthetical reasons, their binding energy and Bohr-radius will be denoted by E_B and a_B without indication of the dimensionality.

Equivalently to the considerations in 3D, the exciton relative oscillator strengths in 2D are supposed to be transferred from the sub-bands to which the excitons are belonging. Note however that their absolute value is expected to be enhanced compared to the 3D-case owing to the smaller Bohr-radius. Normalized to the unit surface area S , it is given by [61]:

$$\frac{f_X}{S} = \frac{4|\mathbf{p}_{cv}|^2 p_{QW}^2}{m_0 E_X} \cdot \frac{1}{\pi a_B^2}. \quad (2.46)$$

Dark Excitons

Due to an endless sequence of emission and reabsorption processes, i.e. the formation of bulk exciton-polaritons, the radiative decay of an exciton population in an infinitely extending bulk crystal is forbidden [41]. The escape of photons is only allowed when the symmetry is broken, e.g. across the sample surface. This restriction is omitted in QWs resulting in a strongly reduced radiative lifetime, which leads to a QW-luminescence that is in contrast to the defect-dominated bulk usually governed by free-excitons [67]. However, in this case momentum conservation across the QW-interface or the sample surface leads to additional restrictions for the radiative decay of excitons, that shall be briefly discussed hereafter.

Depending on their composition, excitons feature a certain total angular momentum J_z^X projected onto the growth axis, which has to be conserved by the emitted photon across the semiconductor-air interface. J_z^X consists of an electron component ($J_z^e = \pm \frac{1}{2}$) and a hole one: $J_z^{hh} = \pm \frac{3}{2}$ and $J_z^{lh/so} = \pm \frac{1}{2}$. Since the photon carries a momentum $J_z^{ph} = \pm 1$, corresponding to left- and right-hand circularly polarized light, only excitons with $J_z^X = \pm 1$ are allowed to decay radiatively. Excitons with total spin $J_z^X = 0$ (lh/so) or $J_z^X = 2$ (hh) cannot couple to light and are thus called dark-excitons.

Another restriction is given by the conservation of the in-plane momentum: bound electron and hole pairs are moving together through the QW-plane, the motion of their center-of-mass being characterized by a certain wave-vector \mathbf{k}_\perp (cf. Eq. (2.43) and Fig. 2.7(b)). When they radiatively recombine this momentum has to be transferred to the emitted photon across the sample surface and vice versa for absorption. Thus, excitons can only couple to the external

¹⁰An alternative model for E_B and a_B based on the fractional dimensionality was proposed by Mathieu and co-workers in Ref. [66]. It is worth mentioning that both approaches yield very similar results.

light-field when \mathbf{k}_\perp lies within the light-cone defined by a maximum in-plane momentum:

$$|\mathbf{k}_{\text{rad}}| = \frac{n}{\hbar c_0} E_X, \quad (2.47)$$

where n denotes the refractive index of the material. This effect is equivalent to the concept of total internal reflection. Note that due to the small momentum of photons \mathbf{k}_{rad} is almost negligible compared to the exciton dispersion, which practically results in peak-like absorption features for excitons. Finally, it is worth mentioning that in photonic structures, such as photonic crystals or microcavities (cf. Ch. 4), excitons can also be dark because they are decoupled from the tailored light-field [68, 69].

2.3.3 Polarization Fields

As already indicated in Sec. 2.1, the peculiarities of the wurtzite-structure cause an intrinsic polarity of III-nitrides. Two effects have to be distinguished: (i) the lack of inversion symmetry in the unit cell causes piezoelectricity, and (ii) the combination of piezoelectricity with a hexagonal unit cell exhibiting a permanent dipole moment additionally leads to pyroelectricity - often referred to as spontaneous polarization. Note that all pyroelectric materials are piezoelectric, but the reverse is not true: for instance, zincblende GaN would be piezo- but not pyroelectric.

Spontaneous Polarization

The deviating length of the metal-nitrogen tetrahedral bonding along the c -direction compared to the three others, the polarity of the former, and the interaction between second-nearest neighbors in the uniaxial crystal lead to the presence of a permanent electric dipole \mathbf{P}_{sp} in the wurtzite unit-cell. It is linearly correlated with the u -parameter and is oriented along the $[0001]$ -direction [70]. Spontaneous polarization becomes particularly effective across a heterostructure interface: a discontinuity of the polarization-vector projection on the growth axis ($P_{\text{sp}}(\Theta) = P_{\text{sp}} \cos \Theta$) between two materials leads to the formation of a compensation charge plane (Fig. 2.8(a)), which potentially causes built-in electric fields in the range of a few MV/cm in III-nitrides. This effect is particularly used in c -plane GaN/AlGaN and GaN/AlInN HEMT structures [71, 72]. Here, the attractive potential close to the cap-layer interface creates a 2D electron gas, which exhibits superior electron mobilities and a high sensitivity to the surface potential making such structures suitable for high-power and sensing applications [73, 74]. In optoelectronic devices such electric-fields are mostly undesired. Corresponding effects and consequences will be discussed in the forthcoming sections.

It is worth emphasizing that only the projection of the polarization-vector on the growth axis matters for the interface discontinuity. Correspondingly, the strongest effects occur for c -plane structures - thus also referred to as the polar growth direction. The other extreme is the non-polar growth ($\Theta = 90^\circ$), i.e. a - or m -plane structures. Here, the polarization vector lies within the surface plane and corresponding heterostructures are thus ideally free of built-in electric fields [75]. An intermediate situation occurs for semi-polar growth directions ($0 < \Theta < 90^\circ$).

A comparison of the III-nitride polarization parameters can be found in Tab. 2.6. The largest bonding ionicity in AlN causes the strongest permanent polarization vector. Note that P_{sp}

	GaN	AlN	InN
P_{sp} (C/m ²)	-0.034	-0.09	-0.042
d_{13} (pm/V)	-1.6	-2.1	-3.5
d_{33} (pm/V)	3.1	5.4	7.6
d_{15} (pm/V)	3.1	3.6	5.5

Table 2.6: Summary of the polarization constants for III-nitride binary alloys [31].

exhibits a strong non-linearity for ternary III-nitride alloys. By analogy with Eq. (2.25), the latter can be described by a bowing parameter [76].

Piezoelectric Polarization

The aforementioned considerations for the spontaneous polarization neglect the influence of strain. By contrast, real epitaxial III-nitride heterostructures are usually subject to a certain lattice deformation owing to the mismatch between the lattice constants (cf. Fig. 2.5) and the deviating thermal expansion coefficients. An exception state AlInN/GaN heterostructures that can be grown perfectly lattice-matched for *c*-plane orientation for an In-content of $\sim 17\%$ [74, 77]. However, in a strained structure the deformation of the lattice will cause an additional change in the anion-cation barycenter separation, an effect that is referred to as piezoelectricity. Its vector \mathbf{P}_{pz} adds up to the spontaneous one forming a macroscopic polarization: $\mathbf{P} = \mathbf{P}_{\text{sp}} + \mathbf{P}_{\text{pz}}$. Its magnitude $P_{\text{pz},i}$ along a certain direction *i* is related to the stress tensor σ from Eq. (2.3) via:

$$P_{\text{pz},i} = \sum_{jk} d_{ijk} \cdot \sigma_{jk}, \quad (2.48)$$

where d_{ijk} denotes the elements of the piezoelectric modulus. Note that contrary to \mathbf{P}_{sp} , the direction of \mathbf{P}_{pz} might deviate from [0001]. Similarly to Hooke's law the general case can be simplified by respecting the hexagonal symmetry of the lattice. For an arbitrary surface orientation, the projection of \mathbf{P}_{pz} along the growth direction is determined by [32]:

$$P_{\text{pz}}(\Theta) = 2d_{15}C_{44}\epsilon_{xz}\sin\Theta + [(d_{13}(C_{11} + C_{12}) + d_{33}C_{13})(\epsilon_{xx} + \epsilon_{yy}) + (2d_{13}C_{13} + d_{33}C_{33})\epsilon_{zz}]\cos\Theta. \quad (2.49)$$

Literature values for the three independent elements of the piezoelectric modulus are summarized in Tab. 2.6. It is worth pointing out that, depending on the nature of the lattice deformation, \mathbf{P}_{sp} and \mathbf{P}_{pz} might either point in the same direction or partially compensate each other. This becomes particularly effective for semi-polar device structures, where a careful stress engineering might lead to polarization compensation [78], and enhance the radiative properties [79].

Quantum-Confined Stark-Effect

In a heterostructure, the polarization discontinuity between two different layers *i* and *j* generates a compensation charge plane $\sigma_{i,j}$:

$$\sigma_{i,j} = -(\mathbf{P}_j - \mathbf{P}_i) \cdot \mathbf{e}_{i,j}, \quad (2.50)$$

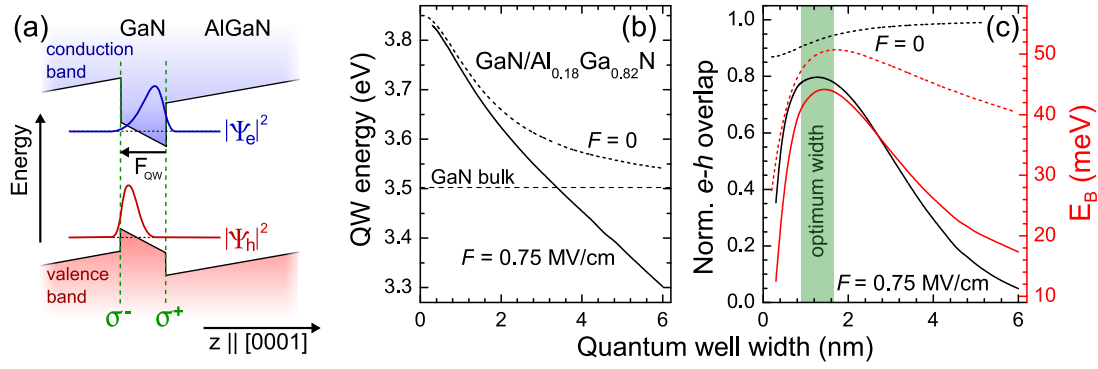


Figure 2.8: (a) Schematic representation of the QCSE in a *c*-plane GaN/AlGaIn QW: an electric field F issued from the charge compensation planes $\sigma^{+/-}$ shifts electron and hole wave-functions toward opposite QW-edges. (b,c) Simulation of a *c*-plane GaN/Al_{0.18}Ga_{0.82}N QW of variable thickness with $F = 0$ (dashed lines) and $F = 0.75$ MV/cm (solid lines) at 4 K and zero carrier-density: (b) QW ground state energy as a function of QW-width. For thick QWs, F pushes the QW-energy below the bulk bandgap E_G . (c) Corresponding evolution of the wave-function overlap (black) and the exciton binding energy (red).

where $\mathbf{P}_{i/j}$ denotes the total polarization vector of the corresponding layer and \mathbf{e}_{i-j} is the interface unit vector. For an infinitely extending interface, such a charge-plane gives rise to a static electric field \mathbf{F} that amounts to:

$$\mathbf{F}_i = -\frac{\sigma_{ij}}{2\epsilon_0\epsilon_{r,i}}\mathbf{e}_{i-j} \quad \text{and} \quad \mathbf{F}_j = \frac{\sigma_{ij}}{2\epsilon_0\epsilon_{r,j}}\mathbf{e}_{i-j}, \quad (2.51)$$

for the respective layers. When now considering a polar single GaN QW sandwiched in between two AlGaIn barriers, the polarization change across the QW-interfaces will form respective charge planes of opposite sign σ^+ and σ^- . These superimpose and act as an effective capacitance forming an electric field F_{QW} in the QW. Figure 2.8(a) depicts this situation schematically.

An insertion of such a distorted QW-potential into Eq. (2.40) yields modified eigenenergies and wave-functions for the QW sub-bands. The variation of the QW-properties due to an electric field and the respective consequences are commonly referred to as the quantum-confined Stark-effect (QCSE) [80]: F_{QW} pushes electron and hole probability densities toward opposite sides of the QW (cf. Fig. 2.8(a)), the wave-function overlap p_{QW} according to Eq. (2.42) is reduced. Figure 2.8(c) shows the simulated evolution for p_{QW} of the ground state as a function of the QW-width for a single GaN/Al_{0.2}Ga_{0.8}N QW with zero carrier-density. In the field-free case, p_{QW} is mainly determined by the different penetration depths of electrons and holes into the barrier, which causes a slight rise with L_{QW} and a convergence toward unity for $L_{QW} \rightarrow \infty$. In comparison, when assuming a realistic field strength of 0.75 MV/cm [81], the situation appears remarkably different: for large QW-widths p_{QW} approaches zero, electron and hole populations are localized at opposite QW-barrier interfaces. For small L_{QW} -values, the vicinity of the confined levels to the CB and VB-energy of the barrier causes again a large penetration depth resulting in a decreasing overlap. Note that the latter is stronger compared to the field-free case due to the preferential penetration of electron and hole wave-functions into opposite barriers caused by their finite potential difference. Conclusively, there is an

optimum QW-width, where p_{QW} is maximized, i.e. for $1 \text{ nm} < L_{\text{QW}} < 1.6 \text{ nm}$. Nevertheless, the maximum value of p_{QW} is reduced by about 15% compared to the $F = 0$ case. As already mentioned, the eigenenergies of the QW are also influenced by the QCSE. Figure 2.8(b) shows the dependence of the ground state energy on L_{QW} for the same QW-example. In both cases, i.e. with and without electric field, the confinement energy decreases with rising L_{QW} as already detailed for Eq. (2.41). However, for large L_{QW} -values the QW-energy converges toward E_{G} for $F = 0$, whereas in the presence of an electric field E_{QW} will even drop below the bulk GaN bandgap [82].

The above-mentioned effects have some more far-reaching impacts on the optical properties of the QW. According to Secs. 2.3.1 and 2.3.2, the reduced overlap of the QW envelope wave-functions causes a decrease of the QW oscillator strength and thus of its radiative recombination efficiency. This detrimental influence has to be carefully considered when designing light-emitting devices or structures aimed for the strong light-matter coupling regime (cf. Ch. 4). Along with this aspect goes the reduction of the exciton binding energy, which critically depends on the overlap between electron and hole probability densities (cf. Eq. (2.45)) and thus follows practically p_{QW} in Fig. 2.8(b). Of minor importance are effects of: (i) a potentially increased inhomogeneous linewidth due to an enlarged barrier penetration depth and a correspondingly increased sensitivity to alloy composition fluctuations, or (ii) the partial lifting of the symmetry restraints for optical transitions between QW sub-bands of different quantum numbers.

Note finally that in structures containing multiple QWs the built-in electric field can be reduced compared to the single QW case due to the geometrical effect [81]: here, barriers of finite thickness accommodate part of the electric-field strength resulting in moderated QCSE effects in the QWs.

Semi- or Non-Polar Quantum Wells

The detrimental impact of the QCSE is the most pronounced for c -plane structures owing to the orientation of \mathbf{P}_{sp} . This became a particular issue in the quest for efficient green InGaN-based LEDs and LDs [83–85], where despite the lower material quality the performance of semi- and non-polar structures competes with that of their c -plane counterparts. As already mentioned, the polarization mismatch in such III-nitride heterostructures can be reduced or even eliminated according to the scalar product of Eq. (2.50), potentially resulting in superior radiative efficiencies [75]. Note however that for semi- or non-polar surface orientations the optical axis features a non-zero in-plane projection, leading to a pronounced anisotropy of the optical properties for corresponding QWs or surface emitting devices. Section 4.7 focuses on microcavities containing QWs of non-polar orientation and details these aspects.

2.3.4 Impact of Carrier Density

The previous considerations concerning the QCSE have been conducted for a QW with a carrier density n_{QW} equal to zero. It is however worth pointing out that the QCSE is not invariant against a finite n_{QW} : the screening effect of the free charge carriers reduces the magnitude of the built-in electric field and correspondingly diminishes all detrimental impacts of the QCSE. Accordingly, E_{QW} , p_{QW} , E_{B} , and f_{osc} become a function of carrier density. The transition

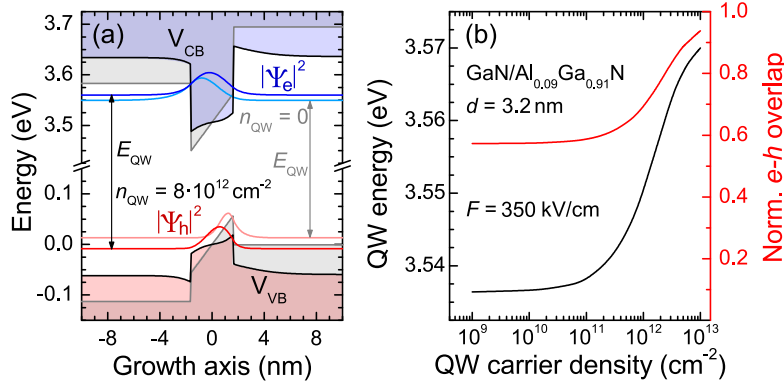


Figure 2.9: QCSE versus QW carrier density in a 3.2 nm thick *c*-plane GaN/Al_{0.09}Ga_{0.91}N QW: (a) comparison of the band-profiles and the QW-states for $n_{QW} = 0$ (light colors) and $n_{QW} = 8 \cdot 10^{12} \text{ cm}^{-2}$ (dark colors). (b) Evolution of the QW-energy and wave-function overlap as a function of n_{QW} (cf. sample SQW-1 in Fig. 3.5).

energy of the QW-exciton is in this case determined by:

$$E_X(n_{QW}) = E_{QW}(0) + \Delta E_{QCSE}(n_{QW}) - E_B(n_{QW}) = E_{QW}'(n_{QW}) - E_B(n_{QW}), \quad (2.52)$$

where ΔE_{QCSE} denotes the ground state energy shift. This QCSE-screening mechanism can be simulated within an iterative Schrödinger-Poisson (SP) algorithm, which is detailed in Sec. A.1. Therein, the one-dimensional Poisson-equation:

$$\frac{\partial^2}{\partial z^2} \Phi(z) = -\frac{\rho(z)}{\epsilon_0 \epsilon_r}, \quad (2.53)$$

is solved self-consistently together with the QW Schrödinger-equation of Eq. (2.40), both being coupled via the modified QW-potential $V'_{QW}(z)$. In Eq. (2.53), $\Phi(z)$ denotes the electrical potential resulting from the differential QW charge-carrier density $\rho(z)$:

$$\rho(z) = -e \cdot n_{QW} \cdot [|\Psi_e(z)|^2 - |\Psi_h(z)|^2]. \quad (2.54)$$

Figure 2.9 shows the QCSE-screening for a single 3.2 nm-thick GaN/Al_{0.09}Ga_{0.91}N QW. For a carrier density $n'_{QW} = 8 \cdot 10^{12} \text{ cm}^{-2}$, which corresponds more to the injection regime of a LD than that of an LED, the strength of the electric field is significantly reduced compared to the zero-density case leading to the changes: $p_{QW} = 0.57 \rightarrow 0.93$ and $E_{QW}(n'_{QW}) - E_{QW}(0) \approx 32 \text{ meV}$. According to Eq. (2.45) this causes simultaneously an increase of the exciton binding energy by about 8 meV. In Fig. 2.9(b) the evolution of $E_{QW}(n_{QW})$ and $p_{QW}(n_{QW})$ indicates that screening effects become only important for carrier concentrations exceeding 10^{11} cm^{-2} , in agreement with previous considerations [86].

Note finally that also the exciton stability, i.e. E_B , is not invariant against n_{QW} , owing to inter-particle interactions that have been neglected so far. This relativizes the nominal increase of E_B due to the increasing wave-function overlap, and causes the alteration of its optical properties and eventually the dissociation of the excitonic complex beyond a certain critical density value. An in-depth discussion of this effect will follow in the next chapter.

3 Highly-injected GaN Quantum-Wells

This chapter deals with the optical properties of high-quality *c*-plane GaN/AlGaN QWs. Starting from the examination of their linear excitonic response, it then focuses on the peculiarities of the high carrier density regime, where effects like exciton saturation and electron-hole plasma emission occur. This injection regime corresponds to the operational conditions of commercial optoelectronic devices and may also partly be reached by the optically-pumped polariton lasers, that are discussed in Ch. 4. To begin with, the experimental techniques and the investigated sample structures shall be introduced.

3.1 Experimental Techniques

3.1.1 Photoluminescence, Reflectivity and PLE

Due to the ease of carrier-injection, large parts of this work will rely on photoluminescence (PL) spectroscopy. Here, an intense laser beam with a photon energy larger than the bandgap (non-resonant excitation) is focused onto the sample. It is absorbed by the material forming hot electron-hole pairs. Owing to inelastic scattering with phonons, these are subsequently relaxing down to the band edges, where they eventually recombine. The emitted photons are analyzed by means of a spectrometer. The emission spectrum provides an insight into the optical and electronic properties of the semiconductor in the vicinity of the bandgap.

Figure 3.1 depicts the setup that was used for high-carrier density continuous-wave (cw) PL measurements. The excitation source consists of an Ar⁺-laser, its 488 nm-line being frequency-doubled to 244 nm (5.08 eV). By means of a high numerical aperture (NA = 0.55) UV microscope objective (focal length 2.5 mm, working distance 9 mm), the laser beam is brought to the sample surface and focused down to a spot diameter below 5 μm. The luminescence signal is collected through the same objective and deflected into the collection line by a non-polarizing beam-splitter (BS) plate. With a magnification factor of ~ 100, the emission is then imaged on a 50 μm pinhole, that allows collecting only the signal stemming from the region of highest and homogeneous excitation. The pinhole is imaged on the entrance slit of the monochromator by two lenses of 10 and 20 cm focal length. Spectra are acquired by means of a 55 cm focal-length monochromator, equipped with three gratings of 150, 1200 and 2400 grooves/mm, in combination with a liquid-nitrogen cooled CCD-array of 512 × 2048 pixels. The spectral resolution limit of this setup amounts to 0.327, 0.04 and 0.019 nm for the three gratings, respectively. The excitation power density P_{exc} is measured with a photo-diode at the BS-plate, and can

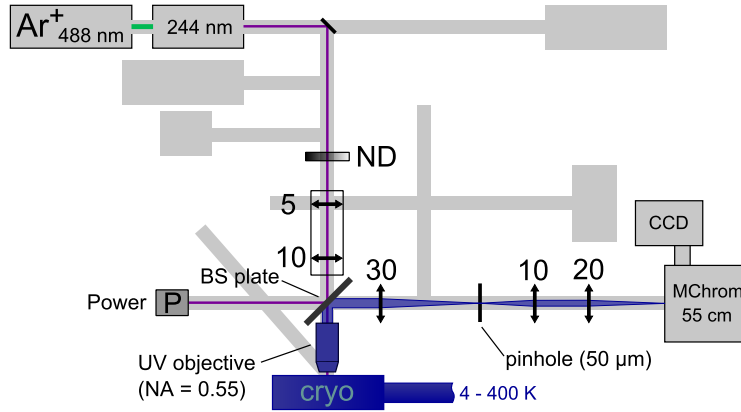


Figure 3.1: High-power continuous wave PL-setup: the sample is excited non-resonantly by the frequency-doubled line of an Ar^+ -laser ($\lambda = 244 \text{ nm}$), which is focused by using a UV microscope objective ($\text{NA} = 0.55$). The PL is collected through the same objective, focused by a 30cm-focal lens to a 50 μm pinhole for spatial filtering. Spectral resolution is obtained in a 55 cm focal-length monochromator that is linked to a CCD. A telescope in the excitation line allows to match the foci of laser and PL.

be varied continuously by using a reflective neutral-density wheel (ND). Behind the latter, a telescope consisting of two lenses with respective focal lengths of 5 and 10 cm allows to adjust the spot size and the focus of the excitation laser. In this way the chromatic aberration of the objective causing different focal lengths for the laser (244 nm) and the PL-signal ($\sim 350 \text{ nm}$) can be corrected. Finally, a liquid-helium cold-finger cryostat allows to vary the sample temperature in between 4 and 400 K.

Depending on the specific requirements of the experiment, the setup can be modified. The excitation sources at disposal are:

- a frequency-doubled Ar^+ -laser providing a cw-output at 244 nm,
- a pulsed frequency-quadrupled Nd:YAG laser emitting at 266 nm with a pulse length $\tau = 500 \text{ ps}$ and a repetition rate $f = 8.52 \text{ kHz}$, which allows reaching very high excitation power densities,
- a Nd:YAG-pumped optical parametric oscillator (OPO) that can be tuned in the wavelength range between 210 and 2300 nm and features a pulsed output with $\tau = 7 \text{ ns}$ and $f = 1 \text{ kHz}$, or
- a 150 W UV-enhanced xenon-lamp, which is mainly used for reflectivity measurements.

Moreover, the signal can also be analyzed as a function of the light-polarization by placing the combination of a $\lambda/2$ wave-plate and a linear polarizer in front of the first lens in the collection line. Larger excitation spot sizes can be obtained by replacing the UV-objective by a lens of 7.5 or 10 cm focus. Eventually, a goniometer offers the possibility to switch to an angle-resolved excitation/collection setup.

Note finally that PL does not exclusively probe intrinsic electronic properties but is strongly affected by thermal occupancy, carrier relaxation, and crystal defects. By contrast, reflectivity

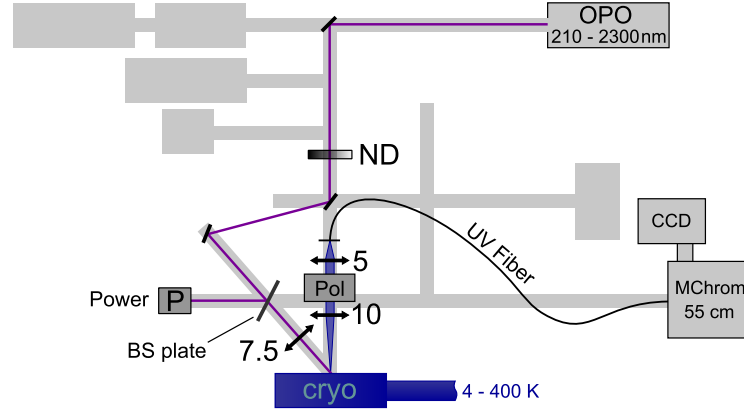


Figure 3.2: Schematic of the PLE-setup: the sample is resonantly excited under an angle of incidence of 45° with the OPO. PL is collected cross-polarized to the laser through a 10 cm-focal lens. It is guided through a UV-enhanced optical fiber to the previously described monochromator-CCD combination providing a spectral resolution of $300\mu\text{eV}$.

and transmission are directly determined by the dielectric function of the material. However, opaque substrates or buffer layers usually prevent transmission measurements for the characterization of GaN/AlGaIn QWs, and reflectivity responses of single QWs are extremely hard to record due to the small amount of active material. Therefore, another technique was applied in order to probe the QW-absorption: PL excitation (PLE) spectroscopy.

Figure 3.2 shows the setup for PLE-measurements. The tunable OPO source is used for resonantly exciting the sample under an angle of 45° with light polarization perpendicular to the plane of incidence. The laser beam is focused down to a spot size of $\sim 100\mu\text{m}$. In order to avoid the direct and scattered reflection of the laser, the PL signal is collected by a 10 cm focal lens at normal incidence in cross-polarization. It is coupled to an optical fiber and guided to the previously described monochromator-CCD combination. The OPO output power varies with the selected wavelength and exhibits fluctuations of $\pm 20\%$ on a sub-second scale. Therefore, a ND wheel in the excitation line was used to keep the photon flux approximately constant and the power density has been averaged over the exposure time.

Assuming the linearity between the number of pump photons that are absorbed in the material and the number of correspondingly excited electron-hole pairs that recombine radiatively, the evolution of the ground state emission intensity of a QW reflects the absorption profile at the pumping wavelength. The linearity condition is particularly fulfilled in high-quality QWs at very low temperature $T = 4\text{ K}$, where the internal quantum efficiency (IQE) is usually assumed to be unity. Figure 3.3(a) displays the PLE-spectrum of a single 3.2 nm-thick GaN/Al_{0.09}Ga_{0.91}N *c*-plane QW in a 2D color plot (cf. Sec. 3.2.1): the spectral emission intensity is mapped as a function of the excitation photon energy E_{exc} at 4 K. For excitation below the QW ground-state energy, i.e. $E_{\text{exc}} < 3.51\text{ eV}$, the QW-structure is transparent and all the detected luminescence stems from the GaN substrate. With increasing E_{exc} the QW-signal emerges and subsequently undergoes slight modulations with changing E_{exc} . Finally, the trace of the integrated QW PL-intensity I_{PL} as a function of E_{exc} corresponds to the PLE-spectrum and thus to the relative QW-absorption. For this specific case it corresponds to the high-power spectrum in Fig. 3.18.

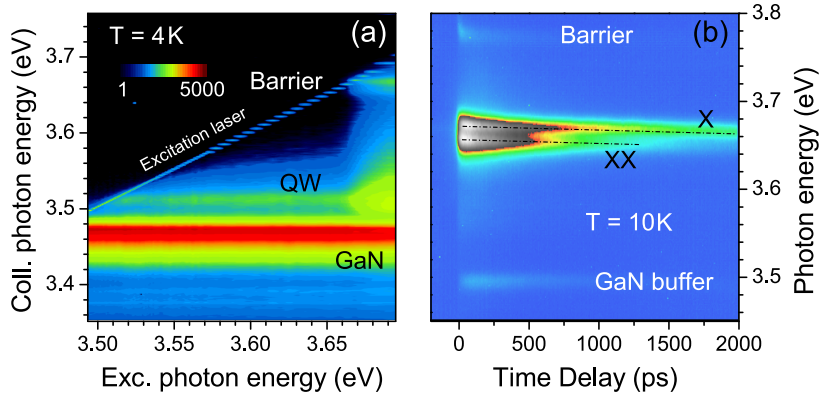


Figure 3.3: (a) PLE-measurement of SQW-1 carried out at $T = 4$ K (log-scaled intensity color map): the PLE-spectrum of the QW corresponds to its PL-intensity variation as a function of the excitation energy. (b) Streak camera image recorded for sample MQW-1 at $T = 10$ K: exciton (X) and biexciton (XX) transitions can be identified via their different decay times.

3.1.2 Time-resolved Photoluminescence

The previously described PL-technique relies on time-integrated measurements, for cw-pumping it reflects thus the properties of an excited semiconductor in a steady-state. Newly absorbed photons and recombining carriers form a quasi-equilibrium, where the absolute number of excited particles is conserved. In order to get a deeper insight into the relaxation and recombination dynamics of the excited charge carriers, additional time-resolved (tr) PL studies have been conducted.

The tr-PL studies rely on non-resonant excitation by the third-harmonic of a mode-locked Ti:sapphire-laser tuned at a wavelength of about 285 nm with a pulse duration $\tau = 2$ ps and a repetition rate $f = 80.7$ MHz. Figure 3.4 shows a schematic of the tr-PL setup. As for the time-integrated PL-studies, the laser beam is focused onto the sample by means of the UV microscope objective yielding an excitation spot size smaller than $5\mu\text{m}$. The collection line resembles that of Fig. 3.1 and contains again a $50\mu\text{m}$ pinhole, which is carefully positioned in the image plane of a 30 cm collection lens for spatial filtering of the emission. The monochromator of this setup has a focal length of 32 cm and provides a spectral resolution of ~ 0.1 nm. It is connected to a streak camera working in synchronous scan mode. Here, the dispersed photon output of the spectrometer hits a photo-cathode that subsequently emits electrons due to the photo-electric effect. These electrons are accelerated and pass in between two condensator plates, which are synchronized to the laser repetition frequency, and deflect the electrons depending on their initial time-delay. Finally, the electron cloud hits a fluorescence screen, which is imaged on a CCD. The temporal-resolution of this setup amounts to ~ 5 ps. The measurements can be carried out as a function of temperature and excitation power. For low injection studies the microscope objective can be replaced by a lens with longer focal length.

Figure 3.3(b) shows a low-temperature streak image of a multiple QW (MQW) structure consisting of 67 1.2 nm-thick GaN QWs embedded in between $\text{Al}_{0.2}\text{Ga}_{0.8}\text{N}$ barriers (cf. Sec. 3.2.3). The excitation pulse arriving at zero time delay creates an initial population of carriers according

3.2. Sample Structures and Basic Optical Properties

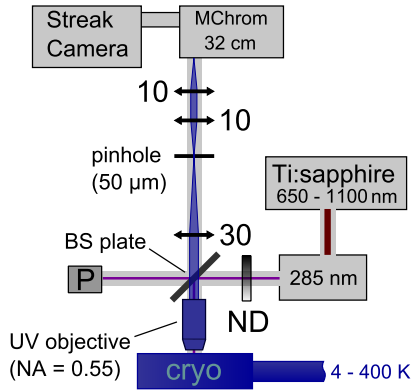


Figure 3.4: Time-resolved PL-setup: the sample is excited by the frequency-tripled line of a Ti:sapphire laser ($\lambda = 285\text{ nm}$, $f = 80.7\text{ MHz}$, $\tau = 2\text{ ps}$), that is focused by means of a UV microscope objective. PL is collected through the same objective and focused down to a $50\mu\text{m}$ pinhole for spatial filtering. Spectra are obtained by a 32 cm focal-length monochromator that is linked to a streak camera. The latter works in synchroscan mode and provides a time-resolution of 5 ps .

to the depth-profile of absorption. Subsequently, they relax to the band edges and recombine either in the GaN-buffer layer, the AlGaIn barriers, or the GaN MQWs. In the latter case, two emission lines are visible: the QW ground state exciton (X) and the corresponding biexciton state (XX, cf. Sec. 3.2.2). Typically, both decay with different time constants, i.e. at long time delay $> 1.5\text{ ns}$ only the X-emission remains. Moreover, a slight redshift with increasing delay time and thus with decreasing carrier density can be identified for the QW-luminescence. It is caused by QCSE-screening and carrier localization.

3.2 Sample Structures and Basic Optical Properties

In order to address the basic properties of GaN QWs and to subsequently explore their high-injection response while probing a well-defined carrier density, the present study concentrates on the simplest system consisting of a single high-quality GaN/AlGaIn QW. The link with Ch. 4 is made by investigating an additional MQW-structure, which corresponds to the active region of the *c*-plane microcavity discussed therein.

3.2.1 Single Quantum-Wells

Within this study three-different GaN/AlGaIn single QWs (SQWs) have been explored:

SQW-1 3.2 nm -thick GaN/ $\text{Al}_{0.09}\text{Ga}_{0.91}\text{N}$ SQW grown on a *c*-plane free-standing GaN substrate by MOVPE. The thickness of the AlGaIn barrier amounts to 30 and 150 nm on the surface and substrate side, respectively. It has been thoroughly studied in Ref. [87].

SQW-2 Same as SQW-1 but consisting of a 2 nm -thick GaN SQW that is embedded in between $\text{Al}_{0.18}\text{Ga}_{0.82}\text{N}$ barriers.

SQW-3 3 nm -thick GaN SQW that is sandwiched in between $\text{Al}_{0.05}\text{Ga}_{0.95}\text{N}$ barriers with top and bottom thicknesses of 50 and 200 nm , respectively. It was grown by MOVPE on top of a $3\mu\text{m}$ GaN-template on *c*-plane sapphire. The dislocation density amounts approximately to 10^9 cm^{-2} . More details about this structure and a comprehensive analysis of the QW-biexciton properties can be found in Refs. [88, 89].

Note further that the free-standing GaN substrates used for SQW-1 and SQW-2 feature an extremely low dislocation density around 10^6 cm^{-2} and that it has been overgrown by a homoepitaxial undoped GaN buffer layer prior to the deposition of the QW structure. All samples are

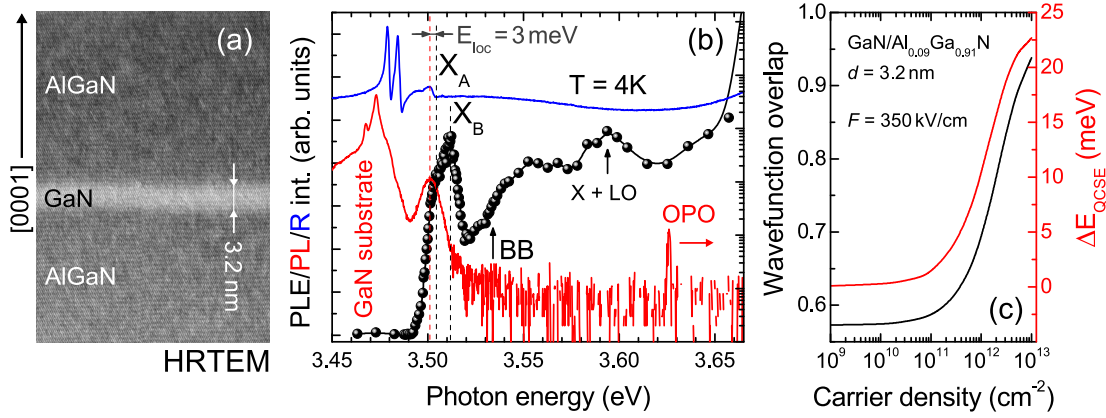


Figure 3.5: Properties of SQW-1 consisting of a *c*-plane 3.2 nm GaN/Al_{0.09}Ga_{0.91}N SQW: (a) high-resolution TEM image. (b) PLE (black dots, line is guide to the eye), quasi-resonant PL (red) and reflectivity (blue) recorded at $T = 4$ K. The PLE-measurements were carried out with a peak power density $P_{exc} \approx 1.7 \text{ kW/cm}^2$. (c) Simulation of the wave-function overlap p_{QW} (black) and the QW ground-state energy shift (red) as a function of the QW-carrier density.

non-intentionally doped, the background doping concentration is estimated to $< 10^{17} \text{ cm}^{-3}$.

Figure 3.5(a) shows a cross-section transmission electron microscopy (TEM) image of sample SQW-1. GaN and AlGaIn layers exhibit smooth interfaces and can be well distinguished by the atomic mass contrast. No strong inhomogeneities can be spotted in the AlGaIn alloy and like all other structures in this chapter, SQW-1 is free of cracks. As evidenced by the low-temperature PLE-spectrum displayed in Fig. 3.5(b), its fundamental electronic state is composed of two excitonic transitions X_A and X_B . Both can be recognized by their peak-like absorption contribution and are partly merged due to their finite linewidth. They are located around 3.5 eV at $T = 4$ K, exhibit a similar oscillator strength and an inhomogeneous linewidth $\gamma_{inh} = 8$ meV. This latter value also corresponds to their approximate energy separation in agreement with the explanations given in Sec. 2.3.1. Toward higher energies, the onset of the band-to-band (BB) absorption and the LO-phonon replica of the QW-excitons can be identified. The latter feature is also often referred to as an exciton-phonon complex (EPC). Those are commonly observed in III-nitride layers [44, 90], owing to the polar character of the material and the correspondingly enhanced Fröhlich interaction. The band edge in Fig. 3.5(b) exhibits an increased broadening compared to the excitons, which hampers a direct conclusion on E_B from the PLE-spectrum. Therefore, SP-simulations have been performed: Due to its *c*-plane orientation SQW-1 is subject to the QCSE. An electric field of 350 kV/cm was adopted [81], which results in a normalized wave-function overlap $p_{QW} = 0.57$ at zero carrier density (cf. Fig. 3.5(c)). Following Ref. [64], $E_B = 30$ meV has been derived for the present QW, which sets the BB position marked in Fig. 3.5(b) and accurately coincides with the steepest rise in absorption. In addition to the narrow exciton linewidth, the high quality of SQW-1 is confirmed by the small localization energy $E_{loc} = 3$ meV, that is extracted from the comparison between the PLE- and a low-injection PL spectrum. Figure 3.5(b) also presents a low-temperature reflectivity spectrum. Here, apart from the conspicuous A- and B-excitons of the GaN substrate that appear around 3.48 eV, no trace of the single QW can be identified, which emphasizes the suitability of PLE for such structures. Note that there is another signature at 3.504 eV, which

agrees admittedly well with the position of X_A determined from PLE. But owing to the smaller linewidth and the lack of an equivalent for X_B , it is attributed to the C-exciton of the GaN substrate, which exhibits a much lower oscillator strength than A and B.

Despite its growth on a sapphire substrate, sample SQW-3 features an even narrower exciton linewidth compared to SQW-1. This can be ascribed to the lower Al-content of the barrier and the respectively reduced alloy composition fluctuations, which have been identified to be the main factor limiting the inhomogeneous linewidth in GaN/AlGaIn QWs [91]. The corresponding PLE measurement, recorded at $T = 4$ K and displayed in Fig. 3.6, reveals two excitonic transitions X_A and X_B , which are located at 3.523 and 3.534 eV and exhibit linewidths of 6 and 7 meV, respectively. On the high energy side, a small shoulder at 3.548 eV can be observed before the steep rise in the PLE spectrum is caused by the onset of absorption in the $\text{Al}_{0.05}\text{Ga}_{0.95}\text{N}$ barrier. This feature might correspond to the BB-absorption edge resulting in $E_B = 25$ meV for SQW-3, in close agreement with the value of 27 meV deduced from SP-simulations. Figure 3.6 additionally shows a low-temperature PL spectrum, that was recorded with an excitation photon-energy slightly above the barrier energy. Here, the PL signal of the $\text{Al}_{0.05}\text{Ga}_{0.95}\text{N}$ barrier around 3.57 eV and the GaN buffer around 3.485 eV are observed in addition to the QW emission. The buffer contribution consists of the A-exciton at higher and the donor-bound exciton (D_0X_A) at lower energy [53], respectively. They are blueshifted by about 10 meV compared to the case of relaxed GaN (cf. Fig. 3.5(b)), which indicates slight compressive strain due to the underlying sapphire substrate.

The QW emission exhibits a double-peak signature in PL: the high-energy one corresponds to X_A revealing a marginal Stokes-shift with $E_{\text{loc}} = 1$ meV. The low energy transition stems from the recombination of biexcitons, i.e. quasi-particles that shall be briefly introduced hereafter.

3.2.2 Quantum-Well Biexcitons

As detailed in Sec. 2.2.2, an exciton represents a hydrogen-like state of a bound electron-hole pair in a semiconductor. In complete analogy with the hydrogen problem, two excitons can also bind together and form an excitonic molecule, the so-called biexciton (XX). Those quasi-particles have been observed in thick III-nitride layers [92, 93], featuring respective binding energies E_B^{XX} of 5.3 meV and 28.5 meV for GaN and AlN, as well as in GaN quantum-dots [94, 95] and recently in GaN/AlGaIn QWs [88, 89]. The eigenenergy of the biexciton ground state is given by:

$$E_{\text{XX}} = 2E_X - E_B^{\text{XX}}, \quad (3.1)$$

where E_B^{XX} is expected to scale with the dimensionality of the structure and the electron-hole mass ratio [96–98]. Based on Schrödinger- $k.p$ simulations m_e^*/m_h^* ratios of about 0.2 can be deduced for the present c -plane GaN/AlGaIn QWs (cf. Figs. 3.14(a,b)),¹ leading to a Haynes factor given by [96, 97, 99]:

$$E_B^{\text{XX}}/E_B = 0.25 \pm 0.05. \quad (3.2)$$

For SQW-3, the biexciton is expected to be located at an energy of ~ 7 eV. Hence, when neglecting any two-photon absorption processes it cannot be observed in the PLE-spectrum

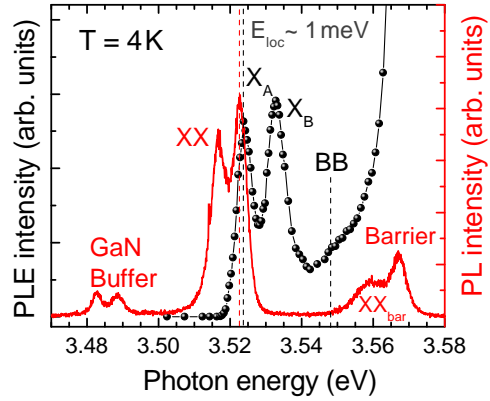
¹Due to the strong non-parabolicity of the VBs, m_h^* has been averaged over the inverse exciton Bohr-radius.

of Fig. 3.6, that only shows the vicinity of the band edge. However, it is visible in PL which can be explained as follows: the biexciton consists of two excitons, which can decay independently of each other. When one of the excitons radiatively recombines it leaves behind a free exciton of energy E_X and thus ideally emits a photon of energy:

$$E_{XX}^{PL} = E_X - E_B^{XX}. \quad (3.3)$$

Figure 3.6 reveals thus a biexciton binding energy of about 7 meV for SQW-3, i.e. a value that fits the prediction of Haynes rule in Eq. (3.2). In a more realistic framework, for disordered structures Eq. (3.3) might be modified due to the different localization energies [69]. Moreover, it was shown that localization might increase the binding energy of biexcitons [100], potentially resulting in a remarkable deviation from Hayne's rule. A similar effect has also been evidenced for biexcitons in AlGaIn-layers [101].

Figure 3.6: PLE-spectrum recorded at $T = 4\text{ K}$ for sample SQW-3 consisting of a c -plane 3 nm GaN/Al_{0.05}Ga_{0.95}N SQW (black dots): A- and B-excitons can be clearly resolved. The comparison with a PL-spectrum ($P_{\text{exc}} \approx 350\text{ W/cm}^2$, red) reveals a small localization energy of 1 meV and the presence of QW biexcitons (XX). The emission of the AlGaIn barrier and that of the GaN buffer layer are also observed.



The biexciton emission features a set of distinctive properties that help to discriminate it from emission bands of other origins, which might be found at a similar energy position, such as localized or defect-bound excitons. In thermal equilibrium exciton and biexciton populations n_X and n_{XX} are linked by the law of mass-action [69]:

$$\frac{n_X^2}{n_{XX}} = \frac{M^* k_B T}{\pi \hbar^2} \exp\left(\frac{E_B^{XX}}{k_B T}\right). \quad (3.4)$$

For excitation power-dependent cw-PL studies, this leads to a quadratic power-law scaling of the biexciton PL-intensity, in contrast to the usually linear exciton one. Thus, biexciton formation is triggered at high carrier densities. However, note that in direct bandgap materials the short lifetime of excitons and biexcitons may cause lower power scalings than the quadratic one [102]. In addition, in tr-PL n_X and n_{XX} are expected to decay with linked time constants τ : $\tau_{XX} = \tau_X/2$ (cf. streak image in Fig. 3.3). Note further that the light-cone restriction for radiative recombination as it was detailed for excitons in Sec. 2.3.2 does not apply for biexcitons. Indeed, in a QW-biexciton with high in-plane momentum one exciton component might still radiatively recombine and transfer the excess momentum to the remaining exciton. This effect causes a characteristic thermal low-energy tail for the biexciton [102], which might however be concealed by other homogeneous or inhomogeneous broadening mechanisms.

At the end of this section, the previously obtained results on biexcitons in GaN/AlGaIn QWs from Refs. [88] and [89] shall be briefly summarized. They deal with sample SQW-3 and an-

other equivalently grown one with an $\text{Al}_{0.09}\text{Ga}_{0.91}\text{N}$ -barrier. In these structures, the biexciton binding energy was evidenced to strongly vary with the well thickness and the Al-content of the barriers. More precisely, E_{B}^{XX} was found to decrease linearly with increasing QW-width and the corresponding slope rises with the Al-content. Both dependencies can mainly be attributed to the impact of QCSE: indeed, as detailed in Sec. 2.3.3 the reduced wave-function overlap due to the built-in electric field reduces the exciton binding energy, and thus also E_{B}^{XX} according to Hayne's rule. Moreover, this effect is likely to be even enhanced for the biexciton owing to the preferential orientation of the excitonic dipole along the direction of the electric field. This results for biexcitons in an effective dipole-dipole repulsion component that is strongly increasing with QW-width and the strength of the built-in field. In the optimum case of a 1 nm-thin $\text{GaN}/\text{Al}_{0.09}\text{Ga}_{0.91}\text{N}$ structure, E_{B}^{XX} was found to reach values as large as 12 meV. As the estimated E_{B} -value for this case only amounts to 33 meV, Hayne's rule might be violated for those QW-structures. Apart from the dipole-dipole repulsion, this can also be caused by the pronounced impact of disorder [100]. It is worth mentioning, that for a certain critical QW-width E_{B}^{XX} falls below the value of bulk GaN and that for even larger widths it will tend to zero. This limitation is responsible for the absence of biexcitons in samples SQW-1 and SQW-2. Indeed, with respect to the experimentally observed exciton linewidth in SQW-1 and Ref. [89], the critical thickness for observing biexcitons in a $\text{GaN}/\text{Al}_{0.09}\text{Ga}_{0.91}\text{N}$ QW amounts to about 2 nm.²

3.2.3 Multiple Quantum-Wells

In order to transfer the findings from the SQW-studies to the physics of microcavities, a stack of MQWs has also been investigated:

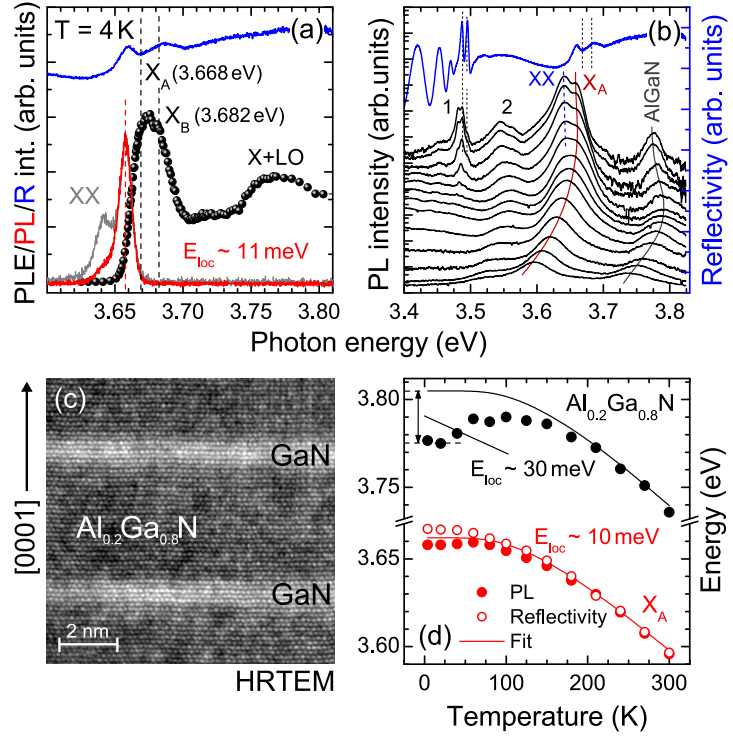
MQW-1 This sample consists of a set of 67 1.2 nm-thick GaN QWs which are separated by 3.6 nm-thick $\text{Al}_{0.2}\text{Ga}_{0.8}\text{N}$ barriers. They have been grown by MOVPE on top of a 3 μm GaN-template on *c*-plane sapphire substrate, and are capped by 35 nm of $\text{Al}_{0.2}\text{Ga}_{0.8}\text{N}$. This structure was grown in the same run as the active medium of the high-quality *c*-plane microcavity of Ref. [23]. Further information can also be found in Refs. [25, 26, 69, 103, 104].

The very low QW-width is due to restrictions imposed by the QCSE: indeed in such a MQW structure with $\text{Al}_{0.2}\text{Ga}_{0.8}\text{N}$ as barrier material, the built-in electric field should be as strong as 0.75 MV/cm [81]. This leads to a very narrow optimum QW-width, where the wave-function overlap and the exciton binding energy are maximized (cf. Fig. 2.8). From SP-simulations zero-density values of 0.8 and 44 meV are deduced for p_{QW} and E_{B} in this structure, respectively.

Figure 3.7(c) shows a high-resolution TEM image of the MQW-1 cross-section. The narrow QWs are clearly observed due to the strong atomic-mass contrast and the sharp interfaces. The barrier thickness of 3.6 nm has been chosen thick enough to avoid the formation of mini-bands due to coupling between adjacent QWs. The $T = 4\text{ K}$ PLE-spectrum in Fig. 3.7(a) is dominated by the QW-exciton absorption around 3.67 eV. As for the SQW-samples, it should be composed of A- and B-excitons being separated by about 10 meV. However, due to the increased inhomogeneous linewidth of the structure $\gamma_{\text{inh}} \approx 15\text{ meV}$, they cannot be clearly resolved. Assuming equal oscillator strengths, the absorption peak has been decomposed into

²This conclusion applies to a greater extent for sample SQW-2.

Figure 3.7: Sample MQW-1 consisting of 67 GaN QWs (1.2 nm) embedded in between 3.6 nm $\text{Al}_{0.2}\text{Ga}_{0.8}\text{N}$ barriers: (a) PLE (black dots), PL (red, gray) and reflectivity (blue) recorded at $T = 4\text{ K}$. (b) cw-PL temperature series (4-300 K) and low-temperature reflectivity spectrum (blue). The transitions 1 stem from the GaN buffer, and 2 corresponds to the QW LO-phonon replica. PL-spectra have been vertically shifted for clarity. (c) Cross-section TEM image. (d) Determined transition energies of the barrier (black) and the MQW (red) as a function of temperature.



two Gaussians yielding transition energies of 3.668 and 3.682 eV for X_A and X_B , respectively. No clear signature of the BB-absorption edge can be identified in the PLE-spectrum. At higher energies only the absorption enhancement due to EPCs is observed. The additionally shown PL-spectrum is dominated by luminescence originating from localized X_A -states. A localization energy of $\sim 11\text{ meV}$ can be deduced, which coincides well with the observed PL-linewidth and the γ_{inh} -value determined from PLE. On the low-energy side of X_A , the biexciton emission can also be observed. The gray PL-spectrum was taken with a slightly larger excitation power and normalized to the exciton emission intensity, highlighting the different power scaling between X and XX. The presence of biexcitons is additionally evidenced by the faster XX decay in the streak image in Fig. 3.3(b), which is following a X^2 dependence according to Eq. (3.4) after thermalization as evidenced in Ref. [69]. Therein, E_B^{XX} has been determined to be about 22 meV, which is significantly violating Hayne's rule likely due to the impact of disorder [100]. Compared to sample SQW-2, the presence of biexcitons in this MQW-structure is facilitated by the narrow QW-width (cf. Sec. 3.2.2) and the geometrical effect [81]. The latter reduces the effective field strength in a MQW structure compared to an equivalent SQW as discussed in Sec. 2.3.3. In contrast to SQW-1, the excitonic response of these MQWs can also be seen in the low-temperature reflectivity spectrum, confirming the results of PLE. The low-temperature PL and reflectivity spectra shown in Fig. 3.7(b) also reveal the contributions of the $\text{Al}_{0.2}\text{Ga}_{0.8}\text{N}$ barriers, the LO-phonon replica of the QW emission, and the response of the GaN buffer layer around 3.49 eV.

Temperature Dependence

When the lattice temperature is raised in a semiconductor, the increased phonon population leads to a rise in the homogeneous broadening according to Eq. (2.33). Furthermore, it causes

an increase in the lattice constants and thus a shrinking of the band edge due to the decreased interaction between overlapping atomic orbitals. Based on the Bose-Einstein occupation of phonon-states, the temperature dependence of E_G can be described by [105]:

$$E_G(T) = E_G(0) - \frac{2\alpha_B}{\exp(\Theta_B/T) - 1}, \quad (3.5)$$

where α_B and Θ_B correspond to averaged values of the electron-phonon interaction strength and the phonon energy, respectively. In the following, $\alpha_B = 86 \text{ meV}$ and $\Theta_B = 391 \text{ K}$ will be used for GaN.³ For AlGaIn alloys the values will be linearly interpolated with those of AlN [106]: $\alpha_B = 168 \text{ meV}$ and $\Theta_B = 527 \text{ K}$.

The evolution of the transition energies for the AlGaIn-barrier and X_A with increasing lattice temperature is displayed in Fig. 3.7(d). They have been determined from the low-injection cw-PL and reflectivity measurements that are shown in Fig. 3.7(b) (the reflectivity is only plotted for $T = 4 \text{ K}$). As already mentioned, the PL energy of X_A at 4 K is reduced with respect to the transition energy deduced from reflectivity by the localization energy. However, with increasing temperature the discrepancy between the two energies decreases, until they nicely coincide for $T > 200 \text{ K}$. This is the process of delocalization: thermal excitation progressively increases the mobility of the charge carriers or excitons until at $k_B T \approx E_{\text{loc}}$ they are free to escape from the localization centers. Note that Eq. (3.5) in combination with the GaN-parameters is not able to accurately reproduce the evolution of X_A . This is most likely due to the 2D confinement and the compressive strain state of the MQWs originating from the sapphire substrate. In contrast to the QW emission, the one of the barrier follows a very strong S-shape when the temperature is raised. From a comparison with the fit, one can expect a barrier localization energy around 30 meV. The large difference between the QW and the barrier localization energies is well accounted for by an inhomogeneous broadening that is mainly caused by alloy fluctuations [91]. In this picture, the inhomogeneous QW linewidth is mainly governed by the fraction of the QW wave-function that is penetrating into the barrier.

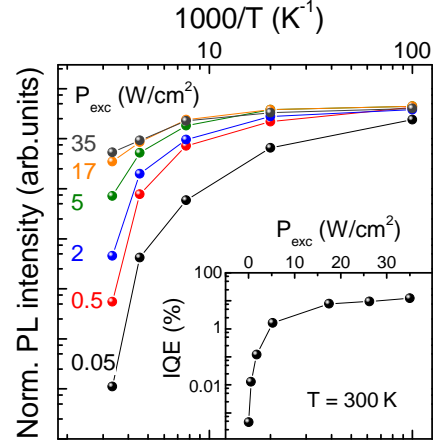
Estimate of the Internal Quantum Efficiency

Another impact of an increasing lattice temperature and the correspondingly rising mobility of the charge carriers is the thermal activation of non-radiative recombination channels. It is reasonable to assume that in a QW at $T = 4 \text{ K}$ the non-radiative carrier lifetime is much longer than the radiative one [107]. In this case the internal quantum efficiency (IQE) of the system is close to 100% and every electron-hole pair that reaches the band edge of the QW will recombine radiatively.

Figure 3.8 shows the evolution of the integrated MQW PL-intensity \bar{I}_{PL} , normalized to the varied laser excitation power density P_{exc} , as a function of lattice temperature. Note that an increasing carrier density is able to saturate certain non-radiative recombination channels leading to increasing IQE and \bar{I}_{PL} values with P_{exc} for a constant T . This effect is very pronounced at elevated temperatures, but it shows almost no influence at 10 K, where these channels are either screened or thermally inactive. It is thus reasonable to normalize the IQE at low temperature to 100%. In doing so, the IQE for MQW-1 at room temperature can be

³The values have been determined from a temperature-dependent PL-series carried out on a free-standing GaN substrate by M. Glauser working at LASPE-EPFL.

Figure 3.8: Sample MQW-1: excitation-power normalized \bar{I}_{PL} of the MQWs as a function of the inverse lattice temperature for different average excitation power densities ranging from 0.05 to 35 W/cm². The sample was excited with the pulsed Nd:YAG laser at 266 nm. The inset shows the deduced IQE at $T = 300$ K as a function of P_{exc} . It reaches values exceeding 10% for the highest injection. Adopted from Ref. [108].



estimated to values around 10% for high excitation power densities, whereas this value drops substantially toward lower injection (inset of Fig. 3.8). Note that due to the non-resonant excitation scheme these IQE values encompass the whole MQW system, including the QWs and the AlGaIn barriers. Taking into account the much stronger carrier localization in the barrier material as observed in Figs. 3.7(b,d) in combination with a correspondingly long radiative lifetime, it is therefore very likely that these room temperature IQE values are limited by non-radiative recombination occurring in the AlGaIn barriers. Hence, the bare QW efficiency might be higher than the reported values, especially in the low carrier density regime.

3.3 The Mott-Transition

As already remarked at the end of the last chapter, the exciton properties are not invariant against an increasing carrier density. This does not exclusively concern the values of its oscillator strength, transition energy and linewidth, but also the stability of the exciton as a whole. Whereas excitons obey Bose-Einstein statistics in the low density limit, an increasing carrier density will reinforce fermionic interactions between the constituents, eventually leading to the dissociation of the excitonic complex. The crossover between an exciton gas in the dilute limit and an uncorrelated and conductive electron-hole plasma at high carrier densities is usually referred to as the *Mott-transition*, according to the predictions made by Sir Nevil Mott in 1961 [109].

This section will be opened by a short theoretical overview about the Mott-transition (MT), which is followed by a comprehensive analysis of the low-temperature MT in GaN/AlGaIn SQWs and the successive discussion of its temperature dependence. At the end of this chapter, the role of biexcitons in the MT will be considered and the behavior of highly-injected GaN/AlGaIn MQWs under pulsed excitation will be analyzed. This latter study will serve as a basis for the subsequent chapter.

3.3.1 Theoretical Background

With respect to the present experimental investigations that exclusively concern QW-excitons, the subsequent considerations will be based on a 2D-system. However, the major part of the conclusions will also be valid for other dimensionalities.

From Bosons to Fermions

Excitons are quasi-particles composed of two fermionic constituents but possess an integer total spin, which suggests that they should share very similar properties with a Bose-gas [110]. Contrary to fermions, bosons of one species are indistinguishable particles. Within the framework of second quantization, the creation and annihilation operators of a boson of wave-vector \mathbf{k} , $\hat{b}_{\mathbf{k}}^{\dagger}$ and $\hat{b}_{\mathbf{k}}$, fulfill the commutation rule:

$$[\hat{b}_{\mathbf{k}}, \hat{b}_{\mathbf{k}'}^{\dagger}] = \delta_{\mathbf{k}, \mathbf{k}'}, \quad (3.6)$$

where δ corresponds to the Kronecker delta. The creation operator of an exciton $\hat{d}_{\mathbf{k}_{\perp}}^{\dagger}$ with in-plane wave-vector \mathbf{k}_{\perp} can be expressed as a linear combination of the uncorrelated electron and hole creation operators. A calculation of the commutator from Eq. (3.6) for the exciton is a quite demanding task, but its mean value for a perfect 2D-system with exciton carrier density n_X has been evaluated to [63, 111]:

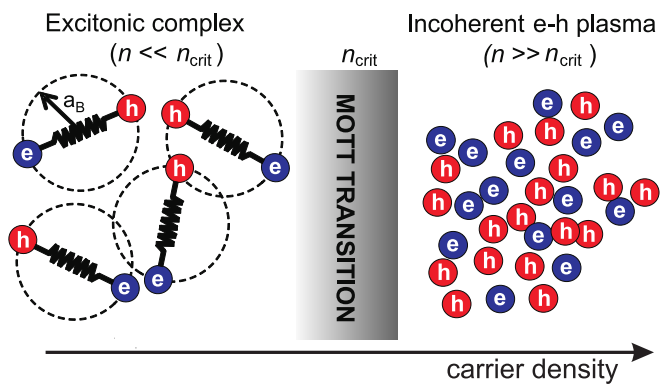
$$[\hat{d}_{\mathbf{k}_{\perp}}, \hat{d}_{\mathbf{k}'_{\perp}}^{\dagger}] = \delta_{\mathbf{k}_{\perp}, \mathbf{k}'_{\perp}} - \mathcal{O}(n_X a_B^2). \quad (3.7)$$

Owing to the finite error \mathcal{O} , this commutation rule is never completely satisfied in presence of a non-zero carrier density. However, in the low density limit, when n_X is much smaller than the inverse exciton volume, a reasonable agreement is achieved with the ideal bosonic case and excitons will obey Bose-Einstein statistics. With rising carrier density the value of \mathcal{O} progressively increases [112]. Thereby, the disappearance of the bosonic nature stems from the increasing role played by Coulomb interactions and the progressive filling of the phase space (Pauli-blocking principle). Both mechanisms become dominant when the inter-particle distance approaches the exciton Bohr-radius: they cause a reduction of E_B and eventually the dissociation of the excitonic complex around a certain critical density n_{crit} , defining the MT (cf. Fig. 3.9). As a first approximation the latter value can be estimated from the simple hard-sphere criterion:

$$n_{\text{crit}}^0 = \frac{1}{\pi a_B^2}. \quad (3.8)$$

Note however that depending on the screening mechanism at play, n_{crit} is expected to be overestimated by one or two orders of magnitude when using this approach [113, 114]. At

Figure 3.9: Schematic representation of the Mott-transition: In the low density limit $n_X \ll n_{\text{crit}}$ the carrier population is composed of excitons, whereas above n_{crit} the system is dominated by an uncorrelated and conductive electron-hole plasma. Adapted from Ref. [108].



low temperatures ($E_B > k_B T$) screening preferentially arises due to cold excitons. For such a mechanism, n_{crit} has been estimated to be around $n_{\text{crit}}^0/10$ in Ref. [113]. At elevated lattice temperature, this value can additionally be influenced by free electron-hole (e-h) pair screening that might even become dominant for GaAs-based QWs [115]. Nevertheless, it has been experimentally and theoretically shown that screening due to both free carriers and excitons should be of comparable efficiency in 2D-systems [113, 116, 117]. With respect to the large E_B -values of the QWs under investigation here, i.e. $E_B \sim 30$ meV for the SQWs and $E_B = 44$ meV for MQW-1, the impact of free electron-hole pairs is assumed to be marginal up to 150 K in the SQW-case and up to room temperature for sample MQW-1, and thus $n_{\text{QW}} = n_X$ [69].

Literature Review

The MT was initially claimed to be an abrupt first-order phase transition [10, 109], being characterized by a discontinuous change in the ionization degree. However, this statement was critically debated repeatedly during the past years: apart from the proposals of an either abrupt or continuous crossover, even a potential bistability has been proposed [118]. For bulk semiconductors, theories and experimental studies exist that claim the MT in one form or the other: as a first-order transition [119, 120], or as a continuous second order one [121–123]. In such 3D-systems the difficulty often consists in generating a well-defined carrier density, since the exponential absorption profile often leads to signal superposition from differently injected regions. More recent results obtained on GaN and ZnO epitaxial layers confirmed a MT of continuous type [56, 114, 124]. In 2D-systems, the situation appears to be different. It was theoretically evidenced that long-range Coulomb interaction due to free e-h pairs are suppressed in QWs [125], and that here exciton screening should mainly arise from phase-space filling arguments [113]. This effect has been evidenced by carrying out transmission measurements on highly-excited GaAs QWs [126]. However, there are still contradictory theoretical expectations concerning the nature of the MT [127–129], whereas experimental studies typically reveal a smooth crossover [130, 131], in agreement with the progressively decreasing commutator in Eq. (3.7). Corresponding studies in III-nitride based structures are very scarce. Most of them concern only bulk GaN layers associated with the aforementioned weakness of an inhomogeneous and hardly quantifiable carrier density. Binet and co-workers investigated the optically-induced MT in bulk GaN layers deposited on sapphire [56]. Based on the observed bandgap renormalization (cf. definition mentioned below), they observed a smooth MT occurring around $2 \cdot 10^{18} \text{ cm}^{-3}$ at low temperature and claimed a distinct rise of n_{crit} with temperature, ascribed to an increasing Debye-Hückel screening length. Consistent results of a smooth MT potentially involving biexcitons have also been evidenced in thick GaN epilayers by high-excitation tr-PL studies [124, 132]. Earlier studies concerning the high-density regime in GaN/AlGaIn QWs are rare and often focus on QCSE screening effects. Examples are given by the time-integrated PL study conducted with pulsed excitation by Lepkowski and co-workers [133], which does not explicitly discuss the possibility of a MT although on the basis of the present results it might have been observed, and by the time-resolved PL measurements presented by Lefebvre and co-workers [134]. Therein, the strong QCSE in the thick GaN/Al_{0.15}Ga_{0.85}N QW reduces the exciton binding energy to values below the inhomogeneous linewidth, preventing an in-depth discussion of the MT even if phase-space filling (PSF) effects may have been observed at short time delays.

Exciton Renormalization

Since the exciton is not invariant against an increasing carrier density, its optical response according to Eq. (2.31) will also be subject to certain modifications when n_X approaches the Mott-density n_{crit} . Various physical effects have to be considered that shall be introduced hereafter.

An excitonic system intrinsically consists of charged particles, which predominantly interact via Coulomb-forces. Owing to the fermionic nature of the exciton constituents, both direct and exchange terms of the Coulomb-interaction have to be considered. In the usually assumed picture that is depicted in Fig. 3.10, the continuum band edge E_G monotonously redshifts with increasing n_{QW} due to the interplay of exchange and multi-particle correlation effects [117, 129]. In 2D and 3D systems, this bandgap renormalization (BGR) is expected to follow a cubic-root density dependence [123, 135, 136]:

$$E_{\text{BGR}}(n_{\text{QW}}) = E_X(n_{\text{QW}} = 0) + E_B(n_{\text{QW}} = 0) - \alpha_{\text{BGR}} \cdot n_{\text{QW}}^{1/3}, \quad (3.9)$$

where α_{BGR} denotes a material and dimensionality-dependent proportionality constant, which can be estimated in a 2D-system to [135]:

$$\alpha_{\text{BGR}} = 3.1 \cdot a_{\text{B}}^{2/3} E_{\text{B}}. \quad (3.10)$$

At the same time, the exciton binding energy is expected to decrease with rising n_{QW} owing to the mutual effects of PSF and exchange-interaction [113]. Whereas few works consider a linear density dependence [137, 138], the major part of conducted experiments revealed only marginal or even negligible exciton energy shifts up to very high densities [123, 131, 139]. These observations are in agreement with other theoretical considerations, which predicted a remarkable independence of the exciton energy on the carrier injection up to n_{crit} owing to the exciton charge neutrality and thus an almost perfect compensation of BGR and exciton-exciton interaction effects [117, 123, 129]. In such a case, a simplified criterion for the MT can also be set by:

$$E_{\text{QW}}(n_{\text{QW}} = n_{\text{crit}}) = E_{\text{BGR}}(n_{\text{QW}} = n_{\text{crit}}) = E_X(n_{\text{QW}} = 0). \quad (3.11)$$

Note that so far the above-mentioned discussion neglects any influence of the QCSE. According to Sec. 2.3.4, as a direct consequence of the QCSE in c -plane heterostructures the QW ground state energy and the exciton binding energy are intrinsically density-dependent. QCSE-screening superimposes to the effects of BGR and the saturation-induced E_{B} reduction and correspondingly increases the complexity of the problem. Figure 3.10 depicts the MT on the basis of experimental results that were recorded on sample SQW-1 at 4 K (cf. Sec. 3.3.2 hereafter). Here, the additional QCSE effects lead to a finite exciton energy shift below n_{crit} and the kink in the E_{BGR} evolution around $3 \cdot 10^{12} \text{ cm}^{-2}$ in Fig. 3.10.

Apart from the energy renormalization, the direct dependence of a_{B} on the decreasing value of E_{B} according to Ref. [65] in combination with Eq. (2.46) gives rise to a saturation of the exciton oscillator strength f_X . Here, PSF becomes particularly effective: already occupied excited states cannot be filled twice owing to the Pauli-blocking principle and thus do not contribute to the light-matter coupling anymore. Different scalings for the f_X saturation with

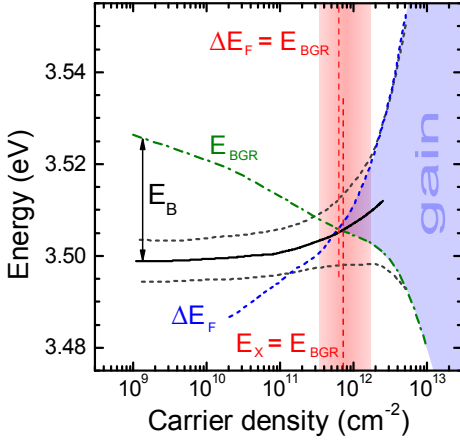


Figure 3.10: Schematic of the MT-defining criteria based on measurements performed on sample SQW-1 at $T = 4$ K: $E_X = E_{BGR}$, i.e. when the exciton merges with the e-h continuum, and $\Delta E_F = E_{BGR}$ marking the onset of gain (based on cw-PL MT at 4 K). The MT range is highlighted with red background, E_X is given by the black solid line and the gray dashed lines mark the upper and lower QW half maximum energies.

carrier density have been proposed [113, 115, 138]. Note that for the III-nitride structures under investigation here, those would be further modified by the QCSE-screening due to the increasing wave-function overlap according to Eqs. (2.42) and (2.46). However, from the PL studies that are presented in this chapter no straightforward conclusion on the f_X behavior can be drawn. For a more detailed discussion, the reader should refer to Sec. 4.5.

Another effect that may emerge in presence of an increasing carrier density is exciton-exciton interaction-induced broadening of the exciton line [55, 140]. The collision-induced homogeneous broadening term discussed in Sec. 2.2.2 will gain importance and result in a density-dependent homogeneous linewidth contribution γ_{col} . Based on the interparticle scattering efficiency, the scaling appears thereby to be linear or sub-linear depending on the excitation conditions [141].

In real structures, nonidealities like carrier localization and pumping-induced sample heating might additionally have to be considered. In the former case the progressive filling of localization centers would result in a blueshifting exciton line in PL measurements, while the intrinsic optical properties are not readily modified when assuming that the density of localized states is much lower than the JDOS. Owing to the high-quality of the studied QW structures, such an effect is expected to occur at densities well below those where QCSE screening and E_B -reduction become effective. A local increase in the lattice temperature may cause a redshift in the emission and an increased homogeneous linewidth. Due to the low duty-cycle used in the tr-PL measurements this effect can be safely neglected. However, this does not directly apply for cw-PL measurements. Here, the GaN-substrate emission close by served as indicator for a potential heating, revealing however no significant impact throughout the study.

The Bernard-Duraffourg Condition

Strictly speaking, the transition rate given by Eq. (2.15) is only valid in absence of excitons for semiconductors in the ground state, i.e. when there are no free electrons and holes. In a more general case the occupancy of excited VB and CB-states has to be taken into account owing to the previously explained PSF, i.e. the Pauli-exclusion principle. The occupancy of states in a semiconductor with bandgap E_G out of thermal equilibrium is given by the electron and hole

quasi Fermi-distributions f_e and f_h , respectively. They are obtained via [142]:

$$f_e(\hbar\omega) = \left[\exp\left(\frac{\mu^*(\hbar\omega - E_G)/m_e^* - E_{F,e}}{k_B T_{\text{car}}}\right) + 1 \right]^{-1}, \quad (3.12)$$

$$1 - f_h(\hbar\omega) = \left[\exp\left(\frac{\mu^*(\hbar\omega - E_G)/m_h^* - E_{F,h}}{k_B T_{\text{car}}}\right) + 1 \right]^{-1}, \quad (3.13)$$

where T_{car} corresponds to the temperature of the charge carriers, and $E_{F,e}$ and $E_{F,h}$ denote the respective electron and hole quasi Fermi-energies, that depend on the carrier concentration n_{e-h} and that are in 2D relative to the band edges given by:

$$E_{F,e} = k_B T_{\text{car}} \cdot \ln \left[\exp\left(\frac{\pi \hbar^2 n_{e-h}}{e m_e^* k_B T_{\text{car}}}\right) - 1 \right], \quad (3.14)$$

$$E_{F,h} = k_B T_{\text{car}} \cdot \ln \left[\exp\left(\frac{\pi \hbar^2 n_{e-h}}{e m_h^* k_B T_{\text{car}}}\right) - 1 \right]. \quad (3.15)$$

For a transition matrix element that is independent of the wave-vector the absorption rate R_{abs} based on Eq. (2.15) is in this case defined as:

$$\begin{aligned} R_{\text{abs}}(\hbar\omega) &= \frac{\pi e^2}{2 \hbar m_0^2 \omega^2} |\mathbf{E}|^2 |\mathbf{p}_{cv}|^2 D_{cv}(\hbar\omega) \cdot f_h(\hbar\omega) [1 - f_e(\hbar\omega)] \\ &= R_0 \cdot f_h(\hbar\omega) [1 - f_e(\hbar\omega)]. \end{aligned} \quad (3.16)$$

Equivalently, the rate for stimulated emission R_{ste} can be obtained via:

$$R_{\text{ste}}(\hbar\omega) = R_0 \cdot f_e(\hbar\omega) [1 - f_h(\hbar\omega)]. \quad (3.17)$$

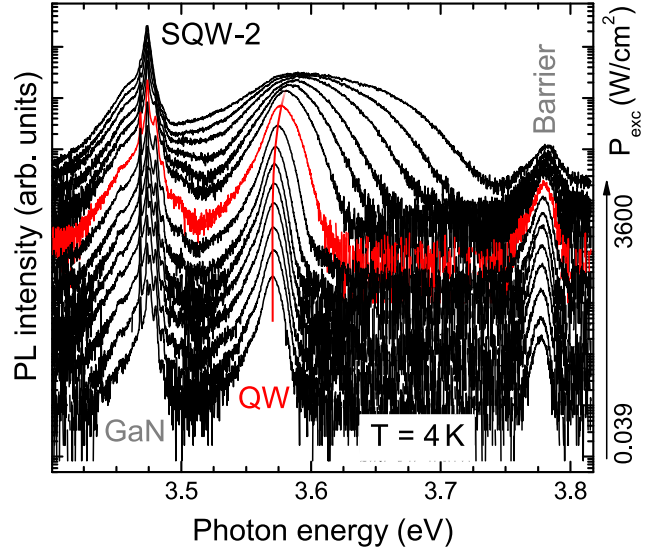
For the net transition rates at the bandgap energy $E_G = E_c - E_v$ holds therefore:

$$\frac{R_{\text{abs}}}{R_{\text{ste}}} = \frac{f_h(E_v) [1 - f_e(E_c)]}{f_e(E_c) [1 - f_h(E_v)]} = \exp \left[\frac{E_G - \Delta E_F}{k_B T} \right]. \quad (3.18)$$

Based on the quasi Fermi-level separation $\Delta E_F = E_G + E_{F,e} + E_{F,h}$, one can distinguish two different cases. In the low carrier density regime, i.e. close to equilibrium when $\Delta E_F < E_G$, absorption dominates at the bandgap energy. However, when $\Delta E_F = E_G$ absorption and emission rates would perfectly compensate each other, giving rise to the effect of a carrier injection-induced transparency and setting the Bernard-Duraffourg limit [8]: if the carrier density is further increased, the absorption coefficient at the bandgap energy given by Eq. (2.35) would turn negative marking the onset of optical gain in a semiconductor. This opens up the operation regime of LDs, where the lasing threshold occurs when the gain overcomes the losses in the device. Note that this is a purely fermionic effect, that requires electrons and holes as dominant carrier species. Another criterion for the MT can thus be set by the onset of gain. It can be easily transferred to other dimensionalities, for a QW E_G has to be replaced by E_{QW} in Eqs. (3.12), (3.13) and (3.18), and the Bernard-Duraffourg condition reads (cf. Fig. 3.10):

$$\Delta E_F(n_{\text{QW}} = n_{\text{crit}}) \geq E_{\text{BGR}}(n_{\text{QW}} = n_{\text{crit}}). \quad (3.19)$$

Figure 3.11: Excitation power dependent cw-PL spectra recorded on sample SQW-2 at 4 K: Starting from 240 W/cm² (red spectrum) the QW-emission strongly extends toward higher energies, while the low-energy edge is subject to an increasing broadening.



3.3.2 Low-temperature Mott-transition

The discussion on the experimental results concerning the MT shall start with the low-temperature data. Owing to the shorter carrier lifetime and the negligible homogeneous broadening, the spectral characteristics of the MT are more pronounced facilitating a comprehensive analysis. Note that the following experimental investigations and the corresponding modeling procedure of the spectra are based on the tr-PL study, that was conducted by Kappei and co-workers on an InGaAs-based SQW in Refs. [131, 143].

Experimental Results

Figure 3.11 shows spectra of an injection-dependent cw-PL series recorded at 4 K on sample SQW-2 using the experimental setup of Fig. 3.1. The single 2 nm-thick GaN/Al_{0.18}Ga_{0.82}N QW features an emission energy around 3.58 eV and thus a large energy splitting from the substrate and barrier emissions. As for the other SQW structures, its ground state is expected to be built from A and B-excitons, which are separated by about 10 meV and exhibit similar oscillator strengths. However, due to the increased inhomogeneous linewidth of 15 meV, which is likely caused by the larger fluctuations of the Al-concentration in the barriers [91], they could not be separately resolved in PLE measurements (not shown here). The excitation power density P_{exc} has been varied from 0.039 to 3600 W/cm². In the low injection regime $P_{\text{exc}} < 20$ W/cm², the QW emission shows a linear power-scaling and only negligible variations in energy. The non-Gaussian low-energy emission tail is likely caused by the contribution of localized states. The barrier emitting at 3.76 eV exhibits an emission linewidth similar to that of the QW and an almost linear emission-intensity scaling, indicating the high-quality of the structure. Proceeding toward higher P_{exc} , the QW emission gains in linewidth and starts to blueshift due to QCSE-screening. This effect can be followed up to the red spectrum corresponding to $P_{\text{exc}} = 240$ W/cm²: starting from there, the high-energy QW emission tail strongly extends reaching almost the barrier energy for the highest densities. At the same time, the amplitude of the QW PL-intensity tends to saturate. Moreover, the low-energy edge is subject to an increasing linewidth of homogeneous origin indicating heating of the carrier

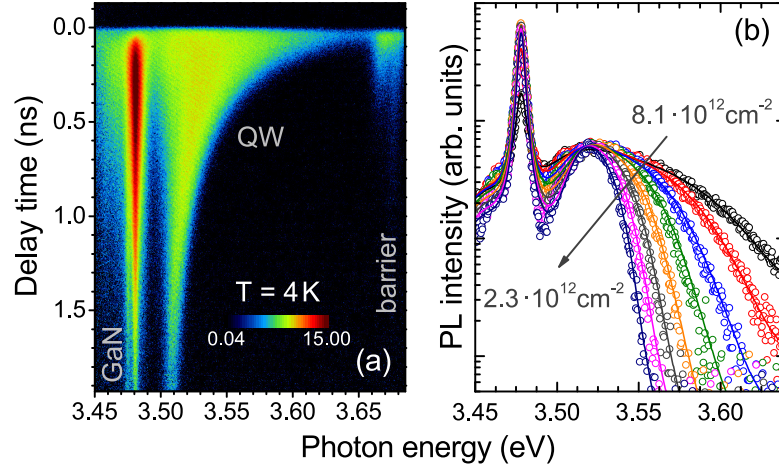


Figure 3.12: High-injection tr-PL carried out on SQW-1 at $T = 4 \text{ K}$: (a) Streak camera image (log-scaled intensity map). (b) Spectral profiles taken at different time delays (steps of 60 ps): Comparison of experimental data (dots) and modeling (lines).

population in agreement with the exponential shape of the high-energy emission tail.

These experimental findings are confirmed by low-temperature high-injection tr-PL studies. Figure 3.12(a) displays a streak image, which was recorded on sample SQW-1 using the setup of Fig. 3.4. The excitation pulses arrived at zero delay-time with an energy of about 3.5 pJ. The emission of the GaN substrate around 3.48 eV, the barrier around 3.68 eV and that of the QW energetically in between can be clearly resolved (cf. Fig. 3.5). Following the excitation pulse, the QW emission emerges with an enormous linewidth of about 100 meV, spanning over nearly the whole spectral range between substrate and barrier. Subsequently, the QW emission band progressively shrinks down with increasing delay time. In this process it exhibits a saturated amplitude, which only starts diminishing when the spectral extension has almost reached its minimum after about 1 ns delay. The emission of the GaN substrate exhibits a much longer rise time than that of the barrier and the QW. In fact, its time constant coincides with the rapid emission decay of the AlGaIn barrier. Indeed, the total thickness of the QW-barrier stack corresponds to about twice the penetration depth at the laser wavelength, which makes photon recycling and carrier transfer from the AlGaIn and the QW the main source for carrier recombination in the substrate.

Note finally that despite the different structure and experimental technique, the spectral profiles taken from the streak image at different time delays and shown in Fig. 3.12(b) closely resemble the cw-PL spectra from Fig. 3.11. This fact and the remarkable conformity of the tr-PL spectra with those obtained by Kappei and co-workers on an InGaAs-based SQW indicate the universality of the experimental observation [131].

Modeling Procedure

Assuming that the QW-PL under the highest injection in Figs. 3.11 and 3.12 stems from an e-h plasma beyond the MT, the spectral emission profiles should be well represented by the radiative recombination rate. Based on Eq. (3.17) the rate of stimulated emission in a QW can

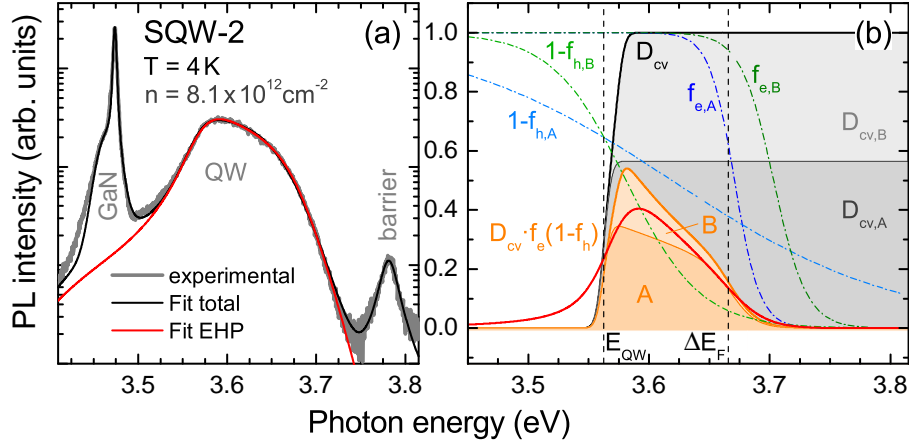


Figure 3.13: Details of the e-h plasma emission modeling procedure: (a) cw-PL emission profile of SQW-2 taken at 4 K and an excitation power density of 3.6 kW/cm² (gray) in comparison to the complete fitting (black) and the bare e-h plasma modeling (red). (b) Schematic of the modeling for the same spectrum taking into account the A and B VBs with different effective masses: the sum of the spontaneous recombination rates of A and B transitions (orange) has been convoluted with a Landsberg-type Lorentzian yielding the final modeled spectrum (red).

be defined as:

$$R_{\text{ste}}(\hbar\omega) = \frac{\pi e^2}{2\hbar m_0^2 \omega^2} |\mathbf{E}|^2 \sum_{j=A,B} \left| \mathbf{p}_{cv,j} \right|^2 D_{cv,j}^{2D}(\hbar\omega) \cdot f_{e,j}(\hbar\omega) [1 - f_{h,j}(\hbar\omega)]. \quad (3.20)$$

Therein, the sum accounts for the A and B valence bands, which have been evidenced to contribute with equal shares to the QW optical response by means of PLE measurements, in agreement with Schrödinger- $k \cdot p$ calculations. Equation (3.20) describes an optical transition process under influence of an external perturbation, i.e. stimulated emission due to a finite number of photons. The spontaneous decay of a carrier population can also be interpreted as its stimulated decay in presence of vacuum-field fluctuations. The spontaneous recombination rate is then obtained via [144]:

$$R_{\text{sp}}(\hbar\omega) = \sum_{j=A,B} \frac{1}{\tau_{\text{rad},j}} D_{cv,j}^{2D}(\hbar\omega) \cdot f_{e,j}(\hbar\omega) [1 - f_{h,j}(\hbar\omega)], \quad (3.21)$$

where τ_{rad} denotes the radiative lifetime that is basically determined by the oscillator strength. With regard to the PLE results and the behavior observed in bulk GaN [53], equal oscillator strengths for A and B related transitions shall be assumed in the following, i.e. $\tau_{\text{rad},A} = \tau_{\text{rad},B}$.

For a certain transition in a perfect two-dimensional QW, the three-dimensional JDOS from Eq. (2.18) can be rewritten as:

$$D_{cv}^{2D}(\hbar\omega) = \frac{2}{4\pi^2} \int_{\text{BZ}} \delta(E_c(\mathbf{k}_{\perp}) - E_v(\mathbf{k}_{\perp}) - \hbar\omega) d^2 \mathbf{k}_{\perp}. \quad (3.22)$$

Assuming parabolic bands with an isotropic in-plane reduced carrier mass μ_{\perp}^* , the solution is

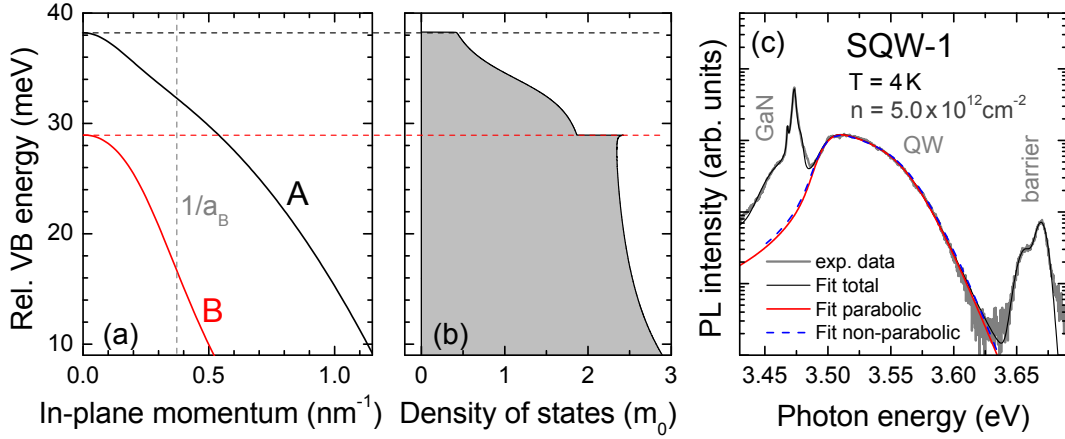


Figure 3.14: (a) In-plane VB dispersion of the fundamental QW transitions A and B as calculated from Schrödinger- $k \cdot p$ simulations for SQW-1. The vertical dashed line marks the inverse of the exciton Bohr-radius. (b) Deduced density of states showing the strong increase in the effective mass of the A-band when going away from the center of the BZ. (c) Modeling procedure of the e-h plasma for SQW-1: cw-PL emission profile of SQW-1 taken at 4 K and at an excitation power density of 3.6 kW/cm² (gray) in comparison to the complete fitting (black), the e-h plasma modeling in the parabolic approximation (red), and the e-h plasma modeling accounting for the non-parabolicity (blue dashed).

given by:

$$D_{cv}^{2D}(\hbar\omega) = \frac{\mu_{\perp}^*}{\pi\hbar^2} \mathcal{H}(\hbar\omega - E_{QW}), \quad (3.23)$$

where \mathcal{H} denotes the Heaviside-function.

The modeling procedure of the e-h plasma emission according to Eq. (3.21) is schematically depicted in Fig. 3.13(b). It is basically identical to the one used in Ref. [131], except that with regard to the commonly increased inhomogeneous linewidth in III-nitride structures, the two-dimensional JDOS for each transition has been additionally convoluted with a Gaussian of linewidth γ_{inh} . Subsequently, the quasi-Fermi distributions have been calculated according to Eqs. (3.12) and (3.13) by assuming parabolic bands with effective carrier masses, which have been calculated by $k \cdot p$ -simulations following the procedure described in Sec. A.1. Whereas the energy of the CB quasi-Fermi level could be calculated by Eq. 3.14, the presence of two VBs with a certain energy separation (8 meV for SQW-1) required an iterative approach for $E_{F,h}$ based on the VB density of states and the absolute carrier density. Note that contrary to the CB, that is parabolic within a good approximation [145], the VBs in GaN typically exhibit a pronounced non-parabolicity: Figs. 3.14(a,b) show the calculated VB structure of SQW-1 and the correspondingly deduced density of states. This effect is particularly apparent for the topmost A-band that emerges with a rather light effective mass of $\sim 0.45m_0$ at zero in-plane momentum, while for finite wave-vectors the mass rises rapidly up to $\sim 1.8m_0$. However, due to the dominant inhomogeneous linewidth (γ_{inh} was fixed to 8 meV) this effect plays only a minor role for the spectral lineshape (cf. Fig. 3.14(c)). Thus, in order to allow a reasonable computing time, A and B valence bands have also been assumed parabolic with an

effective mass that is set by the dispersion at finite in-plane wave-vectors: for sample SQW-1, $m_e^* = 0.2 m_0$, $m_A^* = 1.8 m_0$, and $m_B^* = 0.45 m_0$ have been deduced.

Finally, in agreement with Ref. [131] the summed recombination rates of the A and B transitions have been convoluted with a Landsberg-type Lorentzian accounting for the homogeneous linewidth due to scattering occurring in the Fermi-sea [146]. Its linewidth is calculated via:

$$\Gamma(E) = \Gamma_0 \left[1 - 2.23 \frac{E}{\Delta E_F} + 1.46 \left(\frac{E}{\Delta E_F} \right)^2 - 0.23 \left(\frac{E}{\Delta E_F} \right)^3 \right], \quad (3.24)$$

where $\Delta E_F = E_{QW} + E_{F,e} + E_{F,h}$ denotes the separation of the quasi Fermi-levels. This energy-dependent broadening allows to explain the observed larger broadening on the low-energy side of the QW spectrum. Eventually, the fitting parameters are given by the carrier temperature T_{car} , the two-dimensional charge carrier density n_{QW} , the modeled QW-bandgap energy E_{QW} set by the A-transition, the Landsberg linewidth Γ_0 , and a scaling parameter A for matching experimental and modeled intensities. Note that this fitting model is only valid when neglecting the influence of stimulated emission. This requirement is satisfied by the tiny spot size and detection normal to the QW-plane.

Figure 3.13(a) shows the modeling for the e-h plasma emission of sample SQW-2 in cw-PL (corresponding to the spectrum of highest injection from Fig. 3.11). The experimental spectrum is accurately reproduced by the fit, additional Voigt-profiles have been introduced to account for the substrate and barrier emissions. Excellent coincidence between model and experiment is also obtained for the spectral profiles recorded in tr-PL on SQW-1 shown in Fig. 3.12(b).

Analysis and Discussion

The aforementioned modeling procedure allows to translate the time delay in tr-PL and the injection-dependent cw-PL spectra into absolute QW-carrier concentrations n_{QW} . It is worth recalling that the experimentally applied spatial filtering and the SQW structure are essential for this approach. Only in this case, the collected luminescence comes from a homogeneous well-defined carrier density. Note further that the modeling is only valid for $n_{QW} > n_{crit}$, i.e. when the emission originates from an e-h plasma. Thus in order to obtain an absolute carrier density over the entire explored injection range, n_{QW} has been extrapolated for $n_{QW} < 2 \cdot 10^{12} \text{ cm}^{-2}$ based on the decay of the integrated PL-intensity of the QW (I_{PL}) using:

$$I_{PL} \propto \frac{n_{QW}}{\tau_{rad}(n_{QW})}, \quad (3.25)$$

In this process, the radiative lifetime τ_{rad} was assumed to vary with the injection-dependent change in the wave-function overlap p_{QW} due to QCSE screening. This effect has been considered by replacing τ_{rad} in Eqs. (3.21) and (3.25) with:

$$\tau_{rad}(n_{QW}) = \frac{\tau_{rad,0}}{p_{QW}^2(n_{QW})}, \quad (3.26)$$

in agreement with Eq. (2.46). The density-dependence of p_{QW} has been calculated by the SP-solver described in Sec. A.1.

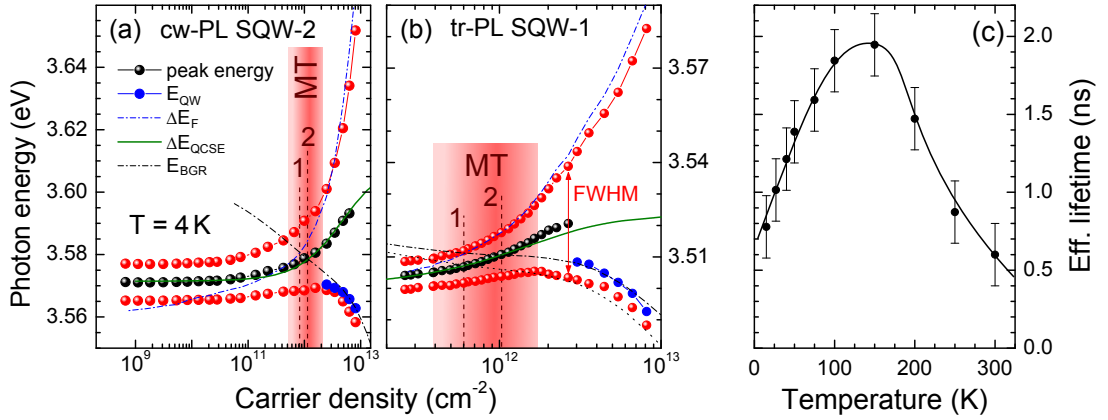


Figure 3.15: Fingerprint of the MT at $T = 4$ K: (a) evolution of the QW emission peak energy, upper and lower half maximum energy (red dots), and the modeled E_{QW} , ΔE_{QCSE} , and ΔE_F as a function of n_{QW} for the cw-PL study of SQW-2 from Fig. 3.11. The dependence of E_{BGR} was fitted using Eq. (3.9). The MT range is shaded in red. The vertical dashed lines mark the MT criteria: 1 - Eq. (3.19), and 2 - Eq. (3.11). (b) Equivalent representation for the tr-PL study of SQW-1 from Fig. 3.12. Here, the E_{BGR} evolution deduced from the cw-PL data of Fig. 3.16 is shown for comparison (black dotted line). (c) Effective QW lifetime as a function of lattice temperature measured at low injection ($n_{QW} < 10^{11} \text{ cm}^{-2}$, the solid line is a guide to the eye).

Although not being absolutely necessary for the present analysis, it is worth emphasizing that the high quality of the present SQW structures is further supported by a predominantly radiative carrier recombination up to elevated temperatures. Figure 3.15(c) shows the temperature dependence of the effective decay time of the QW emission τ_{eff} , which was deduced from low-injection tr-PL for sample SQW-1. Its rise up to 150 K confirms the dominant role of radiative recombination processes in the QW for the same temperature range. Indeed, with increasing lattice temperature excitons populate more and more states lying out of the light-cone. These cannot decay radiatively anymore resulting in an effective increase in τ_{rad} . Considering now that τ_{rad} is much shorter than the non-radiative decay time τ_{nr} , this effect will be transferred directly to τ_{eff} [147]. Finally for $T > 150$ K, non-radiative recombination processes start to dominate resulting in the typical decrease of τ_{eff} with increasing T . Due to a comparable structural quality, it is supposed that SQW-2 behaves in a similar manner.

Figure 3.15(a) displays the fingerprint of the MT as determined from cw-PL measurements on SQW-2 at 4 K: it shows the evolution of the PL peak energy, its full width at half maximum (FWHM) and the determined bandgap energy above n_{crit} as a function of the QW carrier concentration n_{QW} . In agreement with Fig. 3.11 and the corresponding discussion, two different injection regimes can be distinguished: for $n_{QW} < 6 \cdot 10^{11} \text{ cm}^{-2}$, the QW-emission features a symmetric lineshape, which slightly blueshifts and broadens with increasing density. Those two effects become particularly effective when n_{QW} exceeds 10^{11} cm^{-2} . The linewidth increase is attributed to collisional-induced broadening, which is a typical feature of a dense exciton gas [55]. The blueshift of the emission energy results from the screening of the QCSE: the field strength has been estimated to 0.75 MV/cm for SQW-2 [80]. SP-simulations have been performed to reproduce the density-dependent energy shift ΔE_{QCSE} according to Sec. 2.3.4. The computed evolution of the excitonic ground state (green line) properly follows the observed

PL peak energy, which confirms on the one hand the validity of the e-h plasma modeling procedure and on the other one the absence of any exciton blueshift due to a reduction of E_B .⁴ For carrier densities exceeding $6 \cdot 10^{11} \text{ cm}^{-2}$, the spectral width of the QW-emission starts to broaden remarkably. This effect comes from the strongly increasing quasi Fermi-level separation ΔE_F , which eventually exceeds substantially the band edge for $n_{\text{QW}} > 2 \cdot 10^{12} \text{ cm}^{-2}$. In this regime the QW features a plateau-like emission band with an enormous FWHM and without any clear peak energy. At the same time, the modeled bandgap energy E_{QW} starts to redshift with increasing carrier density due to BGR. These data have been fitted according to Eq. (3.9) yielding $\alpha_{\text{BGR}} = 3.8 \cdot 10^{-6} \text{ eVcm}^{2/3}$, i.e. a value in reasonable agreement with the prediction of Eq. (3.10) when using $E_B = 39 \text{ meV}$ and $a_B = 2.1 \text{ nm}$, as deduced from envelope-function calculations for SQW-2 (cf. Tab. 3.1).

Table 3.1: Comparison of theoretical and experimental ($T = 4 \text{ K}$) n_{crit} -values for samples SQW-1 and SQW-2. The values of α_{BGR} have been calculated according to Eq. (3.10). n_{crit}^{0*} corresponds to the frequently used critical density value that was derived by Schmitt-Rink and co-workers in Ref. [113].

Theoretical	SQW-1		SQW-2
E_B (meV)	30		39
a_B (nm)	2.7		2.1
n_{crit}^0 (cm^{-2})	$4.4 \cdot 10^{12}$		$7.2 \cdot 10^{12}$
n_{crit}^{0*} (cm^{-2})	$0.5 \cdot 10^{12}$		$0.8 \cdot 10^{12}$
α_{BGR} ($\text{eVcm}^{2/3}$)	$3.89 \cdot 10^{-6}$		$4.27 \cdot 10^{-6}$
Experimental	<i>tr-PL</i>	<i>cw-PL</i>	<i>cw-PL</i>
$E_{\text{BGR}} = E_X$ (cm^{-2})	$1.0 \cdot 10^{12}$	$0.7 \cdot 10^{12}$	$1.1 \cdot 10^{12}$
$E_{\text{BGR}} = \Delta E_F$ (cm^{-2})	$0.7 \cdot 10^{12}$	$0.6 \cdot 10^{12}$	$0.8 \cdot 10^{12}$
α_{BGR} ($\text{eVcm}^{2/3}$)	$3.3 \cdot 10^{-6}$	$3.8 \cdot 10^{-6}$	$3.8 \cdot 10^{-6}$

To summarize, for $n_{\text{QW}} > 2 \cdot 10^{12} \text{ cm}^{-2}$ the QW emission obviously originates from an e-h plasma excitation, whereas for $n_{\text{QW}} < 6 \cdot 10^{11} \text{ cm}^{-2}$ luminescence likely stems from an exciton gas as no further significant change in the emission lineshape can be identified down to the lowest carrier densities. Hence, the injection regime in between should correspond to the MT. From the modeling in Fig. 3.15(a), the n_{crit} -values corresponding to the criteria given by Eqs. (3.11) and (3.19) can be estimated to $1.1 \cdot 10^{12} \text{ cm}^{-2}$ and $8 \cdot 10^{11} \text{ cm}^{-2}$, respectively. Both values confirm the density range, which was deduced from pure spectral arguments. With a critical density of approximately 10^{12} cm^{-2} , the MT occurs almost one order of magnitude below the hard-sphere limit n_{crit}^0 according to Eq. (3.8). Table 3.1 summarizes the obtained results and compares them to theoretical predictions. Note that the evolution of ΔE_F below n_{crit} comes from the bare modeling and goes without a physical basis as the carrier population is dominated by excitons. It is just visualized for clarifying the trend.

The tr-PL spectra recorded on SQW-1 and displayed in Fig. 3.12 have been analyzed within the same approach. Figure 3.15(b) shows the respective characteristics of the MT in analogy with the above-mentioned discussion on sample SQW-2. A remarkable difference can be identified with respect to the previous cw-PL study: despite larger maximum densities around 10^{13} cm^{-2} , the explored injection range is much narrower. The lowest recorded density still amounts to $3 \cdot 10^{11} \text{ cm}^{-2}$. This fact originates from the relatively long QW lifetime $\tau_{\text{eff}} \sim 500 \text{ ps}$ in combination with the limited maximum temporal window of the streak camera, amounting

⁴Note that the recorded blueshift due to QCSE screening remains lower than the exciton binding energy justifying its treatment as a perturbation. However, this does not hold for thicker QWs, where QCSE effects become more important and may even dominate over quantum confinement and E_B [134], which would make the analysis in such a scenario more complex.

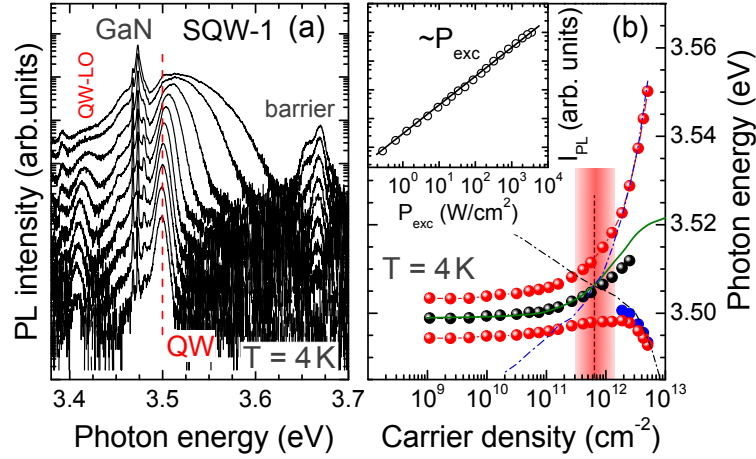


Figure 3.16: Low-temperature cw-PL MT-study on SQW-1: (a) Injection-dependent PL spectra for excitation power densities ranging between 0.3 and 3600 W/cm². (b) MT analysis in analogy with Fig. 3.15(a). The inset shows the evolution of the integrated PL intensity of the QW with increasing P_{exc} .

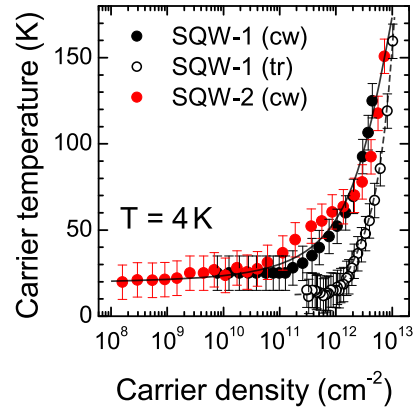
to 2 ns. However, apart from this difference the MT appears almost identical in this tr-PL study, both from spectral arguments and from the bare MT-criteria: Eqs. (3.11) and (3.19) yield values of $1.0 \cdot 10^{12} \text{ cm}^{-2}$ and $7 \cdot 10^{11} \text{ cm}^{-2}$ for sample SQW-1, respectively. Even if these are slightly reduced with respect to sample SQW-2, the difference appears lower than it would be expected from the smaller a_B value and the correspondingly reduced n_{crit}^0 (cf. Tab. 3.1). Anticipating the results of cw-PL discussed hereafter, this effect is likely caused by the different experimental conditions, e.g. the reduced T_{car} observed in tr-PL (cf. Fig. 3.17). A similar interpretation may also apply for the observed BGR. The deduced value for α_{BGR} is considerably reduced with respect to that determined for SQW-2 in cw-PL. It amounts only to $3.3 \cdot 10^{-6} \text{ eVcm}^{2/3}$.

In order to complete the picture of the low-temperature MT, SQW-1 was also investigated in cw-PL. Corresponding spectra and results are summarized in Fig. 3.16. The linear power-dependence of the integrated PL intensity over the whole injection range shown in the inset confirms the purely radiative character of the QW recombination. However, both the QW-emission spectra and the density-evolution of the modeled quantities support the previously discussed tr- and cw-results and their corresponding discussion. The Mott-transition criteria $E_{\text{BGR}} = E_X$ and $E_{\text{BGR}} = \Delta E_F$ result in respective values of $7 \cdot 10^{11} \text{ cm}^{-2}$ and $6 \cdot 10^{11} \text{ cm}^{-2}$ for n_{crit} . These values are slightly reduced compared to the tr-PL findings, but reflect much better the expected n_{crit} difference between SQW-1 and SQW-2 in Tab. 3.1. Indeed, under identical experimental conditions in cw-PL the determined n_{crit} values for both structures amount to about 15% of the hard-sphere limit n_{crit}^0 , and are thus close to the prediction of Ref. [113]. Further differences concern the observed redshift of the band edge beyond the MT: it appears much more pronounced in cw-PL. The deduced α_{BGR} value amounts equally to about $3.8 \cdot 10^{-6} \text{ eVcm}^{2/3}$ for SQW-1 at $T = 4 \text{ K}$. Such a discrepancy is also observed at higher temperatures (cf. Fig. 3.19(b)), where the BGR-induced redshift in tr-PL might even be suppressed for the highest n_{QW} values, i.e. for the shortest time delays. Thus, it appears likely that the lower α_{BGR} value deduced from tr-PL is directly related to the injection conditions. Indeed, in tr-PL shortly after the arrival of the pulse, impinging hot carriers from the AlGaIn

barrier will disturb the equilibrium conditions in the QW, whereas cw-PL relies on pure steady-state conditions. In the following, the α_{BGR} values as determined from cw-PL will therefore serve as a reference. For both samples, SQW-1 and SQW-2, these amount to about $3.8 \cdot 10^{-6} \text{ eVcm}^{2/3}$ at $T = 4 \text{ K}$, i.e. a value in good agreement with Eq. (3.10).

Figure 3.17 shows the evolution of the modeled T_{car} as a function of n_{QW} for all three low-temperature experiments. Obviously, the cw measurements yield higher carrier temperatures than tr-PL. This effect results from the different experimental conditions: whereas in tr-PL after a certain time delay all initially hot carriers have cooled down to the band edges, cw-excitation results in a static hot carrier population. These circumstances might explain the observed difference between the n_{crit} values deduced from tr-PL and cw-PL experiments. It has been shown that the exciton screening efficiency can be altered by a hot carrier population [113]. Nevertheless, for high injection the obtained carrier temperatures reach very similar values for both experimental schemes and sample structures. This might indicate an intrinsic heating mechanism, either collisional-induced or due to hot-phonons and/or Auger heating [148].

Figure 3.17: Evolution of the determined carrier temperatures as a function of the QW carrier density. In tr-PL, the absence of a static hot carrier population leads to lower T_{car} -values compared to cw-PL. Lines are guides to the eye.



In conclusion, the low-temperature MT in high-quality GaN-based SQWs was found to be of continuous type in agreement with established theories and previous experimental results [126, 129, 149]. In both explored experimental schemes, i.e. tr-PL and cw-PL, it shares many characteristics with the MT as it was observed by tr-PL in an InGaAs/GaAs SQW [131]: subtracting the additional influence of the QCSE, the exciton remains at constant energy independent of n_{QW} while undergoing a slight linewidth increase until E_{B} vanishes, in good agreement with most theories [117, 129]. At this stage the band edge starts redshifting due to BGR and the high-energy emission tail extends toward higher energies, while exhibiting a constant amplitude owing to PSE. A difference consists in the luminescence emerging from the continuum bandgap, which was observed by Kappei and co-workers below n_{crit} , but which remains completely absent in the present structures due to the increased E_{B} -value and the correspondingly low thermal occupation. Indeed, in Ref. [131] the band edge strictly remained at constant energy below n_{crit} and only followed the BGR-trend beyond the MT. The observed pinning of the exciton energy, in agreement with Refs. [116, 124, 126, 129, 131], partially contradicts certain results reporting a blueshift in the order of E_{B} that were preferentially observed in tr-experiments under resonant excitation conditions [149, 150]. Depending on the actual exciton binding energy and on the excitation conditions, the MT was found to occur at carrier densities around 10^{12} cm^{-2} , which is slightly less than one order of magnitude lower than the hard-sphere model prediction in good agreement with Refs. [113, 131]. The BGR-induced

redshift of the band edge beyond the MT can be described by a cubic root dependence with a proportionality parameter that is close to the theoretical prediction of Eq. (3.10), but does not show a significant dependence on E_B .

The Mott-Transition in PLE

As already detailed in Sec. 3.1.1, a PLE-spectrum recorded on a QW-structure does only correspond to absorption in the low-injection linear regime. By contrast, in the vicinity of the MT the QW properties feature pronounced non-linearities: E_X , f_X , and γ_X are strongly depending on the carrier density. Even though PLE is in this respect clearly not the ideal tool to gain a reliable insight into the MT, it can provide an additional qualitative perspective.

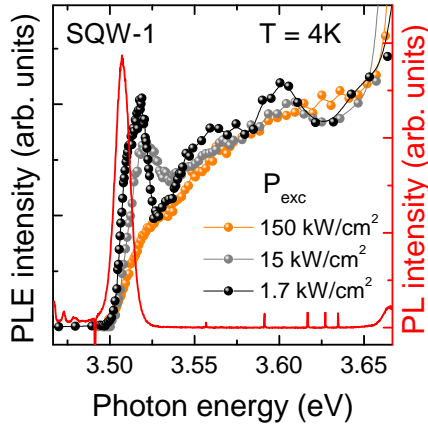


Figure 3.18: Qualitative view of the MT: PLE-spectra of SQW-1 as a function of the excitation power density. The low- P_{exc} spectrum corresponds to that of Fig. 3.5 and was taken at a slightly different position, but shifted in energy to match the low-injection PL peak-energy with the other spot. A non-resonant low injection PL-spectrum (red) is shown for comparison.

Figure 3.18 shows PLE-spectra recorded on SQW-1 using different excitation peak power densities at 4K. The low-injection spectrum corresponds to that of Fig. 3.5(b)⁵ and exhibits the typical conspicuous exciton absorption peaks building the QW ground state. However, an increase in P_{exc} by about one order of magnitude causes an already significant reduction of the exciton absorption amplitude and an increase in the linewidth. Moreover, the exciton lines appear blueshifted due to QCSE-screening and the visibility of the LO-phonon replica of the QW-exciton is diminished. When increasing P_{exc} by another factor of ten, the excitonic absorption features, direct ones and the LO-phonon replica, completely disappear. The MT is certainly crossed and the PLE-spectrum features an almost square-root like rise, as expected for direct bandgaps without excitonic effects in bulk semiconductors. Interestingly, the absorption edge appears at the former energy position of the exciton, confirming the picture of a BGR-induced MT according to Fig. 3.10. These results are in complete agreement with PLE-records from GaAs-based nano-structures [151].

3.3.3 Temperature Dependence

The consistency of the obtained low-temperature results with previous reports on GaAs-based systems illustrates an important fact: despite the different material system and the associated drawbacks, such as the increased inhomogeneous linewidth or the additional impact of QCSE, the investigated III-nitride heterostructures represent indeed a proper QW-system. Having this

⁵It was taken on a slightly different region and is therefore plotted with a shifted energy axis accounting for the different PL-emission energies of the two spots.

in mind, the next logical step consists in benefiting from the altered (or respectively improved) optical properties that come along with the material. With E_B exceeding the thermal energy at room temperature and an LO-phonon energy of 92 meV, excitons in these structures are very robust against thermal dissociation facilitating a comprehensive study of the MT temperature dependence. Despite existing theories, corresponding experimental results are extremely scarce or even non-existent in the case of QWs.

Given that the MT occurs when E_B vanishes, the excitonic complex should dissociate as soon as the screening length of the Coulomb-potential approaches the order of the excitonic Bohr-radius [114]. Despite this plausible statement, the exact definition of the screening length sets both the general uncertainty on n_{crit} and the temperature dependence of the latter in this approach. According to Ref. [152], an increasing Debye-Hückel screening-length λ_{DH} would result in a rise of the critical density with lattice temperature. The observation of such an effect was claimed in the study of Refs. [123] and [56]. In the former, the disappearance of the excitonic resonance in the absorption spectrum of bulk Ge was probed as a function of carrier density up to $T = 60$ K. The slope of n_{crit} versus temperature was found to be existent, but to be slightly lower than expected from the prediction of λ_{DH} . However, with respect to the limitation of the temperature range due to $E_B = 1.9$ meV and owing to the inconsistencies that arise when describing $n_{\text{crit}}(T)$ with λ_{DH} , namely $n_{\text{crit}}(T \rightarrow 0) = 0$ and $n_{\text{crit}}(T \rightarrow \infty) = \infty$ [114], those results remain at least controversial.

By contrast other approaches, e.g. based on Thomas-Fermi screening, remain without any clear temperature dependence. A similar conclusion applies to the aforementioned MT-defining criteria: the $E_{\text{BGR}} = E_X$ one from Eq. (3.11) gives reason to expect only a marginal temperature dependence of n_{crit} owing to the definition of the BGR based on structural parameters in Eq. (3.10).⁶ Equivalently one might only expect a weak rise of n_{crit} with T from the gain criterion of Eq. (3.19), caused by the temperature impact on the quasi Fermi-distributions. Given once more the invariance of E_B and a_B with T , the hard-sphere limit should also remain unaffected.

The temperature dependence of the MT has been studied on sample SQW-1 by using both tr- and cw-PL measurements. With respect to the exciton stability and the need of a predominantly radiative recombination character, the explored temperature window was restricted to 150 K at the maximum (cf. Fig. 3.15(c)).

Time-Resolved Experiments

Temperature-dependent tr-PL measurements have been performed in analogy with those depicted in Fig. 3.12 keeping a constant pulse energy and spot-size. By contrast, due to the thermal drift of the cryostat and the small spot, the exact sample region could not be kept over the T -scan.

Figure 3.19(a) displays PL-spectra recorded at 150 K for different time-delays. The spectral details remain quite similar compared to the 4 K-case in Fig. 3.12: at short time delays, the QW emission exhibits an enormous linewidth with an exponential high-energy tail. But owing to the increased carrier and lattice temperature the low energy-edge appears broader and the emission plateau due to PSF is less pronounced. The emission of the GaN substrate expected

⁶ E_B and a_B are only expected to be weakly temperature dependent based on ϵ_r (cf. Sec. 2.2.2).

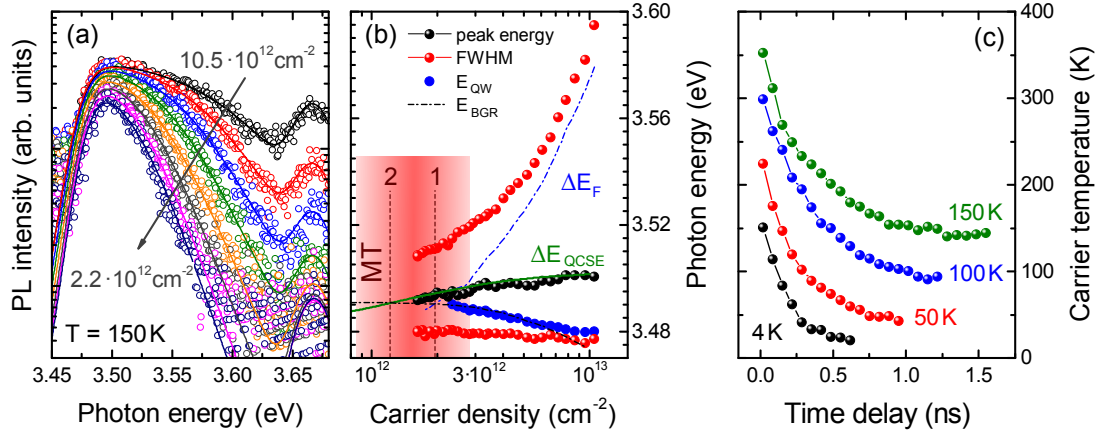
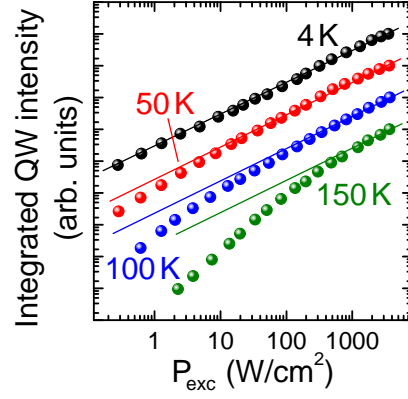


Figure 3.19: Temperature-dependence of the MT studied in tr-PL on SQW-1: (a) spectral profiles at different time delays measured at $T = 150$ K (steps of 150 ps): comparison of experimental data (dots) and modeling (lines). (b) Corresponding evolution of QW emission peak energy, upper and lower half maximum energy (red dots), and the modeled E_{QW} , ΔE_{QCSE} , and ΔE_{F} as a function of n_{QW} . The dependence of E_{BGR} was fitted using Eq. (3.9). (c) Temporal cool-down of the carriers at different lattice temperatures for $n_{\text{QW}} > 2 \cdot 10^{12} \text{ cm}^{-2}$.

to appear on the low-energy side is already quenched at this temperature.

The emission spectra have been analyzed using the same modeling procedure yielding an accurate fit in Fig. 3.19(a) and the evolution of the emission characteristics as a function of QW-density shown in Fig. 3.19(b). Despite the naturally increased linewidth, another remarkable difference in comparison to Fig. 3.15(b) consists in the minimum recorded carrier density, which still amounts to $1.5 \cdot 10^{12} \text{ cm}^{-2}$ compared to $3 \cdot 10^{11} \text{ cm}^{-2}$ at 4 K. Indeed, whereas the initial densities remain around 10^{13} cm^{-2} simply defined by the pulse energy, the increased carrier lifetime at 150 K (cf. Fig. 3.15(c)) and the temporal window of the streak camera strongly restrict the accessible density window. However, due to this and the absence of any substrate emission, the effect of BGR can be much better observed at this temperature. In fact, after the decay of the barrier, which is comparably fast as at low temperature (~ 200 ps), the determined carrier densities remain well above n_{crit} giving rise to a pronounced blueshift of E_{QW} with increasing time-delay. Nevertheless, the deduced α_{BGR} -value is even smaller than that obtained at 4 K in tr-PL. It amounts only to $3.2 \cdot 10^{-6} \text{ eV cm}^{2/3}$. Anticipating the conflicting cw-PL results shown hereafter, this effect can have multiple reasons: first, the relaxation toward equilibrium might not be completely finished, in agreement with the determined carrier temperatures shown in Fig. 3.19(c) that remain well above the lattice one at these densities. And second, owing to the very limited carrier density range, almost exclusively exploring densities above n_{crit} , the determined peak energies and thus the computed QCSE-screening may not exactly correspond to the evolution of E_{X} below n_{crit} but be affected by thermal occupation and PSF-effects. Correspondingly, the deduced Mott-criteria from Eqs. (3.11) and (3.19) will also be subject to an increased uncertainty. They yield values of $2 \cdot 10^{12} \text{ cm}^{-2}$ for $\Delta E_{\text{F}} = E_{\text{BGR}}$ and $1.2 \cdot 10^{12} \text{ cm}^{-2}$ for $E_{\text{X}} = E_{\text{BGR}}$. Thereby, the strong increase of n_{crit} due to the gain criterion, arising from the increased carrier temperatures, is also confirmed by the 50 and 100 K measurements.

Figure 3.20: Evolution of the integrated QW-emission intensity I_{PL} as a function of excitation power density P_{exc} for various lattice temperatures. Normalized intensities have been vertically shifted for clarity. The lines correspond to a linear power-law.



Continuous-Wave Experiments

Owing to the long carrier lifetimes the high-temperature tr-PL results are only partly exploitable, especially in view of the $E_X = E_{\text{BGR}}$ criterion, which lies out of the explored density range in Fig. 3.19(b). To overcome this restriction T -dependent cw-PL-measurements have been conducted giving access to a much larger range of carrier densities.

Contrary to the 4 K case, the evolution of I_{PL} shown in Fig. 3.20 for higher temperatures does not follow a strictly linear power dependence over the whole injection-range anymore. In the low-density limit the QW-emission intensity grows superlinearly with excitation power, which with respect to the predominantly radiative recombination in the QW indicates a mechanism that increases the IQE of the system by saturation of non-radiative recombination channels in the $\text{Al}_{0.09}\text{Ga}_{0.91}\text{N}$ -barrier. These are successively activated with increasing T leading to a decrease of the non-radiative lifetime in the barrier. Note that this effect is only modifying the carrier concentration in the QW, but has no impact on the validity of the modeling procedure.

The cw-PL experiments at 150 K shown in Fig. 3.21 largely confirm the modified characteristics observed in tr-PL. Nevertheless, there are some additional details visible: a significant occupation of X_B and even free carrier states is observed at low-injection as manifested by the high-energy shoulder in the exciton emission profile and the still present exponential high-energy tail far below n_{crit} . The tail has been fitted in the spectra of Fig. 3.21(a) yielding almost thermalized carrier temperatures around 170 K. Even if the band edge cannot be clearly identified, these fits highlight the non-exponential high-energy edge of an exciton line-shape at low carrier densities. With increasing n_{QW} , this detail progressively fades out until the QW-emission exhibits a purely mono-exponential high-energy tail at around 450 W/cm^2 . This feature is also visible at 100 K and marks the vanishing of the exciton emission line-shape, setting thus another criterion for the MT.

The output of the modeling in Fig. 3.21(b) reveals the characteristics of the MT at 150 K. Here, the determined peak energies do not directly correspond to the energy of the A-exciton owing to the contribution of excited B-exciton states. Moreover the overall emission energy blueshift remains lower than the predicted QCSE-screening. This discrepancy progressively emerges with rising T . Multiple reasons may apply: for instance, the superposition of an increased linewidth, the contribution of the B-exciton, and the onset of PSF-effects may conceal the true evolution of the QW-energy or alternatively, at these temperatures ionized donor electrons due to the background doping concentration ($\sim 10^{17} \text{ cm}^{-3}$) might pre-screen the QCSE. In any case,

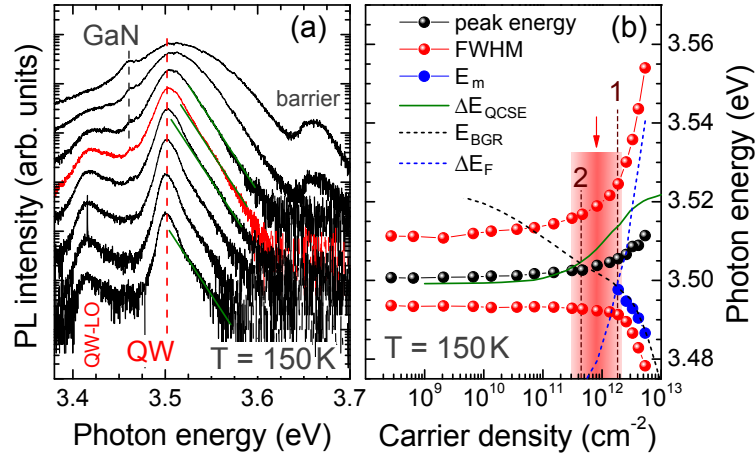


Figure 3.21: MT-study in cw-PL on SQW-1 at 150K: (a) injection-dependent PL spectra for excitation power densities ranging between 4 and 3600 W/cm². Exponential fits (green) of the high-energy tail mark the transition to an excitonic lineshape (red spectrum). (b) MT at 150K in analogy with Fig. 3.15. The red arrow marks the position of the red spectrum in (a), vertical dashed lines mark the MT criteria: 1 - Eq. (3.19), and 2 - Eq. (3.11).

this causes an increased uncertainty for the $E_X = E_{BGR}$ criterion. As already discussed the α_{BGR} value deduced from cw-PL significantly differs from that of tr-PL experiments at 150K. In fact, even an increased value compared to the 4 K case of $4.1 \cdot 10^{-6} \text{ eV cm}^{2/3}$ is determined from cw-PL. In combination with the impact of T_{car} , this leads to critical densities of $4.5 \cdot 10^{11} \text{ cm}^{-2}$ and $1.9 \cdot 10^{12} \text{ cm}^{-2}$ for the criteria $E_X = E_{BGR}$ and $\Delta E_F = E_{BGR}$, respectively. Both values comprise the n_{crit} , which was deduced from the aforementioned exciton line-shape criterion (indicated by the red spectrum/arrow in Fig. 3.21): $8 \cdot 10^{11} \text{ cm}^{-2}$.

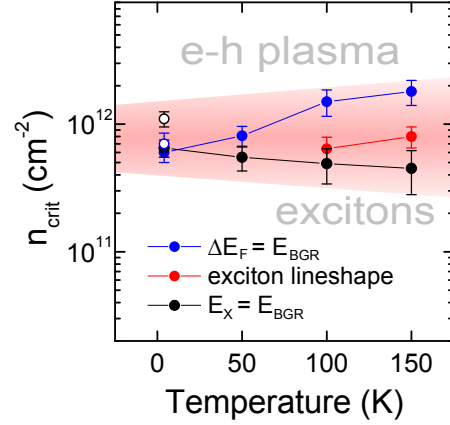
Analysis and Discussion

Figure 3.22 summarizes the temperature dependence of the n_{crit} -values as determined from the different MT-criteria. For the tr-PL measurements only the 4 K values are shown, owing to the lifetime restriction of the explored carrier density range and the uncertainties that arise with it. It is nevertheless worth mentioning that the omitted values also confirm the confidence interval of the MT that is shaded in red. While both criteria from Eqs. (3.11) and (3.19) yield similar values around $0.7 \cdot 10^{12} \text{ cm}^{-2}$ at low temperature, their trend with rising T is different. Owing to a slightly increasing BGR proportionality factor, the $E_X = E_{BGR}$ criterion yields n_{crit} -values that marginally decrease with temperature. This effect is overcompensated by the impact of T_{car} on the quasi-Fermi distributions leading to a considerable rise in n_{crit} with T when defining it via the onset of gain.

Probably the most reliable criterion for the MT consists in the disappearance of the excitonic lineshape. With the need for a sufficiently high temperature in order to occupy continuum states, it is only applicable for $T \geq 100 \text{ K}$, showing a small rise with increasing T . Eventually, no definitive trend on n_{crit} can be inferred within the explored T -range. The MT invariably takes place between 0.4 and $2 \cdot 10^{12} \text{ cm}^{-2}$, which corresponds to a value that is lowered by a factor of 2 to 10 compared to n_{crit}^0 , and which is more than one order of magnitude larger than the

n_{crit} -value of InGaAs-based QWs [131]. The absence of a distinct temperature dependence of the Mott-density contradicts the interpretation of an increasing screening length as employed in Ref. [123], but it agrees well with the findings and considerations of Klingshirn and co-workers for ZnO [114], where n_{crit} is defined by the BGR redshift and exhibits thus only a weak T -dependence. Nevertheless, in agreement with Ref. [131] the effect of BGR was exclusively observed above the critical density, which eventually leaves open questions that can only be solved by a comprehensive theory.

Figure 3.22: Dependence of n_{crit} on lattice temperature as deduced from various criteria based on cw-PL measurements: $\Delta E_F = E_{\text{BGR}}$ (open black dots), disappearance of an excitonic lineshape (cf. Fig. 3.21, red dots), and $E_X = E_{\text{BGR}}$ (black dots). The tr-PL results at 4 K are shown for comparison. The red shaded area marks the confidence interval.



There is certainly a motivation to extend the explored range toward higher temperatures. From the experimental point of view, both tr-PL and cw-PL measurements can surely be done for $T > 150$ K. However, difficulties will rather arise from the analysis side. Apart from the further increasing linewidth blurring all spectral characteristics, the increasing role of non-radiative recombination would lead to very large uncertainties in the extrapolated carrier densities below the MT and the mass-action law governing the dissociation of excitons would progressively promote thermal free electrons and holes as dominant carrier species.

3.3.4 Recombination Dynamics

Before concluding this section, the recombination dynamics in tr-PL shall be discussed in more detail. Figure 3.23(a) compares the decays of I_{PL} and the determined n_{QW} values for sample SQW-1 at 4 and 150 K. They are all non-exponential and qualitatively feature the expected lifetime difference according to the τ_{eff} values from Fig. 3.15(c). The temporal decays have been modeled within the approach of bimolecular recombination (BMR) using Eq. (3.21), while assuming the density-dependent radiative lifetime according to Eq. (3.26) and the evolution of T_{car} extracted from Fig. 3.19(c). As the only fitting parameter remains $\tau_{\text{rad},0}$ according to Eq. (3.26). It corresponds to the radiative lifetime for an envelope wave-function overlap of unity. The agreement between data and modeling is accurate at 150 K and quite decent at 4 K. In the latter case the stronger non-exponential character of the experimental data cannot be fully reproduced. Figure 3.23(b) compares the determined $\tau_{\text{rad},0}$ values with τ_{eff} from Fig. 3.15(c) that has been corrected for the calculated zero-density wave-function overlap. Considering the strongly different excitation conditions and the probing of completely different spots on the sample, the agreement is quite fair. Thus, BMR reproduces the recombination dynamics in the vicinity of the MT in a reasonable manner. The density-dependent wave-function overlap in c -plane GaN QWs leads to a strong non-exponential

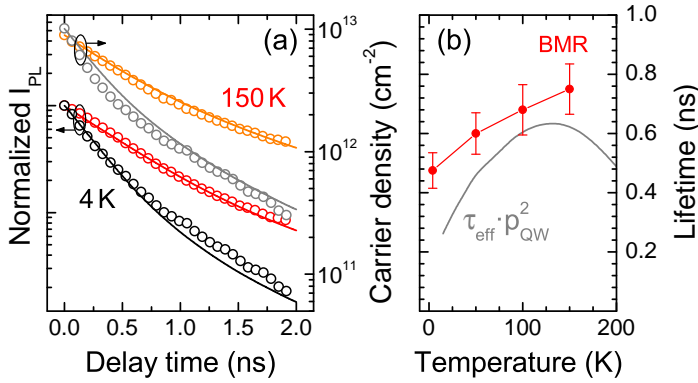


Figure 3.23: (a) Temporal decay of n_{QW} and I_{PL} in sample SQW-1 at 4 K (gray/black dots) and 150 K (orange/red dots), including modeling via BMR (lines). See text for details. (b) Normalized QW-lifetime as a function of T as determined from the modeling. The overlap corrected τ_{eff} from Fig. 3.15(c) is shown for comparison.

intensity decay, in contrast to the case of InGaAs-based QWs [131].

Auger-Recombination

Apart from the emission of a photon, the released energy of a recombining e-h pair can also be transferred to another free particle located close by. The rate of such an Auger-process scales with n^3 and is therefore especially effective in the high-injection limit. This non-radiative recombination mechanism is controversially considered to be the main reason for the commonly-observed efficiency droop of InGaN-based LEDs occurring at high driving currents [6, 7]. According to the cubic dependence on the carrier-density, if present it should appear as an ultra-fast initial decay in the tr-PL traces of Fig. 3.23(a) or as a saturation of the intensity at high P_{exc} in Fig. 3.20. However, the absence of such features excludes Auger-scattering as a non-radiative loss process in the present QW up to densities as high as $5 \cdot 10^{12} \text{ cm}^{-2}$, i.e. far beyond the Bernard-Duraffourg limit [8]. It is nevertheless worth mentioning that this statement does not necessarily need to apply directly to InGaN-based LEDs, although they are supposed to work well below the transparency limit. Indeed, Auger-effects occurring in In-containing QWs might be significantly enhanced, e.g., due the lower bandgap and the strongly increased carrier lifetime [6, 7]. Moreover, they operate at RT or above, which favors free electrons and holes as prevalent carrier species, that may behave in a partly different manner. Here, subsequent studies performed on high-quality InGaN SQWs would be required.

3.4 The Role of Biexcitons

Whereas the biexciton remains absent in samples SQW-1 and SQW-2 due to the pronounced impact of the QCSE [89], its quadratic power scaling according to Eq. (3.4) should make it dominating the high-injection regime when present. However, owing to its smaller binding energy and the correspondingly increased Bohr-radius it is supposed to be less robust against Coulomb-screening and PSF effects [153], which gives reason to expect a complex behavior of the biexciton in the vicinity of the MT. As an illustration, Hayamizu and co-workers have studied the onset of gain in presence of biexcitons in a 1D GaAs quantum wire [154]. Interestingly, gain occurred at the biexciton energy as soon as its intensity overcame the exciton one, an effect that was ascribed to exciton-biexciton population inversion. At even higher densities the biexciton gain band broadens and eventually converges to the broad e-h plasma gain

band beyond the MT. This fact indicates that the role of excitonic molecules in the crossover toward an e-h plasma excitation might be more intricate than initially expected from their small binding energy. However, for a 2D QW-system such an effect was not studied yet. In order to probe the impact of biexcitons in the MT, sample SQW-3 featuring strong biexcitonic emission (cf. Fig. 3.6) has been examined using the same experimental configurations as for SQW-1 and SQW-2 before.

Continuous-Wave Experiments

Figure 3.24(a) shows injection-dependent cw-PL spectra that were recorded on sample SQW-3 at 4 K. Leaving the buffer and barrier emissions aside, the QW-emission is governed by X_A and XX in agreement with Fig. 3.6. At low-injection XX is absent and the asymmetric low-energy emission edge rather emerges from localized excitons showing an only linear power scaling (not shown here). However, with increasing pumping power XX strongly gains in intensity, eventually overtaking the exciton in the red spectrum corresponding to $P_{\text{exc}} = 490 \text{ W/cm}^2$. In Fig. 3.24(c), the emission intensity of XX follows a power-law that is still super-linear but lower than the expected quadratic one. This effect is frequently observed and might be ascribed to the short carrier lifetimes [102]. Up to this power-density, both X and XX exhibit a small blueshift and only marginal variations in the emission line-shape. By contrast, starting from the red spectrum both emission bands undergo a significant modification: the linewidth strongly increases indicating the occurrence of the MT. At the same time, they feature only a sub-linear power-scaling in this high-injection regime. Note here that the connection to the MT might be purely fortuitous: an escape of carriers from the QW into the barrier is triggered as soon as the thermal high-energy tail reaches the barrier energy. Owing to the shallow confinement potential of SQW-3, this already takes place shortly after the MT. For even higher carrier densities, this escape mechanism prevents the formation of a clear plateau-like emission band, as expected from PSF and observed for samples SQW-1 and SQW-2. This

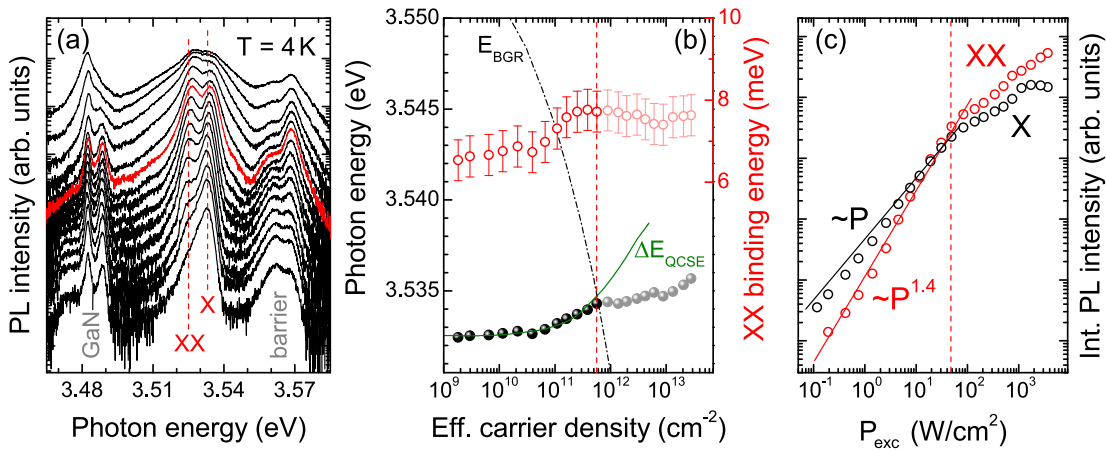
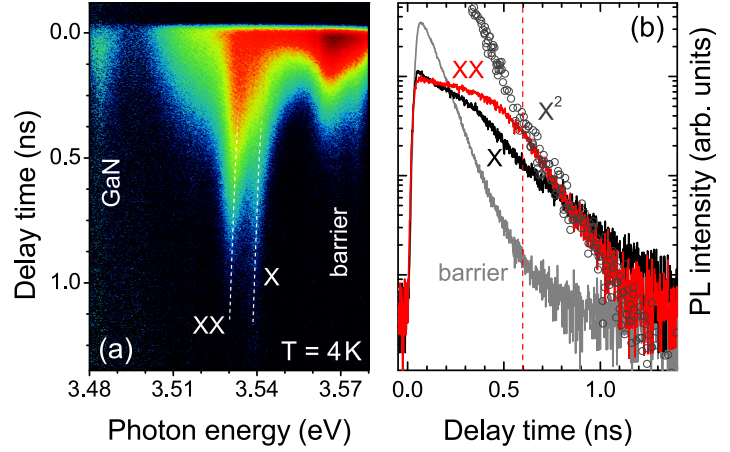


Figure 3.24: MT in cw-PL for SQW-3 measured at $T = 4 \text{ K}$: (a) PL power series recorded for power densities ranging in between 0.03 and 3700 W/cm^2 . The red spectrum marks the MT. (b) Deduced E_X and E_B^{XX} values as a function of the effective QW carrier density. The criterion $E_X = E_{BGR}$ (vertical red line) sets the MT corresponding to the red spectrum in (a). See text for details. (c) Integrated PL-intensities of X and XX as a function of excitation power density.

Figure 3.25: High-injection tr-PL of SQW-3 carried out at $T = 4\text{K}$: (a) Streak camera image (log-scaled intensity map). (b) Temporal decays of the XX, X and barrier PL intensities. The square of the X-intensity is also reported indicating the thermodynamic equilibrium between X and XX populations after approximately 600 ps (red dashed line).



effect hampers any sophisticated modeling of the emission lineshape and thus a conclusion to be drawn on the absolute carrier density for this set of measurements. However, due to the significance of the red spectrum concerning the line shape, it is attributed to the MT. Surprisingly, at this carrier density the biexciton is still well-resolved, which states a clear contrast to the intuitive picture of a lower XX stability due to its reduced binding energy.

With $E_B = 25\text{ meV}$ according to Fig. 3.6, sample SQW-3 features a Bohr radius of about 3.2 nm and thus $n_{\text{crit}}^0 = 3.1 \cdot 10^{12}\text{ cm}^{-2}$. Relation (3.10) predicts a value around $3.6 \cdot 10^{-6}\text{ eVcm}^{2/3}$ for α_{BGR} . The corresponding dependence of E_{BGR} on the carrier density is plotted in Fig. 3.24(b) together with the computed evolution of the QW ground state energy due to QCSE-screening. For the latter effect an electric field strength of 180 kV/cm has been assumed [81]. The crossing of both curves yields a realistic value of $n_{\text{crit}} = 5.3 \cdot 10^{11}\text{ cm}^{-2}$, i.e. about 20% of n_{crit}^0 . In the following this density has been adopted for the red spectrum in Fig. 3.24(a) and all remaining density values have been extrapolated based on the integrated QW PL-intensity while taking into account the change of the wave-function overlap. The evolution of the determined exciton peak energies agrees well with the predictions of SP-simulations below the MT, whereas beyond the latter the combined influence of BGR and PSF causes a strong deviation. Please note that due to the complexity of the system beyond the MT, i.e. when carrier exchange with the barrier occurs, the extrapolated high-injection carrier densities are subject to a very large uncertainty, which is emphasized by the pale colors in this range in Fig. 3.24(b). However, the reported evolution of the biexciton binding energy, which was obtained from a simple Voigt-profile modeling of the X and XX lines, confirms the unexpected stability of biexcitons against the MT: within the error bars of the fit, E_{B}^{XX} remains constant, independent of the injection level. In order to confirm this effect additional tr-PL measurements have been conducted.

Time-Resolved Experiments

Figure 3.25(a) shows a streak-camera image that was recorded in the same experimental configuration as for Fig. 3.12 on sample SQW-3 at $T = 4\text{ K}$. Shortly after the excitation pulse, the barrier exhibits its highest PL-intensity and the QW emission extends up to the barrier energy (cf. Fig. 3.26(a)). This effect of PSF is also evidenced by the saturated emission amplitude around the XX energy over the first 400 ps in the decay traces of Fig. 3.25(b). Shortly after the excitation pulse, the carrier escape from the QW to the barrier is overcompensated by the

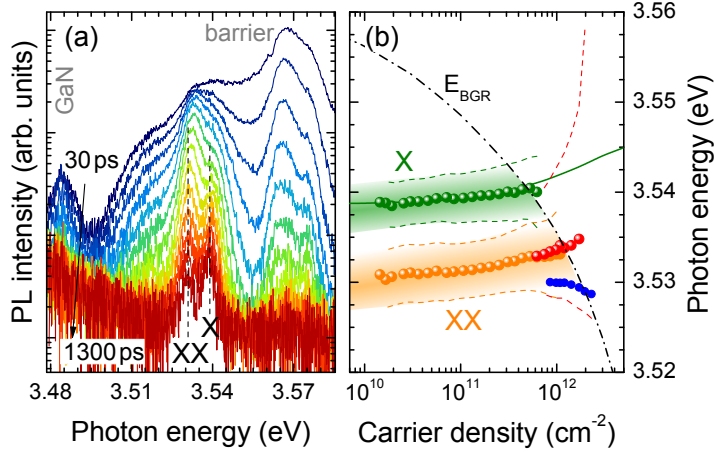


Figure 3.26: (a) Spectral profiles extracted from Fig. 3.25(a) at different time delays (steps of 90 ps). (b) Fingerprint of the MT in SQW-3: peak energy (dots) and FWHM (dashed lines) of X (green), XX (orange), and the e-h plasma (red). The fitted bandgap energy (blue dots) and the computed evolutions of E_{BGR} (black) and ΔE_{QCSE} (green line) are shown in addition.

feeding from the enormously populated barrier. After this time span the PL intensity at the XX energy starts to decay mono-exponentially. The behavior around the X-energy is quite different: at early time delays (< 400 ps), the amplitude decays with a long time constant. This regime is governed by the superposition of two effects: first, the QW recombination empties the phase-space, and second, escape and refilling processes with the barrier disturb the thermal equilibrium. The latter mechanism also causes the non-equilibrium between XX and X populations during the first 600 ps: only when the barrier intensity approaches zero, the squared exciton intensity in Fig. 3.25(b) follows the XX-decay indicating the achievement of a thermodynamic equilibrium between both species according to Eq. (3.4).

The observed PSF at early time delays allows to apply the modeling procedure from Sec. 3.3.2 and thus to translate the delay time into absolute carrier densities as for sample SQW-1. Figure 3.26(a) shows the analyzed spectral profiles taken at different time delays from the streak-camera image in Fig. 3.25(a). They could be adequately fitted for the time span between 70 and 200 ps after excitation. Out of this range carrier densities have been extrapolated based on the integrated QW PL-intensity and taking into account the calculated density-dependent wave-function overlap. This leads to the fingerprint of the MT in presence of biexcitons as shown in Fig. 3.26(b). In agreement with the cw-PL results, XX and X emissions modeled by Voigt-profiles are slightly blueshifting in the low-injection range due to QCSE-screening, while maintaining an approximately constant energy separation and undergoing a progressive increase in the linewidth. Starting from about $6 \cdot 10^{11} \text{ cm}^{-2}$, the exciton cannot be resolved anymore, in agreement with the crossing of E_{BGR} using the before-calculated $\alpha_{BGR} = 3.6 \cdot 10^{-6} \text{ eV cm}^{2/3}$. On the contrary, the biexciton remains observable in this range. For higher densities up to 10^{12} cm^{-2} , the biexciton emission broadens and transforms into the typical e-h plasma emission, while the low-energy emission edge starts redshifting due to BGR.

In conclusion, in both cw- and tr-PL measurements no decrease in the biexciton binding energy is observed up to the MT. Instead, the biexcitonic complex appears to be even more robust against fermionic interactions than the exciton, resulting in a higher critical density for biexcitons. This observation coincides with the interpretation of a MT due to BGR [114] and the experimental findings recorded on GaAs quantum wires [154]. It eventually urges for the elaboration of an improved theory of excitons and biexcitons in the vicinity of the MT.

Remark

Before closing this section, brief attention shall be given to the MT occurring in the thick GaN buffer and bulk layers visible in Figs. 3.11, 3.16(a), and 3.24(a). Note that these GaN layers are located underneath an AlGaIn epilayer, which causes the formation of a 2D electron gas in the GaN due to the polarization discontinuity at the heterointerface, in analogy to corresponding HEMT structures. The major part of the GaN emission stems from here or regions close by, which with respect to the inhomogeneous carrier distribution in the bulk makes the subsequent discussion nothing more than purely qualitative. However, the emission of GaN epilayers at low-temperature is usually dominated by the donor-bound exciton (D_0X_A) located about 6 meV below X_A [53]. Both transitions are visible in the low-injection regime in Fig. 3.24(a). For samples grown on free-standing substrates the sharp acceptor-bound exciton (A_0X_A) can additionally be identified on the low-energy side. When now following the emission of those transitions up to high excitation densities, X_A first broadens and eventually disappears. By contrast, the emission at the D_0X_A energy keeps growing while undergoing an increase in its homogeneous linewidth. This effect is surprising as the density of donors in the material is limited and in the non-degenerate case much lower than the free JDOS. This gives rise to expect a saturation of the D_0X_A amplitude before reaching the MT, as observed for A_0X_A in Fig. 3.16(a). However, for even higher power-densities this emission transforms into the broad emission of an e-h plasma (not shown here). In this case, the interpretation of the MT might be very similar to the 2D case: The biexciton binding energy in pure GaN equally amounts to about 6 meV [92, 124]. Thus D_0X_A and XX in bulk GaN appear at almost identical energies, which hints for a biexciton-mediated MT also in 3D bulk semiconductors.

3.5 Multiple Quantum-Wells

This last section of the chapter is aimed at transferring the acquired knowledge about the MT in SQWs to more complicated structures and bridging in this manner the gap with the upcoming chapter on III-nitride based microcavities.

Compared to the SQW-case, the difficulty to demonstrate the MT in a MQW-based structure arises from two different facts: first, the exponential absorption profile at the excitation wavelength will, even when applying spatial filtering, lead to an inhomogeneous vertical carrier distribution, which results in the simultaneous detection of a PL signal originating from highly and weakly injected regions. And second, owing to the large number of QWs and the limited amount of barrier material in between them, the excitation power density has to be increased drastically to reach equivalent carrier densities. For this reason the Nd:YAG laser had to be used, causing another issue emerging from the combination of time-integrated measurements and a pulsed excitation source. Indeed, from Ref. [69] the time constant of the exciton decay in MQW-1 is known to be close to the duration of the excitation pulse (500 ps) at low temperatures (cf. also the streak-image in Fig. 3.3(b)). Due to the relative proximity of both time scales, the recorded PL signal will also represent a mixture of a high-density signal, when carriers are continuously supplied by the laser, and of the integrated decay of the decreasing carrier population at the end of each pulse. According to those experimental constraints, there will be an excitonic signature in the spectra of MQW-1 even when the MT has already been crossed during the pulse and the visibility of any exciton energy shift will be reduced. Nevertheless, the recorded spectra are expected to be dominated by the emission of the QWs

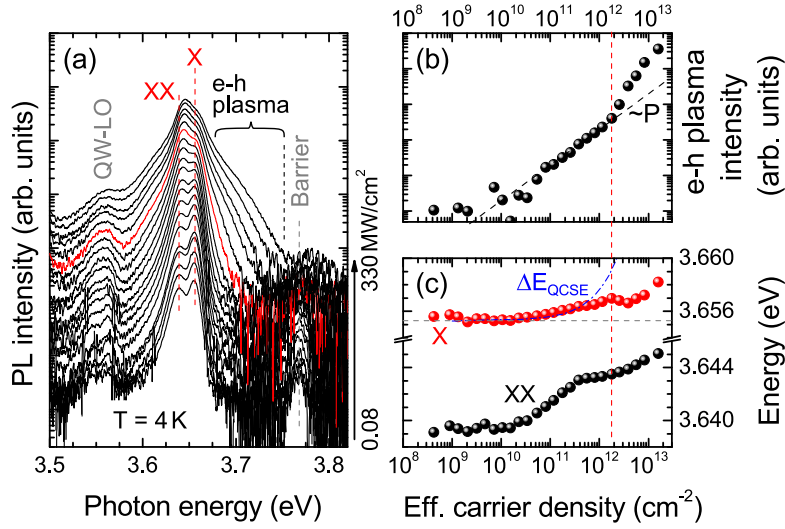


Figure 3.27: MT under pulsed excitation on MQW-1 measured at $T = 4$ K: (a) PL power series recorded for peak power densities ranging in between 0.08 and 330 MW/cm^2 . Corresponding evolution of (b) the e-h plasma emission intensity integrated between 3.69 and 3.75 eV and (c) E_X and E_{XX} . The vertical dashed line marks the onset of the MT corresponding to the red spectrum in (a). See text for details.

with highest injection.

Figure 3.27(a) displays a PL power-series performed at 4 K on sample MQW-1 under identical experimental conditions as shown in Fig. 3.1 except for the excitation by the Nd:YAG laser. The peak excitation power density is varied from 0.08 to 330 MW/cm^2 . In agreement with the discussion of Fig. 3.7, the spectra are dominated by the emission of the QW, namely X_A at 3.656 eV and XX at 3.639 eV [69]. The presence of biexcitons can be concluded from the super-linear power scaling of the emission intensity in Fig. 3.27(a). Owing to the non-idealities of the present experiment, both lines remain visible over the whole range of explored power densities. In addition, the LO-phonon replica of these transitions located $\sim 92 \text{ meV}$ below in energy and the emission of the $\text{Al}_{0.2}\text{Ga}_{0.8}\text{N}$ barrier at 3.775 eV can be identified. This power-series shares several similarities with that of sample SQW-3 displayed in Fig. 3.24(a). For low excitation power densities only marginal spectral changes can be identified: both X and XX undergo a slight blueshift ($< 2 \text{ meV}$ for X) and become negligibly broader toward the onset of the MT. The latter presumably corresponds to the red spectrum in Fig. 3.27(a), being linked to the appearance and the subsequent rise of an additional emission band that is superimposed to the high-energy tail of the exciton. This effect can also be followed when considering the non-linear evolution of the integrated PL intensity in this energy window in Fig. 3.27(b).

Using the values $E_B = 44 \text{ meV}$ and $a_B = 1.8 \text{ nm}$ obtained from envelope-function calculations, n_{crit}^0 for MQW-1 amounts to $9.8 \cdot 10^{12} \text{ cm}^{-2}$ and α_{BGR} should be comparable to that of SQW-2 around $3.8 \cdot 10^{-6} \text{ eV cm}^{2/3}$. Figure 3.28(a) shows the expected density-dependent variation of E_X , as obtained from SP-simulations, and E_{BGR} . Both curves cross at $1.7 \cdot 10^{12} \text{ cm}^{-2} \approx n_{\text{crit}}^0/5$, yielding a realistic value for n_{crit} according to Eq. (3.11). As a first approximation, this value has been assumed to be an effective QW carrier density for the red spectrum shown in

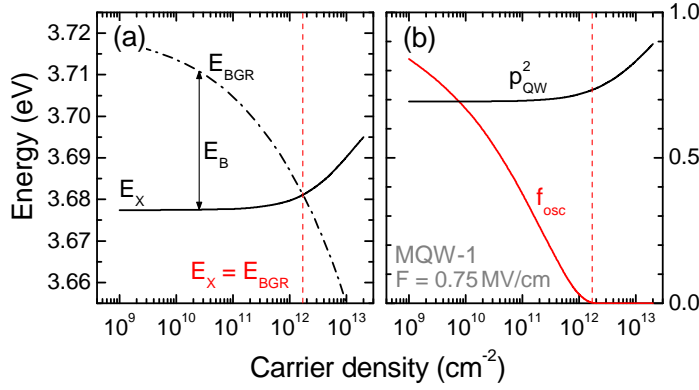


Figure 3.28: (a) SP-simulations for MQW-1: density-dependent shift of the exciton ground state E_X and E_{BGR} with $\alpha_{BGR} = 3.6 \cdot 10^{-6} \text{ eVcm}^{2/3}$ cross at $n_{\text{crit}} = 1.8 \cdot 10^{12} \text{ cm}^{-2}$. (b) Corresponding evolution of p_{QW}^2 and the relative oscillator strength according to Eq. (2.46).

Fig. 3.27(a). The corresponding effective densities for the other spectra have been extrapolated on the basis of the calculated evolution of p_{QW} , equivalent to the procedure employed for Fig. 3.24(b). The evolution of the peak energies in Fig. 3.27(b) could thus be displayed as a function of the effective carrier density. Especially at high densities the observed blueshift of the exciton is lower than expected from SP-simulations, confirming the concealing effect of the inhomogeneous carrier injection.

In conclusion, the MT in this MQW-based structure exhibits many similarities with that observed in the SQWs: it is in particular linked to the rise of the e-h plasma emission on the high-energy side of the exciton energy. Nevertheless, in the MQW-case a comprehensive analysis of the MT is prevented by the inhomogeneous injection.

3.5.1 Saturation of Oscillator Strength

Whereas the variation in the exciton energy and its linewidth can be inferred from such PL-studies, a direct conclusion on the evolution of the exciton oscillator strength cannot be drawn. Nevertheless, using the determined E_{BGR} and the density-dependent changes in the exciton energy and p_{QW} deduced from SP-simulations, the evolution of the relative exciton oscillator strength f_{osc} toward the MT can be derived on the basis of Eq. (2.46). In principle this could be done for all samples, but in view of the upcoming chapter it shall be discussed representatively for MQW-1. The density-dependence of f_{osc} was calculated assuming the MT occurs as depicted in Fig. 3.28(a). It is shown in Fig. 3.28(b). Due to the narrow QW-width the increase of the wave-function overlap only plays a minor role, in contrast to the considerations raised for thicker QWs in Ref. [155]. The decrease in f_{osc} is rather caused directly by E_{BGR} . Due to its cubic-root density dependence, it is expected to give rise to a drop of f_{osc} already well below n_{crit} . In other words already two orders of magnitude below the MT the exciton oscillator strength should be reduced to two third of its initial value.

Note finally that the evolution of E_{BGR} in an excitonic system below n_{crit} remains highly controversial: neither in the present experiments nor in the studies of Refs. [123, 131] an impact of BGR could be tracked below MT, which calls the calculated f_{osc} -evolution into question. Moreover, various scaling behaviors of f_{osc} with increasing carrier density have been observed and claimed [113, 115, 138]. A more detailed discussion about this saturation effect and consequences on the light-matter coupling regime in microcavities is provided in Sec. 4.5.

4 Polariton Condensation in III-nitride based Microcavities

All previous considerations concerned light-matter interaction occurring between a semiconductor medium and the continuum of the vacuum field. In contrast, this chapter addresses the optical properties of III-nitride systems, in which the light-matter coupling is altered due to a tailored distribution of allowed photonic modes. In 1946 Purcell evidenced that for radio-frequency transitions between different nuclear magnetic moments the spontaneous emission rate could be drastically enhanced by bringing the absorber into resonance with an external high quality-factor cavity [36]. Similarly, the emission rate of a semiconductor excitation and thus the light-matter coupling according to Sec. 2.2.1 can be engineered by restricting the optical mode volume. This can for instance be achieved by means of photonic crystals [156–158], whispering gallery mode resonators [159], or as in the present case in planar microcavities (MCs). In the latter, the optical mode is confined in one dimension by means of two plane-parallel mirrors that are separated by a multiple integer of a half wavelength. Such Fabry-Perot cavities represent a straightforward approach that guarantees compatibility with conventional semiconductor processing techniques. They are for instance used for commercial vertical cavity surface emitting lasers (VCSELs) and allowed the first observation of cavity-polaritons in 1992 [12].

This chapter is organized as follows: after a brief introduction to MCs, including the different light-matter coupling regimes and cavity-polariton physics, previous achievements in III-nitride based MCs and their suitability for future applications will be critically reviewed. This will serve as a basis for the subsequent discussion on the novel experimental results obtained within this work, that will be opened by explanations concerning the experimental setup and the investigated sample structures. The following sections will discuss the influences of biexcitons and exciton saturation effects on the way toward the polariton condensation threshold. In Sec. 4.6 the characteristics of polariton condensates will be discussed in more detail. Finally, this chapter will be closed by a comprehensive investigation of a non-polar MC, which gives rise to a unique anisotropic light-matter coupling regime.

4.1 Polaritons in Planar Microcavities

This section provides a brief introduction to the physics of semiconductor MCs. The beginning focuses on basic optical properties of cavity resonators and peculiarities of their eventual realization in semiconductor layer stacks via distributed Bragg-reflectors. Afterwards, potential

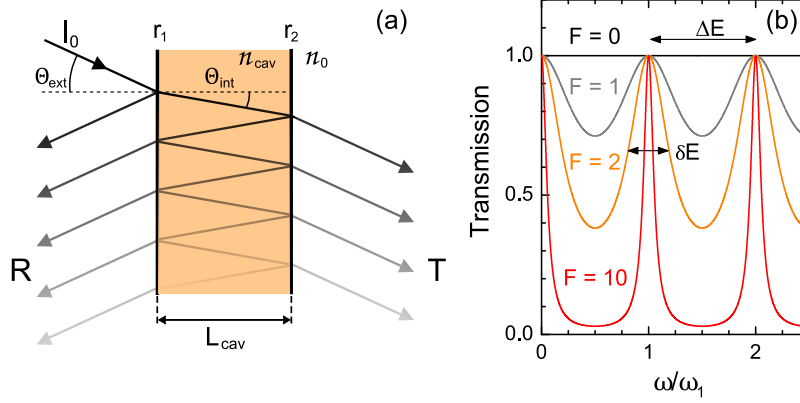


Figure 4.1: (a) Schematic representation of a Fabry-Perot cavity: The reflected (R) and transmitted (T) intensities result from interference of an infinite number of internal reflections between the metallic mirrors with reflectivity coefficients r_1 and r_2 . (b) Simulation of the spectral Fabry-Perot transmission for different values of the finesse F . See text for details.

modifications of the light-matter coupling will be discussed. Special attention is paid to the strong-coupling regime, which gives rise to cavity polaritons as new eigenstates. These are admixed quasi-particles composed of light and matter, that allow exceptional effects related to polariton condensation that will be discussed at the end of this section.

4.1.1 Microcavity Basics

Microcavities denote photonic structures that confine an optical mode to the order of its wavelength. The simplest representation is given by a Fabry-Perot resonator, where a dielectric spacer layer of thickness L_{cav} and refractive index n_{cav} is sandwiched between two highly-reflective metallic mirrors.

Fabry-Perot Resonator

Figure 4.1(a) depicts the structure of such a Fabry-Perot cavity. In the following, a plane light wave with electric field vector \mathbf{E}_0 shall be considered that impinges from the ambient medium with refractive index $n_0 = 1$ with an external angle Θ_{ext} . The metallic mirrors to each side of the cavity (1 and 2) are characterized by their complex reflectivity and transmission coefficients, i.e. $r_{1/2}$ and $t_{1/2}$, that connect reflected and transmitted electric-field amplitudes to the incident one, respectively.¹ When the light wave arrives at the first mirror, a fraction of the field amplitude is transmitted into the resonator. The internal angle of propagation is changed according to Snell's law:

$$\sin(\Theta_{\text{ext}}) = n_{\text{cav}} \sin(\Theta_{\text{int}}) . \quad (4.1)$$

Inside the resonator, the light wave undergoes an infinite number of back and forth reflections, that progressively diminish the electric-field amplitude based on the high but finite reflectivity of the mirrors. Summing the geometric series of interfering field amplitudes, that escape to

¹The polarization of the incoming light beam shall be neglected in a first approximation.

the left and to the right-hand side of the cavity, leads to the total reflection and transmission coefficients of the Fabry-Perot cavity according to:

$$r_{\text{FP}} = r_1 + t_1^2 r_2 \exp(i2\beta) \frac{1}{1 - r_1 r_2 \exp(i2\beta)}, \quad (4.2)$$

$$t_{\text{FP}} = t_1 t_2 \exp(i\beta) \frac{1}{1 - r_1 r_2 \exp(i2\beta)}, \quad (4.3)$$

where β denotes the phase thickness, which depends on the vacuum wavelength λ of the incoming light wave:

$$\beta = 2\pi \frac{L_{\text{cav}}}{\lambda} n_{\text{cav}} \cos(\Theta_{\text{int}}). \quad (4.4)$$

Finally, the relative reflection and transmission coefficients of the light intensity, i.e. R_{FP} and T_{FP} , are given by the squared moduli of r_{FP} and t_{FP} , respectively. As no absorption is considered they fulfill: $R_{\text{FP}} = 1 - T_{\text{FP}}$. According to the coefficients given in Eqs. (4.2) and (4.3), resonances in the reflection and transmission spectrum of the cavity will appear when:

$$\beta = q\pi \quad \text{or} \quad q \frac{\lambda}{2} = L_{\text{cav}} n_{\text{cav}} \cos(\Theta_{\text{int}}), \quad (4.5)$$

where q denotes an integer. The separation between adjacent cavity modes ΔE , also referred to as the free spectral range, and the linewidth of the resonances δE define the finesse of the resonator, which for a lossless cavity with high mirror reflectivities can be approximated by:

$$F = \frac{\Delta E}{\delta E} \approx \pi \frac{\sqrt{r_1 r_2}}{1 - r_1 r_2}. \quad (4.6)$$

Figure 4.1(b) shows simulated spectral transmission curves for Fabry-Perot cavities featuring two identical metallic mirrors $r_1 = r_2$ and different values of the finesse. The energy axis is given in relative units of the fundamental cavity mode $E_1 = \hbar\omega_1$, corresponding to $q = 1$. A high mirror reflectivity leads to high finesse values and thus to an increased spectral purity of the cavity. The finesse is also connected to the quality factor Q via:

$$Q = q \cdot F = \frac{E_q}{\delta E}, \quad (4.7)$$

where E_q represents different cavity mode energies according to the conditions given by Eq. (4.5). Note that even if the definition of the Q appears quite similar to that of F , it features a different physical interpretation. The Q -factor corresponds to the ratio between the stored energy in the cavity and the optical losses during each roundtrip. It will be of critical importance for the discussion on cavity-polaritons, since it is directly linked to the photon lifetime:

$$\tau_{\text{cav}} = \frac{\hbar Q}{E_q}. \quad (4.8)$$

The dependence of the resonance condition from Eq. (4.5) on the internal propagation angle leads to a characteristic angular dispersion of the cavity modes. Here, it is convenient to write the photonic wave-vector \mathbf{k}_{cav} in the projected components: $\mathbf{k}_{\text{cav}} = \mathbf{k}_{\perp} + \mathbf{k}_{\parallel}$. Owing to the translational invariance at each cavity interface the in-plane component \mathbf{k}_{\perp} is conserved while

the component parallel to the growth axis² obeys the resonance condition of Eq. (4.5). The cavity mode dispersion can thus be expressed as:

$$\begin{aligned} \sqrt{\left(\frac{E_q n_{\text{cav}}}{\hbar c}\right)^2 - |\mathbf{k}_\perp|^2} &= \frac{q\pi}{L_{\text{cav}}} = |\mathbf{k}_\parallel|, \\ E_q(\mathbf{k}_\perp) &= \frac{\hbar c}{n_{\text{cav}}} \sqrt{\left(\frac{q\pi}{L_{\text{cav}}}\right)^2 + |\mathbf{k}_\perp|^2}. \end{aligned} \quad (4.9)$$

For small in-plane wave-vectors the cavity mode dispersion is almost parabolic and can be approximated by:

$$E_q(\mathbf{k}_\perp) = E_{q,0} + \frac{\hbar^2 |\mathbf{k}_\perp|^2}{2m_{\text{ph}}}. \quad (4.10)$$

Here, $E_{q,0}$ and m_{ph} denote the cavity mode energy and the photon effective mass at $\mathbf{k}_\perp = 0$, respectively. They are defined by:

$$E_{q,0} = \frac{q\pi\hbar c}{n_{\text{cav}}L_{\text{cav}}} \quad \text{and} \quad m_{\text{ph}} = \frac{q\pi\hbar n_{\text{cav}}}{cL_{\text{cav}}}. \quad (4.11)$$

Distributed Bragg-Reflectors

Owing to the limited reflectivity of metallic mirrors, which especially in the UV range remains around 90% or below, and the difficulty to deposit high-quality semiconductor nano-structures on top of it, vertical semiconductor MCs usually rely on so-called distributed Bragg-reflectors (DBRs). These are composed of transparent bilayer stacks that consist of a low and a high refractive index material, i.e. n_1 and n_2 with $n_1 < n_2$. Depending on its refractive index n_i and the targeted vacuum wavelength for the reflection maximum λ_{DBR} (corresponding to the photon energy E_{DBR}), each of the layers thereby features a physical thickness equal to $\lambda_{\text{DBR}}/4n_i$. By this means, the reflections of an incoming light wave interfere constructively at each boundary, while the transmission is heavily damped by destructive interference. In absence of absorption, the maximum reflectivity R_{DBR} of a DBR is thus only determined by the number of bilayer pairs N_{DBR} and the refractive-index contrast $\Delta n = n_2 - n_1$. It holds [160]:

$$N_{\text{DBR}} = \frac{1}{2} \ln \left(\frac{n_0}{n_s} \cdot \frac{1 - \sqrt{R_{\text{DBR}}}}{1 + \sqrt{R_{\text{DBR}}}} \right) / \ln \left(\frac{n_1}{n_2} \right), \quad (4.12)$$

where n_0 and n_s denote the refractive indices of the medium on the reflection and transmission sides, respectively. Contrary to metallic mirrors, which exhibit a broad reflectivity response with a high-energy limit set by the plasma frequency, DBRs only feature a limited reflection band based on the interference phase-matching conditions described above. It is usually referred to as the DBR-stopband and corresponds to the forbidden gap of a 1D photonic crystal. The width of the stopband ΔE_{DBR} critically depends on Δn . For high N_{DBR} values, it can be approximated by [160]:

$$\Delta E_{\text{DBR}} \approx \frac{4E_{\text{DBR}}}{\pi} \cdot \frac{n_2 - n_1}{n_1 + n_2}. \quad (4.13)$$

²The growth axis is oriented perpendicular to the mirror planes.

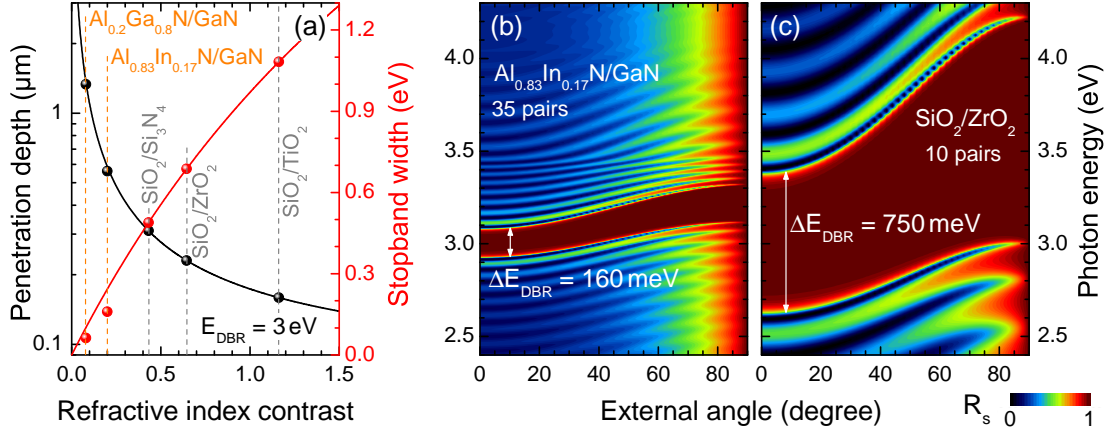


Figure 4.2: (a) Penetration depth (black) and stopband width (red) simulated for different dielectric DBRs centered at 3 eV using SiO₂ as low- n material according to Eqs. (4.13) and (4.14). Gray dashed lines mark typical dielectric UV-DBR compositions. Two III-nitride based UV-DBR solutions are shown for comparison (orange dashed lines). (b) TMS of the angle-resolved reflectivity spectrum for a 35-pair GaN/Al_{0.83}In_{0.17}N DBR. The light-polarization was set perpendicular to the plane of incidence. (c) Equivalent results for a 10-pair SiO₂/ZrO₂ dielectric DBR. All simulations were performed with $n_0 = 1$ and employing GaN as substrate, absorption was ignored.

Another peculiarity of DBRs is their finite penetration depth: indeed, whereas reflection on a metallic mirror occurs directly at the surface and wave propagation inside the medium is massively damped, the fulfillment of the interference conditions in a DBR requires a finite number of bilayer pairs according to Eq. (4.12). The amplitude of an incoming electro-magnetic wave is progressively damped across each interface. Its penetration length into the DBR L_{DBR} is then given by [160]:

$$L_{\text{DBR}} = \frac{\lambda_{\text{DBR}}}{4n_0} \frac{\min\{n_0, n_1\}}{\max\{n_0, n_1\}} \cdot \frac{n_2}{n_2 - n_1}. \quad (4.14)$$

Figure 4.2(a) shows the correspondingly derived evolution of L_{DBR} and ΔE_{DBR} for $E_{\text{DBR}} = 3$ eV as a function of the refractive index contrast, when using SiO₂ as low-index material and air as ambient medium. It is obvious that high Δn -values lead to short penetration depths and wide DBR-stopbands. Three different examples for dielectric DBRs are shown: first, a DBR consisting of SiO₂/TiO₂ bilayer pairs exhibits the highest Δn and thus the best performance. Such DBRs are used for III-nitride based VCSELs or MCs emitting in the visible or near-UV spectral range [161]. This limitation originates from the absorption edge of TiO₂, that causes drastic optical losses for photon energies exceeding ~ 3.3 eV. For structures that emit in the UV-range, different materials have to be exploited. The two MCs investigated in this work either rely on a SiO₂/Si₃N₄ or on a SiO₂/ZrO₂-based DBR, that are transparent up to photon energies as high as 4.5 eV and beyond, respectively. They will be introduced in Secs. 4.3.2 and 4.7.

Such dielectric DBRs commonly exhibit an amorphous structure, making them unsuitable as growth template for a high-quality QW-structure. Thus, the DBR on the substrate side

(bottom-DBR) usually consists of an epitaxial bilayer stack, that ideally conserves the crystal structure and quality while featuring a refractive-index contrast as large as possible. When targeting UV-DBRs for III-nitride based MCs, two different approaches exist: the low refractive-index material can either be based on an AlGaN or an AlInN compound. Note that for *c*-plane structures the latter solution usually provides the higher Δn and the better optical quality, as it can be grown lattice-matched to GaN or a low Al-content AlGaN alloy (cf. Fig. 2.5 and Ref. [74]). For other surface orientations this compromise might be revised (cf. Sec. 4.7). Figure 4.2(a) also shows two epitaxial DBR-solutions for comparison. Due to the limited Δn , they exhibit significantly larger penetration depths and narrower stopbands than their dielectric counterparts.

Note that Eqs. (4.13) and (4.14) were derived for ideal structures with an infinite number of bilayer-pairs. A more realistic approach to model DBR-structures consists in simulating their optical response directly via transfer-matrix simulations (TMS). Here, the multi-layer interference for a finite N_{DBR} or for an arbitrary layer stack can be calculated on the basis of the real refractive index dispersion. Appendix A.2 introduces the TMS-formalism and provides further information about the refractive index dispersion applied to the individual layers. Figure 4.2 additionally shows two angular reflectivity dispersions that were calculated by TMS for: (b) an epitaxial 35-pair GaN/Al_{0.83}In_{0.17}N DBR, and (c) a 10-pair SiO₂/ZrO₂ dielectric DBR, both centered around 3 eV. The obtained stopband widths coincide well with the predictions of Eq. (4.13) shown in Fig. 4.2(a). However, note that due to the low Δn , the III-nitride DBR requires much more bilayer pairs to reach a similar R_{DBR} than a dielectric solution according to Eq. (4.12). With increasing external angle the DBR-stopbands blueshift owing to the increasing phase thickness in Eq. (4.4). Due to Snell's law and the lower average refractive index, this blueshift is commonly stronger for dielectric DBRs. Apart from the DBR-stopband, both reflectivity responses feature additional dispersive optical modes corresponding to standing waves in the layer stack. They are referred to as Bragg-modes (BM).

Semiconductor Microcavities

As previously mentioned the bottom-DBR in a semiconductor MC usually consists of an epitaxial DBR, while for the top case no structural restrictions exist allowing the use of dielectric mirrors. An exception represent flip-chip MCs, which profit from highly-reflective dielectric DBRs on both sides, but require an advanced surface lift-off handling for the active region. Figure 4.3 displays the results of TMS for an empty³ III-nitride MC relying on a $5\lambda/2$ GaN spacer layer, and employing a 35-pair GaN/Al_{0.83}In_{0.17}N and an 8-pair SiO₂/ZrO₂ DBR on the bottom and top sides, respectively. The reflectivity spectrum at normal incidence shown in Fig. 4.3(a) reveals the impact of the two different stopbands and the narrow dip of the cavity mode at $E_{\text{cav}} = 3$ eV. Note the typical modulations of the broad top-DBR stopband for $R > 0.9$ issued from the BMs of the bottom-DBR. In the spectral range of both DBR stopbands the response is flat with $R \approx 1$ only interrupted by the cavity dip. The latter features a *Q*-factor of about 5000. In Fig. 4.3(b) the depth profile of the refractive index and the corresponding electric-field distribution at the cavity mode energy give access to further details. The GaN spacer layer corresponds to a high-index cavity giving rise to field antinodes at both DBR-cavity interfaces. Owing to the $5\lambda/2$ thickness, four distinct maxima of the field strength can

³The word empty refers to a cavity layer that is characterized only by the dispersive real part of the refractive index, i.e. the impact of absorption is omitted.

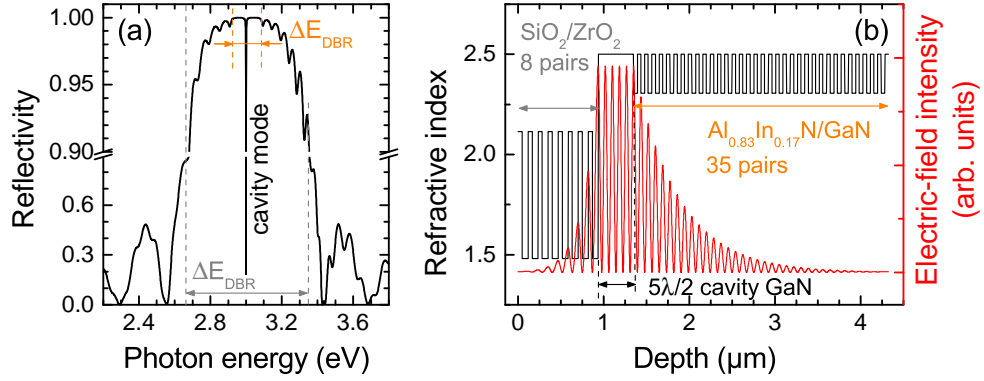


Figure 4.3: TMS of an empty $5\lambda/2$ GaN cavity consisting of a 35-pair GaN/ $\text{Al}_{0.83}\text{In}_{0.17}\text{N}$ bottom-DBR and an 8-pair $\text{SiO}_2/\text{ZrO}_2$ top-DBR: (a) Reflectivity spectrum at normal incidence showing the different DBR-stopbands and the narrow dip of the cavity mode. (b) Depth profile of the refractive index (black) and the electric-field intensity (red) at the cavity mode energy 3 eV.

be spotted in the spacer layer. Moreover, the exponential damping of the electric-field in the DBRs follows the trend shown in Fig. 4.2(a): L_{DBR} -values of 170 and 530 nm are deduced for the top and bottom sides, respectively.

The main difference between a semiconductor MC and a Fabry-Perot resonator concerns the cavity length. Indeed, contrary to the ideal case in a semiconductor MC the electric field significantly leaks into the DBRs, which gives rise to an increased effective cavity length defined by: $L_{\text{eff}} = L_{\text{cav}} + L_{\text{DBR},1} + L_{\text{DBR},2}$. This becomes essential when discussing the light-matter coupling in the subsequent section. Moreover, due to the finite overlap of the photon-field with the DBR bilayers, the refractive index governing the cavity dispersion should also be replaced by an effective index n_{eff} in Eqs. (4.10) and (4.11), which is averaged over the electric-field standing-wave.

4.1.2 Light-Matter Coupling in a Microcavity

A solid-state electronic excitation that is coupled to the vacuum field will decay exponentially based on Fermi's golden rule (cf. Secs. 2.2.1 and 3.3). This applies for both bulk- and QW-excitons as soon as they enter the light-cone. However, their behavior can be modified in presence of a tailored light-field in a cavity, i.e. when there is a restricted number of accessible photon modes. Staying in the perturbative regime, the spontaneous emission rate can be engineered by a careful cavity design on the basis of the Purcell-effect [36]. It can either be suppressed or enhanced, whereas the temporal decay of excited states remains exponential and irreversible. In this case the cavity is said to be in the weak coupling regime (WCR). On the contrary, when the photon lifetime inside a cavity exceeds the time-scale that is needed for the photon to be reabsorbed by the active medium, or more precisely when the coupling strength between photonic and electronic modes overcomes their respective damping rates, the light-matter coupling can no longer be treated perturbatively. The cavity system switches to the so-called strong coupling regime (SCR). This state of the light-matter interaction has first been observed for an atom cavity at room temperature in 1983 [162]. In the following years intensive research efforts have been spent on strong-coupling phenomena in atomic

physics. However, it was not until 1992 that the SCR was also demonstrated in a semiconductor MC. Here, Weisbuch and co-workers evidenced the existence of cavity exciton-polaritons, i.e. quasi-particles resulting from the strong coupling between an excitonic and a photonic resonance in a cavity, by their typical anticrossing behavior in a GaAs-based system [12].

This chapter focuses on cavity-polaritons observed in III-nitride based MCs. The upcoming sections shall introduce their peculiar physical properties and provide the basic understanding for the experimental part.

Exciton-Polaritons

In an ideal and infinite bulk crystal the radiative decay of an exciton population is prohibited by an endless series of emission and subsequent reabsorption processes [41]. Exciton and photon populations are strongly-coupled and form admixed quasi-particles, so-called bulk exciton-polaritons. In thick layers, where the 3D-symmetry is broken at the interfaces, excitons are allowed to decay through the light-cone, but high-momentum and in-plane propagation are still governed by exciton-polaritons.

The situation in a MC operating in the SCR appears very similar. When the cavity mode and the exciton transition are in resonance, an emitted photon will be stored in the cavity-light field while undergoing multiple back and forth reflections, until it may eventually be reabsorbed by the active material. Thus, when the coupling strength between excitons and photons overcomes their respective damping rates, the light-matter coupling becomes non-perturbative, and exciton and cavity modes split-up into the new eigenmodes of the system: the lower and upper polaritons (LP and UP, respectively). These cavity exciton-polaritons, or to make it short cavity-polaritons, are interacting quasi-particles that share properties of light and matter and obey Bose-Einstein statistics, with a limitation to low-densities inherited from the excitonic component. Contrary to their 3D counterparts, the 1D photonic confinement in a MC gives rise to a well-defined energy minimum at zero in-plane momentum. This unique property will become particularly important when discussing the non-linear emission properties of cavity-polaritons in Sec. 4.1.3.

The Coupled-Oscillator Model

The very basic properties of cavity polaritons are intuitively accessible when considering the analogy to the classical problem of two harmonic oscillators with damping rates γ_1 and γ_2 that are coupled by a spring with stiffness constant g . This situation is depicted in the scheme of Fig. 4.4. Only one of the oscillators shall initially be deflected. For small values of the coupling constant $g \ll \gamma_{1/2}$, mutual affectation is prohibited and after a negligible initial energy transfer

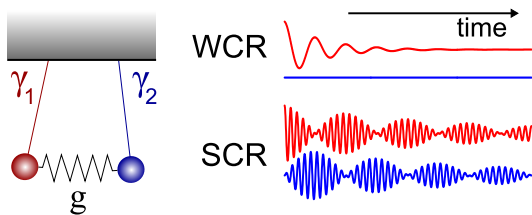


Figure 4.4: Two mechanical oscillators with respective damping rates $\gamma_{1/2}$ that are coupled by a spring with stiffness constant g . The right-hand side schematically shows the temporal decay of the oscillation amplitudes in the WCR and SCR.

both oscillation amplitudes are damped independently. The oscillators are weakly-coupled. In the opposite case when $g \gg \gamma_{1/2}$, the system can efficiently exchange mechanical energy and both oscillators undergo a coupled motion with alternating amplitudes. The SCR takes place and the system can be described by new eigenmodes, i.e. an acoustical one that describes the in-phase motion and an optical one where both oscillators move antisymmetrically. This outcome applies very similarly also to coupled quantum oscillators.

Within the framework of second quantization, the Hamiltonian for an undamped and interacting exciton-cavity system with in-plane wave-vector \mathbf{k}_\perp can be expressed as:

$$\hat{H}_{\mathbf{k}_\perp} = E_C(\mathbf{k}_\perp) \hat{c}_{\mathbf{k}_\perp}^\dagger \hat{c}_{\mathbf{k}_\perp} + E_X(\mathbf{k}_\perp) \hat{d}_{\mathbf{k}_\perp}^\dagger \hat{d}_{\mathbf{k}_\perp} + g_0 \left[\hat{c}_{\mathbf{k}_\perp} \hat{d}_{\mathbf{k}_\perp}^\dagger + \hat{c}_{\mathbf{k}_\perp}^\dagger \hat{d}_{\mathbf{k}_\perp} \right], \quad (4.15)$$

where $E_C(\mathbf{k}_\perp)$ and $E_X(\mathbf{k}_\perp)$ are the cavity-photon and exciton dispersions, and $\hat{c}_{\mathbf{k}_\perp}^\dagger$ and $\hat{d}_{\mathbf{k}_\perp}^\dagger$ ($\hat{c}_{\mathbf{k}_\perp}$ and $\hat{d}_{\mathbf{k}_\perp}$) denote their respective creation (annihilation) operators. The last term in Eq. (4.15) corresponds to the light-matter interaction. Here, non-diagonal terms have been neglected and the interaction constant g_0 is assumed to be independent of the in-plane momentum. For a QW-based MC with $R_{\text{DBR}} \approx 1$, it is in reasonable approximation given by [68, 163]:

$$g_0 = \hbar \sqrt{\frac{e^2}{2\epsilon_0 m_0} \cdot \frac{N_{\text{QW}}^*}{n_{\text{eff}}^2 L_{\text{eff}}}} f_X. \quad (4.16)$$

Here, N_{QW}^* denotes the number of QWs that are effectively coupled to the light field of the cavity mode as defined in Ref. [68]. It can be reduced with respect to the geometrical number of QWs N_{QW} when the overlap between the electric-field intensity of the cavity mode (cf. Fig. 4.3) and the distribution of QWs in the resonator is not perfect, i.e. when there are QWs located close to the nodes of the field. Two extreme cases can be distinguished: (i) QWs are only located at the antinodes of the cavity field. In this case $N_{\text{QW}}^* \approx N_{\text{QW}}$, and (ii) the QWs are homogeneously distributed over the cavity spacer. Here, N_{QW}^* tends to half the geometrical value. In the latter case, excitons in QWs located apart from the antinodes of the cavity mode cannot couple to the light, radiative recombination is forbidden and they are thus also referred to as dark-excitons (cf. Sec. 2.3.2). The coupling strength in Eq. (4.16) further depends critically on the oscillator strength of the QW-exciton f_X according to Eq. (2.46) and on the effective cavity length L_{eff} , preferring highly-reflective dielectric DBRs over epitaxial ones.

The diagonalization of the Hamiltonian of Eq. (4.15) succeeds when introducing the LP and UP creation operators according to:

$$\begin{aligned} \hat{p}_{\mathbf{k}_\perp}^{\dagger, \text{LP}} &= F_X(\mathbf{k}_\perp) \hat{d}_{\mathbf{k}_\perp}^\dagger + F_C(\mathbf{k}_\perp) \hat{c}_{\mathbf{k}_\perp}^\dagger, \\ \hat{p}_{\mathbf{k}_\perp}^{\dagger, \text{UP}} &= -F_C(\mathbf{k}_\perp) \hat{d}_{\mathbf{k}_\perp}^\dagger + F_X(\mathbf{k}_\perp) \hat{c}_{\mathbf{k}_\perp}^\dagger. \end{aligned} \quad (4.17)$$

Here, F_X and F_C denote exciton and cavity Hopfield-coefficients, respectively. Their squared absolute values correspond to the excitonic and photonic fractions of the polariton eigenstate and obey the transformation: $|F_X|^2 + |F_C|^2 = 1$. The Hamiltonian of Eq. (4.15) reads in this basis:

$$\hat{H}_{\mathbf{k}_\perp} = E_{\text{LP}}(\mathbf{k}_\perp) \hat{p}_{\mathbf{k}_\perp}^{\dagger, \text{LP}} \hat{p}_{\mathbf{k}_\perp}^{\text{LP}} + E_{\text{UP}}(\mathbf{k}_\perp) \hat{p}_{\mathbf{k}_\perp}^{\dagger, \text{UP}} \hat{p}_{\mathbf{k}_\perp}^{\text{UP}}. \quad (4.18)$$

The eigenvalues $E_{\text{LP}}(\mathbf{k}_{\perp})$ and $E_{\text{UP}}(\mathbf{k}_{\perp})$ correspond to the energy dispersion of the LP and UP branches. They depend on the in-plane momentum dependent detuning $\delta_{\mathbf{k}_{\perp}} = E_{\text{C}}(\mathbf{k}_{\perp}) - E_{\text{X}}(\mathbf{k}_{\perp})$ and are given by:

$$\begin{aligned} E_{\text{LP}}(\mathbf{k}_{\perp}) &= \frac{1}{2}\delta_{\mathbf{k}_{\perp}} + E_{\text{X}}(\mathbf{k}_{\perp}) - \frac{1}{2}\sqrt{\delta_{\mathbf{k}_{\perp}}^2 + 4g_0^2}, \\ E_{\text{UP}}(\mathbf{k}_{\perp}) &= \frac{1}{2}\delta_{\mathbf{k}_{\perp}} + E_{\text{X}}(\mathbf{k}_{\perp}) + \frac{1}{2}\sqrt{\delta_{\mathbf{k}_{\perp}}^2 + 4g_0^2}. \end{aligned} \quad (4.19)$$

The minimum energy distance in between them occurs when $\delta_{\mathbf{k}_{\perp}} = 0$. It is usually referred to as the vacuum Rabi-splitting Ω_0 :

$$\Omega_0 = E_{\text{UP}}(\delta_{\mathbf{k}_{\perp}} = 0) - E_{\text{LP}}(\delta_{\mathbf{k}_{\perp}} = 0) = 2g_0. \quad (4.20)$$

This equation holds in the ideal case of a zero linewidth, marked by the index 0. Ω_0 defines the frequency that determines the oscillations occurring between excitonic and photonic populations in a strongly-coupled MC in analogy to the mechanically-coupled oscillators from Fig. 4.4. These so-called Rabi-oscillations feature typical time scales between a hundred of femtoseconds to a few picoseconds and were first observed for a GaAs-based MC in 1994 [164]. Two years after a conclusive quantum-mechanical description of this effect has been provided by Savona and Weisbuch [165]. The vacuum Rabi-splitting and the detuning between exciton and cavity mode at zero in-plane momentum $\delta_{\mathbf{k}_{\perp}}(\mathbf{k}_{\perp} = 0) = \delta$ are the two main parameters defining the polariton dispersion: among others they set excitonic and photonic fractions, the lifetime, and the effective mass of the cavity polaritons. In order to illustrate corresponding effects it is convenient to express Eq. (4.15) in its matrix form:

$$\hat{H}_{\mathbf{k}_{\perp}} |\psi\rangle = \begin{pmatrix} E_{\text{C}}(\mathbf{k}_{\perp}) - i\gamma_{\text{C}} & g_0 \\ g_0 & E_{\text{X}}(\mathbf{k}_{\perp}) - i\gamma_{\text{X}} \end{pmatrix} |\psi\rangle = E |\psi\rangle. \quad (4.21)$$

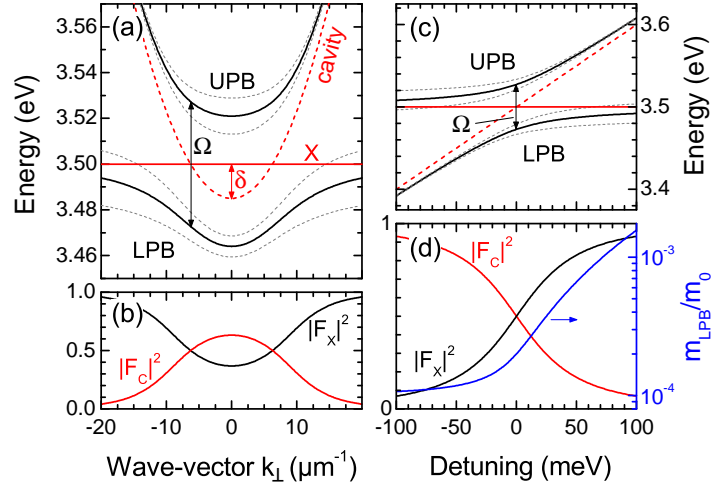
In this case the eigenvalues of the matrix correspond to the LP and UP dispersion and the eigenvector components to the Hopfield-coefficients. Moreover, finite homogeneous linewidths of the uncoupled modes, i.e. γ_{C} and γ_{X} , can easily be taken into account by a complex energy representation.

Figure 4.5 shows simulations on the basis of this coupled-oscillator model (COM) using typical parameters of a III-nitride based MC in the SCR: $m_{\text{ph}} = 10^{-4}m_0$, $\gamma_{\text{X}} = 25 \text{ meV}$, $\gamma_{\text{C}} = 3.5 \text{ meV}$, $g_0 = 30 \text{ meV}$, and $\delta = -15 \text{ meV}$. In Fig. 4.5(a), the polariton mode dispersion is displayed as a function of the in-plane momentum. Compared to cavity photons, QW-excitons feature a very heavy effective mass ($M^* \approx m_0$). It is therefore assumed to remain dispersionless at constant energy. In presence of finite exciton and cavity mode linewidths the Rabi-splitting is reduced with respect to $\Omega_0 = 2g_0$:

$$\Omega = 2\sqrt{g_0^2 - \left(\frac{\gamma_{\text{X}} - \gamma_{\text{C}}}{2}\right)^2}. \quad (4.22)$$

It amounts in the case of Fig. 4.5 to $\sim 55 \text{ meV}$ and is visible at a finite in-plane momentum as $\delta \neq 0$. The LP branch (LPB) exhibits a well-defined energy minimum at $\mathbf{k}_{\perp} = 0$ and converges at high in-plane momentum toward the exciton dispersion, while featuring the characteristic inflection point. In contrast, the UP branch (UPB) tends toward the cavity-mode at high

Figure 4.5: COM simulations using $m_{\text{ph}} = 10^{-4} m_0$, $\gamma_X = 25 \text{ meV}$, $\gamma_C = 3.5 \text{ meV}$, and $g_0 = 30 \text{ meV}$: (a) In-plane dispersion of coupled (black, gray = FWHM) and uncoupled modes (red) for $\delta = -15 \text{ meV}$, and (b) corresponding evolution of $|F_X|^2$ and $|F_C|^2$. (c) Impact of the detuning on the energy positions at $\mathbf{k}_\perp = 0$ analog to (a), and (d) respective evolution of $|F_X|^2$, $|F_C|^2$, and the effective mass of the LPB ground state.



angles. Figure 4.5(b) shows the respective evolution of the photonic and excitonic fractions along the LPB dispersion. In a straightforward interpretation, they correspond to the duration during one Rabi-oscillation period, in which polaritons exist as their respective matter or light projections. Correspondingly, all intrinsic properties of polaritons, such as the homogeneous linewidth, the scattering cross-section, and their effective mass and lifetime will be weighted by $|F_X|^2$ and $|F_C|^2$. For instance, exciton-like polaritons spend more time as an exciton and will thus be much more interactive and long-lived than their photon-like counterparts. Owing to the lower γ_C value and its predominantly photonic character $|F_C|^2 = 0.65$, the LPB ground state in Fig. 4.5(a) features a rather narrow linewidth, that increases toward higher momenta together with the excitonic fraction. The right-hand side of Fig. 4.5 shows the impact of the detuning around $\mathbf{k}_\perp = 0$. For negative δ values, polaritons in the LPB ground state are photon-like, they exhibit thus a short lifetime, typically in the order of a picosecond according to Eq. (4.8), a low effective mass and a low interaction cross-section. Indeed, as photons are non-interacting bosons, the ability of polaritons to interact with other particles stems from their excitonic component and is thus quenched for very photon-like states. In comparison, LPs for positive detuning values are very interactive but exhibit a high-effective mass - they are exciton-like.

The COM represents a rather crude approximation, especially in view of MCs based on wide-bandgap semiconductors: it neglects the dispersion of the refractive index, any inhomogeneous linewidth contribution, the influence of the electron-hole continuum absorption, and potential modifications of the optical confinement for high in-plane momenta. Nevertheless, its ease of use and the generally good agreement observed with experiments justifies its application.

Transfer-Matrix Simulations

A more accurate description of the polariton dispersion in the linear light-matter interaction regime can be gained by performing optical TMS. It overcomes all above-mentioned issues of the COM by considering the exact MC structure, including the complex refractive index dispersion of each layer and the correct field distribution inside the cavity. Cavity properties,

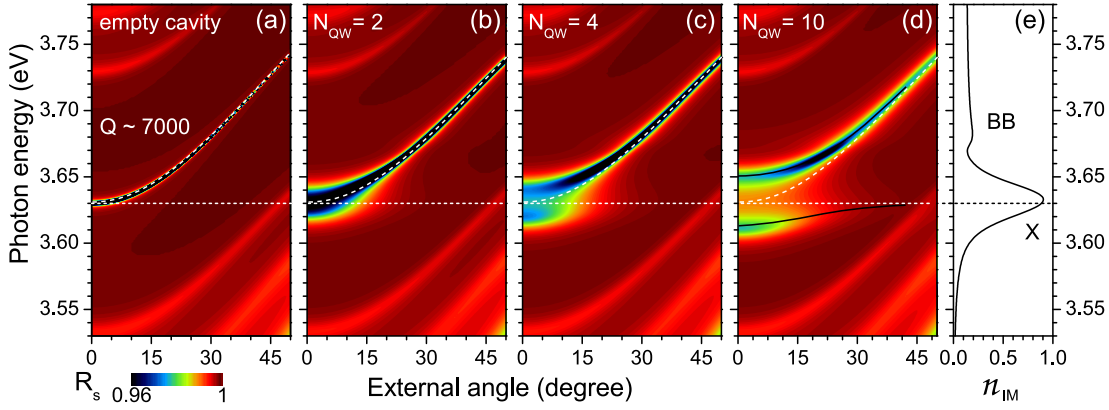


Figure 4.6: Simulated angle-resolved reflectivity for a $3\lambda/2$ $\text{Al}_{0.2}\text{Ga}_{0.8}\text{N}$ -cavity containing a varying number of GaN QWs (1.2 nm-thick, $f_X = 2.1 \cdot 10^{13} \text{ cm}^{-2}$, $\gamma_{\text{hom}} = 25 \text{ meV}$, $\gamma_{\text{inh}} = 15 \text{ meV}$), that are embedded at the two field antinodes: (a) 0, (b) 2×1 , (c) 2×2 , and (d) 2×5 QWs. The bottom-DBR consists of 35 $\text{Al}_{0.2}\text{Ga}_{0.8}\text{N}/\text{Al}_{0.85}\text{In}_{0.15}\text{N}$ bilayer pairs and the top-DBR is composed of eight $\text{SiO}_2/\text{ZrO}_2$ pairs. Uncoupled modes are indicated by white dashed lines. In (d) the black lines highlight the dispersion of the polariton branches. (e) Imaginary part of the QW refractive index.

such as n_{eff} , N_{QW}^* , and the DBR contribution by L_{eff} are thus intrinsically considered, and the eventual Rabi-splitting is a direct output of the simulation only depending on the applied value of f_X . Thanks to the 2D-nature of cavity polaritons, angle-resolved TMS provide direct access to the dispersion properties. When cavity-polaritons leave the MC, their in-plane momentum as well as their polarization and energy properties are transferred to the escaping photon.⁴ It is thus possible to scan the in-plane dispersion of exciton, photon and polariton modes via angle-resolved TMS (and optical experiments) according to Snell's law:

$$|\mathbf{k}_{\perp}| = \frac{E}{\hbar c_0} \sin(\Theta_{\text{ext}}). \quad (4.23)$$

TMS have been performed using the isotropic 2×2 -formalism introduced in App. A.2. Imaginary parts of the refractive indices have been neglected except for the QWs. The exciton lineshape was represented by a Voigt-profile resulting from the convolution of a homogeneous and an inhomogeneous broadening contribution, i.e. $\gamma_X = \gamma_{\text{hom}}$ and γ_{inh} , respectively. Figure 4.6 shows computed angle-resolved reflectivity curves of a $3\lambda/2$ $\text{Al}_{0.2}\text{Ga}_{0.8}\text{N}$ -cavity that is sandwiched in between a 35-pair $\text{Al}_{0.2}\text{Ga}_{0.8}\text{N}/\text{Al}_{0.85}\text{In}_{0.15}\text{N}$ bottom-DBR and an 8-pair $\text{SiO}_2/\text{ZrO}_2$ top-DBR. The evolution of the optical modes is shown when inserting a different number of QWs at each of the two antinodes of the electric field. Each of these QWs consists of 1.2 nm GaN embedded in the previously mentioned $\text{Al}_{0.2}\text{Ga}_{0.8}\text{N}$ cavity matrix characterized by $E_X = 3.63 \text{ eV}$, $f_X = 2.1 \cdot 10^{13} \text{ cm}^{-2}$, $\gamma_{\text{hom}} = 25 \text{ meV}$, and $\gamma_{\text{inh}} = 15 \text{ meV}$. The resulting imaginary part of the QW-refractive index is shown in Fig. 4.6(e). The BB absorption edge was also taken into account, using a Gaussian-broadened Heaviside-function shifted by $E_B = 44 \text{ meV}$ to higher energies.

Figure 4.6(a) shows the empty cavity with its bare photon-dispersion. Owing to the refractive

⁴This will apply vice versa in the case of resonant optical excitation.

index increase and the dependence $\mathbf{k}_\perp \propto \sin(\Theta_{\text{ext}})$, the mode deviates from the parabolic dispersion at high angles and becomes rather linear.⁵ In absence of any absorption, the Q -factor is exclusively determined by the maximum DBR-reflectivities and amounts to about 7000 for the present structure. With a cavity-mode energy $E_C = 3.63$ eV at zero in-plane momentum the MC represents the case $\delta \approx 0$. When now placing an active medium into the cavity spacer, the mode dispersion becomes significantly altered. For the case $N_{\text{QW}} = 2$, corresponding to one QW positioned at each of the two electric-field antinodes, the light-matter interaction constant is not sufficient to overcome the detrimental influence of the finite exciton linewidth $\gamma_{\text{hom}} = 25$ meV according to Eq. (4.22). This effect will be discussed in more detail hereafter. The cavity is in the WCR giving rise to an optical mode that follows the photon dispersion and that is broadened due to the absorption of the QWs. When doubling the number of QWs, the reinforced coupling strength (Eq. (4.16)) overcomes the damping rates and produces a hardly visible but finite mode-splitting at $\mathbf{k}_\perp = 0$. The apparent Rabi-splitting amounts to ~ 20 meV. Owing to the large exciton broadening, corresponding to room temperature conditions, the LPB is only visible around zero in-plane momentum. Certainly, the absorption spectrum would give better access to the modes, but reflectivity was chosen as it provides better comparability with the bare photon dispersion. By contrast, the UPB is much better visible owing to its large photonic fraction and the correspondingly lower linewidth. While it follows the photon dispersion at high-angles, its evolution around normal incidence deviates significantly from the cavity-mode energy. The effects of the SCR become more pronounced when considering the case $N_{\text{QW}} = 10$ in Fig. 4.6(d). Here, the Rabi-splitting of ~ 40 meV allows following the polariton dispersions up to higher angles. The emerging modes closely resemble the outcome of the COM in Fig. 4.5(a), including the inflection point in the LP dispersion. Note that for $\Theta_{\text{ext}} > 45^\circ$ the LPB runs out of the optical confinement. At this angle its flat dispersion crosses the first low-energy BM of the bottom-DBR allowing polaritons to leak out from the cavity. Thus, BMs are also often referred to as leaky modes.

From the analysis shown in Fig. 4.6 it appears that the occurrence of the SCR can be prevented by a finite mode linewidth, in particular for a small number of QWs and a correspondingly reduced value of g_0 . Such effects shall be discussed in more detail hereafter.

Impact of Mode Broadening and Requirements for the SCR

In order to discuss the influence of a finite linewidth of the uncoupled modes on the light-matter coupling in a MC, it is convenient to distinguish between homogeneous and inhomogeneous broadening mechanisms. Interpreting the homogeneous linewidths of exciton and cavity-photon as damping constants in analogy to the mechanically-coupled oscillators in Fig. 4.4, the dephasing time can be approximated by Heisenberg's uncertainty principle: $\tau_{\text{hom}} \approx \hbar/\gamma_{\text{hom}}$. If now τ_{hom} is shorter or close to the Rabi-oscillation period, given by $T_\Omega = 2\pi\hbar/\Omega$, an efficient energy transfer between both oscillators is prevented and the system remains weakly coupled. This intuitive criterion for the occurrence of the SCR can be expressed as:

$$\begin{aligned} T_\Omega &\gg \max(\tau_X, \tau_C) , \text{ or equivalently} \\ \Omega_0 &\gg \max(\gamma_X, \gamma_C) . \end{aligned} \tag{4.24}$$

⁵It actually follows a sine dependence up to 90° , as obvious for the BMs and DBRs in Figs. 4.2(b,c).

An alternative expression for the homogeneous linewidth limitation can be obtained via the COM and Eq. (4.22). As the Rabi-splitting is only defined as a real quantity, it holds:

$$\Omega = \begin{cases} 0 & \text{when } g_0 \leq \frac{|\gamma_X - \gamma_C|}{2}, \text{ and} \\ 2\sqrt{g_0^2 - \left(\frac{\gamma_X - \gamma_C}{2}\right)^2} & \text{when } g_0 > \frac{|\gamma_X - \gamma_C|}{2}. \end{cases} \quad (4.25)$$

When considering typical III-nitride based MCs featuring $Q \approx 1000$, the more severe limitation will arise from the excitonic linewidth, in particular at room temperature when $\gamma_X \gg \gamma_C$. In this case both above-mentioned approaches would yield identical criteria for observing the SCR. Note that in low-quality cavities, where $\gamma_X \approx \gamma_C \gg 2g_0$, Eq. (4.25) would still yield finite values for the vacuum Rabi-splitting, even though the SCR could not be observed according to the criterion defined in Eq. (4.24) and the potential presence of any polariton mode would be blurred by the immense broadening. A more refined theory abolishing this artifact has been provided by Savona and co-workers in Ref. [68]. Therein, they examined the Rabi-splitting values that occur in the reflection (R), absorption (A), and transmission (T) spectra of the MC and evidenced that it should hold: $\Omega_A \leq \Omega_T \leq \Omega_R$. The most stringent condition is thus given by the absorption:

$$\Omega_A = \begin{cases} 0 & \text{when } g_0^2 \leq \frac{\gamma_X^2 + \gamma_C^2}{2}, \text{ and} \\ 2\sqrt{g_0^2 - \frac{\gamma_X^2 + \gamma_C^2}{2}} & \text{when } g_0^2 > \frac{\gamma_X^2 + \gamma_C^2}{2}. \end{cases} \quad (4.26)$$

Note that for the case $\gamma_X \gg \gamma_C$ (or vice versa) all three criteria yield equivalent restrictions for the SCR.

Contrary to the homogeneous linewidth the impact of a statistical contribution, due to disorder, defects and layer-thickness fluctuations giving rise to an inhomogeneous broadening cannot be modelled within the COM. These non-idealities often play an only minor role in GaAs-based structures, but they are omnipresent in III-nitride ones. This is not necessarily due to the lower crystal quality, but rather caused by a much smaller exciton Bohr-radius and a therefore increased sensitivity to alloy composition fluctuations and crystal defects. In order to account for the inhomogeneous linewidth TMS have been performed. The considered MC-structure is almost identical to the one investigated in Fig. 4.6(c): it just consists of a 3λ cavity-layer with five QWs at each of the five field antinodes, the detuning was adjusted to $\delta \approx 0$. The zero-linewidth Rabi-splitting Ω_0 of this structure amounts to ~ 52 meV.

Figure 4.7(a) shows the absorption spectra at zero in-plane momentum for a QW-exciton with constant $\gamma_{\text{hom}} = 25$ meV as a function of the inhomogeneous exciton linewidth. The impact of γ_{hom} reduces the value of Ω_0 for γ_{inh} equal to zero to $\Omega = 48$ meV. Owing to the steep tails of the Gaussian-profile, the impact of a $\gamma_{\text{inh}} \ll \Omega$ is marginal. Both the linewidth and the Rabi-splitting remain almost unaffected in agreement with the outcome of Ref. [166]. However, when the FWHM of the Voigt-profile approaches the initial mode-splitting Ω the coupling regime starts to be modified: the linewidth increases and the Rabi-splitting starts to decrease strongly. The SCR is eventually lost when $\gamma_{\text{inh}} \approx \Omega_0$. This condition sets the requirements for the MC design and its structural and optical quality: a high number of QWs

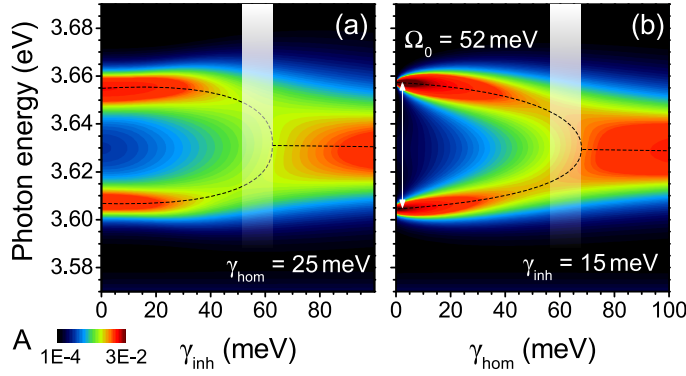


Figure 4.7: Absorption spectra computed by TMS at $\mathbf{k}_\perp = 0$ for the MC-structure of Fig. 4.6, but as a 3λ -cavity with 5 QWs at each of the 5 antinodes ($\delta \approx 0$): (a) impact of γ_{inh} for $\gamma_{hom} = 25$ meV, and (b) impact of γ_{hom} for $\gamma_{inh} = 15$ meV. Dashed lines highlight the mode maxima and shaded regions mark the transition region to the WCR.

featuring a high exciton oscillator-strength in order to maximize Ω_0 , and a sufficient structural quality to minimize the detrimental impact of γ_{inh} [167]. Whereas this quest can be won for GaN/AlGaIn-based MCs [168, 169], it appears intricate to overcome the inhomogeneous linewidth issue in InGaIn-based active media [170, 171]. At this stage it is worth mentioning that the present discussion neglects any influence of carrier localization. Indeed, being based on an infinite and ultra-fast sequence of emission and reabsorption processes, that have to occur at the same photon energy, the SCR relies on the free-exciton resonance, i.e. the absorption properties. Hence, as long as the localization dynamics occur on a longer time-scale than the Rabi-oscillation period or as long as the Stokes-shift (cf. Sec.3.2) allows a reasonable overlap between the emission and absorption spectra, the SCR can still take place in disordered system. This states however only a qualitative frontier, which is likely crossed in strongly-disordered InGaIn systems.

TMS also provide the possibility to compare homogeneous and inhomogeneous broadening impacts: Fig. 4.7(b) shows equivalent simulations of the absorption spectrum as a function of the homogeneous linewidth, while keeping γ_{inh} at a constant value 15 meV. In agreement with Ref. [166], no impact of the inhomogeneous broadening appears in the polariton system for low values of γ_{hom} , leading to very sharp resonances and a Rabi-splitting close to Ω_0 for $\gamma_{hom} \rightarrow 0$. Contrary to the inhomogeneous case, with increasing γ_{hom} the polariton lineshape and Rabi-splitting are directly affected in agreement with the predictions of the COM.

At the end of this section the impact of the cavity-mode lineshape shall also be discussed briefly. For a homogeneous broadening issued from a finite mirror reflectivity, the restrictions occur equivalently to the exciton case. However, differences emerge for an inhomogeneous contribution. In order to examine its effect, one has to consider the radius of a cavity-mode according to [172]:

$$r_{cav} = \sqrt{\frac{\lambda_{cav} L_{cav}}{\pi n_{cav}}} \frac{(R_1 R_2)^{1/4}}{1 - (R_1 R_2)^{1/2}}, \quad (4.27)$$

where R_1 and R_2 denote the reflectivity of the top- and bottom-DBRs at the cavity mode wavelength λ_{cav} , respectively. For GaIn-based MCs, this value lies in the range of a few micrometers. Two cases can be distinguished: first, the photonic disorder occurs at a similar or larger spatial scale compared to r_{cav} . In this case, the different cavity modes give independently rise to the SCR. This results in a simple averaging of the polariton dispersion over the probed spot

size, while the SCR cannot be affected by the photon disorder. On the contrary, when cavity disorder occurs at a scale smaller than r_{cav} , the cavity mode itself would average over the interface roughness leading basically to a decrease of the Q -factor and thus an increase of γ_C .

4.1.3 Polariton Condensation

All previous considerations focused on the linear light-matter interaction describing the polariton system close to the zero carrier-density limit, i.e. the quantum-nature of polaritons and interactions occurring in a polariton gas have been neglected so far. This section aims at introducing the potentially occurring non-linearities in a polariton system.

Polaritons as Bosons

As photons are non-interacting bosons and excitons obey the bosonic indistinguishability rule for low carrier-density (cf. Sec. 3.3.1), the polaritonic quasi-particles will behave as good bosons in the dilute limit. Contrary to free electrons and holes that follow Fermi-Dirac statistics in Eqs. (3.12) and (3.13), the occupancy of states for polaritons will be defined by the Bose-Einstein distribution:

$$f_{\text{BE}}(E, T, \mu) = g_E \left[\exp \left(\frac{E - \mu}{k_B T} \right) - 1 \right]^{-1}, \quad (4.28)$$

where g_E marks the degeneracy of the state with energy E and μ denotes the chemical potential, that corresponds to the Fermi-energy in the Fermi-Dirac statistics and is defined by the total number of particles in the system N_{tot} . Note that both distribution functions, the fermionic and the bosonic ones, converge to the classical Boltzmann-distribution for high temperatures marking the loss of the quantum-mechanical particle character. The latter and the respective interactions occurring between quantum-particles are intrinsically defined by the particle wave-functions. These are antisymmetric for fermions, giving rise to the Pauli-exclusion principle due to destructive interference, and symmetric for bosons, which causes an attractive interaction potential. The extension of the particle wave-function and thus of the quantum-mechanical interaction potential is given by the de Broglie wavelength:

$$\lambda_{\text{DB}} = \frac{h}{\sqrt{2\pi m k_B T}}. \quad (4.29)$$

It emphasizes the two parameters governing the occurrence of quantum-effects: temperature and the particle mass. Both quantities have to be minimized in order to increase λ_{DB} and make particles quantum-mechanically interacting when their wave-functions interfere, i.e. when λ_{DB} reaches the mean interparticle distance d . This case is schematically depicted for bosons in Fig. 4.8. For high temperatures, the particles behave as a classic ideal gas. Cooling down the boson ensemble increases λ_{DB} and triggers quantum-effects when $\lambda_{\text{DB}} \approx d$. Due to constructive quantum-interference between symmetric wavefunctions, particles will start to massively populate the system ground state with energy E_0 , forming a so-called Bose-Einstein condensate (BEC) surrounded by a thermal gas cloud below a certain critical temperature T_{crit} . Based on the condition $\lambda_{\text{DB}} = d$, one can alternatively define a critical carrier density

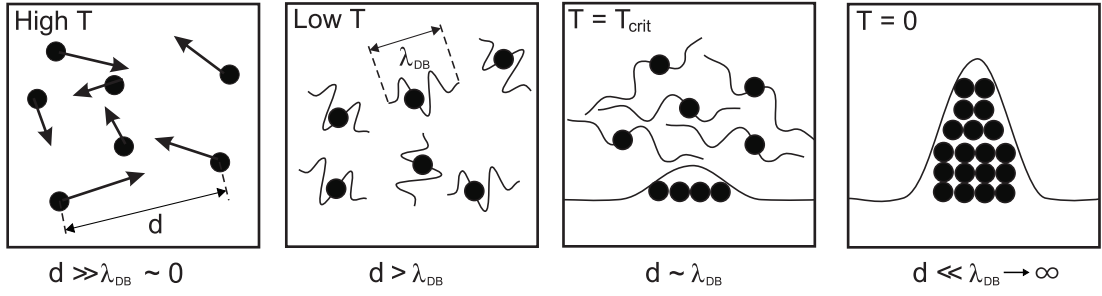


Figure 4.8: Cooling-down a boson-gas: for high temperature T the particles behave like a classical gas. With decreasing T their quantum-nature emerges: the wave-function extension given by λ_{DB} increases and approaches the interparticle distance d . The equality between the two is eventually reached for $T = T_{\text{crit}}$, and bosons start to accumulate in the ground state. For zero temperature all particles occupy the system ground state. Reproduced from Ref. [108]

n_{BEC} for the occurrence of a BEC.⁶

The formation of a BEC can also be deduced from f_{BE} in Eq. (4.28). The chemical potential in a bosonic system is a quantity that is smaller than E_0 and increases with carrier density. When μ approaches the ground-state energy, i.e. when $(E_0 - \mu) \rightarrow 0$, f_{BE} diverges at $E = E_0$ giving rise to a massive occupation of the ground-state, while the thermal cloud of particles in excited states saturates. It is worth noting that the formation of a BEC does not require any classical interaction between the bosonic particles, it is rather a direct consequence of the quantum-mechanical particle indistinguishability.

The theory of BECs has been established by Bose and Einstein in 1924 and 1925 [13–15], respectively. The first experimental observation succeeded in dilute atomic vapors in 1995 at about the same time by the groups of Wieman and Cornell [173], and that of Ketterle [174]. This discovery has been awarded the Nobel-prize in physics in 2001. The large mass of the investigated alkali-atoms restricts T_{crit} in this case to values ~ 100 nK. In order to push the limits toward higher temperatures, systems with lighter particles have to be employed. Several candidates have been proposed over the past decades, and the observation of a BEC was claimed for indirect excitons [175], magnons [176], and even pure photons [177]. BEC in a cavity-polariton system was first evidenced by Kasprzak and co-workers in 2006 for a CdTe-based planar MC [17]. Note that the BEC-theory has initially been established for a closed 3D-system in thermal equilibrium and without interactions, and that cavity-polaritons state the exact opposite: they interact and form an open non-equilibrium system par excellence. Thus, certain definitions of a BEC have to be refined to account for the condensation of polaritons.

The motivation to make use of cavity-polaritons to establish high-temperature condensation of bosons stems from various aspects [11]. First, contrary to the 3D-case the LPB dispersion in a planar MC as visible in Fig. 4.5 provides a well-defined energy minimum at zero in-plane momentum, marking a BEC-compatible ground state. Here, the polariton mass can be largely reduced based on the photonic polariton-component. Indeed, whereas pure excitons feature

⁶This critical carrier density should not be confused with n_{crit} marking the occurrence of the Mott-transition in an exciton system as discussed in Ch. 3.

masses around m_0 leading to T_{crit} -values in the range of a few Kelvin, the polariton mass can be decreased by up to four orders of magnitude pushing the theoretical T_{crit} toward ambient conditions (cf. Fig. 4.5(d)). Moreover, due to their matter fraction polaritons are interacting particles, allowing despite their short lifetime a potentially efficient thermalization process. Finally, in Ref. [11] it was proposed that the spontaneous luminescence originating from a polariton condensate should share very similar properties with the emission of a conventional LD, while a corresponding device would work far below the Bernard-Duraffourg limit. More precisely, the occurrence of condensation at the center of the BZ should be accompanied by a strongly non-linear rise in the emission intensity and a jump in the temporal and spatial coherence of the emission. In combination with the compatibility of planar MC-structures with today's semiconductor-processing technology, this initiated the ongoing quest for coherent light emitters with ultra-low threshold, i.e. so-called polariton lasers.

Polariton Relaxation

With cavity-photon lifetimes lying typically in the range of a few picoseconds (or even below in the case of III-nitrides), cavity-polaritons represent an extremely short-living non-equilibrium system. In order to reach and occupy the ground state they have to thermalize and relax their excess energy very rapidly. This becomes particularly important when charge carriers are injected non-resonantly, either optically by a pump laser as in this work or electrically as in an eventual device. In the case of optical injection, the initial carrier population consists of a hot electron-hole plasma featuring an excess energy of ~ 1 eV. Most of it can be transferred to the lattice by emission of LO-phonons within the first few tens of femtoseconds [178]. Note that this process is accelerated in III-nitride semiconductors compared to other III-V compounds owing to the strong polarity of the crystal and the correspondingly increased LO-phonon energy and Fröhlich-coupling between charge carriers and optical phonons. This relaxation mechanism is very efficient until the excess energy of carriers drops below the value of the LO-phonon energy, i.e. 92 meV for GaN. From here, thermalization with the lattice can only occur through interactions with acoustic phonons. With a scattering time ~ 10 ps [63], such processes are rather slow. On top of this, they do not allow to exchange a significant amount of energy, typically around 1 meV. Eventually, the formation of excitons or very exciton-like LPs in a MC at high in-plane momentum, lying predominantly out of the light-cone, can be assumed to be rather fast (cf. also the slow rise-time of QW excitons in tr-experiments in Sec. 3.3). They possess a long lifetime of a few hundreds of picoseconds, i.e. close to the exciton one, and create the incoherent excitonic reservoir [179]. To form a condensate at the center of the BZ, these high- k exciton-like polaritons have to enter the light-cone and relax along the LPB dispersion. This process is hampered by two effects linked to the increasing photonic fraction of cavity-polaritons: the interaction cross-section drops progressively and the decreasing particle lifetime enhances the escape of polaritons. Both effects prevent the polariton population to thermalize efficiently and lead to the appearance of a relaxation bottleneck [179], i.e. a strongly depleted and non-thermal polariton branch occupancy in the light-cone. In a straightforward approach, this effect can only be overcome by increasing the cavity lifetime and/or reinforcing interparticle interactions, e.g. by increasing the carrier density [180, 181]. It intrinsically limits the polariton condensation threshold. However, it is worth mentioning that under special conditions, for instance when the energy difference between the exciton reservoir and the LPB ground-state amounts exactly to the LO-phonon

energy, these relaxation limitations can be partly overcome [69, 182, 183]. A more detailed discussion of such issues in III-nitride based MCs follows in Secs. 4.2.2 and 4.4.

Note that when switching to resonant or quasi-resonant excitation these relaxation issues can be circumvented. For cavity-polaritons this is usually done by exciting the MC at the magic angle close to the inflection point of the LPB [184]. In such a configuration, resonant scattering of polaritons conserving energy and momentum is triggered, which allows bypassing relaxation issues by generating signal and idler states at the center of the BZ and in the exciton reservoir, respectively. However, for the final aim of building a polariton device such a pumping geometry is rather unrealistic. It will thus be only casually discussed in the forthcoming sections.

Polariton Condensation: Challenges, Realizations, and Chances

In the early attempts for achieving polariton condensation, the aforementioned bottleneck issues frequently caused the loss of the SCR before reaching the non-linear emission regime in GaAs-based MCs [115, 185, 186]. In these studies, the number of particles required to reach unity occupancy of the ground-state and achieve condensation was higher than the critical carrier density that caused the MT to occur in the QWs. In such a case, the excitonic resonance is bleached, the exciton oscillator strength and the bosonic particle nature vanish, and the system switches back to the WCR. Multiple approaches have been proposed or followed to overcome this problem, for instance: (i) increasing the cavity-photon lifetime and thus preventing the premature escape of unthermalized polaritons [187], (ii) enhancing the particle scattering rates [180], or (iii) reinforcing light-matter coupling in various ways [188, 189]. In the latter case, the number of cavity-polaritons that can be injected into the MC without bleaching the exciton can be increased, e.g. by increasing N_{QW} .

Eventually, the non-linear emission regime has been reached in strongly-coupled MCs: first in a non-resonant injection scheme [16], and then under resonant excitation conditions [190]. Later a comprehensive analysis of the transition in a CdTe-based MC evidenced a thermal BEC-like condensation regime [17]. Since then, fascinating quantum-fluid effects have been studied in polariton condensates, such as integer and half-integer quantum-vortices [18, 191], superfluidity [19, 192] and solitons [193]. Based on their unique properties inherited from their mixed light-matter nature and driven by the potential to bring quantum-effects to an ambient environment, they have been proposed for various optoelectronic and spin-optronic applications. These include the generation of entangled photon pairs [184, 194], the fabrication of novel coherent light-emitters [11, 16, 22], ultra-fast optical spin switches [195, 196], micro-optical parametric oscillators and amplifiers [21, 184, 197], or mesoscopic optical interferometers [198, 199], but also for the realization of spin-sensitive devices [200–202], high-temperature superconducting circuits [203]. Nevertheless, so far the majority of these studies was conducted at cryogenic temperatures and under resonant optical pumping, which makes the practical realization of corresponding devices working under ambient conditions in the near future rather unlikely. The discussion of the way toward a polariton-based device will be continued in Sec. 4.2.3.

Until now, polariton condensation in planar MCs has been evidenced in the following material systems: GaAs [189, 204], CdTe [17], GaN [22, 23], in different organic semiconductors [205, 206], and rather recently in ZnO [207, 208]. Despite the realization of a GaAs-based

electrically-injected polariton LED operating at room temperature [209], and claims for electrically-injected polariton lasers operating at cryogenic temperatures [210, 211], it appears that thereby the critical temperature for the occurrence of polariton condensation T_{cut} is determined by the thermal stability of the excitonic complex [21], i.e. $k_B T_{\text{cut}} \approx E_B$. Indeed, until now the maximum temperatures for observing polariton-related non-linearities was restricted to 70 and 50 K for GaAs and CdTe-based MCs (cf. Fig. 1.1), respectively. The observation of condensation-related effects under ambient conditions and thus the realization of eventual polariton-based devices is therefore likely limited to wide-bandgap organic and/or inorganic semiconductor MCs, where excitons remain robust up to room temperature. The proof of polariton condensation at $T = 300$ K succeeded first in a bulk GaN-based MC [22]. A short chronological review about GaN-based MCs will be provided in Sec. 4.2.

When speaking about condensation of polaritons, it is worth emphasizing once more that cavity-polaritons are extremely short-lived quasi-particles. They emerge from the strong-coupling between a volatile photonic mode and an electronic excitation of the solid-state, and represent thus an intrinsically open non-equilibrium system. Maintaining the quasi-equilibrium of a macroscopic polariton condensate population requires continuous pumping that compensates for the losses. In this sense a polariton condensate does certainly not correspond to a BEC in the classical sense. Nevertheless, both phenomena share several characteristics, which lead to the commonly-accepted denomination of non-equilibrium BEC for cavity-polaritons [212]. Note that the terminology used here for defining polariton condensation encompasses both polariton lasing and polariton BEC. In the former case, the system switches abruptly from an uncondensed phase to a condensed one and exhibits neither below nor above the polariton condensation threshold a thermal occupancy [26]. In contrast, for a polariton BEC the carrier population features a well-defined temperature, below and above the critical density [17].

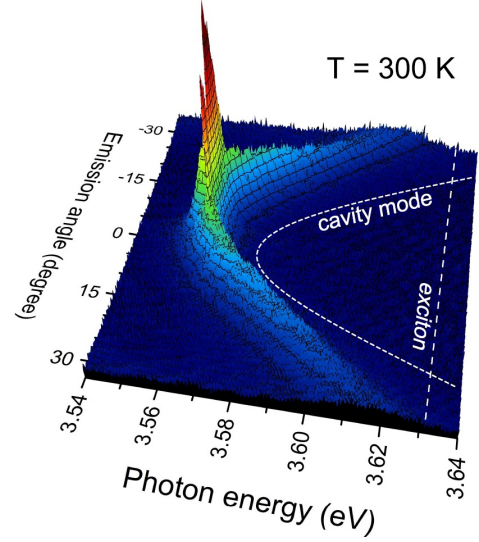
4.2 III-nitride based Structures - Review and Opportunities

As already indicated the motivation to explore GaN-based optical structures for light-matter coupling applications is mainly based on the increased value of the exciton binding energy. It amounts to about 25 meV in a bulk crystal and allows excitons and thus polaritons to survive up to room temperature (cf. Fig. 1.1). Further advantages in this viewpoint originate from the huge Fröhlich-coupling in III-nitrides, that promotes carrier thermalization and limits exciton dissociation by LO-phonons, and the increased oscillator strength, which is approximately five times larger than in GaAs [168]. The investigation of III-nitride structures is additionally facilitated by well-controlled deposition and doping techniques, and established device processing methods. The major advances in III-nitride heterostructure growth coincide with breakthroughs in the fabrication of blue LEDs and LDs in the 1990s [4, 5].

The first observation of strong coupling in a III-nitride based structure was reported in 2003: Antoine-Vincent and co-workers covered a simple $\lambda/2$ GaN-layer deposited on Si with a dielectric top-DBR and observed a Rabi-splitting of about 30 meV at low temperature [213]. Two years after, the same group demonstrated the SCR up to 300 K using a similar structure with a metallic top-DBR. At this stage, the poor Q -factors prevented the observation of non-linear polariton effects. Therefore, a new approach consisted in the fabrication of crack-free lattice-matched AlInN-based bottom-DBRs that allowed to overgrow them with high-quality

epitaxial active regions. Pioneering advances have been implemented by Carlin and co-workers at EPFL [214, 215], that reported maximum DBR reflectivity values exceeding 99%. These structures allowed first the achievement of very high Q -factor MCs [216–218] and subsequently the observation of the SCR in a bulk GaN-based and a GaN/AlGaIn QW-based MC at room temperature [219, 220]. In the following years EPFL also succeeded in demonstrating polariton lasing under ambient conditions.

Figure 4.9: Emission of the LPB under non-resonant optical pumping slightly above threshold in MC-1, i.e. the c -plane GaN MQW-based MC from Ref. [23] (for additional information, see description of MC-1 in Sec. 4.3.2) at 300 K ($\delta \sim -50$ meV). The uncoupled modes are shown with dashed white lines.



4.2.1 Polariton Condensation at Room Temperature

The first realization of a room-temperature polariton condensate was reported by Christopoulos and co-workers in 2007 [22]. Therein, a bulk $3\lambda/2$ GaN-layer deposited on top of an AlGaIn/AlInN-based highly-reflective bottom-DBR was optically-pumped under pulsed non-resonant conditions. Angle-resolved PL-measurements evidenced a Rabi-splitting of about 35 meV in this structure. When increasing the pumping power the LPB exhibited a blueshift, splitting up directly into multi-mode lasing as soon as the threshold was passed. The latter feature was likely caused by localization due to the strong photonic disorder that typically emerges when depositing such structures on top of foreign substrates [218]. Just one year after this achievement, the EPFL group also reported on polariton condensation in a MQW-based MC at room temperature [23]. This MC-structure relies on 67 GaN/Al_{0.2}Ga_{0.8}N QWs as active medium and is also investigated within this work (MC-1). A detailed sample description will follow in the upcoming section. Figure 4.9 shows a LPB-dispersion measured under non-resonant optical injection slightly above threshold at 300 K. The advantages of QWs over a bulk region as active medium stem from the increased value of E_B and the reinforced oscillator strength according to Sec. 2.3, giving rise to an enhanced exciton stability and a Rabi-splitting of ~ 60 meV. In the subsequent years, multiple studies have been conducted on these two samples, from which a few selected will be reviewed here briefly.

The formation of a BEC, which corresponds to a macroscopically occupied quantum-state that is entirely described by a single wave-function and a well-defined temperature, is accompanied by an abrupt occurrence of long-range spatial and temporal coherence [221]. Such a phase transition is typically linked to the rise of an order parameter, that ideally remains around a

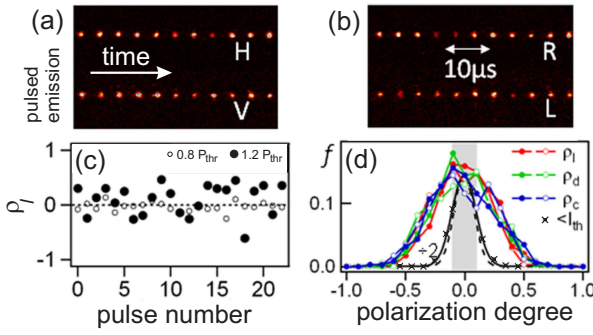


Figure 4.10: Polarization-resolved LPB emission in a bulk GaN MC at 300 K above threshold in: (a) linear, and (b) circular bases. (c) Deduced degree of linear polarization for each excitation pulse below and above the polariton lasing threshold. (d) Histogram of the fraction of each polarization state f along linear, diagonal, and circular bases for nearly 2000 condensate realizations. Taken from Ref. [24].

stochastic zero in the uncondensed system but acquires high values with a randomly-chosen phase upon BEC-formation. This effect is usually referred to as spontaneous symmetry breaking and can be considered as a necessary property of a BEC [222]. In 2008, Baumberg and co-workers investigated the condensate formation at room temperature in the previously-mentioned bulk GaN MC [24]. They excited the cavity non-resonantly with femtosecond pulses and were able to record the complete polarization degree ρ of each single condensate realization (see Fig. 4.10). It turned out that in the uncondensed phase ρ remained around zero, while across threshold the latter rises up with a stochastically-oriented phase. Thereby, ρ remained at finite values considerably below unity, which was ascribed to the limited condensate coherence time. Similar experiments concerning the order parameter have also been conducted on the MQW-based MC at 300 K [103, 223]. Using a quasi-cw non-resonant excitation scheme the large linear polarization degree above threshold was evidenced to be preferentially pinned along the crystal axes. This effect has already been observed earlier in other QW-based MCs [17, 224]. It was mainly attributed to the complex strain landscape that forms during heterostructure growth and may cause local asymmetries. Moreover, in Ref. [103] starting from $\rho \approx 0.8$ at threshold a significant reduction of the linear polarization degree was observed when further increasing the excitation power. Based on a stochastic Gross-Pitaevskii approach, the depinning of the order parameter was attributed to the Larmor-precession induced by the asymmetric interactions occurring between polaritons with different spin projections [225]. Finally, the mapping of the detuning dependence of the maximum ρ -value at threshold yielded a pronounced drop around $\delta \approx -55$ meV, which can be ascribed to the special relaxation conditions, that occur here at room temperature and that shall be discussed now.

4.2.2 The Condensation Phase Diagram

For a given structure with a defined Rabi-splitting, detuning and temperature are the two main parameters that govern and alter the polariton properties. Thereby, the detuning defines the mixture of the light-matter composition for polaritons, setting the interaction cross-section, the lifetime, and the mass of polaritons within the light-cone. On the contrary, the lattice temperature determines the homogeneous exciton linewidth and the polariton-relaxation efficiency [226], it regulates the thermal-activated escape of polaritons from the LPB-trap, and further sets the rise of the critical density that is needed to reach unity occupancy of the ground state and trigger condensation.

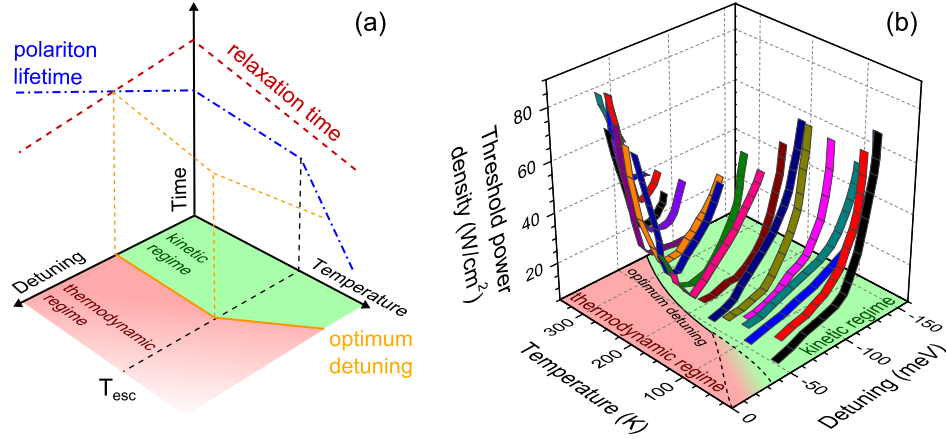


Figure 4.11: Condensation phase diagram of a *c*-plane GaN-based MC (see MC-1 for structural details): (a) schematic representation of the time-scales driving the optimum threshold conditions. See text for details. (b) Experimental results: evolution of the polariton condensation threshold as a function of detuning and temperature. The optimum detuning separates kinetically and thermodynamically-driven regimes. Data are reproduced from Refs. [25, 26].

At low temperatures and large negative detuning conditions, the relaxation rate along the LPB is slow owing to the high photon fraction, while the lifetime of polaritons approaching the center of the BZ becomes very short. These conditions prevent an efficient thermalization and condensation can only be achieved by further increasing the carrier density and enhancing interparticle scattering [181]. The polariton lasing threshold is driven by the carrier-scattering kinetics and increases for more negative detuning values (cf. Fig. 4.11(a)). Staying at low temperature and increasing the detuning, will modify the balance between lifetime and relaxation efficiency: the high-excitonic fraction increases the polariton lifetime and interactions, leading to an efficient thermalization process. This is the thermodynamic regime, where the polariton condensation threshold is governed by the polariton mass that sets λ_{DB} according to Eq. (4.29). In consequence, there should be an optimum detuning condition defined by the trade-off between relaxation-kinetic and thermodynamic limitations, that corresponds in good approximation to the situation where the mean polariton lifetime coincides with the relaxation time needed to reach the LPB ground state.

An increase of the lattice temperature increases the scattering rates between the polariton ensemble and acoustic phonons, which was shown to enhance the relaxation efficiency in a bulk GaN-based MC [226]. It is reasonable to assume that MQW-based MCs are influenced in an equivalent manner. Thus, the relaxation time-scale will shorten, while the polariton lifetime is expected to vary only moderately with temperature in the center of the BZ based on the excitonic broadening impact (cf. Fig. 3.15(c)). This leads to a shift of the optimum detuning conditions toward more negative detunings, that is further enhanced by the decrease of λ_{DB} with T . Increasing further the temperature, beyond a certain T_{esc} the thermal agitation starts to trigger the escape of polaritons from the LPB-trap toward higher-momentum states, which intrinsically shifts the optimum conditions toward even more negative detuning values.

These carrier relaxation dynamics have been comprehensively analyzed and modeled by a kinetic Boltzmann-equation approach for the GaN MQW-based MC in Ref. [26]. The modeling

was able to qualitatively reproduce the experimentally observed variation of the threshold power density P_{thr} with temperature and detuning [25], that is shown in Fig. 4.11(b). It turned out that for each combination $\{\delta, T\}$ there is an optimum detuning δ_{opt} where P_{thr} is minimized. This condition depends critically on the investigated MC-structure, but may appear significantly apart from $\delta = 0$, which sets an essential distinguishing mark compared to VCSELs based on the matter-character of polaritons [223]. For the present GaN MC this optimum occurs for $\delta_{\text{opt}} \approx -55$ meV at 300 K and close to zero detuning at low temperature, i.e. a situation very similar to GaAs and CdTe-based MCs where it was evidenced to appear around zero and slightly positive detuning [189, 227], respectively.

4.2.3 Toward a Polariton Laser Diode

With respect to the emerging market for III-nitride based devices and applications, the final aim of studying polariton condensation in such MCs consists certainly in realizing an electrically-injected polariton laser diode (PLD). Depending on the ultimate realization, it would certainly emit in the blue-UV spectral range. Telecommunication working in the near-IR transparency region will therefore be dropped out from the list of potential applications. The same remark applies for high output-power applications: PLDs will most probably rely on a VCSEL-like design and be operated at carrier densities significantly below the MT in order to keep excitons stable, yielding a comparably low output power. The list of potential applications is thus not fully defined yet, but properties such as a high-efficiency, a highly-coherent directional output, or the possibility to create interacting BECs by electrical means in a compact housing under ambient conditions may open up new fields with hindsight that cannot even be guessed from here. First examples are given by ultra-fast optical spin switches and terahertz sources [202, 228].

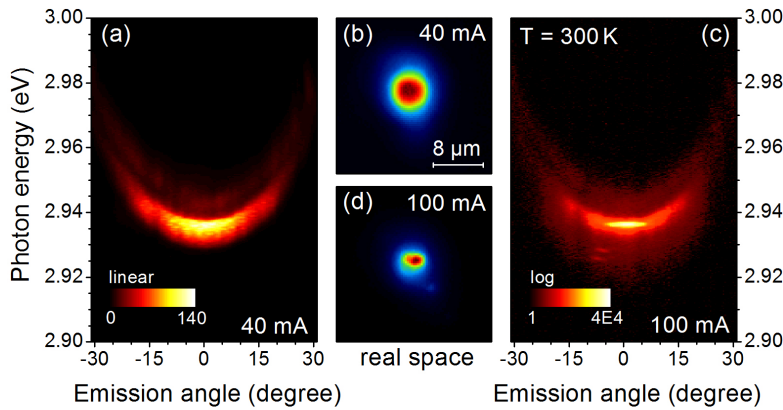


Figure 4.12: Emission of an InGaN-based monolithic VCSEL under pulsed electrical-injection at room temperature: (a) angle-resolved emission spectrum below threshold, and (b) corresponding real-space image. (c) Angle-resolved emission spectrum above threshold in a logarithmic color scale, and (d) corresponding real-space emission pattern. More details can be found in Ref. [161].

GaN versus InGaN-based Devices

At first sight, there are two different possibilities to achieve a III-nitride based PLD: either based on a GaN/AlGaN or an InGaN/GaN-based active region. A variety of restrictions and consequences come along with this choice. GaN/AlGaN based QWs provide superior crystal and optical qualities that allow reaching a robust SCR. Nevertheless, for electrical injection purposes restrictions arise for instance from the increasing difficulty in obtaining an efficient *p*-type doping with rising Al-contents and the lack of transparent while sufficiently conductive layers in the UV-region. The electrical characteristics might additionally suffer from the density of point defects emerging from the bottom-DBR that is likely based on AlGaN/AlInN bilayers and can thus not be grown lattice-matched on free-standing GaN substrates. The latter issue could be partially overcome when going to a flip-chip design but would be penalized by a more expensive processing. All these drawbacks could be circumvented when switching to an InGaN-based active region: *p*-type doping of GaN is well-established, indium-tin oxide can be used as transparent front contact and the whole structure, except for the QWs, could be grown lattice-matched based on optimized GaN/AlInN-based bottom-DBRs [77]. All those processes are well-developed for InGaN/GaN-based optoelectronic structures and led recently to the demonstration of first monolithic electrically-driven VCSELs [161, 229]. Corresponding energy dispersions and real space emission patterns below and above the lasing threshold from Ref. [161] are reported in Fig. 4.12.

Despite all these advantages, the InGaN/GaN system brings one major drawback: the optical quality of such QWs has not yet proven sufficient to reach the SCR [170, 230]. The main issue consists in the inhomogeneous linewidth, that remains around 40 meV even for the highest quality structures. Carrier localization and the Stokes-shift keep a similar energy scale. Thereby, the origin of exciton disorder likely stems from random alloy fluctuations in the QW-material [231, 232] or QW-width variations [233]. Another problem might arise from the different optimum growth temperatures for InGaN and GaN layers, i.e. $T_{\text{InGaN}} < T_{\text{GaN}}$ [234]. When an In-rich InGaN-based QW ($x_{\text{In}} > 15\%$) is overgrown with a high-temperature GaN the QW-properties may be significantly degraded. Additionally taking into account the reduced oscillator strength due to the lower E_{B} value and the increased impact of QCSE, the optical quality achieved for InGaN-QWs until now remains insufficient to reach the SCR according to the restrictions explained in Sec. 4.1.2.

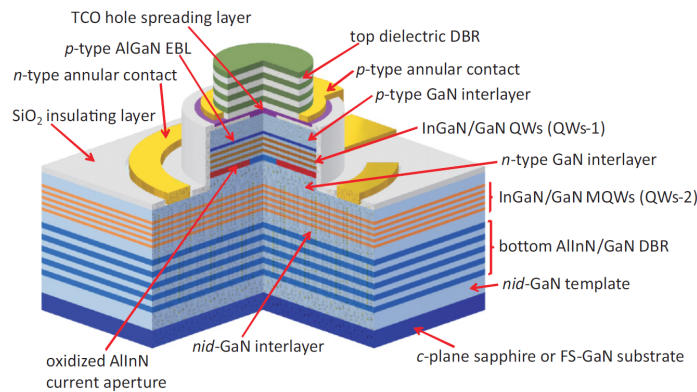


Figure 4.13: Schematic cross-section of an InGaN/GaN MQW-based PLD relying on an intra-cavity pumping geometry. Reproduced from Ref. [171].

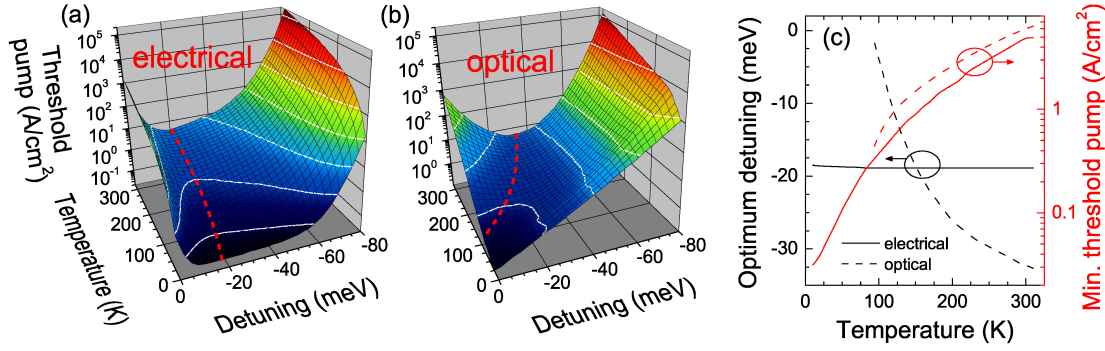


Figure 4.14: Dependence of the condensation threshold current density on detuning and temperature for: (a) direct electrical, and (b) intracavity optical pumping schemes. (c) Evolution of the optimum detuning (black) and minimum threshold current density (red) as a function of lattice temperature for direct (solid lines) and intracavity (dashed lines) geometries. Taken from Ref. [171].

Approaches and Simulations

Given that the required quality for InGaN/GaN QWs may be reached in the future, some additional issues would arise when designing a corresponding PLD. Indeed, whereas the optimum number of QWs lies in between one and five for an InGaN-based VCSEL structure [161], limited by the need for an effective carrier injection and the low hole-mobility, N_{QW} has to be drastically increased for a PLD in order to enhance the light-matter coupling from Eq. (4.16). A promising compromise combining both requirements could consist in using an intra-cavity pumping scheme as depicted in Fig. 4.13 [235]. Therein, the electrical carrier injection would drive a conventional InGaN-based LED-structure that optically pumps a set of InGaN/GaN MQWs located beneath. While featuring a lower emission energy than the LED, these MQWs would be responsible for establishing the SCR. The rest of the structure resembles the VCSEL design of Ref. [161].

The temperature and detuning-dependent input-output characteristics of InGaN-based PLDs have been studied theoretically by employing a set of coupled semi-classical Boltzmann-equations in Ref. [171]. The article focuses thereby on the comparison between the intra-cavity pumping and the less-realistic direct pumping scheme where the complete set of MQWs is electrically-injected. Figure 4.14 compares the computed estimates of the threshold current density as a function of the $\{\delta, T\}$ -combination for both geometries. For the intra-cavity (optical) pumping the optimum detuning conditions are expected to vary in a very similar manner as for the optically-excited GaN/AlGaIn MQW-based MC described in Sec. 4.2.2. By contrast, the direct electrical injection scheme does not show any significant variation of δ_{opt} with temperature. This behavior was ascribed to the modified free-electron scattering rates. It is further worth mentioning that the estimated threshold current densities are quite similar for both pumping geometries and that despite some approximations they remain significantly below state-of-the-art VCSEL thresholds. Note finally that for an intra-cavity pumping scheme the high-frequency modulation response as well as the eventual device efficiency would be dictated by the LED, which is canceling certain advantages of PLDs.

Device Competitors

Certainly, III-nitrides are not the only promising material system when aiming at the realization of PLDs. The upcoming discussion is closely connected to the final considerations in Sec. 4.1.3 and shall review the most serious competitors briefly.

Due to their superior quality, MC systems employing GaAs or CdTe-based active media revealed the most fascinating physics of polariton condensates so far (cf. Sec. 4.1.3). In view of device realization, the growth and processing techniques for these material systems are well-controlled, but issues will more likely arise from the low value of E_B in corresponding QWs (cf. Tab. 4.1). Indeed, despite the proof that excitons may be injected electrically at low temperatures [236], and the realization of a polariton LED that operates in the linear SCR at room temperature [209, 237], the limited robustness of excitons in such structures is likely to prevent the observation of polariton condensation related non-linearities under ambient conditions [21, 209]. This conclusion is certainly more valid for GaAs than for CdTe, for which E_B can reach values similar to bulk GaN [17]. But unfortunately, there are no further high-temperature studies existing for CdTe-based MCs.

At this point, it is worth noticing that very recently the realization of electrically-injected polariton LDs was claimed by two different groups [210, 211]. Both systems consisted of a GaAs-based MC, that was operated at low temperature and that has been placed in a strong magnetic field. Polariton lasing was concluded exclusively based on the observation of a non-linear emission intensity increase and a linewidth narrowing, that occurred in presence of a magnetic field of a few Tesla, but could not be observed without the latter. The need for a magnetic field is in both works motivated by an increased exciton oscillator strength by a few percent, which however leaves in view of the complete absence of any condensation signature in the field-free case many open questions. Moreover, the proximity between the claimed polariton and photon lasing thresholds in case of Ref. [211] states a clear contradiction with the continuous MT observed in semiconductor QWs. Indeed, while polariton lasing needs a strong exciton resonance, photon lasing relies on gain overcoming the Bernard-Duraffourg condition and the internal losses of the structure. It is thus hard to imagine, that this transition can be completely overcome when increasing the carrier density by a factor of only two. Even in the case that against all odds both emissions correspond to polariton condensation in the common sense, the low-temperature and high-magnetic field requirements are not compatible with any interpretation of a device. Therefore, the quest continues.

As already mentioned and with respect to the work of Saba and co-workers [21], the observation of polariton condensation at room temperature will likely be limited to material systems that feature an exciton binding energy exceeding the thermal energy at room temperature, i.e. $E_B > 25$ meV. In addition to GaN (preferentially QW-based), only ZnO and organic semiconductors remain as suitable candidates in Tab. 4.1, that have already proven to feature polariton condensation under room temperature conditions.

With respect to its high exciton binding energy and oscillator strength, ZnO has been proposed as the most-promising material system for high temperature polariton condensation and the realization of corresponding devices in 2002 [242]. Until now, the SCR has been achieved with various geometries, preferentially based on bulk active layers: in fully-hybrid micro-crystalline ZnO MCs relying on two dielectric DBRs [243, 244], in epitaxial ZnO that was deposited on top of a III-nitride based bottom-DBR [207, 245, 246], very recently even in a monolithic

Chapter 4. Polariton Condensation in III-nitride based Microcavities

Table 4.1: Exciton binding energy E_B , vacuum Rabi-splitting Ω , and present temperature limit T_{\max} for observing polariton condensation in planar MCs based on different material systems.

Material	GaAs (QW)	CdTe (QW)	GaN (bulk)	GaN (QW)	ZnO (bulk)	Organics (bulk)
E_B (meV)	10 [238]	25 [17]	25 [53]	45 [23]	60 [239]	~ 1000 [205]
Ω (meV)	15 [238]	26 [17]	36 [24]	60 [69]	130 [207]	256 [205]
T_{\max} (K)	70 [240]	50 [17]	300 [22]	340 [26]	300 [241]	300 [205]

ZnO/ZnMgO QW-based structure at low temperature [247], and it was claimed for ZnO-based nano-wires with Ω -values as large as $\Omega_{\text{VRS}} \sim 280$ meV [248]. Even if the SCR appears to be very robust against temperature [249], polariton condensation has only been reported very recently [207, 208, 250], being claimed even at room temperature [241]. Despite considerable research efforts, the moderate optical quality prevented performing more sophisticated studies on this material system so far and in view of realizing devices the limited long-term stability and the difficulty of achieving a reliable p -type doping in ZnO set major drawbacks.

The fundamental electronic excitation in organic semiconductor compounds is commonly described in the framework of Frenkel-excitons [251]. These are localized electron-hole pairs that are strongly-bound $E_B \sim 1$ eV and feature a large oscillator strength. When taking further into account that the corresponding optical transitions often occur in the visible spectral range and that doping is quite well-established, organic active media exhibit certain essential advantages over inorganic ones. These are further complemented by the potential of a low-cost device fabrication. Until now, the SCR up to 300 K was evidenced for various planar MC-designs [252–258]. However, non-linear polariton emission has only been reported in an anthracene-based structure under non-resonant optical excitation [205], and very recently in a TDAF-based MC [206]. Despite their obvious advantages, the limited thermal, mechanical and chemical stability of organic compounds may hamper the way toward devices.

Note that the SCR has also been evidenced in an epitaxial ZnSe-based MC lately [259]: these II-IV semiconductors combine good structural qualities with quite high exciton binding energies (cf. Fig. 1.1) and might enter the competition as soon as the non-linear emission regime can be reached.

4.3 Experimental Details and Basic Microcavity Properties

Before heading toward the experimental part, the modifications of the optical techniques from Sec. 3.1, that have been applied to investigate the MC-structures, and the basic properties of the c -plane structure MC-1 shall be introduced.

4.3.1 Fourier-Space Imaging

Owing to the in-plane translational invariance and the symmetry-breaking at the sample surface, various properties of the cavity-polariton dispersion are already accessible via angle-resolved measurements according to Sec. 4.1. This can simply be done by using a goniometer setup as employed for the excitation in PLE experiments, or in a more sophisticated way by

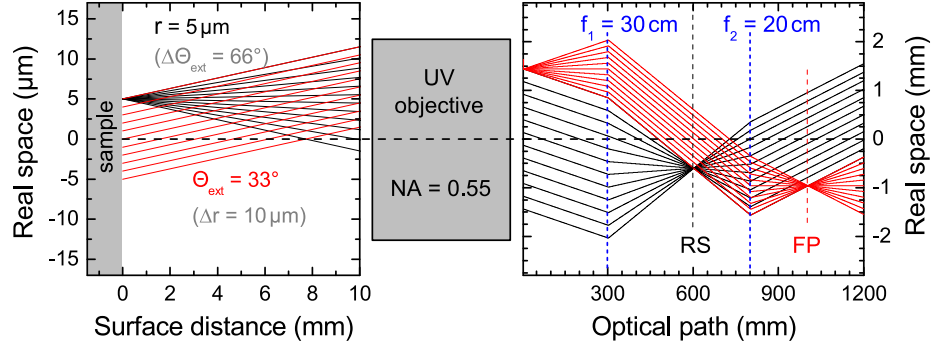


Figure 4.15: Simulation of the optical path in the Fourier-spectroscopy setup: (left) between the sample surface and the NA = 0.55 UV-objective, and (right) between the objective and the entrance slit of the spectrometer. Black rays originate from the real space position $r = 5 \mu\text{m}$, red rays are emitted from all over the focus spot with an emission angle $\Theta_{\text{ext}} = 33^\circ$. The Fourier-plane (FP) forms directly at the output of the objective and is imaged on the entrance slit of the monochromator by means of two lenses with respective focal lengths $f_1 = 30 \text{ cm}$ and $f_2 = 20 \text{ cm}$. The real space focus (RS) emerging in between f_1 and f_2 is also indicated. Adopted from Ref. [108].

imaging the Fourier-plane (FP). The latter corresponds to the Fourier-transform of the near-field emission pattern and is formed directly at the back-focal plane of the UV-microscope objective when the sample surface is situated in the focus of the latter. This approach is depicted in Fig. 4.15. The NA = 0.55 objective collects emission angles with $\Delta\Theta_{\text{ext}} = 66^\circ$. All rays emitted from a certain real space spot (in Fig. 4.15 exemplarily located at $r = 5 \mu\text{m}$) are transformed by the objective into parallel beams, that can be refocused by an additional lens with $f_1 = 30 \text{ cm}$ yielding the real space image RS. By contrast, all rays that are emitted from the surface with identical external angles Θ_{ext} will be focused to identical paraxial coordinates r at the exit of the objective forming FP. Inserting a second lens $f_2 = 20 \text{ cm}$ in the collection line FP can then be imaged on the entrance of the spectrometer. A finite slit width will filter out an angular profile, that is energetically dispersed in the monochromator. Finally, the read-out of the CCD-pixel array yields a dispersion curve as shown in Fig. 4.12(a).

Note that the paraxial approximation $\Theta_{\text{ext}} \approx \tan(\Theta_{\text{ext}})$ does not hold over the whole numerical aperture of the UV objective. Thus, the radial coordinate in the Fourier-plane r_{FP} has to be corrected by the angular collection according to:

$$r_{\text{FP}} = \frac{f_1}{f_2} f_{\text{obj}} \cdot \tan(\Theta_{\text{ext}}), \quad (4.30)$$

where $f_{\text{obj}} = 2.5 \text{ mm}$ denotes the focal length of the microscope objective. Note that compared to the goniometer-setup, Fourier-spectroscopy may suffer from aberrations and the limited range of accessible angles based on NA = 0.55. Nevertheless, it provides much smaller spot diameters $\sim 5 \mu\text{m}$ and the essential advantage of acquiring a complete dispersion curve in a single shot.

Figure 4.16 shows the modified setup scheme. All excitation sources listed in Sec. 3.1.1 can be used. The collection arm leading to the spectrometer is used to image the Fourier-plane, while

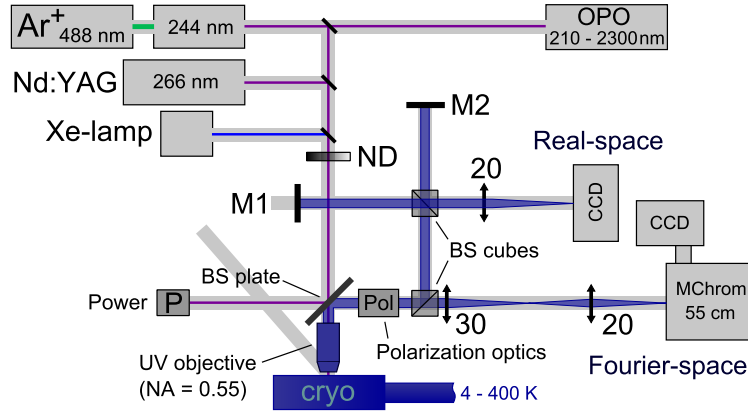


Figure 4.16: Schematic of the Fourier-spectroscopy setup: The sample can be excited by various sources through a NA = 0.55 microscope objective. A BS-cube positioned in the collection line separates the signal: In the first arm, the Fourier-plane is imaged onto the entrance slit of the monochromator by means of two lenses with respective focal lengths of 30 and 20 cm. The second arm images the real space and consists of a Michelson-interferometer and another UV-enhanced CCD. The sample response can be studied as a function of temperature, power and polarization. See text for more details.

a BS-cube in front of the first collection lens can deflect part of the light into another arm. Here, the real space emission pattern can be investigated by means of a UV-enhanced CCD-camera. The light can optionally be guided through a Michelson-interferometer setup for probing coherence properties. Polarization resolution can be obtained by placing the combination of a $\lambda/2$ wave-plate and a linear polarizer between the BS-plate separating excitation and collection lines and the previously-mentioned BS-cube. The slightly polarizing response of the BS-plate has been taken into account by measuring white-light reflection.

4.3.2 Structural Description of the *c*-plane Microcavity

The major part of the experimental investigations reported in this chapter except for Sec. 4.7 have been performed on a *c*-plane GaN MQW-based MC-structure, which is in the following named MC-1 and shall be introduced hereafter.

MC-1 The whole structure was grown by MOVPE on top of a *c*-plane sapphire substrate. The initial 3 μm GaN-buffer was overgrown by a strain-relieving template that is composed of two GaN/AlN super-lattices (SLs), which are separated by a GaN spacer layer. The subsequently deposited 1 μm -thick $\text{Al}_{0.2}\text{Ga}_{0.8}\text{N}$ buffer layer provides the basis for the lattice-matched 35-pair $\text{Al}_{0.85}\text{In}_{0.15}\text{N}/\text{Al}_{0.2}\text{Ga}_{0.8}\text{N}$ bottom-DBR. The overgrown 3λ -cavity was fabricated in the same run as sample MQW-1 and consists equally of 67 1.2 nm-thick GaN QWs that are separated by 3.6 nm-thick $\text{Al}_{0.2}\text{Ga}_{0.8}\text{N}$ barriers. The cavity section is sandwiched in between two $\lambda/4$ $\text{Al}_{0.2}\text{Ga}_{0.8}\text{N}$ spacers. Finally, the dielectric top-DBR was deposited by electron-beam evaporation. It consists of 13 $\text{SiO}_2/\text{Si}_3\text{N}_4$ bilayer pairs on top of a 67 nm-thick Si_3N_4 spacer layer, that was inserted to shift the cavity mode toward more negative detunings.

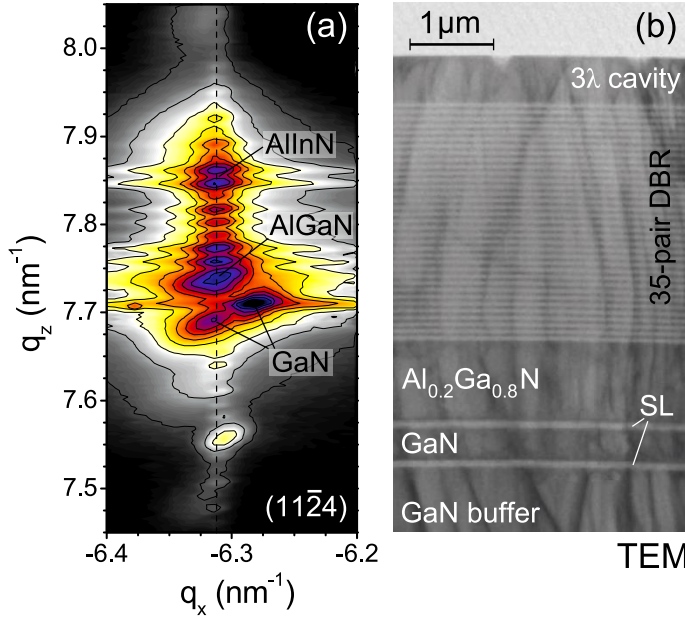


Figure 4.17: Structural details of MC-1: (a) XRD-RSM of the asymmetric $(11\bar{2}4)$ reflex. Cavity and DBR-sections were grown pseudomorphically with in-plane lattice constants different from that of the GaN-buffer. The indicated reflexes of the main alloys are subject to interference modulations. The GaN-peak at lower q_z emerges from the QWs, the other one from the GaN-buffer layer. (b) Cross-section view of the III-nitride layer stack in TEM. The DBR bilayers and the strain-relieving GaN/AlN SLs are clearly resolved [168].

Figure 4.17 shows a cross-section TEM micrograph of the III-nitride layer stack and a reciprocal space map (RSM) of the asymmetric $(11\bar{2}4)$ reflex measured by X-ray diffraction (XRD). In the latter the strain relaxation occurring in the SLs is clearly resolved by the shift of the inverse in-plane lattice constants q_x : from the GaN buffer at $q_x = -6.28 \text{ nm}^{-1}$ to the DBR-cavity layer stack, that is marked by the vertical dashed line and features equal in-plane lattice constants indicating pseudomorphic growth. The cavity section features smaller in-plane lattice constants than the almost relaxed GaN buffer, causing compressive strain to the GaN QWs and tensile relaxation along the growth axis. The latter can be followed from the larger lattice constants of the GaN-QW peak along the growth direction, corresponding to q_z . The TEM cross-section view in Fig. 4.17(b) reveals the high quality of the lattice-matched bottom-DBR that maintains, in combination with the strain-relieving GaN/AlN SLs located underneath, the dislocation density and the interface quality of the GaN-buffer layer. The whole MC-structure is free of cracks.

4.3.3 Basic Optical Properties

The compressive strain issued from the bottom-DBR leads to an increase of the exciton transition energy in MC-1 by about 35 meV compared to the sample MQW-1, that was grown during the same run. By contrast, all other properties of the present QW-excitons, such as their binding energy, oscillator strength, linewidth, the presence of biexcitons, and the localization energy appear identical to MQW-1. While the high number of QWs, i.e. $N_{\text{QW}} = 67$, was adopted to enforce the light-matter coupling strength according to Eq. (4.16), the uniform distribution of the latter and the small QW-width aims at minimizing the detrimental impact of the QCSE on the exciton oscillator strength. Indeed, with $L_{\text{QW}} = 1.2 \text{ nm}$ these MQWs meet the optimum conditions given in Fig. 2.8(c) and the homogeneous distribution even apart from the cavity antinodes reduces the QCSE-related electric-field strength based on the geometrical effect, where part of the polarization fields is accommodated in the relatively thin AlGaIn barriers

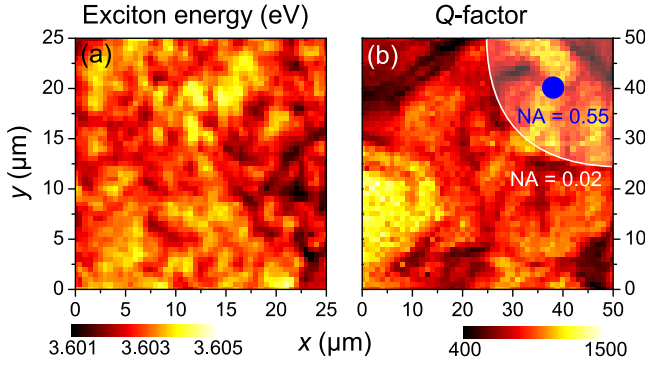
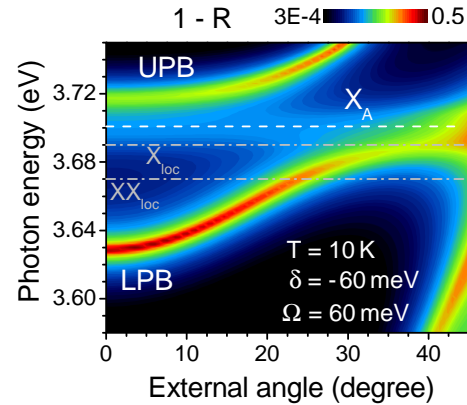


Figure 4.18: Micro-PL mapping of (a) the exciton energy in MQW-1 and (b) the MC-1 Q -factor recorded at 300 K [104]. The blue and white circles represent the approximative excitation spot size when using the microscope objective ($NA = 0.55$) and a conventional lens ($NA = 0.02$), respectively.

[81, 168].

The first report on the optical properties of MC-1 evidencing the SCR can be found in Ref. [168]. Therein, the Rabi-splitting was given with a value of 50 meV at room temperature, while for the first demonstration of non-linear polariton emission in this MC in Ref. [23], the value was rectified to about 56 meV. Indeed, a few studies later, it can be stated that Ω in MC-1 may vary depending on the probed sample spot, but usually reaches values around 60 meV in the low-density regime. This fluctuation is imprinted by the local photonic disorder, e.g. the cavity-photon lifetime, that can be extracted from the mapping of the Q -factor in Fig. 4.18(b). Here, the PL-emission was probed using the micro-PL setup under weak non-resonant cw-excitation conditions using an additional diaphragm in front of the UV-objective to restrict the angular collection to $\pm 3^\circ$. In this configuration the spot size is slightly increased, but the narrow angular selection allows to accurately determine the linewidth at $\mathbf{k}_\perp = 0$, that can be translated to the Q -factor based on the Hopfield coefficients. The strong Q -factor fluctuations, emerging at a spatial scale of a few microns and ranging from 400 to 1500, become essential when probing the emission properties up to the condensation threshold as they directly affect the polariton lifetime (cf. Sec. 4.5). Note that spatial averaging of the Q -factor yields a value ~ 1000 , consistent with that of Ref. [168]. Conversely, the excitonic disorder appears on a significantly smaller spatial scale and is basically characterized by a small energy fluctuation of 2–3 meV. In view of the comparably larger inhomogeneous linewidth, it is thus expected to play only a minor role.

Figure 4.19: Angle-resolved reflectivity ($1-R$ in logarithmic color scale) of MC-1 computed by TMS for $T = 10$ K [69]: QW-excitons have been modeled by $\gamma_{\text{inh}} = 11$ meV, $\gamma_{\text{hom}} = 5$ meV, and $f_X = 2.1 \cdot 10^{13} \text{ cm}^{-2}$. Due to the inhomogeneous linewidth and the homogeneous distribution of the QWs in the cavity a signature in reflectivity appears at the energy of the excitonic resonance X_A . The positions of the localized exciton and biexciton luminescence are indicated by dash-dotted lines.



The SCR of MC-1 with $\Omega = 60$ meV can also be reproduced by TMS: the eigenmode dispersion shown in Fig. 4.19 was generated by adopting a reasonable oscillator strength value $f_X =$

$2.1 \cdot 10^{13} \text{ cm}^{-2}$. Apart from the computed LPB and UPB dispersions, and the BM visible at high angles, attention shall be paid to the faint reflectivity dip emerging at the free-exciton energy. Based on a COM with 67 independent QWs, the SCR would be expected to give rise to two bright modes, namely the LPB and UPB being coupled to the light-field, and 66 dark exciton modes, that are decoupled from the cavity. In this ideal frame, the observation of bare excitons would be forbidden. However, due to certain characteristics of MC-1 part of the oscillator strength is transferred to dark exciton modes. These comprise in particular the inhomogeneous exciton linewidth [166], the finite DBR reflectivity, and the location of QWs apart from the cavity light-field antinodes [69]. Note further that contrary to these simulations the UPB is hardly observable in MC-1, owing to the absorption of the continuum states (cf. PLE spectrum of MQW-1 in Fig. 3.7).

As already mentioned in Sec. 4.2, MC-1 allows polariton condensation up to room temperature and above [23]. It further provided the basis for the studies concerning the condensation phase diagram in Refs. [25, 26], and the polarization properties beyond the polariton lasing threshold [103].

4.4 Polariton Relaxation: The Impact of Biexcitons

While cavity-polaritons were initially proposed for the realization of almost thresholdless coherent light emitters [11], later theoretical and experimental works revealed the crucial dependence of the actual condensation threshold under non-resonant injection on the relaxation efficiency of polaritons along the LPB [179]. Indeed, as already discussed due to the rising photonic fraction and the correspondingly reduced interaction cross-section, the scattering rate of lower polaritons is continuously decreasing toward the center of the BZ while their lifetime is shortened [179, 181]. This frequently results in the appearance of a relaxation bottleneck, i.e. a non-thermal LPB occupancy characterized by a highly-populated exciton reservoir at large in-plane wave-vectors and a depleted LPB ground state. Note that the interactions governing the polariton relaxation encompass both polariton-acoustic phonon and interparticle scattering.⁷ They are thus intrinsically temperature and carrier-density dependent, i.e. the scattering efficiency rises with both quantities [140, 181]. The formation of a relaxation bottleneck at a given carrier density is eventually defined by the $\{\delta, T\}$ -combination.

Figure 4.20 shows Fourier-space PL-images for two different detunings measured under cw low-injection at 10 K. As expected, the bottleneck can be clearly observed for highly photonic polaritons in the case $\delta = -61 \text{ meV}$. In comparison, when going toward positive detuning values, e.g. $\delta = 9 \text{ meV}$ in Fig. 4.20(b), the high excitonic fraction imposes increased scattering rates and a longer lifetime to the lower polaritons, eventually resulting in a rather thermal LPB occupancy. The continuous change in the polariton relaxation efficiency between those two extreme cases can also be followed by the measured LPB occupancy shown for various detuning values in Fig. 4.20(c). Note that all spectra have been taken under identical excitation conditions and that therefore the respective occupancy levels can be directly compared. In the thermodynamic framework, the condensation threshold is governed by the ratio between the effective mass and the population of the polariton ground state, triggering condensation when the occupancy reaches unity. Taking into account the only moderately varying polariton mass

⁷The term interparticle scattering encompasses polariton-polariton, polariton-exciton, and polariton-free-carrier scattering mechanisms [180, 181].

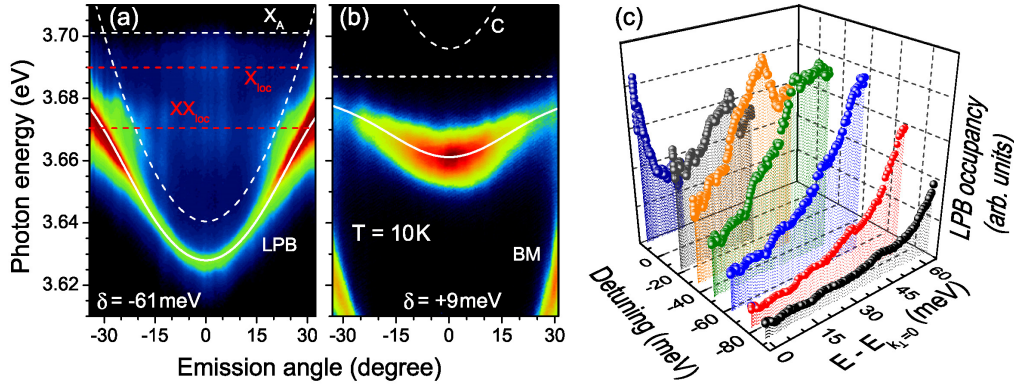


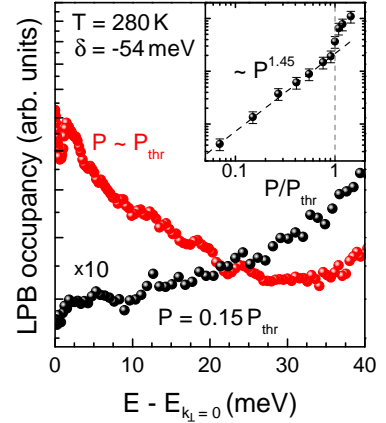
Figure 4.20: Angle-resolved PL-spectra of MC-1 measured at 10 K for a detuning (a) $\delta = -61$ meV and (b) $\delta = 9$ meV (arbitrary logarithmic color scale) taken from Ref. [69]. The spectra have been recorded under identical cw-excitation conditions with a low power density of 75 W/cm^2 . White solid lines mark the dispersion of the LPB, while the uncoupled modes are shown with white dashed lines. Localized exciton and biexciton states are well resolved (red dashed lines) for negative detuning in (a), while being absent for positive detuning values in (b). Here, leakage through BMs appears. (c) Experimentally determined LPB occupancy under equivalent excitation conditions for different δ -values.

under negative detuning conditions in Fig. 4.5(d) and the strongly increasing ground-state occupancy toward positive detuning values visible in Fig. 4.20(c), the optimum threshold conditions are expected to occur for small negative detunings. With increasing lattice temperature the scattering efficiency of polaritons increases due to a thermal acoustic-phonon population, shifting the optimum detuning conditions toward more negative δ -values (cf. Sec. 4.2.2).

The density-dependent effect of interparticle interactions can be followed in Fig. 4.21, that analyses the LPB occupancy of the Fourier-PL power-series shown in Figs. 4.29(e-g). This series was taken at $T = 280 \text{ K}$ close to the optimum detuning conditions ($\delta = -54$ meV). While the occupancy far below threshold remains non-thermal, limited by the relaxation kinetics, the increasing interparticle scattering efficiency succeeds in creating an almost thermal carrier population at threshold [180, 181]. Note that the deduced carrier temperature in the vicinity of the ground state ($T_{\text{car}} \approx 700 \text{ K}$) significantly exceeds the lattice one. This fact emphasizes the still present non-equilibrium character at the optimum detuning conditions, i.e. at the crossover between thermodynamic and kinetic relaxation regimes [26]. The density-dependent character of the interparticle scattering efficiency is further confirmed by the super-linear rise of the ground-state occupancy with excitation power below threshold [189], shown in the inset of Fig. 4.21.

Eventually, the formation of a polariton condensate requires a relaxation rate from the excitonic reservoir toward the ground state that exceeds the radiative decay rates of polaritons [260, 261]. Once the condensate is formed the standard relaxation path along the LPB via acoustic phonons and interparticle interactions is easily circumvented due to bosonic final-state stimulation that facilitates a macroscopic ground-state population. Nevertheless, it is worth noticing that even below threshold alternative channels may exist that allow a more efficient relaxation of polaritons toward the center of the BZ. This may particularly occur when

Figure 4.21: Analysis of the Fourier-PL power series displayed in Figs. 4.29(d-f): LPB occupancy as a function of the energy distance from the ground state for low injection (black) and pumping close to the threshold (red). The low-injection spectrum was multiplied by a factor of ten. The inset shows the evolution of the LPB ground-state occupancy as a function of the relative excitation power evidencing a super-linear rise below threshold.



the energy difference between a reservoir state and the bottom of the LPB is equal to the LO-phonon energy. Such a process was first evidenced in a CdTe-based MC [182], where for the resonance condition the threshold pump power decreased by a factor of about two. Very similar results have also been obtained for GaAs- and ZnO-based MCs [183, 262]. In view of the strong presence of biexcitons in the MC-1 active medium, this section aims at examining the influence of a biexciton population on the polariton relaxation. It is based on Ref. [69].

4.4.1 Biexcitons in the bare Quantum Wells

The existence of biexcitons in MQW-1 has already been partly discussed in the excitation power-dependent PL-studies presented in Figs. 3.7(a) and 3.27. This characterization shall be complemented here. Figure 4.22(b) shows spectral profiles of the QW luminescence taken at different delay times from the streak-camera image of Fig. 3.3(b). By replacing the microscope objective in the tr-PL setup scheme of Fig. 3.4 with a 10 cm focal lens, it was taken with a large spot size and thus a rather low excitation power. As expected from the mass-action law in Eq. (3.4), the biexciton luminescence on the low-energy side decays significantly faster than the high-energy exciton peak. This can also be followed when considering the respective intensity decays presented in Fig. 4.22(c). Similarly to the investigation of SQW-3, the biexcitonic decay follows the squared excitonic one after about 650 ps, indicating the achievement of thermalization between both populations. Apart from the different decay times, it is obvious that both emission bands show a certain redshift with increasing delay in Fig. 4.22(b), amounting to about 3 meV and 7 meV for the X and XX lines after 650 ps, respectively. Two effects have to be considered: QCSE-screening and carrier localization. They have been evidenced in the high-carrier density PL-experiments shown in Fig. 3.27 and the PLE-spectra shown in Fig. 3.7(a), respectively. To distinguish between both mechanisms, the QW-emission of the low-injection cw-PL temperature-series displayed in Fig. 3.7(b) has been carefully deconvoluted into X and XX-contributions yielding the temperature-dependent energy difference in PL shown in Fig. 4.22(a). Due to the low excitation power, i.e. $P \approx 175 \text{ W/cm}^2$ (cf. the power scale in Fig. 3.27), the influence of QCSE can be assumed to be marginal in these measurements. It is evident that the splitting between X and XX PL-lines increases with temperature. It starts from 16 meV at 4 K and reaches approximately 22 meV at 200 K, before the biexciton vanishes due to thermal dissociation. Assuming that at low temperature both, X and XX, are localized

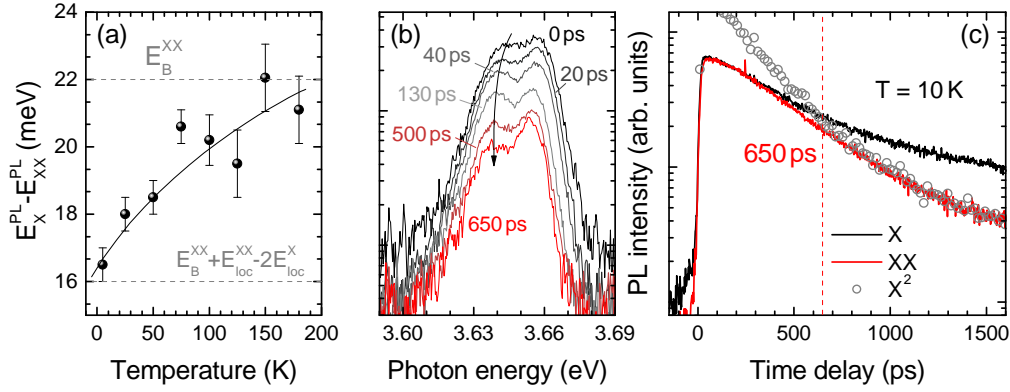


Figure 4.22: Additional studies of the biexciton in MQW-1 [69]: (a) Temperature-dependent energy difference between X and XX emission bands deduced from PL-spectra displayed in Fig. 3.7(b). The solid line is a guide to the eye. (b) QW-emission spectra at different time delays at $T = 10$ K taken from the streak-camera image shown in Fig. 3.3(b) showing the localization of XX. Corresponding intensity decays at the X and XX energies are shown in (c). At a time delay of about 650 ps both populations are thermalized according to Eq. (3.4).

the biexciton emission energy from Eq. (3.3) should be modified to [69]:

$$\begin{aligned} E_{\text{XX}}^{\text{PL}} &= (E_{\text{XX}} - E_{\text{loc}}^{\text{XX}}) - (E_X - E_{\text{loc}}^{\text{X}}) \\ &= E_X + E_{\text{loc}}^{\text{X}} - E_{\text{loc}}^{\text{XX}} - E_B^{\text{XX}}. \end{aligned} \quad (4.31)$$

In other words, the recombination of a biexciton with localization energy $E_{\text{loc}}^{\text{XX}}$ yields a photon of energy $E_{\text{XX}}^{\text{PL}}$ and leaves behind a localized exciton with energy: $E_X - E_{\text{loc}}^{\text{X}}$. The emission-energy splitting according to Fig. 4.22(a) is thus given by:

$$E_X^{\text{PL}} - E_{\text{XX}}^{\text{PL}} = (E_X - E_{\text{loc}}^{\text{XX}}) - E_{\text{XX}}^{\text{PL}} = E_B^{\text{XX}} + E_{\text{loc}}^{\text{XX}} - 2E_{\text{loc}}^{\text{X}}. \quad (4.32)$$

While this relation defines the energy splitting at 4 K, an increasing lattice temperature will cause the delocalization of X and XX carrier populations, i.e. $E_{\text{XX}}^{\text{PL}}$ will converge toward the ideal case of Eq. (3.3). Assuming $E_{\text{loc}}^{\text{X}} = 11$ meV as deduced from PLE-measurements and further that both carrier species are fully delocalized at $T = 200$ K, the present experiments can consistently be described using $E_B^{\text{XX}} = 22$ meV and $E_{\text{loc}}^{\text{XX}} = 16$ meV. Note that these values are absolutely consistent with an almost complete carrier delocalization at 200 K, as evidenced by simulations based on Saha's law given in Ref. [69].

Considering an exciton binding energy $E_B = 44$ meV as deduced from envelope function calculations in Sec. 3.2.3, Hayne's rule from Eq. (3.2) seems to be significantly violated with a value $E_B^{\text{XX}}/E_B \approx 0.5$ in these MQWs. This observation agrees with the studies in Refs. [88, 89], and confirms the mechanism of a disorder-enhanced biexciton binding energy [100, 263, 264].

4.4.2 Cavity Biexcitons

Apart from the LPB, two additional modes can be identified in the Fourier-space PL-image of Fig. 4.20(a). They are non-dispersive and feature an only weak emission intensity, being

located at energies of 3.661 and 3.69 eV, respectively. When performing measurements at even higher emission angles, they are observed to cross the LPB-dispersion without any obvious interaction (not shown here, cf. Ref. [108]). In order to identify the origin of these modes tr-PL measurements equivalent to those of Figs. 4.22(b,c) have been performed on MC-1 (cf. setup description in Sec. 3.1.2): the energy of the non-resonant picosecond excitation pulse was kept below 2 pJ, yielding a relatively low excitation density with a spot diameter of $\sim 50 \mu\text{m}$. The PL was collected with a narrow angular selection of 1° around $\mathbf{k}_\perp = 0$. The corresponding PL-decays are shown in Fig. 4.23 and resemble the X and XX decays recorded on MQW-1 in Fig. 4.22(c). The low-energy mode (XX) decays almost exponentially with $\tau_{XX} = 335 \text{ ps}$ and follows after $\sim 800 \text{ ps}$ the squared emission-intensity decay of the high-energy mode (X), which decays in a rather non-exponential manner. According to the predictions of the mass-action law given in Eq. (3.4), both modes are thus ascribed to the radiative decay of X and XX populations, respectively.

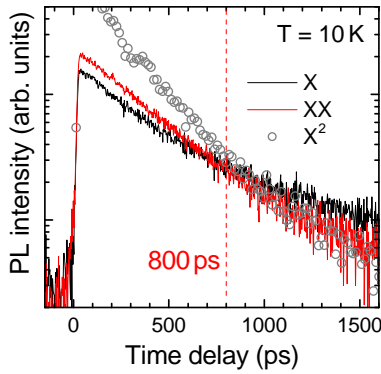
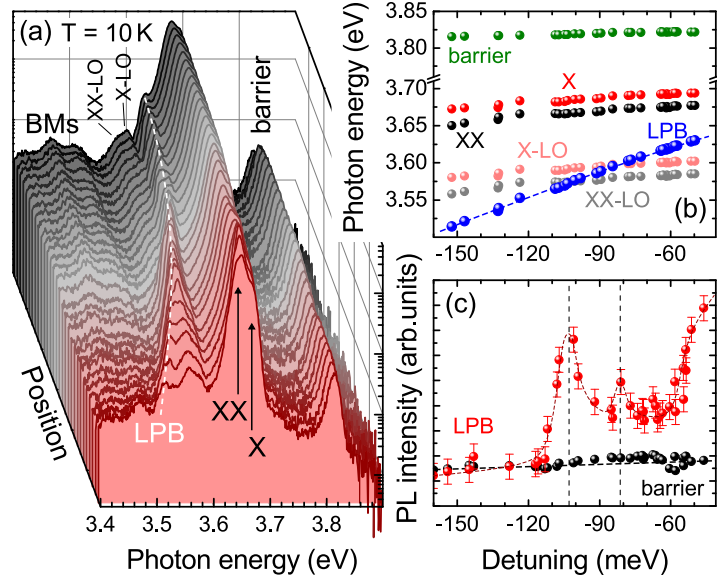


Figure 4.23: As for the decays measured for MQW-1 shown in Fig. 4.22(c), X and XX populations in MC-1 thermalize after a time delay between 600 and 800 ps (cf. also Fig. 4.25). The radiative decay of these states in a strongly-coupled MC is allowed due to certain non-idealities of the structure. Measurements were taken at $T = 10 \text{ K}$, $\delta = -61 \text{ meV}$, and $\mathbf{k}_\perp = 0$ with a large spot diameter $\sim 50 \mu\text{m}$. See text for details.

Closely linked to this observation, the question comes up how these modes can be observed in a MC that is with certainty in the SCR. Indeed, as already detailed in Sec. 4.3.3 the non-ideality of the structure, including the presence of QWs apart from the cavity-field antinodes and the inhomogeneous exciton linewidth lead to a partial sharing of oscillator strength between the bright polariton modes and the dark exciton modes [166, 265]. Thus, even if the MC preserves the SCR, dark excitons being ideally decoupled from the cavity mode may exhibit an optical signature in absorption, reflectivity, and PL experiments. In agreement with this discussion, there appears a weak reflectivity dip at the exciton energy in the TMS results of Fig. 4.19, that has also been observed experimentally in MC-1 [69].

As discussed in Ref. [265], uncoupled excitons in MC-1, that are initially created by the exponential absorption profile at the pumping wavelength, can efficiently bind into biexcitons. Note that contrary to the case examined in Ref. [266] these are in the WCR. Following their excitation both X and XX species can efficiently localize in the QW disorder landscape owing to their long lifetime, similarly to what has been observed for excitons in MQW-1. As both samples, MQW-1 and MC-1, were grown during the same run, the localization energies can be assumed to be very similar, in agreement with the observed energy splittings between free and localized excitons, and the localized biexcitons in Fig. 4.20(a). Note that the reflectivity between the LPB and the free-exciton energy in Fig. 4.19 remains below 100%, allowing localized X and XX populations to escape from the cavity.

Figure 4.24: Detuning dependent PL of MC-1 recorded at normal incidence at 10 K [69]: (a) PL-spectra as a function of sample position. The LPB dispersion is highlighted by the white line. (b) Emission energy of the barrier (green), X (red), XX (black), their respective LO-phonon replica (light red and gray), and the LPB as a function of δ . (c) Corresponding I_{PL} for the LPB (red) and the AlGaIn barrier (black). In (b,c) lines are guides to the eye.



4.4.3 Evidences of a Biexciton-mediated Polariton Relaxation

Once these cavity biexcitons are formed, they can radiatively recombine leaving either behind a dark exciton, a lower polariton, or an upper polariton. It is worth recalling that contrary to the light-cone restriction for excitons, biexcitons are allowed to recombine radiatively whatever their actual in-plane wave-vector. The excess momentum can simply be transferred to the remaining particle. Considering the heavy X and XX-masses and the limited extension of the light-cone, the most probable relaxation channels for biexcitons are those either leaving behind a dark exciton or a lower polariton in the reservoir. From this analysis the recombination path, that relies on a remaining upper polariton, can already be excluded since the cavity-biexciton emission should occur at much lower energies in such a case. In order to examine the relative weights of the different relaxation paths and the influence of cavity biexcitons on the polariton relaxation toward the condensation threshold, detuning-dependent experiments have been conducted.

Figure 4.24(a) shows the evolution of the time-integrated PL-spectra of MC-1 when scanning over the sample wedge. They have been recorded at zero in-plane momentum with the previously used tr-PL setup at 10 K. The excitation power density was kept constant during the scan, as evidenced by the constant PL-emission intensity of the $\text{Al}_{0.2}\text{Ga}_{0.8}\text{N}$ barrier centered around 3.82 eV (cf. black dots in Fig. 4.24(c)). Toward lower energy the dark exciton and biexciton luminescence can be identified, that give further rise to their respective LO-phonon replica located 92 meV below. At even lower energies BMs of the bottom-DBR appear that shift slightly with the wedge. The latter effect is much more pronounced for the LPB-emission that appears close to the biexciton band for sample regions with thinner cavity sections (black spectra) and moves toward more negative detuning when the cavity thickness increases. Note that it even crosses the LO-phonon replica of the uncoupled exciton and biexciton modes. This drift of the LPB energy can be nicely followed in Fig. 4.24(b), where the sample wedge has been translated to a detuning shift. The larger cavity thickness for more negative detuning values is confirmed by a slight exciton and biexciton energy redshift, issued from an increased QW-width. Conversely, the barrier emission stays at almost constant energy indicating that

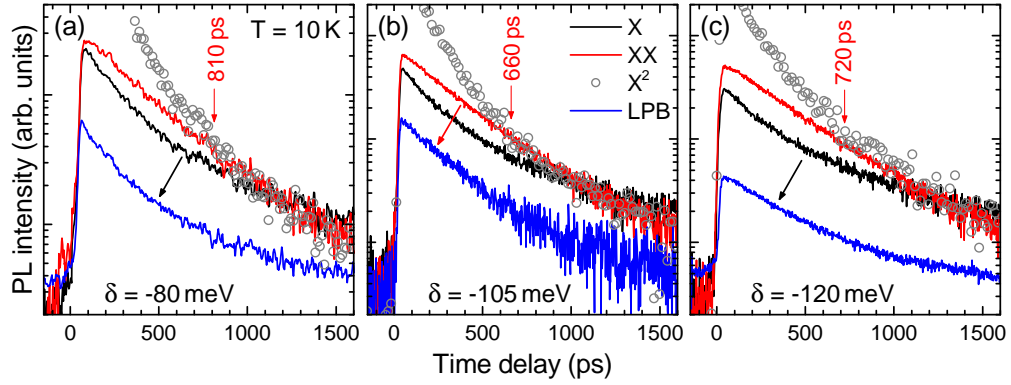


Figure 4.25: Low-temperature PL decays for the LPB (blue), X (black), and XX (red) emission bands in MC-1 recorded at $\mathbf{k}_\perp = 0$ for different detuning values: (a) $\delta = -80$ meV, (b) $\delta = -105$ meV, and (c) $\delta = -120$ meV. In (a) and (c) the LPB follows the same dynamics as X, while for $\delta = -105$ meV the LPB adapts to the XX recombination (indicated by black/red arrows). After a thermalization time ranging between 600 and 800 ps, the XX emission intensity follows the square of that of X (gray circles) for all detuning values.

the material composition remains constant.

In contrast to the barrier emission intensity that maintains a constant value with changing detuning, the evolution of the integrated LPB emission intensity displayed in Fig. 4.24(c) exhibits conspicuous modulations. Starting from the highest accessible detuning it first decreases before giving rise to two intensity maxima at $\delta = -80$ meV and $\delta = -105$ meV and subsequently converging toward zero for even more negative δ -values. Given that the behavior of the barrier emission is a good indicator for a constantly injected carrier density, the variation of the ground state population can directly be related to the polariton relaxation efficiency. The high occupancy at the most positive detuning values arises from the increased exciton fraction and the correspondingly enhanced scattering cross-section. Equally, the overall drop toward more negative detuning is due to the loss of the matter fraction of polaritons. The two PL-maxima emerging in between cannot be explained in this framework. However, when comparing the position of the peaks with the detuning-dependent LPB energy shift in Fig. 4.24(b), it appears that these intensity peaks occur when the LPB matches the energy of the exciton and biexciton LO-phonon replica at δ -values of -80 and -105 meV, respectively.

This observation is supported by the detuning dependent temporal decays of the different emission bands shown in Fig. 4.25. They have been measured using the same experimental configuration as the data shown in Figs. 4.22(b,c) and 4.23. For every accessible detuning in MC-1, X and XX populations thermalize within a time delay between 600 and 800 ps, confirming the excitonic and biexcitonic identities of these emission bands. Contrary to the previous experiments, Fig. 4.25 additionally shows the decay of the LPB. For almost the entire accessible detuning range, it follows the dynamics of the exciton and thus of the polariton reservoir, e.g. for $\delta = -80$ meV and $\delta = -120$ meV shown in Figs. 4.25(a,c). Indeed, due to the short lifetime of polaritons at the bottom of the LPB (< 1 ps), their decay can be assumed to occur instantaneously within the exciton decay time-scale. Thus, the ground-state occupancy is simply imprinted by the feeding reservoir population. However, for $\delta = -105$ meV the situa-

tion appears to be different: the LPB clearly follows the exponential decay of the biexciton population.

Conclusively, the enhancement of the LPB ground-state occupancy at a detuning of -105 meV seems to originate from the LO-phonon assisted radiative dissociation of cavity biexcitons, either leaving behind an exciton or a lower polariton (LP) of high in-plane wave-vector:

$$\begin{aligned} XX &\rightarrow LP(\mathbf{k}_\perp = 0) + LO + X, & \text{or} \\ XX &\rightarrow LP(\mathbf{k}_\perp = 0) + LO + LP(\mathbf{k}_\perp \gg 0). \end{aligned} \quad (4.33)$$

In the same manner, the intensity increase at $\delta = -80$ meV can be ascribed to the feeding of the LPB ground state from the exciton reservoir due to LO-phonon resonance conditions, i.e. $X \rightarrow LP(\mathbf{k}_\perp = 0) + LO$, similar to what has first been observed in CdTe-based MCs [182]. These interpretations are in complete agreement with the detuning-dependent evolution of the polariton lasing threshold in Fig. 4.26, that was measured at 4 K using non-resonant excitation with the Nd:YAG laser and a large spot diameter of $50\mu\text{m}$. According to the discussion of the LPB occupancy from Fig. 4.24(c) and the condensation phase-diagram in Fig. 4.11(b), the threshold globally increases toward more negative values based on the limiting polariton relaxation kinetics. Nevertheless, despite the noise issued from the photonic disorder two minima can be identified, that benefit from the resonance conditions $XX - LO = LP(\mathbf{k}_\perp = 0)$ and $X - LO = LP(\mathbf{k}_\perp = 0)$.

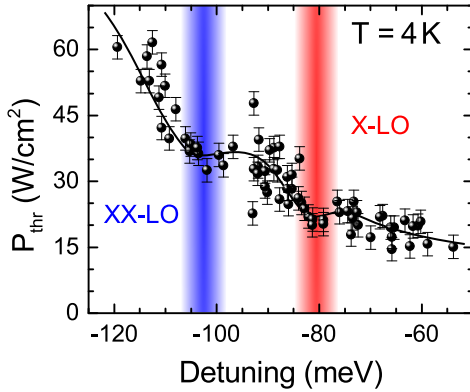


Figure 4.26: Polariton lasing threshold power density (P_{thr}) measured at 4 K under non-resonant pumping with the Nd:YAG laser as a function of detuning [69]. Two local minima in P_{thr} are observed when $\delta = -80$ meV and $\delta = -105$ meV. The black line is a guide to the eye.

It is worth mentioning that in Ref. [69] the direct feeding of the LPB ground state from a cavity biexciton population has been evidenced for the first time, whereas the LO-phonon assisted transfer from the exciton reservoir can be commonly observed [182, 183, 262]. Biexcitons in strongly-coupled MCs are expected to strongly interact with the polariton population and may alter the light-matter coupling. A deeper insight into such properties is thus of fundamental interest. For instance, under resonant excitation conditions the presence of biexcitons has been evidenced to initiate a progressive transfer of oscillator strength from the exciton-polaritons to the favor of biexciton polaritons with increasing carrier injection [266]. Moreover, the formation of biexcitons composed of two excitons with opposite spins was shown to detrimentally impact on the light-matter coupling by creating a non-linear loss term, while favoring a certain spin state at the expense of the other one [201]. Based on such fundamental impact, it appears essential to include the biexcitonic state in the usual framework describing interactions occurring within a polariton population. Indeed, whereas in the common picture the value of repulsive forces in between polaritons of equal spin is

assumed to exceed the attractive potential between polariton pairs of opposite spin [137], an attractive biexciton-mediated interaction may significantly modify this balance [225, 267]. Furthermore, the presence of biexcitons is also expected to increase the interparticle scattering efficiency by introducing a transient biexcitonic singlet-state [187]. In the end, based on the strong biexciton presence III-nitride based MCs could serve as a suitable playground for further experimental studies concerning cavity biexcitons.

4.5 Polariton Renormalization

One of the most striking characteristics of cavity-polaritons is their ability to interact, which stems from their excitonic matter component. Apart from the previously-discussed issues [179], this facilitates carrier thermalization and the eventual formation of polariton condensates [17, 22, 204]. Note however that the experiments and the corresponding analysis discussed in Ch. 3 evidenced that the excitonic properties are not invariant when the carrier density is increased, but can be significantly altered when approaching the MT. More precisely, based on the combined effects of Coulomb-interaction and PSF [113], the exciton energy E_X , its corresponding homogeneous linewidth γ_X , and the oscillator strength f_X may be renormalized. When a semiconductor MC is operated in such a carrier-density regime the varying exciton properties would directly impact the light-matter coupling and correspondingly modify the polariton properties, ultimately leading to the loss of the SCR across the MT when f_X tends to zero or γ_X overcomes the Rabi-splitting.

Material	GaAs	CdTe	GaN	ZnO	Anthracene
Reference	[238]	[17]	[23]	[207]	[205]
$(\Omega/E_B)^2$	0.22	0.09	0.09	0.29	< 0.01

Table 4.2: Theoretical impact of saturation for MCs based on different material systems following Ref. [140].

In the commonly considered framework, particularly applied to GaAs- and CdTe-based MCs, it is often assumed that saturation effects due to PSF or Coulomb-exchange interaction can be omitted in the renormalization of the polariton properties. In other words, the frequently observed blueshift of the LPB ground state is usually ascribed to an interaction-based blueshift of the exciton resonance [204, 225, 268], while a decrease of f_X is neglected based on an earlier theoretical work [140]. In the latter the ratio between the different contributions of saturation and interaction to the polariton renormalization was traced back to a scalable material and sample-dependent quantity: $(\Omega/E_B)^2$. Note that at the time of this publication, polariton-related non-linear effects had only recently been observed experimentally [16], and that this ratio has been derived for the zero-temperature case and shows no strong density dependence. It may thus not apply to realistic systems. Moreover, when considering a few recent MC-examples based on different materials, the calculated fraction of saturation-driven polariton renormalization appears far from being negligible (cf. Tab. 4.2). This fact and the universality of the MT occurring in semiconductor QWs across different material systems (cf. Ch. 3) raised the motivation to investigate the modification of the polariton properties under the influence of an increasing carrier density in more detail.

A deeper insight into the polariton renormalization mechanisms, below and above the condensation threshold, seems further essential for completing the description of the interactions

driving polariton relaxation and promoting the eventual formation of a condensate. Specific problems may for instance arise when the ground state population, stating an absolute key parameter in the description of polariton-related non-linear effects, is derived based on the LPB energy shift at normal incidence $\Delta E_{\text{LP}}(\mathbf{k}_{\perp} = 0) = \Delta E_{\text{LP},0}$ [260, 268]. Such a description would only be valid in the bosonic limit when $\Delta E_{\text{LP},0}$ is exclusively issued from the density-dependence of the chemical potential $\mu(n_0)$, with n_0 marking the polariton ground state population. In a scenario where various mechanisms contribute to $\Delta E_{\text{LP},0}$, this approach would inevitably result in an overestimation of the condensate occupancy. The examination of the correct ratio between saturation and interaction-induced $\Delta E_{\text{LP},0}$ becomes also important when considering polariton fluids [19], that may be decoupled from the reservoir: here, a density-dependent change of the polariton dispersion would cause a strongly spatially and time-dependent polariton mass, which could have profound consequences for the physics of polariton fluids.

The upcoming discussion aims at transferring the knowledge about the modification of the QW-exciton in the high-carrier density regime from Ch. 3 to the physics of strongly-coupled III-nitride based MCs. In major parts it is based on Ref. [104] and will focus on the renormalization of the LPB studied below threshold in MC-1 under non-resonant optical injection with the pulsed Nd:YAG laser. Depending on the focusing lens the probed spot diameter amounts to 5 or 50 μm for the Fourier-space PL measurements with the UV objective and for $\mathbf{k}_{\perp} = 0$ PL measurements with a 10 cm focal lens (NA = 0.02, cf. Fig. 4.18), respectively.

4.5.1 Exciton Saturation in the Coupled-Oscillator Model

As detailed in Sec. 3.3.1, the dielectric response of the exciton according to Eq. (2.31) is not invariant in presence of a sufficiently high carrier density n . Various effects, such as QCSE-screening or Coulomb-interaction, can cause a shift of the resonance energy, collisional-induced broadening affects the homogeneous linewidth γ_X , and when approaching the Mott-density n_{crit} the exciton oscillator strength f_X will ultimately vanish. Before proceeding to the experimental parts, the impact of exciton renormalization on the polariton dispersion shall be discussed based on the COM from Eq. (4.21). In the following zero-subscripted physical quantities will denominate the values at zero carrier density, e.g. in presence of a finite carrier density the polariton branches according to Eq. (4.19) will undergo a transformation:

$$E_{\text{LP}}(n=0) = E_{\text{LP},0} \xrightarrow{\Delta E_{\text{LP}}} E_{\text{LP}}(n) \quad \text{and} \quad E_{\text{UP}}(n=0) = E_{\text{UP},0} \xrightarrow{\Delta E_{\text{UP}}} E_{\text{UP}}(n).$$

Figure 4.27 shows the polariton eigenmode spectrum using realistic zero carrier-density values for MC-1 at room temperature: $E_X = 3.631 \text{ eV}$, $\gamma_X = 25 \text{ meV}$, $\delta = -15 \text{ meV}$, an effective cavity refractive index $n_{\text{eff}} = 2.65$, $\gamma_C = 4 \text{ meV}$, and a coupling strength $g_0 = g(n=0) = 30 \text{ meV}$ [168]. The polariton modes for $n = 0$ are in all sub-figures given in black and exhibit a minimum initial energy splitting $\Omega_0 = 56 \text{ meV}$. The latter value is reduced with respect to $2g_0$ owing to the finite mode linewidths.⁸

The impact of an exciton energy that was arbitrarily shifted by $\Delta E_X = 3.5 \text{ meV}$ is shown in Fig. 4.27(a). Note that based on the general observation of an LPB blueshift with increasing n , the case $\Delta E_X < 0$ shall be neglected in the following. Assuming that the cavity mode remains

⁸Contrary to Sec. 4.1.2, here Ω_0 already contains the influence of a finite mode linewidth according to Eq. (4.22).

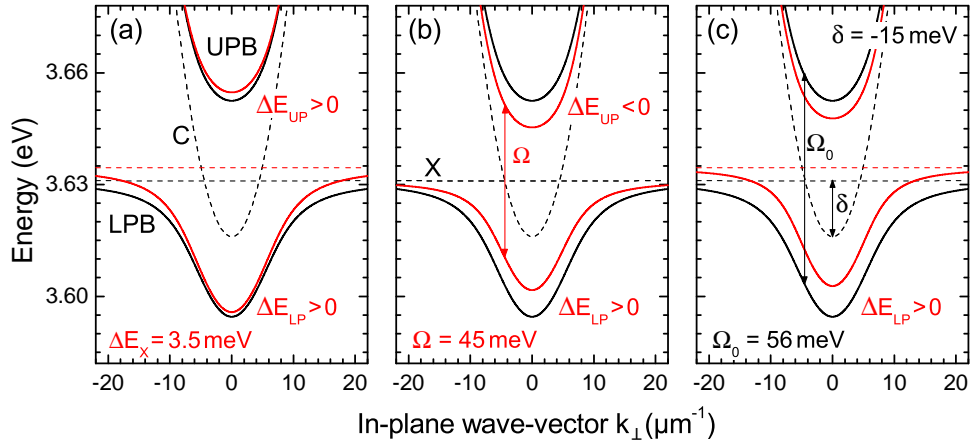


Figure 4.27: Modeling of the polariton dispersion renormalization with COM based on MC-1 with $\delta = -15$ meV at RT. Zero-density dispersions are shown in black: polariton modes (LPB, UPB) with solid lines and uncoupled modes (C, X) with dashed lines. Renormalized modes are correspondingly given in red: (a) impact of an exciton blueshift $\Delta E_X = 3.5$ meV, (b) decrease of the initial Rabi-splitting Ω_0 down to $\Omega = 45$ meV, and (c) combination of both effects.

unaffected, an exciton blueshift simply causes a change of the detuning δ . Both polariton branches are displaced by ΔE_X weighted with the in-plane momentum dependent excitonic fraction $|F_X|^2$, that is for the LPB defined by:

$$|F_X(\mathbf{k}_\perp)|^2 = \Omega^2 / \left(\Omega^2 + 4[E_{LP}(\mathbf{k}_\perp) - E_X(\mathbf{k}_\perp)]^2 \right). \quad (4.34)$$

Under negative detuning conditions, this only causes a marginal shift around zero in-plane momentum for the LPB, whereas the high- \mathbf{k}_\perp excitonic part is much more affected. It is worth pointing out that both LPB and UPB undergo a blueshift for $\Delta E_X > 0$.

As obvious from Fig. 4.27(b), the situation changes when an increasing γ_X or a decreasing f_X are considered. The polariton dispersion is subject to a decreasing Rabi-splitting $\Omega_0 \rightarrow \Omega$, while the uncoupled exciton and photon modes remain unchanged. In the following such a scenario will be referred to as saturation-induced polariton renormalization. If γ_X is affected, the Ω -reduction follows directly from Eq. (4.22), while a decrease of the exciton oscillator strength affects the light-matter coupling constant according to Eq. (4.16): $g_0 \rightarrow g$. Note that a PSF-induced f_X -change will also cause a lowering of the refractive index of the active material according to the Kramers-Kronig relation in Eq. (2.37). In extreme cases, primarily in bulk active media, this may alter the cavity-mode dispersion leading to an apparent blueshift. However, in the present situation, these effects are assumed to be marginal due to the limited amount of active material in a QW-based cavity spacer and the moderate injection regime. In Fig. 4.27(b) the Rabi-splitting was artificially decreased down to 45 meV. This could either be realized by a reduction in f_X of 30% or alternatively by an increased exciton linewidth of $\gamma_X = 44$ meV. Contrary to the case of an exciton blueshift, saturation causes opposite shifts to the polariton branches: $\Delta E_{LP} > 0$ and $\Delta E_{UP} < 0$, the absolute value of the displacement being set by the in-plane momentum dependent detuning. It is maximal for the resonance condition $E_X = E_C$.

Finally, Fig. 4.27(c) shows the combination of both renormalization effects. Interestingly, ΔE_{LP} appears rather independent of the in-plane momentum, i.e. the summed contribution of ΔE_X and saturation compensates the \mathbf{k}_\perp -dependence of the single components. This finding is purely fortuitous depending on the respective weights of both effects and the actual δ -value, but it emphasizes the varying impacts and confirms previous experimental observations on MC-1 [25].

Despite the oversimplification of the MC structure in the COM (cf. Sec. 4.1.2), it is employed here as a suitable toolbox to analyze the linear emission regime under non-resonant optical pumping, where the LPB renormalization is mainly issued from the excitonic reservoir and the ground-state occupancy remains negligible [269]. On the contrary, significantly above threshold the macroscopic condensate population is supposed to dominate the LPB ground-state renormalization and should be carefully taken into consideration. Indeed, theoretical studies based on the mean-field approximation [212], or following a semi-classical Boltzmann formalism [171], give reason to expect a strict clamping of the reservoir population above the condensation threshold to a certain value n_{thr}^* , in analogy to the saturation of the excited states in BEC-theory [17]. At the same time, the condensate occupancy n_0 increases linearly with injection: $n_0 \propto (n - n_{\text{thr}}^*)/\gamma_C$. Despite the different physical origin, this situation resembles the operating conditions of a semiconductor LD above threshold, when identifying n_0 with the photon field and n_{thr}^* with the inverted e-h population [171].

Saturation of the Exciton Oscillator Strength

While Fig. 4.27 only showed the fundamental influences of the exciton non-linearities on the polariton eigenmodes, a comprehensive analysis of their renormalization requires a detailed knowledge about the scaling of f_X , ΔE_X , and γ_X with carrier injection. The last two quantities could be tracked in the MT-study of Ch. 3: up to the MT the exciton energy remains at almost constant energy except for a slight shift due to QCSE-screening, and the collision-induced broadening moderately appears about one order of magnitude below n_{crit} . By contrast, from these experiments no conclusion could be drawn on the evolution of f_X . The dependency $f_{\text{osc}}(n)$ shown in Fig. 3.28(b), which has been computed based on the E_{BGR} modeling and Eq. (2.46), remains purely theoretical, in particular in view of Ref. [131] that described a remarkable constancy of the e-h bandgap energy below MT.

Different $f_X(n)$ -scalings have been proposed in the literature. Figure 4.28 compares the result of Fig. 3.28(b) in f_{osc} and $g/g_0 \propto \sqrt{f_{\text{osc}}}$ with a selection of them, that shall be briefly noted hereafter: a straightforward approach consists in assuming a linear reduction of f_X with carrier density as adopted in Refs. [113, 152]. Alternatively, Utsunomiya and co-workers assumed a linear reduction of the light-matter coupling strength g with increasing density for modeling their data [138], unfortunately without providing any theoretical basis. In both former cases the saturation density n_{sat} that causes vanishing of f_X coincides with n_{crit} describing the MT, equivalently to the result of Fig. 3.28(b). Conversely, the empirical saturation relation proposed by Refs. [115, 185] sets n_{sat} to the carrier density at which f_X is reduced to half its initial value:

$$f_X(n) = \frac{f_{X,0}}{1 + n/n_{\text{sat}}} \quad \text{or equivalently} \quad g(n) = g_0 \sqrt{\frac{1}{1 + n/n_{\text{sat}}}}. \quad (4.35)$$

Here, it holds $f_{X,0} = f_X(n=0)$ and f_{osc} is defined by $f_X(n) = f_{\text{osc}}(n) f_{X,0}$. Obviously, in this

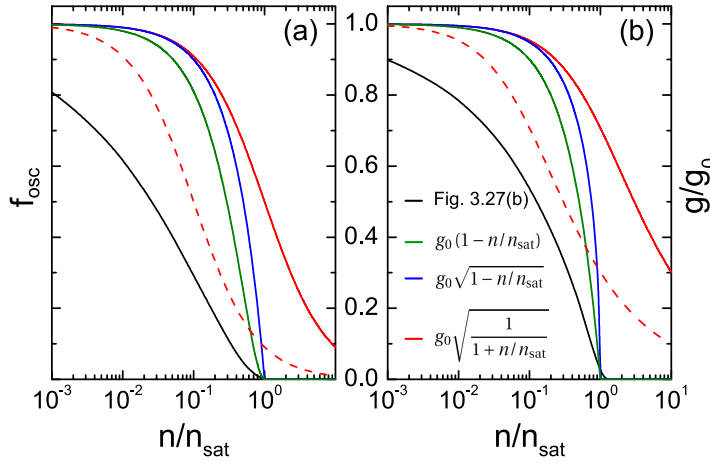


Figure 4.28: (a) Different scaling proposals for f_{osc} with increasing QW carrier density n according to: Ref. [138] (green), Ref. [152] (blue), Ref. [115] (red), and Eq. (2.46) and Fig. 3.28(b) (black). The red dashed line also corresponds to Ref. [115], but with n_{sat} shifted by a factor of ten. (b) Corresponding evolution of the normalized light-matter coupling strength g .

case n_{sat} does not define the MT, but should be significantly smaller than n_{crit} as exemplarily shown by the red dashed line in Fig. 4.28. It is further evident that g and f_X in Eq. (4.35) only converge to zero for an infinite carrier density. The loss of the SCR would thus require a finite mode linewidth according to the definition of the Rabi-splitting in Eq. (4.22).

While the renormalization of the exciton oscillator strength could not be observed in the PL-study of Ch. 3, the power-dependence of the Rabi-splitting in a strongly-coupled MC should give direct access to f_X based on Eq. (4.16). Thus, the evaluation of the various $f_X(n)$ -scaling proposals will follow based on the examination of the experimental results reported hereafter.

4.5.2 Experimental Results

The wide range of accessible δ -values in MC-1, ranging from about -120 up to 10 meV, in combination with measurements of the far-field emission allows probing very photon-like states at the bottom of the LPB and very exciton-like ones at higher emission angles at the same time. Thus, effects associated to a drop of the light-matter coupling strength or to an exciton energy shift can easily be distinguished, which facilitates a comprehensive analysis of the renormalization mechanisms. Figure 4.29 shows angle-resolved PL power-series performed up to the polariton condensation threshold for two different $\{\delta, T\}$ combinations, i.e. $\{-5 \text{ meV}, 40 \text{ K}\}$ and $\{-54 \text{ meV}, 280 \text{ K}\}$. These two series represent a large number of measurements at various $\{\delta, T\}$, that all behave in a very similar manner.

The LPB dominates the spectrum and features a pronounced blueshift when the excitation power density is raised. The power-dependent modification of the polariton dispersion has been analyzed within the aforementioned COM yielding an accurate fitting only when a reduction of the Rabi-splitting was considered. Indeed, while the LPB energy shift is particularly well-marked around zero in-plane momentum, it is hardly observed at higher angles. Based on the previous COM-discussion, a large blueshift of the QW-exciton can thus be excluded in absolute agreement with the experimental findings of Ch. 3. This is especially true for the negative detuning series at 280 K shown in Figs. 4.29(e-g): the LPB ground state is characterized by an excitonic fraction of around 18% and exhibits a blueshift of $\sim 6 \text{ meV}$ up to threshold. Modeling this while neglecting any impact of saturation requires a ΔE_X value exceeding 30 meV ,

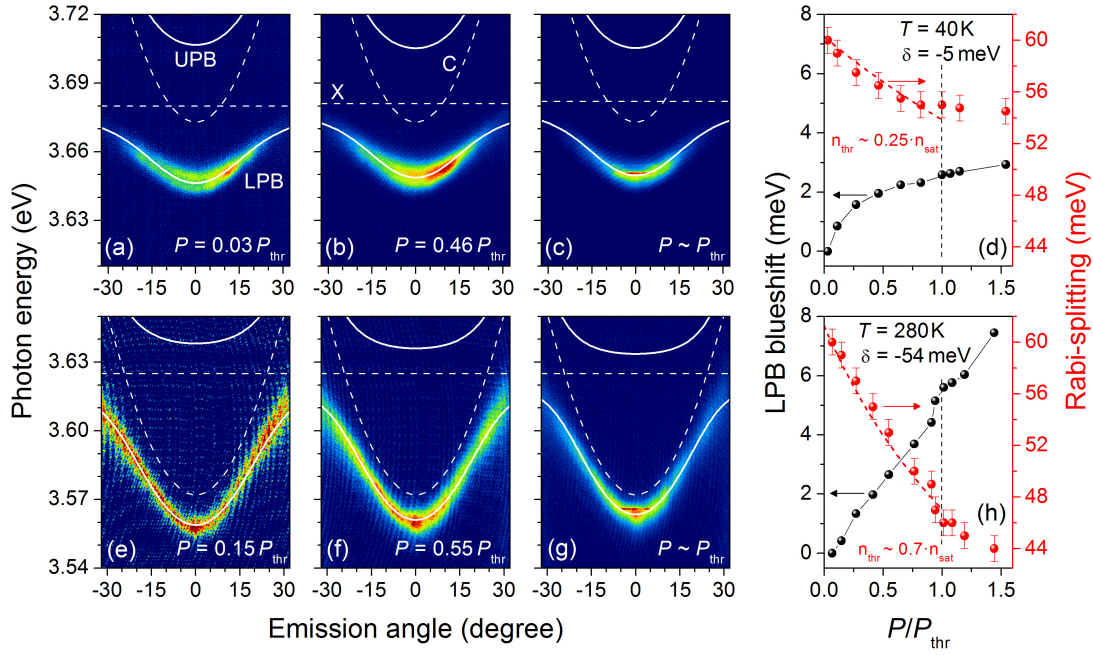


Figure 4.29: Power-dependent Fourier-space PL-patterns of MC-1 recorded under non-resonant pulsed excitation at (a-c) 40 K for $\delta = -5$ meV and (e-g) 280 K for $\delta = -54$ meV. Taken from Ref. [104]. Dashed and solid lines highlight the uncoupled and polariton modes, respectively. The corresponding power-dependent evolution of the LPB blueshift and the fitted Rabi-splitting are displayed in (d) and (h). Therein, red dashed lines reproduce the expected Ω -reduction from the COM-modeling, while accounting for different threshold carrier densities. See text for details.

which represents a clear contradiction with the present experiments and the MT as reported in Ch. 3. It can thus be stated that renormalization in MC-1 is dominated by saturation effects.

In order to distinguish between the respective weights of collisional-induced exciton broadening and f_X saturation, the linewidth of the LPB γ_{LPB} shall be inspected in more detail. The low temperature series shown in Figs. 4.29(a-c) features a rather thermal branch occupancy and a significant excitonic fraction $\sim 45\%$ of the ground state. Nevertheless, no significant γ_{LPB} changes can be traced up to the threshold, the linewidth remaining constant at (10 ± 0.5) meV. In comparison, the high-temperature series behaves in a slightly different manner. Owing to the very photon-like ground state it is convenient to examine γ_{LPB} at high momentum. For $\Theta_{\text{ext}} = 30^\circ$ the LPB linewidth rises from 16 to about 19 meV at the polariton lasing threshold. Considering the local Q -factor ~ 600 and a homogeneous exciton linewidth around 25 meV, the increase of γ_X can be estimated by the COM to about 5 meV in this case. Such moderate, or for the low-temperature series even negligible, values may only explain an Ω -reduction of about 1 meV and are in complete agreement with the previous analysis of the MT. Having eliminated γ_X and ΔE_X as potential origins, the polariton renormalization in this sample appears to be clearly driven by exciton saturation, or more precisely by a decrease of f_X with rising carrier injection.

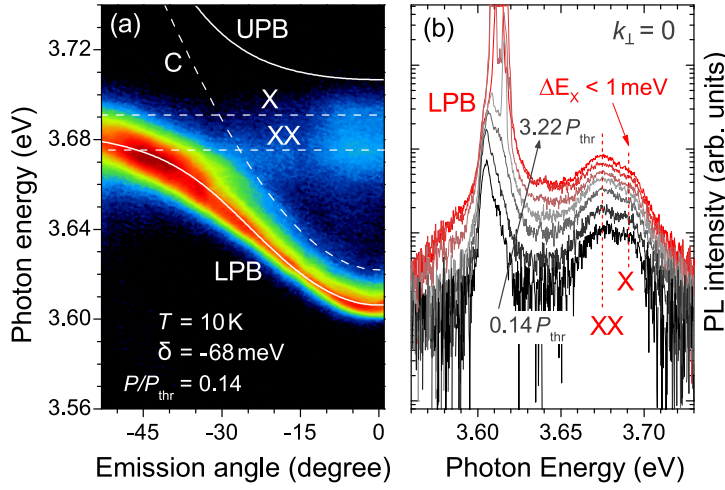


Figure 4.30: (a) Fourier-space PL-image of MC-1 measured at 10 K for $\delta = -68\text{ meV}$ below the polariton lasing threshold. Dashed and solid lines mark the uncoupled and polariton modes, respectively. (b) Spectral profiles at $\mathbf{k}_{\perp} = 0$ recorded at the same spot under identical excitation conditions for an injection ranging from 0.14 to $3.22P_{\text{thr}}$. The position of X and XX lines is highlighted with red dashed lines. From Ref. [104].

It is further worth emphasizing that the SCR is preserved over the entire explored injection range: the LPB at $\mathbf{k}_{\perp} = 0$ remains well below the cavity mode energy and its dispersion invariantly exhibits the characteristic inflection point. Another interesting feature, which is commonly observed and especially pronounced for the $T = 40\text{ K}$ power-series, consists in the remarkable slow-down of the Ω -decrease that is observed once the threshold has been crossed. This is likely due to the clamping of the reservoir population and the decrease of the mean polariton lifetime owing to a significant ground-state population [171, 212], which decreases the slope of n with excitation power. Such an observation hints toward a polariton renormalization that is predominantly driven by the population of the reservoir, in agreement with polariton-propagation experiments performed in GaAs-based MCs [269–271], and the findings of Ref. [272] to be discussed in Sec. 4.7.

Further evidences for a saturation-dominated polariton renormalization can be found when considering that certain non-idealities in the structure of MC-1 allow to probe excitonic properties while being in the SCR by means of optical measurements (cf. Sec. 4.4). Although most of this dark exciton signal in PL-measurements stems from uncoupled QWs, the latter are expected to be significantly populated according to the laser penetration depth of $\sim 100\text{ nm}$, which determines the initial distribution of carriers over the uniform QW-barrier SL in the cavity section.

Figure 4.30(a) displays the far-field emission of MC-1 up to high angles for a moderately-injected spot with $\delta = -68\text{ meV}$ at low-temperature. Apart from the LPB, that exhibits a clear inflection point, dark exciton and biexciton signatures are observed. Their injection-dependent behavior is revealed in the spectral profiles at $\mathbf{k}_{\perp} = 0$ shown in Fig. 4.30(b). No significant changes in the dark exciton PL-signal can be spotted over the whole injection range up to $3.22P_{\text{thr}}$. When deconvoluting the X and XX contributions, an exciton energy shift in excess of 1 meV can be excluded in agreement with the findings for MQW-1 shown in Fig. 3.27. Moreover, the high-energy tail of the X-emission shows no significant variations, indicating a sub-MT injection and a minor influence of collisional-induced broadening.

4.5.3 Impacts of a Saturation-dominated Polariton Renormalization

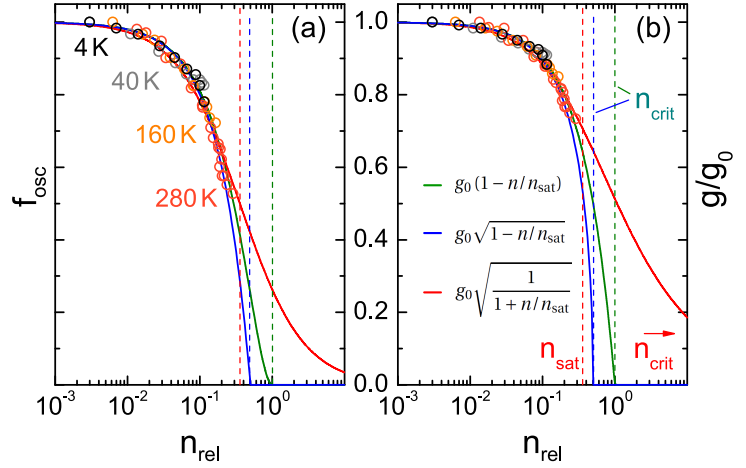
Eventually, it appears obvious that in agreement with Ref. [25] the polariton renormalization in MC-1 is fully dominated by a decreasing Rabi-splitting. Only marginal blueshifts $\delta E_X < 2 \text{ meV}$ due to QCSE-screening could be traced in Figs. 4.29(a-c) and 4.30(b). Evaluating the respective influences of exciton blueshift and oscillator strength saturation for the whole accessible $\{\delta, T\}$ -range based on the COM yields a saturation impact that is generally in excess of 90%. Thus, ΔE_X can widely be neglected. In the following the density-dependence of f_{osc} and the impact of a $\{\delta, T\}$ -dependent condensation threshold according to Sec. 4.2.2 shall be discussed in more detail.

Conclusion on the Exciton Oscillator Strength Scaling

Each PL power-series such as shown in Fig. 4.29 allows to access the power-dependent decrease of Ω (cf. Figs. 4.29(d,h)), that can be easily translated into a scaling of f_{osc} with excitation power density P based on Eq. (4.16). Here, the actual difficulty stems from the unknown relation between P and n , defined by the IQE and the mean particle lifetime. Indeed, while the absolute carrier density could be revealed based on a sophisticated lineshape analysis in a simple SQW-system beyond n_{crit} in Ch. 3, an exact determination of n in a complex structure such as MC-1 is prevented in many aspects. First, all drawbacks inherited from an inhomogeneous carrier injection, both spatially and temporally due to the pulsed excitation source, as discussed for MQW-1 in Sec. 3.5, apply in the same manner for MC-1. Note here that the population of radiative exciton-polaritons may indeed be equilibrated in the cavity region due to Rabi-oscillations, but that at the same time dark excitons remain predominantly distributed according to the absorption profile at the laser wavelength. Moreover, with respect to the analysis drawn in Fig. 3.8 and the power-series of MQW-1 in Fig. 3.27, that shows a strict linearity for the QW and barrier I_{PL} with P over several orders of magnitude, it is known that at low temperature the IQE of the MQW-1 QW-barrier system remains close to 100% regardless of n . Thus, one can reasonably assume the proportionality $n \propto P$ at 4 K. However, for higher temperatures this statement must be partly reconsidered owing to the effect visible in Fig. 3.20: the progressive activation of non-radiative recombination channels decreases the IQE and causes a pronounced power-dependence due to the saturation of certain recombination centers. This leads to a super-linear increase of n and I_{PL} with excitation power at elevated temperatures, which can also be followed from the power-dependent IQE increase at 300 K shown in the inset of Fig. 3.8. The whole situation is additionally complicated by the mean particle lifetime that may be changed in a polariton system when carrier relaxation occurs along the LPB toward the center of the BZ. Note however that this becomes particularly effective beyond the threshold P_{thr} , when the ground-state population rises dramatically, and is expected to be much less pronounced below the latter. Here, the major part of injected carriers populates the reservoir, while the LPB occupancy remains limited due to the relaxation bottleneck. Hence, the overall polariton lifetime sticks to the excitonic one [69], and for a certain T the proportionality between n and P can be reasonably assumed.

In summary, an accurate examination of the relation between excitation power and carrier density in such a complicated system appears clearly out of reach. In order to gain a qualitative insight despite the above-mentioned complexity, in an oversimplified approach the proportionality $n \propto P$ shall be assumed for all P and T -values, in line with the treatment

Figure 4.31: (a) $f_{\text{osc}}(n)$ for multiple Fourier-PL P -series at different T (circles) as deduced from the reduction of Ω assuming $n \propto P$. Proposed $f_{\text{osc}}(n)$ -scalings of Ref. [138] (green), Ref. [152] (blue), and Ref. [115] (red) are shown for comparison with adjusted n_{sat} -values to reproduce the data (vertical dashed lines). (b) Corresponding evolution of g/g_0 .



shown in Ref. [26]. Figure 4.31 shows values of the oscillator and coupling strength gathered in a variety of Fourier-PL power-series for different $\{\delta, T\}$ combinations as a function of a relative carrier density n_{rel} , that was arbitrarily adjusted in between the different series to obtain a continuous evolution. These data appear astonishingly consistent and exclude the scaling proposed in Fig. 3.28(b): the disappearance of f_{osc} seems to occur much more abrupt than the decrease of E_{B} modeled via E_{BGR} estimates. Note that this does not necessarily put a question mark on Eq. (2.46), but rather calls for a comprehensive theory of BGR in presence of an exciton-dominated carrier population. By contrast, all other f_{osc} -scaling proposals from Refs. [115, 138, 152] are able to reproduce the experimental data within the experimental error margins, when the ratio $n_{\text{sat}}/n_{\text{rel}}$ is adjusted. Their respective intersections with $f_{\text{osc}} = 0$ set the confidence region for n_{crit} : in the most pessimistic scenario given by Ref. [152] the experimental point with the lowest f_{osc} corresponding to the condensation threshold of a $\{-28 \text{ meV}, 280 \text{ K}\}$ series would be separated by about a factor of two from n_{crit} . Note that even in this case the SCR does not need to be lost at twice the threshold: owing to the decreasing mean particle lifetime of the system the proportionality between P and n is relieved in favor of a sub-linear power-scaling of n .

In the end, all three $f_{\text{osc}}(n)$ predictions would yield very similar results within the explored power-density range below threshold. In the following, all modeling data will thus refer to the law given by Eq. (4.35) and Ref. [115]. It has been experimentally confirmed and seems appropriate for describing the continuously occurring MT evidenced in Ch. 3. It is worth pointing out once more that in this case $n_{\text{sat}} < n_{\text{crit}}$, while the exact ratio between them remains to be evaluated.

Impact of the Condensation Phase Diagram

In Figs. 4.29(d,h), the experimentally determined decrease of the Rabi-splitting has been fitted with the COM and Eq. (4.35) neglecting any variation of E_{X} or γ_{X} and leaving the ratio $n_{\text{thr}}/n_{\text{sat}}$ as the unique adjustable parameter. The agreement is quite accurate and yields threshold carrier densities n_{thr} situated below but close to n_{sat} : $0.25n_{\text{sat}}$ and $0.7n_{\text{sat}}$ for the $\{-5 \text{ meV}, 40 \text{ K}\}$ and $\{-54 \text{ meV}, 280 \text{ K}\}$ power-series, respectively. The ultimate drop of Ω at threshold is in this case simply given by n_{thr} , which in turn crucially depends on the $\{\delta, T\}$ combination via the condensation phase diagram shown in Fig. 4.11 [25, 26].

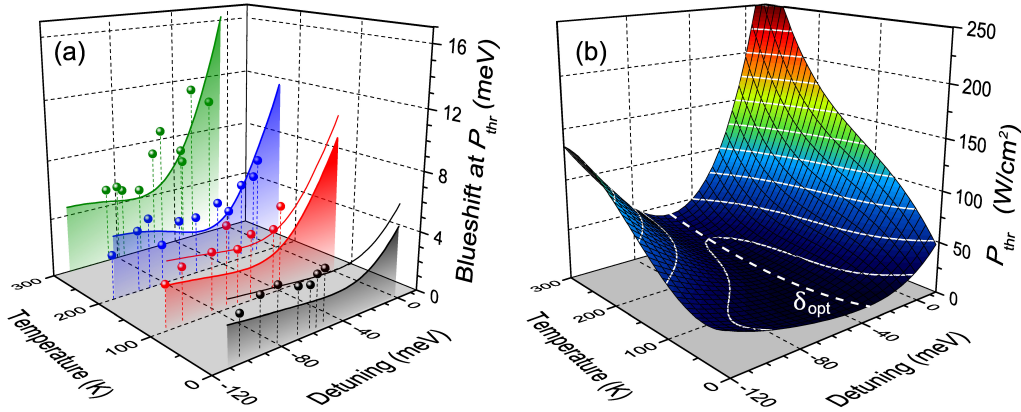


Figure 4.32: (a) Dependence of the LPB-blueshift at $\mathbf{k}_{\perp} = 0$ measured at $P = P_{\text{thr}}$ as a function of T and δ : comparison of COM-modeling exclusively accounting for f_{osc} saturation (solid lines) and experimental data (dots). For $T \leq 100$ K artificially upshifted (by 2 meV) modeling curves are added to account for the non-linear blueshift mechanism present at low temperatures. (b) Dependence of the polariton lasing threshold power density on T and δ according to a polynomial fit of the experimental data from Fig. 4.11(b). Taken from Ref. [104].

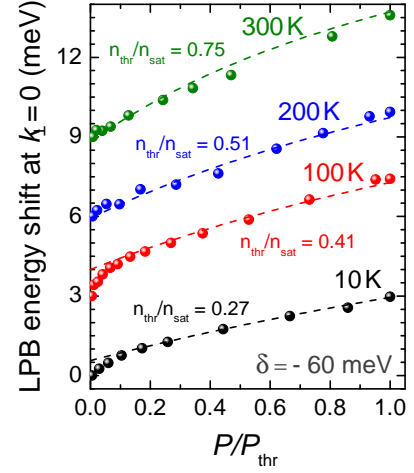
In order to verify the impact of the phase diagram on the polariton renormalization, the LPB blueshift at threshold and zero in-plane momentum ΔE_{thr} has been analyzed as a function of δ and T for a large number of Fourier-PL power-series such as shown in Fig. 4.29. Unfortunately, these data (that are not shown here but can be found in Ref. [108]) appear extremely scattered and lack any signature of a correlation between ΔE_{thr} and the predicted $n_{\text{thr}}(\delta, T)$ from Fig. 4.11. This noise can certainly be attributed to the pronounced impact of photonic disorder, which is omnipresent in III-nitride based MCs and dramatically affects the polariton relaxation kinetics. Indeed, the strong fluctuations of the Q -factor shown in Fig. 4.18(b) can be directly linked to the polariton lifetime, which immediately impacts the sensitive balance between kinetics and thermodynamics according to Fig. 4.11(a) and causes a n_{thr} value fluctuating at the same lateral scale. To eliminate this unpredictable statistic influence the $\Delta E_{\text{thr}}(\delta, T)$ study has been repeated using a larger spot size ($\text{NA} = 0.02$) that averages over the photonic disorder.

In contrast to the micro-PL study, the correspondingly recorded data $\Delta E_{\text{thr}}(\delta, T)$ shown in Fig. 4.32(a) reveal certain correlations. Whereas for $T \leq 100$ K, one can state a conspicuous independence of the LPB blueshift from δ , the latter exhibits a strong rise toward positive detuning at room temperature. For $T = 200$ K an intermediate situation is observed. ΔE_{thr} is generally increasing with temperature, but the variation for $T < 200$ K remains very low.

The COM in combination with Eq. (4.35) was applied in order to reproduce the experimental data with a saturation-induced polariton renormalization.⁹ In agreement with the previous discussion and Ref. [26] the proportionality between n and P is assumed to hold over the whole explored temperature and carrier injection range. The variation of the threshold power-density due to the condensation phase diagram was taken into account by reproducing the experimental variation $P_{\text{thr}}(T, \delta)$ from Fig. 4.11(b) with the 2D polynomial fit shown in Fig. 4.32(b) and adjusting the n/P ratio by the scaling parameter $P(n = n_{\text{sat}}) = 65 \text{ W/cm}^2$. The

⁹The simulations have been performed assuming $\gamma_{\text{C}} = 4 \text{ meV}$, $\gamma_{\text{X}} = k_{\text{B}} T$ and $g_0 = 30 \text{ meV}$.

Figure 4.33: Evolution of the LPB-energy at $\mathbf{k}_\perp = 0$ versus normalized excitation power density P/P_{thr} for different T from 10 to 300 K for a constant detuning around -60 meV. The dashed lines correspond to fits accounting for the $\{\delta, T\}$ -dependent condensation threshold and f_{osc} -saturation in the COM. Data for higher temperatures have been vertically shifted with respect to the 10 K-case. Taken from Ref. [104].



computed results are shown by the down-projected solid lines in Fig. 4.32(a). As a result of the increasing thermodynamic condensation threshold [26], they show for a given detuning a monotonous increase of ΔE_{thr} with temperature. However, more striking appears the strong rise of the expected blueshift toward positive detuning conditions. Owing to the inaccessibility of corresponding δ -values, this effect remains absent in the experiments performed at low temperature, while it is well-confirmed by the measurements for $T \geq 200$ K. Note that this effect is on the one side caused by the rising impact of saturation when δ tends to zero (cf. Sec. 4.5.1), and further relies on the triggered thermal escape of polaritons from the LPB trap, which increases the condensation threshold [25, 26]. It is thus expected to appear very similar in a scenario where the renormalization would be set by ΔE_X . Toward more negative detuning values the modeling confirms the temporary constancy of ΔE_{thr} , i.e. its independence on δ . Here, the evolution is driven by two opposite contributions: first, the saturation impact decreases when going away from the resonance condition $\delta = 0$, and second the rise of P_{thr} due to the kinetic threshold limitation. Both effects partly compensate each other for an intermediate δ -range. Eventually, for even more negative values beyond the explored range, ΔE_{thr} should tend to zero owing to the loss of the matter character and the convergence to the purely photonic case.

While $\Delta E_{\text{thr}}(\delta, T)$ can be accurately reproduced for high lattice temperatures, the experimental data for $T \leq 100$ K follow only qualitatively the model, i.e. they are upshifted by about 1.5 meV. In order to address this feature the power-dependent evolution of ΔE_{thr} shall be reconsidered in more detail. Figure 4.33 shows $\Delta E_{\text{LP}}(P)$ series at $\mathbf{k}_\perp = 0$ and a fixed detuning of about -60 meV for various lattice temperatures, corresponding to single points in the diagram of Fig. 4.32(a). When assuming a constant n/P ratio and a saturation-dominated renormalization these curves including their partially convex shape should be well described by Eq. (4.35), whatever the $\{\delta, T\}$ combination. In agreement with the treatment of Figs. 4.29(d,h), each curve has been modeled correspondingly by adjusting only the relation between n_{thr} and n_{sat} . The fitted ratios remain well below unity, they rise with temperature, and they adequately match the predictions of the phase diagram. For $T_{\text{lat}} \geq 200$ K the experimental data including the slight sub-linear scaling are well reproduced by this model. On the contrary, a significant deviation from the expected behavior is observed at low lattice temperatures. For $P/P_{\text{thr}} \leq 0.15$, an additional blueshift mechanism is revealed that was found to be existent for $T_{\text{lat}} \leq 100$ K

whatever the probed region, spot size, and detuning. It is also present in the $T = 40\text{ K}$ -series of Fig. 4.29. The restriction of this effect to low carrier densities and the absence of any detuning dependence excludes oscillator strength saturation, collisional-induced broadening, or a QCSE-induced exciton blueshift as potential origins. Those mechanisms would be expected at high carrier densities and exhibit a pronounced detuning sensitivity according to the excitonic fraction. Thus, this blueshift mechanism cannot be adequately described by a COM-based modeling. It appears to be the reason for the static offset observed between experiment and modeling for $T \leq 100\text{ K}$ in Fig. 4.32(a) and may correspondingly lead to an overestimation of the $n_{\text{thr}}/n_{\text{sat}}$ ratio. Other potential origins shall be briefly discussed hereafter.

From Sec. 4.4 it is known that biexcitons play an important role in MC-1 at low temperatures. From a theoretical point of view, these are expected to mediate an attractive polariton-polariton interaction scaling non-linearly with the injected carrier density [225, 267]. However, this mechanism involves mainly virtual scattering states which cancels any strong temperature dependence and the restriction of the blueshift mechanism to very low densities makes a biexcitonic impact very unlikely. By contrast, the constraint to low P and T could favor an interpretation based on carrier localization. Indeed, as already mentioned before, the applied COM-modeling represents a rather crude approximation as it neglects any variation of the n/P ratio with lattice temperature and carrier density. Based on $E_{\text{loc}} \sim 11\text{ meV}$ (cf. Sec. 4.4), dark excitons in the reservoir may however be partly localized at $T \leq 100\text{ K}$, which would increase the effective carrier lifetime in the system and cause a larger n/P ratio. Given that the exciton localization is exactly lifted in this low-injection window, the carrier lifetime and the n/P ratio should decrease with carrier density and cause a decreasing blueshift rate in agreement with the experimental observation. An alternative mechanism related to carrier localization was proposed in Ref. [185]: scattering processes occurring in the local disorder landscape could initiate a population transfer between radiative and non-radiative states, potentially impacting the light-matter coupling. Note however that localization of radiative carriers in the SCR should play a rather negligible role, while the impact of localized dark exciton states on the light-matter coupling should be marginal owing to their low density of states. Moreover, when taking into account the absence of any injection-induced delocalization process in the measurements of Fig. 3.27, even carrier localization effects should be called into question as potential origin.

Eventually, based on the present experiments a conclusion on the exact mechanism, which governs the renormalization in this temperature and density regime, is strongly hampered by the unidentified relation existing between injected power density and the actual carrier density. In line with this, it is worth pointing out once more that the COM represents an oversimplified approach. This applies simultaneously to the assumed f_{osc} power-scaling that needs to be experimentally and theoretically verified, in particular in view of the unknown ratio between n_{crit} and n_{sat} . Indeed, while the first quantity describes the dissociation of the excitonic complex according to the MT, n_{sat} only sets the carrier density when f_{osc} is decreased to half its initial value. Establishing a relationship between them stays beyond the reach of the current study. More advanced experiments, that allow the simultaneous determination of an exact carrier density and the absorption properties of the QW, would be required. This could for instance be achieved by merging the tr-PL measurements discussed in Ch. 3 with a pump-probe setup scheme.

Note finally that the presence of a clear anticrossing at and above the condensation threshold

ensures that the system operates in the SCR and thus below the Bernard-Duraffourg limit. Nevertheless the pronounced impact of exciton saturation suggests that the MT is not very far. Depending on the eventually probed $\{\delta, T\}$ and Q -factor combination, it is likely that at threshold the carrier population lies only one and not more than two orders of magnitude below the critical density.

Remarks and Consequences

An exact determination of the carrier-injection regime and a deep insight into the renormalization mechanisms at play in a MC-structure are of fundamental interest for achieving an accurate description of polariton condensates and for the realization of an eventual device.

The present study proves that saturation effects may have an important influence in strongly-coupled MCs even if they are often assumed to be negligible. One might reasonably argue that MC-1 does not reach the high-quality of a GaAs or CdTe-based MC-structure, but the comparable value of the expected saturation influence given by Tab. 4.2 and various experimental observations suggest that such high-density effects should widely be considered. Indeed, early studies have clearly revealed the increasing role played by exciton saturation in both GaAs [115, 185], and CdTe-based MC systems [273]. Similarly to the conclusion drawn for MC-1, its influence becomes dominant about one or two orders of magnitude below the critical density. And even if those early structures did not reach the polariton lasing regime, the relative proximity between polariton and photon lasing thresholds recorded in state-of-the-art MCs [238], gives reason to expect a general operation of polariton lasers only one or two orders of magnitude below the MT. This statement is confirmed by other experiments that evidenced a redshift of the UPB [17, 25] (cf. Fig. 4.27(b)) or a decreasing Rabi-splitting [272]. By contrast, MCs based on an organic active medium can likely be excluded from this conclusion based on the giant binding energy of Frenkel-excitons, in agreement with the absence of any LPB blueshift in power-dependent experiments [274].

Finally, it is worth highlighting that the analysis drawn here, remains exclusively valid below the polariton condensation threshold. A comprehensive study above the latter in a GaN-based MC is strongly hampered by photonic disorder, that creates traps for the condensates usually leading to a strong discontinuity in ΔE_{LP} and the occurrence of multi-mode emission. Note however that while in the linear regime the polariton renormalization is predominantly driven by the polariton reservoir population, the interaction occurring in an eventually formed condensate might strongly alter the renormalization characteristics. Apart from the changing mean particle lifetime, hints for such effects are given by a modification of the ΔE_{LP} power-law across the threshold [269, 275], or by the observed slow down of the Ω decrease in this study.

4.6 High-Temperature Polariton Condensates

While the preceding sections dealt mainly with the polariton properties below threshold, this section focuses on the characteristics of polariton condensates forming in a highly disordered landscape. Such systems have already been studied in a spectacular manner in CdTe-based MCs at low temperature, for instance yielding quantized vortices pinned to lattice imperfections [18, 191] or a quantum Josephson-junction between two adjacent defects [20]. It was also proposed that polariton condensates established in a disordered landscape may constitute

a Bose-glass phase [276]. However, experiments revealed that depending on the magnitude of the disorder potential condensates, which seem to be spatially isolated at first sight, may also be synchronized while exhibiting macroscopic coherence [17, 268, 277]. In the present III-nitride based MCs the disorder scale is expected to be further increased compared to the CdTe case. Thus, synchronization of localized condensates should likely be prevented as also reported for certain sample spots in Ref. [277]. On the contrary, compared to the less-disordered GaAs or CdTe-based systems, the striking advantage of GaN-based MCs consists in the ability of tuning the lattice temperature over a wide range and thus to study the impact of phonon-induced decoherence and thermal agitation on polariton condensates.

In order to gain a first insight, the Fourier-space imaging technique is complemented by monitoring the real space emission pattern according to the setup schematic of Fig. 4.16. Throughout this section the Nd:YAG laser serves as non-resonant excitation source. The subsequently presented results are very recent and have not been published yet. They should thus be seen as very preliminary, rather representing an outlook to what could follow in successive works.

Thermalization in the Real-Space

Below the condensation threshold P_{thr} the real-space emission pattern of the LPB usually follows the pump-spot profile [268, 269, 278]. In such a situation carrier diffusion and localization effects are limited by the exciton diffusion length ($\sim 100\text{ nm}$ in GaN QWs at low temperature [279]) and the strongly decreasing polariton lifetime toward the center of the BZ. Thus the injected polariton population is rather immobile and remains mostly distributed according to the pump profile. Figure 4.34 shows power-dependent near-field emission patterns recorded on MC-1 below threshold at 150 K. Due the collection through the UV-microscope objective, the emission has been integrated over the whole Fourier-plane ($-33^\circ < \Theta_{\text{ext}} < 33^\circ$). The probed spot with a diameter of about $10\mu\text{m}$ is characterized by a detuning of -50 meV , i.e. a value close to the optimum conditions of the condensation phase diagram shown in Fig. 4.11. For the lowest excitation power ($P = 0.36P_{\text{thr}}$) the LPB exhibits a strongly non-thermal branch occupancy (cf. Figs. 4.34(d,e)) and an emission pattern reproducing the pump spot profile (cf. Fig. 4.34(a)).¹⁰

As previously discussed for Fig. 4.21, a characteristic of the optimum detuning conditions consists in the transition from a non-thermal to a quasi-thermal LPB occupancy when approaching the condensation threshold. For the present spot, this trend can be followed in Fig. 4.34(e). Along with thermalization comes a modification of the near-field emission pattern: while in Fig. 4.34(a) the two intensity maxima A and B share very similar amplitudes, an increasing excitation power in Figs. 4.34(b,c) causes a progressive intensification of the emission originating from the lower pump spot maximum B. Based on the collection conditions widely leaving out the exciton reservoir (cf. Fig. 4.34(d)), the signal increase can directly be transposed to the LPB occupancy. Hence, it seems that the thermalization of the LPB is more efficient in B than in A, most likely due to an increased cavity-photon lifetime based on the photonic disorder (cf. Fig. 4.18(b)).

¹⁰Due to degradation of the Nd:YAG laser pattern, the beam profile for these recent measurements exhibited distinct intensity modulations along the vertical axis, resulting in a strongly-structured excitation density profile.

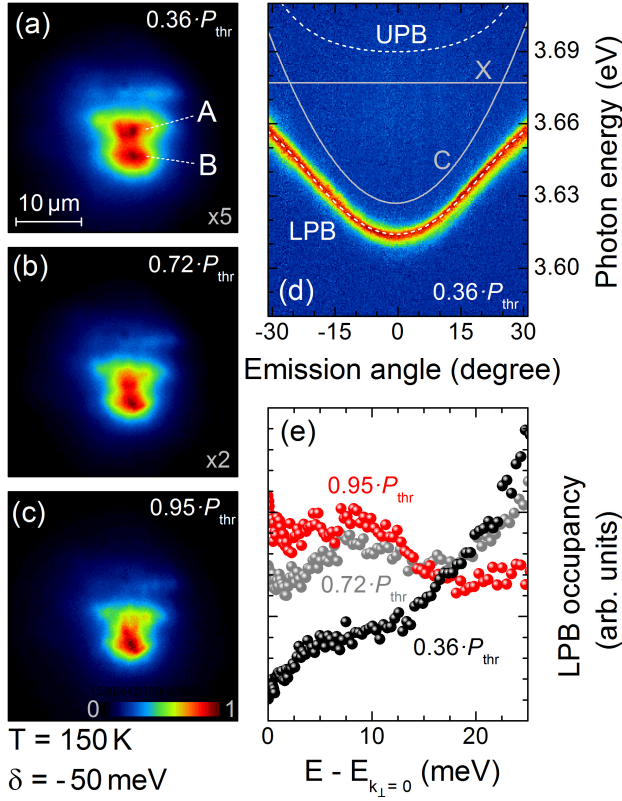


Figure 4.34: Real space monitoring of the polariton thermalization toward the condensation threshold at 150 K: (a-c) Normalized real space emission patterns at different excitation power densities ranging in between 0.36 and $0.95 P_{\text{thr}}$. The spots A and B mark two pump power maxima originating from the laser beam shape. (d) Far-field emission for $P = 0.36 P_{\text{thr}}$. Coupled modes are shown with white dashed lines, uncoupled ones with gray solid lines. (e) Relative LPB occupancy corresponding to the real space emission patterns displayed in (a-c), showing the transition from a non-thermal to a quasi-thermal carrier distribution.

4.6.1 Polariton Condensates emerging in a disordered Landscape

At even higher excitation power density it is also region B that transits first into the non-linear emission regime. Figure 4.35 shows the follow-up of the near-field monitored power series of Figs. 4.34(a-c). Directly at threshold condensation occurs solely in a potential trap close to the center of region B. Figure 4.36(a) shows a simultaneously recorded Fourier-PL image in logarithmic color scale. The linear emission of the renormalized 2D LPB is still observed and lasing occurs blueshifted by $\Delta E_{\text{loc}} \approx 2$ meV with respect to the bottom of the LPB. This blueshift of the condensed phase is commonly observed and can either be related to the recombination kinetics [189], the finite excitation spot size [280], or more likely in the present case to the impact of disorder [278]. In the latter scenario, the beam divergence $\Delta\Theta_{\text{ext}}$ in the far-field image amounting to $\sim 12^\circ$ in Fig. 4.36(a) can be related to the dimension of the localization center. Using classical divergence theory to link the far-field spectrum of a circular and uniformly illuminated aperture to its radius r_A , the latter can be expressed via [172]:

$$r_A \approx \frac{\lambda}{2\Delta\Theta_{\text{ext}}}, \quad (4.36)$$

where λ denotes the vacuum wavelength of the condensate emission. In the present case this yields a localization diameter of about $1.5\mu\text{m}$ in good agreement with the near-field images in Fig. 4.35. This length scale seems also consistent with the photonic disorder mapping shown in Fig. 4.18(b).

When further raising the excitation power the initially localized polariton population seems to

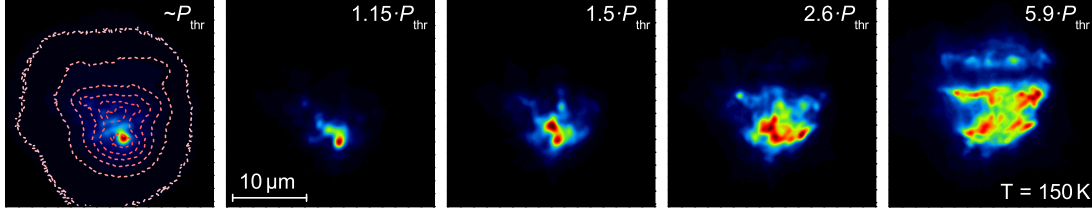
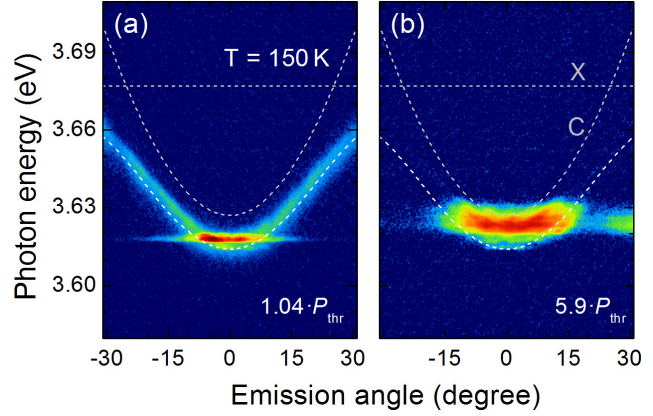


Figure 4.35: Power-dependent real space emission profiles recorded at $T = 150$ K at the same spot position as the measurements shown in Fig. 4.34. The excitation conditions were kept identical. For the pattern at threshold (left), the contour lines of Fig. 4.34(a) are shown for comparison. They correspond approximately to the excitation power density profile.

progressively flood side valleys in the disorder landscape outgoing from region B, eventually giving rise to additional emission hot spots. Despite being exposed to a similar power density, region A transits to the non-linear emission regime at a much higher injection level than B. Only for the highest probed power density, i.e. $P = 5.9P_{\text{thr}}$, both regions exhibit comparable emission intensities. Surprisingly, at this point the maximum emission intensity comes from sites that are considerably located apart from the pump power maxima A and B. This could hint to the influence of a reservoir-induced blueshift and despite disorder to a certain mobility of the condensate. Indeed, in agreement with the findings of Sec. 4.5 it has been evidenced that the LPB blueshift, whatever its eventual origin, is imprinted by the exciton reservoir population, which is generated according to the pump spot profile [270, 281, 282]. This leads for high excitation powers to an expulsion of mobile condensed polaritons from the center of the pump spot. Such a mechanism should ideally be confirmed by the far-field emission pattern. Figure 4.36(b) shows a corresponding measurement recorded simultaneously to the emission profile with the highest injection in Fig. 4.35. In absence of disorder, when polaritons escape radially from the center of a sufficiently small pumping spot, the emission of the propagating condensate should distinctly appear at a finite in-plane momentum [270, 282]. However, when the spot size is increased compared to the typical polariton propagation length or to the lateral scale of disorder this feature will first become less prominent and eventually vanish into a broad PL distribution in k -space [280]. This is likely to be the situation observed in Fig. 4.36(b), where PL arises from a wide range of k -vectors with maximum values limited by the zero-density LPB dispersion. Indeed, as evidenced by the real-space emission patterns the probed spot size slightly exceeds the scale of photonic disorder causing propagation of polaritons only along certain valleys in the potential landscape. Corresponding channels of motion could be imaged by future tomographic measurements of the Fourier-space [280]. Note further that the expulsion of the emission maximum from the pump spot center excludes a conventional semiconductor lasing mechanism based on the Bernard-Duraffourg condition. Indeed, in such a case the emission intensity maximum should *a priori* coincide with the one of the excitation power density, e.g. as observed in Ref. [269].

Spectral information of this power series have been extracted from simultaneously recorded far-field images such as shown in Fig. 4.36. Figure 4.37(a) shows corresponding spectral profiles at zero in-plane momentum. The related evolution of the integrated emission intensity I_{PL} is displayed in Fig. 4.37(b), and the power-dependent modifications of the LPB emission energy and its FWHM are summarized in Fig. 4.37(c). The onset of polariton lasing is characterized by

Figure 4.36: Fourier-space PL-images of MC-1 measured above threshold at $T = 150$ K corresponding to different points from the real-space emission series of Fig. 4.35 with excitation power densities of (a) $P = 1.04 \cdot P_{\text{thr}}$ and (b) $P = 5.9 \cdot P_{\text{thr}}$ (arbitrary logarithmic color scale). The uncoupled modes and the LPB from Fig. 4.34(a) are shown for comparison.



a strong exponential rise in I_{PL} and an abrupt drop in the LPB emission FWHM far below the cavity mode linewidth (local Q -factor ~ 650), indicating strong temporal coherence [17, 22]. Note that the minimum linewidth indicated in Fig. 4.37(c) is limited by the spectral resolution of the setup amounting to 1.2 meV in this case. It is thus likely overestimated directly at threshold and should rather exhibit a value significantly smaller than 1 meV, as determined in Ref. [23]. However, despite the multimode emission and the limited spectral resolution a careful deconvolution of individual modes above threshold indicates a slight power-dependent linewidth increase as it may be expected from polariton self-interactions [17, 283]. This finding agrees well with the LPB blueshift, which is observed to scale slightly sub-linearly with power below and above threshold. While the responsible mechanism below P_{thr} has been evidenced to arise predominantly from exciton saturation effects in Sec. 4.5, the blueshift in the non-linear emission regime is likely to be driven by interactions occurring within the polariton condensate population [280]. Although partly hidden by the logarithmic power axis, Fig. 4.37(c) also shows the temporary slow-down of the blueshift at threshold as observed in Fig. 4.29.

Note that the recorded LPB blueshift, amounting to about 11 meV for an injection ten times above threshold, covers an already significant fraction of the Rabi-splitting. This fact hints at an injection regime, which is not far from the saturation limit and thus from the WCR to SCR crossover in agreement with the conclusion drawn in the previous section. Unfortunately, the examinable power density range was limited to maximum values of about 200 W/cm^2 in order to guarantee the integrity of the top-DBR. For even higher excitation densities the strong absorption in the contained Si_3N_4 layers in combination with their low thermal conductivity leads to an irreversible damage of the top-DBR. However, within the explored power density range no definitive evidence for a coupling regime conversion could be traced. The emission intensity maximum always remains below the cavity mode energy (cf. Fig. 4.37(c)),¹¹ indicating that the SCR is still preserved, in agreement with the interpretation of the near-field emission pattern shown in Fig. 4.35. Nevertheless, the pronounced multi-mode character of the emission hampers a more in-depth analysis and might also prevent probing the coherence properties far above threshold in forthcoming experiments.

Finally it is worth stating that the reported behavior about multiple emission hot spots emerging in the real-space pattern above threshold appears very similar to what was observed in

¹¹ Note that the non-linear refractive index coefficient in GaN is negative around the bandgap [284], which rules out a power-dependent redshift of the cavity mode.

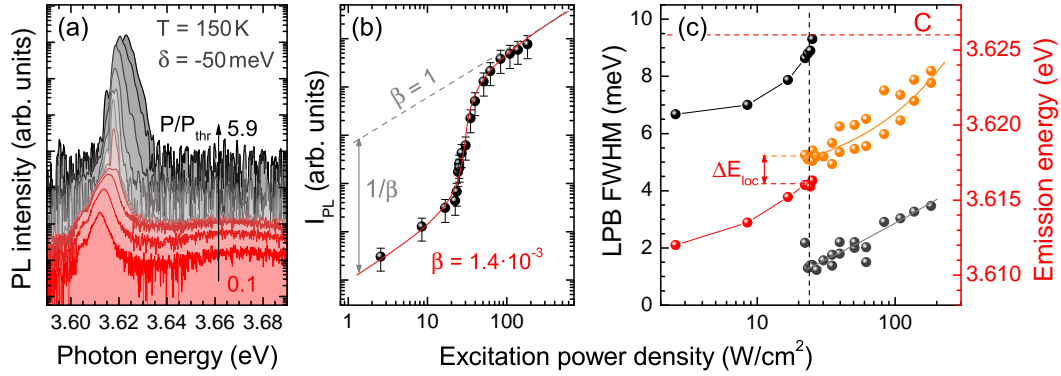


Figure 4.37: (a) Spectral profiles of the power-series measured at $T = 150\text{ K}$ and $\delta = -50\text{ meV}$ of Figs. 4.34 and 4.35 at zero in-plane momentum. (b) Corresponding integrated LPB emission intensity as a function of P_{exc} (black dots + error bars): the evolution could be adequately reproduced by Eq. (4.37) yielding $\beta = 0.0014$. The gray dashed line represents the ideal case $\beta = 1$. (c) Evolution of LPB ground state emission energy (red) and linewidth (black) as a function of carrier injection: corresponding lasing modes above threshold (vertical dashed line) are marked with orange and gray dots, respectively. Due to the disorder influence the lasing mode is blueshifted with respect to the 2D-continuum branch by $\Delta E_{\text{loc}} \approx 2\text{ meV}$ at threshold. Note that despite the significant blueshift the emission energy remains below the cavity mode energy at all times (horizontal dashed line).

a disordered CdTe-based MC [17, 268]. As already mentioned, Baas and co-workers have shown on the same structure that these condensate fractions may synchronize by forming a single extended system ground state with large spatial coherence [277]. The efficiency of this synchronization was evidenced to heavily depend on the local disorder landscape, i.e. very strong disorder could prevent the interaction between localized condensates. In the present measurements for $P < 1.2P_{\text{thr}}$ the emission pattern in Fig. 4.35 shows an only slight spatial variations and the emission spectrum in Fig. 4.37(a) consists solely of a main mode and a weaker excited mode. The emission is thus likely to arise from a single coherent condensate. These two main emissions can be followed up to about $2.2P_{\text{thr}}$ in Fig. 4.37(a), but merge into the multi-mode spectrum for even higher excitation densities. At this point it remains elusive to identify the nature of the different modes. They might either arise from independent condensates or from the excited states of one and the same condensate. A potential future study could thus rely on spatially and energetically resolved coherence measurements such as presented in Refs. [270, 277].

Input-Output Characteristics

A performance indicator of conventional lasing devices with small mode volumes is given by the fraction of spontaneous emission that is coupled to the photonic mode, which is represented by the β -factor. The input-output transfer function is then obtained via [285]:

$$I_{\text{PL}} \propto r - 1 + \sqrt{(r - 1)^2 + 4\beta r} \quad (4.37)$$

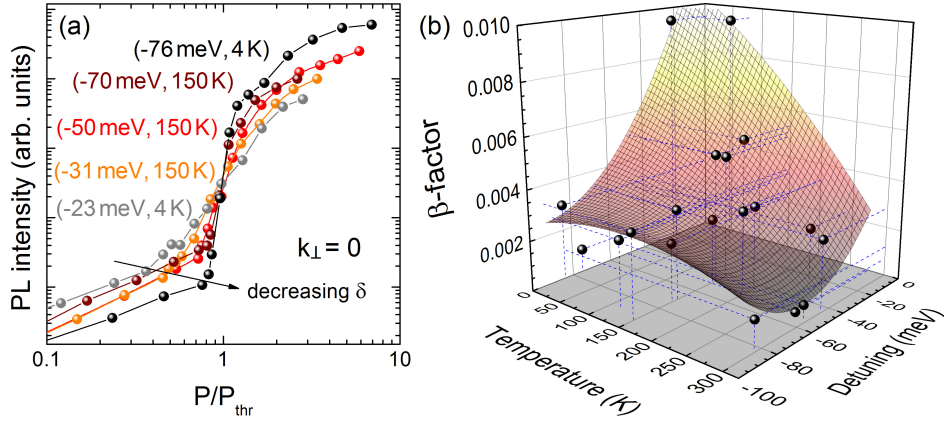


Figure 4.38: (a) Integrated LPB intensity at $\mathbf{k}_\perp = 0$ as a function of carrier injection normalized to threshold power and intensity for various detuning values ($T = 4\text{ K}$ or 150 K): the more negative the detuning, the steeper the rise of I_{PL} at threshold. (b) Determined β -factors as a function of $\{\delta, T\}$ (dots): the polynomial surface fit indicates the global trends.

where $r = P/P_{\text{thr}}$ denotes the normalized injection rate. This formalism applies preferably to VCSELs, where the radiative escape occurs exclusively through a single cavity mode [161]. In such structures, the fraction of emitted photons can only be increased when passing the threshold conditions for stimulated emission. In the hypothetical case of a thresholdless device described by $\beta = 1$, all generated photons leak out through the cavity mode. At threshold the recombination mechanism would switch from spontaneous to stimulated emission and I_{PL} would simply be a linear function of P [286, 287].

The driving mechanisms and the threshold conditions for non-linear light emitters based on polariton condensation or conventional lasing are intrinsically different. Discrepancies appear in particular in the sub-threshold regime: while a VCSEL operated in the spontaneous emission regime satisfies $I_{\text{PL}} \propto P$, a polariton laser does so solely in the very low density regime, when relaxation is governed by acoustic-phonon scattering. For higher carrier densities polariton pair-scattering comes into play and the transfer function becomes superlinear (cf. Fig. 4.21), i.e. quadratic in an ideal scenario [269]. Once the threshold condition is fulfilled, bosonic final state stimulated scattering is triggered and the condensate occupancy rises exponentially. However, apart from the differences in the underlying physics the rate equations describing the input-output characteristics of both device solutions appear to be very similar [171] and the output transfer function of polariton lasers is commonly also described using Eq. (4.37) [22, 288]. In this case the physical interpretation of β is slightly different: it determines the inverse number of optical modes via which polaritons may spontaneously escape the MC and is thus also applicable to multi-mode emissions.

The evolution of I_{PL} as a function of excitation power displayed in Fig. 4.37(b) has been fitted by Eq. (4.37) using $\beta = 1.4 \cdot 10^{-3}$. The reproduction appears accurate and has been repeated for a variety of $\{\delta, T\}$ -combinations yielding the data points displayed in Fig. 4.38(b). For low temperature and toward positive detuning conditions the radiative coupling of polaritons seems more efficient, whereas a decreasing δ and an increasing T cause an overall drop of the β -factor. Multiple parameters have to be considered: for instance, the dependence

of the polariton lasing threshold on the $\{\delta, T\}$ combination as discussed in Sec. 4.2.2, the IQE of the QW-exciton reported in Sec. 3.2.3, and the rise of the thermodynamic threshold with temperature [289]. In particular, the theoretical modeling of a potential polariton LD in Ref. [171] predicts a pronounced dependence of the β -factor on the actual condensation threshold density,¹² predominantly based on the polariton scattering rates (cf. also Sec. 4.2.3). The intracavity pumping scheme analyzed therein corresponds most closely to the experimentally used optical pumping conditions and gives reason to expect a continuous rise of β with detuning at low temperature. This prediction agrees well with the present experiments: Fig. 4.38(a) displays a set of input-output curves taken at $T < 150$ K for different detuning values. It clearly shows the trend of an increasing intensity jump at threshold and thus a decreasing β -factor toward more negative detuning values, in agreement with Ref. [171]. These experiments give only a first idea about the underlying physics. They call for a comprehensive study of the threshold behavior as a function of $\{\delta, T\}$ in order to verify the considerations given in Ref. [171] and define further distinguishing marks between polariton and photon lasers. Further theoretical insights concerning this topic can also be found in Ref. [63].

Concluding Remarks and Prospects

As indicated in the beginning, this section remains provisional. In these first measurements, no distinct dependencies of the condensate formation on temperature could be tracked via real space monitoring. The exemplarily discussed power series recorded at $\delta = -50$ meV and 150 K should rather be seen as a representative for all hitherto explored $\{\delta, T\}$ -combination snapshots. Future studies should unconditionally comprise spatial and temporal coherence measurements, ideally with an optimized top-hat laser beam profile of adjustable diameter [280]. A comprehensive examination of the $\{\delta, T\}$ dependence may reveal the impact of thermal agitation in a disordered potential landscape. Such an analysis seems necessary to evaluate the potential of disordered polariton condensates for an eventual realization of a cavity-polariton based device. In addition to the omnipresent disorder, MC-1 also contains a variety of defects that may give rise to anomalous polariton properties, such as for instance discussed in Ref. [291]. This discussion is going to be continued in Sec. 5.2.

4.7 Non-polar III-Nitride based Microcavities

All aforementioned studies concerned MC-1, which is based on a *c*-plane oriented III-nitride layer stack, offering the highest structural and optical quality, and an almost isotropic optical response. However, it is worth recalling that such structures suffer from the QCSE as described in Sec. 2.3.3 [80]: the strong built-in electric field causes a detrimental decrease of the wavefunction overlap p_{QW} and thus a reduction of the exciton oscillator strength f_{X} according to Eq. (2.46). At the same time, the decrease in the radiative recombination rate can cause a drop in the overall efficiency of QW-based optoelectronic devices.

In order to circumvent these drawbacks the use of semi-polar or non-polar III-nitride heterostructures is widely considered as an alternative nowadays [75]. Here, for non-polar structures with $(10\bar{1}0)/m$ -plane or $(11\bar{2}0)/a$ -plane surface orientation (cf. Fig. 2.1) the polarization-vector projection along the growth axis amounts to zero, which leads to intrinsically field-free

¹²Note that for conventional semiconductor lasers the relation between the β -value and the threshold current density is expected to be very similar [285, 290].

QW-potential profiles with p_{QW} -values close to unity like in a GaAs-based QW system (cf. the field-free calculation in Fig. 2.8(c)). By contrast, in semi-polar structures the projection of the spontaneous polarization vector \mathbf{P}_{sp} onto the growth axis is admittedly reduced compared to its c -plane counterpart but it remains finite. Nevertheless, by means of a sophisticated strain management the piezoelectric polarization component can be used to compensate \mathbf{P}_{sp} and generate almost field-free QWs featuring high radiative efficiencies [78, 79]. This opened up the competition between c -plane, non-polar and semi-polar surface orientations for the realization of efficient InGaN-based LDs emitting in the green spectral region [85, 292].

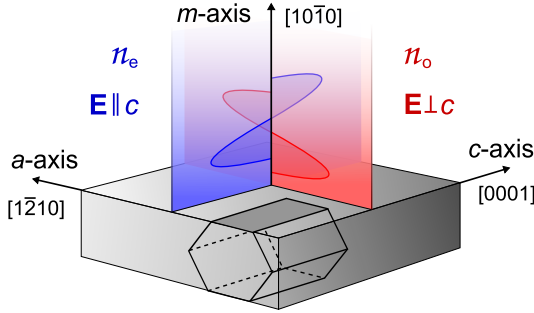


Figure 4.39: Schematic representation of the m -plane crystal orientation and the corresponding anisotropic optical response.

In addition to the reduced or even suppressed influence of the QCSE, such semi- or non-polar structures exhibit a pronounced anisotropic optical response governed by birefringence and dichroism according to Sec. 2.2.3. These effects arise from the uniaxial character of the complex refractive index tensor in Eq. (2.39) and the finite component of the optical c -axis perpendicular to the growth axis for such orientations. Figure 4.39 depicts this situation schematically for an m -plane structure. The electric-field vector of the incoming light can either be polarized parallel or perpendicular to the c -axis: the propagation and absorption of light in the anisotropic medium is thus governed by the complex refractive index components n_e and n_o , respectively.

With regard to exciton-polaritons in strongly-coupled MCs, the interest in investigating semi- or non-polar III-nitride structures is twofold: first, the increased wave-function overlap favors the light-matter coupling and promises higher efficiencies in prospect of an eventual device. And furthermore, in line with the proof of concept motivation, the pronounced optical anisotropy of photonic and excitonic modes are expected to give rise to an exotic polarization-dependent light-matter coupling regime.

4.7.1 Sample Structure

The upcoming experimental studies and theoretical considerations refer to an m -plane III-nitride based MC:

MC-2 In order to achieve the highest possible structural and optical quality the structure was grown on top of a 100 μm -thick m -plane bulk GaN substrate that was provided by our collaborators from Unipress in Warsaw [293]. In doing so, lattice mismatch and differences in thermal expansion coefficients are reduced to a minimum. The substrate dislocation density amounts to $2 \cdot 10^6 \text{ cm}^{-2}$. The growth performed by MBE using ammonia as a nitrogen source started with the deposition of a 300 nm-thick homoepitaxial GaN buffer layer. Subsequently, a 50-pair $\text{Al}_{0.15}\text{Ga}_{0.85}\text{N}/\text{Al}_{0.35}\text{Ga}_{0.65}\text{N}$ bottom-DBR was

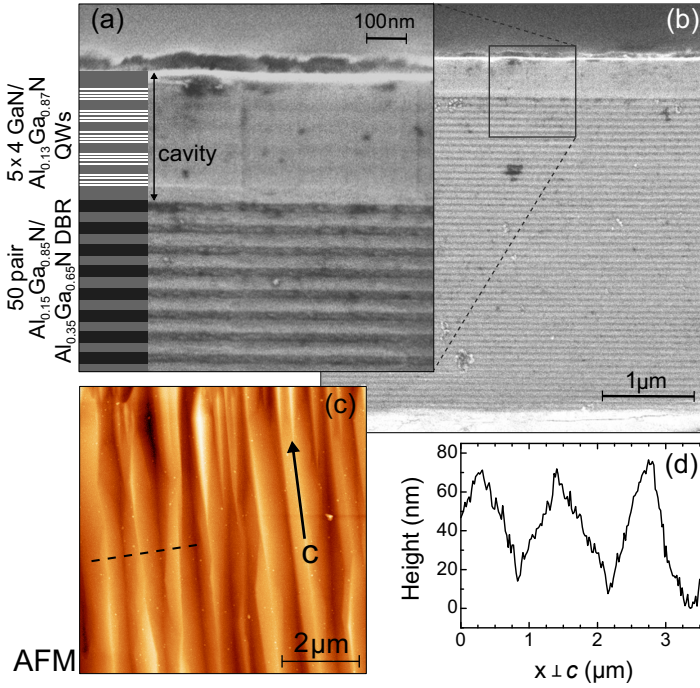


Figure 4.40: Structural properties of the MC-2 III-nitride layer stack: (a) enlarged cross-section SEM image of the cavity section deposited on top of a 50-pair AlGa_{0.65}N-based DBR, including a sketch of the corresponding layer sequence on the left-hand side. (b) Cross-section SEM view of the whole structure. (c) AFM-scan of the III-nitride layer-stack showing a saw-tooth profile aligned with the *c*-axis. (d) Height profile along the dashed line in (c).

grown with respective nominal layer thicknesses of 31.8 nm and 34.8 nm, that should yield a stopband centered around 3.55 eV. The overgrown cavity section consists of five QW-sets, which are located at the field antinodes of the 3λ cavity and separated by 30.8 nm Al_{0.13}Ga_{0.87}N spacer layers. Each QW-set is formed by four 5 nm-thick GaN QWs embedded in between 5 nm-thick Al_{0.13}Ga_{0.87}N barriers. The active region is surrounded by two Al_{0.13}Ga_{0.87}N spacer layers with a thickness of 48.3 nm. Finally, the MC was completed by an 8-pair SiO₂/ZrO₂ dielectric top-DBR that was deposited by electron-beam evaporation.

In contrast to MC-1, the cavity section of MC-2 relies on a design with QWs located at the field antinodes, that optimizes the coupling strength and is commonly used for QCSE-free GaAs or CdTe-based structures [17, 238]. Figures 4.40(a,b) show cross-section scanning electron microscopy (SEM) images of the half MC-structure without top-DBR. The cavity section on top of the 50-pair bottom-DBR is clearly observed. A closer inspection separates even the QW-containing sections from the Al_{0.13}Ga_{0.87}N spacer layers. Below the active region, the pairs of the AlGa_{0.65}N-based bottom-DBR are clearly visible, evidencing smooth interfaces and a significant atomic-mass contrast issued from the different Al-contents. Despite disadvantages such as a considerable layer stress and the low refractive index contrast, the use of a purely AlGa_{0.65}N-based bottom-DBR is motivated by the well-developed growth handling for such non-polar structures in MBE. Owing to the different adatom sticking coefficients at the different surface facets and the resulting anisotropic growth rates, the surface morphology of the III-nitride layer stack features a typical sawtooth-profile as evidenced by the atomic force microscopy (AFM) measurement shown in Figs. 4.40(c,d) [294]. The lateral extent of these structures gives reason to expect a remarkable photonic disorder in the complete MC-structure.

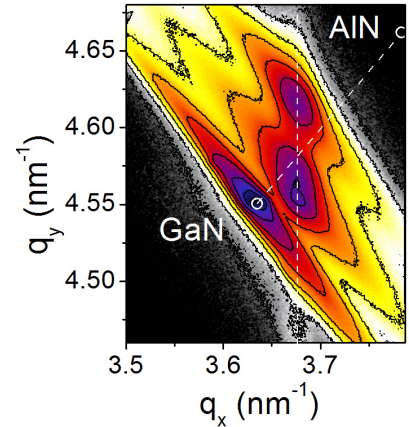
Unfortunately, the initial XRD study of MC-2 remained incomplete and more recent XRD-measurements of MC-2 indicate a strain state, that is modified with respect to the initial

analysis probably due to aging of the sample. This detail will be commented in the end of Sec. 4.7.2. Figure 4.41 shows a RSM of the asymmetric $(20\bar{2}3)$ reflex of a MC-structure that is nominally identical to that of MC-2, but which was fabricated more recently. Three distinct peaks can be observed: one coming from the unstrained bulk GaN substrate at $q_x = 3.64 \text{ nm}^{-1}$, and two others being equally located at $q_x = 3.675 \text{ nm}^{-1}$ but at different q_y . The last two peaks originate from the two different AlGaIn components of the bottom-DBR. Their location at equal inverse in-plane lattice constants q_x indicates pseudomorphic strain conditions for the major part of the DBR. Indeed, the marked separation from the q_x of the GaN substrate hints at a rapid strain relaxation occurring within the first DBR bilayers toward intermediate lattice constants. These are given by the intersection between the zero-strain line connecting the relaxed lattice parameters of pure GaN and AlN in Fig. 4.41 and $q_x = 3.675 \text{ nm}^{-1}$. It corresponds to the equilibrium lattice constants of an AlGaIn alloy with an Al-content x_{Al} around 28%. This value is close to the geometrical value:

$$x_{\text{geo}} = \frac{d_1 x_1 + d_2 x_2}{d_1 + d_2} \approx 0.26, \quad (4.38)$$

where $d_{1/2}$ and $x_{1/2}$ denote the thicknesses and Al-contents of the DBR bilayer components, respectively. Although not shown here, it is worth mentioning that this XRD interpretation is in perfect agreement with complementary TEM studies.

Figure 4.41: XRD-RSM of the asymmetric $(20\bar{2}3)$ reflex in a MC-structure nominally identical to MC-2. Lattice parameters of unstrained GaN and AlN are marked by open circles. Plastic relaxation occurs in the first DBR-pairs leading to a cavity-DBR layer stack that is strained on intermediate lattice constants given by the intersection of the two dashed lines $x_{\text{Al}} \approx 0.28$.



No clear signature of the cavity section can be resolved in the RSM of Fig. 4.41. But owing to the relatively small thickness ($\sim 400 \text{ nm}$) and the low average Al-content around 10%, it can be reasonably assumed that it adapts to the lattice constants imprinted from the bottom-DBR. This theory is confirmed by the TEM-study revealing no further plastic relaxation at the DBR-cavity interface and by the bump, that is visible in the RSM around $q_x = 3.675 \text{ nm}^{-1}$ and $q_y = 4.5 \text{ nm}^{-1}$ indicating the contribution of the GaN QWs.

4.7.2 Optical Properties of the MQWs: The Impact of Strain

A comprehensive study of the optical properties of the MC active medium constitutes a prerequisite for interpreting and understanding the optical response of the complete MC structure. Therefore, this section focuses on the examination of the optical properties of the half MC, i.e. the III-nitride layer stack of MC-2 without top-DBR. They were probed with PL

and reflectivity techniques as described in Sec. 3.1.1.

Experimental Results

Figure 4.42(a) shows a micro-PL temperature series of the MC-2 MQWs recorded under non-resonant cw-injection without polarization selection ($P_{\text{exc}} \approx 2 \text{ kW/cm}^2$). The emissions coming from the QWs and the AlGaIn-barriers, respectively centered around 3.55 eV and 3.71 eV at 4 K, can be easily followed up to room temperature (RT). At low temperature both transitions feature an additional weak emission band located about 45 meV below in energy. It vanishes rapidly with increasing temperature and is likely related to basal-plane stacking faults (BSF), i.e. defects that are frequently observed in non-polar III-nitride structures [295]. On the low-energy side of the QW-emission, the LO-phonon replica (QW-LO) is well resolved for all temperatures. In Fig. 4.42(b), the temperature redshift of the QW-exciton between 4 and 300 K amounts to approximately 55 meV. A comparison with the expected energy shift according to Eq. (3.5) yields a moderate localization energy E_{loc} around 15 meV, in agreement with a low-temperature linewidth of $\sim 18 \text{ meV}$ and an exciton delocalization occurring when $E_{\text{loc}} \approx k_B T$. Indeed, whereas the QW emission energy remains well below the model prediction at low T , both coincide for $T > 200 \text{ K}$. By contrast, carrier localization is much more pronounced for the AlGaIn barrier. The emission follows a strong S-shape with increasing temperature emphasizing the strong impact of alloy fluctuations. Indeed, due to the absence of QCSE and the large QW width, the penetration depth of the QW wave-functions into the barrier material is reduced to a minimum, which minimizes the influence of barrier disorder on the QW-exciton and causes a shallower localization potential in the QW.

In view of its eventual role as active medium in MC-2, it is worth mentioning that the observed exciton linewidths meet the requirements for reaching the SCR according to Sec. 4.1.2. This is certainly true at low temperatures, where the emission linewidth is assumed to correspond to the inhomogeneous broadening, i.e. $\gamma_{\text{inh}} \sim 18 \text{ meV}$. At RT the SCR conditions might be more critical owing to observed linewidths around 50 meV. However, note that here the occupation of states at higher energy cannot be neglected anymore and thus the observed linewidth might overestimate the actual exciton one.

The presence of another exciton located at slightly higher energy is revealed by the polarization-

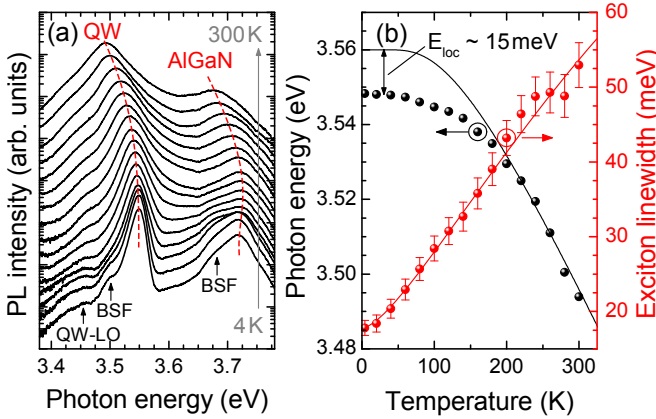
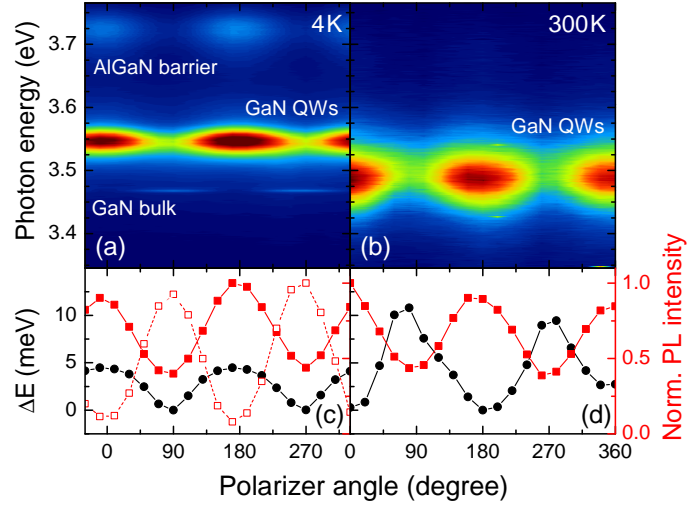


Figure 4.42: (a) T -dependent micro-PL spectra of MC-2 without top-DBR obtained under cw-excitation. Spectra are vertically shifted for clarity. The red lines are a guide to the eye for the main emission peaks arising from the QW exciton and the AlGaIn barrier. (b) Peak energy (black) and linewidth (red) of the QW emission as a function of T . According to a fit with Eq. (3.5) $E_{\text{loc}} \approx 15 \text{ meV}$ (black line). From Ref. [169].

Figure 4.43: Polarization-resolved PL-spectra of MC-2 without top-DBR obtained under pulsed excitation: (a) at 4 K and (b) at 300 K. Corresponding evolutions of peak energy (black) and intensity (red solid squares) of the QW-emission are shown below: (c) 4 K and (d) 300 K. In (c) the intensity of the bulk GaN emission is shown for comparison (red open squares). Polarization $\mathbf{E} \parallel c$ corresponds to a zero polarizer angle. Taken from Ref. [169].



resolved PL-measurements displayed in Fig. 4.43. Here, the sample was excited non-resonantly with a large spot size of about $50\mu\text{m}$ by means of the pulsed Nd:YAG laser providing a high peak power density of 65 kW/cm^2 . Thus, even at low temperature PL is expected to be dominated by free carriers, giving direct access to the selection rules. The RT spectra in Fig. 4.43(b) are dominated by the QW emission, which exhibits a pronounced polarization dependence in intensity and emission energy (cf. Fig. 4.43(d)). Both quantities are notably anti-correlated: the highest PL peak intensity I_{PL} appears for the lowest peak energy along the extraordinary direction ($\mathbf{E} \parallel c$) and vice versa along $\mathbf{E} \perp c$. The relative peak-energy shift ΔE_{PL} amounts to about 10 meV. This behavior indicates the existence of (at least) two partially orthogonal polarized exciton levels with an energy separation smaller than their linewidth. Their relative weight in PL is then determined by the thermal occupancy and the distribution of oscillator strength. Thereby, the observed ΔE_{PL} represents a lower limit for the real level splitting ΔE . Both values become equal when the linear polarization degree ρ of the participating levels equals unity, i.e. when both excitons are completely counter-polarized. The degree of linear polarization in PL is defined by:

$$\rho = \frac{I_{\text{PL}}^{\mathbf{E} \parallel c} - I_{\text{PL}}^{\mathbf{E} \perp c}}{I_{\text{PL}}^{\mathbf{E} \parallel c} + I_{\text{PL}}^{\mathbf{E} \perp c}}. \quad (4.39)$$

According to the electronic properties of GaN at the Γ -point, these two levels are ascribed to the A- and the B-excitons, i.e. X_A and X_B , respectively.

The behavior at low temperature shown in Fig. 4.43(a) is remarkably different: two additional emission bands are resolved originating from the AlGaIn barrier and from the unstrained GaN substrate/buffer. The QW-emission follows a similar polarization dependence over the whole temperature range. It is co-polarized with the barrier-PL and counter-polarized with respect to the emission of bulk GaN. The latter exhibits the largest I_{PL} for $\mathbf{E} \perp c$. For the QW and the bulk GaN emission bands ρ was derived to be equal to 0.39 and -0.85 , respectively. Interestingly, at 4 K the maximum intensity of the QW-emission coincides with the highest peak energy, i.e. the opposite situation compared to the RT case. Two effects have to be considered to explain this

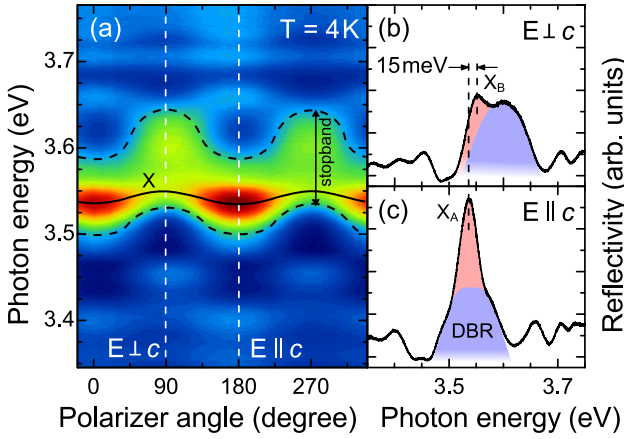
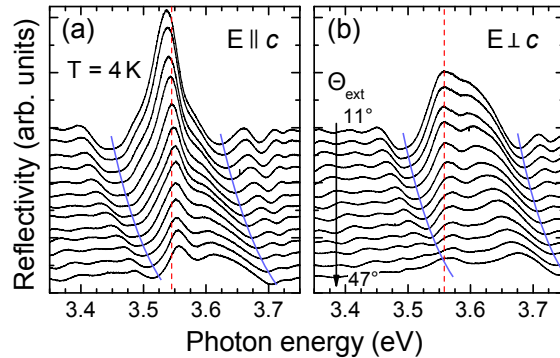


Figure 4.44: Polarization-resolved reflectivity of MC-2 without top-DBR recorded at 4 K under an angle of 11° : (a) color map of the spectra. The black solid line marks the position of the excitonic response. Spectra along the white dashed lines are shown on the right-hand side and nearly correspond to polarization (b) perpendicular and (c) parallel to the c -axis. Separate contributions due to excitons and the DBR are shaded in red and blue, respectively. Taken from Ref. [169].

behavior. First, owing to a splitting $\Delta E \geq 10$ meV the thermal population and thus the influence of X_B states is expected to be negligible at this temperature, and second: the contribution of defect-states has to be taken into account at 4 K. They are present in the low-energy tail of the QW-emission (cf. BSF in Fig. 4.42(a)) and will potentially follow a different polarization behavior. In a previous study they have been even found to be unpolarized [296]. In such a case their influence would increase in the polarization direction where the QW free-exciton emission is low. As a result, the superposition of PL from localized and free excitons would appear at lower energies.

The interpretation of the PL results is in perfect agreement with the low-temperature reflectivity measurements shown in Fig. 4.44. They have been acquired close to normal incidence (11°) in the goniometer configuration. The DBR stopband is clearly visible. It features a width of approximately 100 meV (cf. Fig. 4.2(a)) and a pronounced polarization-dependence for the central energy E_{DBR} . The latter property is caused by birefringence [297], leading to different phase thicknesses in Eq. (4.4). According to Fig. 2.6, n_o is always smaller than n_e in the transparency range in III-nitrides causing for a given layer thickness a lower E_{DBR} for $E \parallel c$.

Figure 4.45: Angle-resolved reflectivity spectra of MC-2 without top-DBR measured at 4 K for: (a) $E \parallel c$ and (b) $E \perp c$. Modes of photonic origin (blue) can be clearly separated from excitonic ones (red) due to their pronounced dispersion.



On top of the stopband the excitonic contribution is well resolved for all polarization angles. Its polarization-dependent energy shift can be followed in the spectral profiles corresponding to $E \perp c$ and $E \parallel c$ given in Figs. 4.44(b,c), respectively.¹³ Note that owing to the complexity of

¹³Only minor deviations are caused by the finite angle of incidence.

the structure, including occurrent non-idealities such as interface roughness and thickness inhomogeneities, and due to the uncertainty in the optical constants of each layer, the excitonic response could not be accurately modeled in the reflectivity spectra. Nevertheless, the features ascribed to excitons in Fig. 4.44 were evidenced to be free of any PL contribution and to be almost non-dispersive in the low-temperature angle-resolved reflectivity measurements shown in Fig. 4.45. Indeed, therein modes of photonic origin such as the DBR stopband follow a pronounced angular dispersion governed by the variation of the optical thickness in Eq. (4.4), whereas excitonic modes remain at almost constant energy and undergo only phase modulations due to interference. Thus, the absolute exciton energy position cannot be concluded from reflectivity measurements, but the polarization dependence hints at the relative energy shift. The observed energy variation with polarization is consistent with the PL results obtained at RT (cf. Fig. 4.43), confirming the presence of two partially counter-polarized excitonic levels. From Figs. 4.44(b,c), the energy splitting between X_A and X_B amounts to ~ 15 meV. This value exceeds ΔE_{PL} indicating the influence of thermal occupation in PL experiments and an only partial polarization, i.e. $|\rho| < 1$.

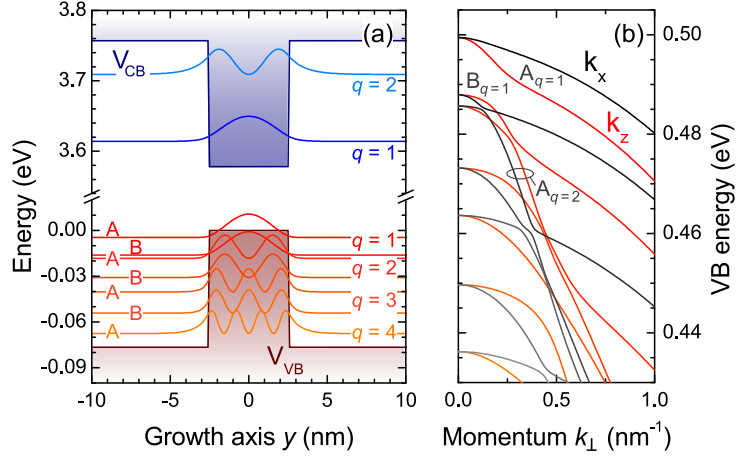
To conclude the experimental studies, the fundamental state of these m -plane GaN MQWs seems to consist of two excitonic transitions, which obey eminently counter-polarized selection rules and that are separated by an energy splitting ranging somewhere in between 10 and 15 meV. The value of the energy splitting validates the contribution of X_B -states to the QW-emission at elevated temperatures in Figs. 4.42(a) and 4.43(b), further implicating that the real exciton linewidth at RT is potentially lower than the FWHM reported in Fig. 4.42(b). By contrast, owing to a negligible thermal population at 4 K the PL-spectra shown in Fig. 4.43(a) should be dominated by X_A . As a result, the weight of the relative oscillator strengths for X_A along ordinary and extraordinary polarization directions can be estimated based on the observed $\rho = 0.39$. Indeed, since the occupancy around the Γ -point is independent of the light-polarization, the ratio of the PL-intensities translates directly into the oscillator strengths leading to $f_{osc,A}^{E\parallel c} : f_{osc,A}^{E\perp c} \approx 70 : 30$.

The Influence of Strain

The experimental PL and reflectivity measurements reveal a counter-polarization of the QW-exciton and AlGaIn barrier emissions with respect to the expectations for unstrained GaN (cf. Tab. 2.4) and the observed behavior for the GaN substrate in Figs. 4.43(a,c). The emission of the latter exhibits a strong linear polarization $\rho = -0.85$ along $E \perp c$ and an emission energy around 3.47 eV at 4 K. Both quantities match the expectations for D_0X_A and X_A in nearly relaxed GaN [53, 298]. The modified behavior of the AlGaIn barrier can be understood when considering the large negative crystal-field splitting Δ_{cf} in AlN. Already for low Al-contents in between 4 and 10% depending on the strain state, this leads to a reversed VB ordering and a counter-polarized optical response with respect to relaxed GaN. In this case, the VB with the highest energy is B dominating for $E \parallel c$ [44]. By contrast, the discrepancy between the polarization-dependence of the QW-emission and the behavior observed for the GaN substrate cannot be explained in a straightforward manner. Here, the 2D-confinement of the QW and the impact of strain issued from the AlGaIn-based bottom-DBR, which exhibits smaller lattice constants (cf. Fig. 4.41), have to be taken into account.

In order to provide a comprehensive picture of the non-polar MQW properties, the experimen-

Figure 4.46: Simulation of a 5 nm-thick *m*-plane GaN QW in between $\text{Al}_{0.13}\text{Ga}_{0.87}\text{N}$ barriers: (a) eigenenergy levels and corresponding squared wave-functions. (b) VB dispersion as a function of the in-plane wave-vector \mathbf{k}_z (red-orange) and \mathbf{k}_x (black-gray).



tal results shall be complemented and evaluated by an appropriate theoretical modeling based on the *k.p*-method for wurtzite crystals [40, 299]. While wide parts of this study on MC-2 are based on Refs. [169, 272], the *k.p*-formalism presented therein was strictly speaking only valid for strained bulk GaN layers. By contrast, the present section will take the QW-structure fully into account, using the Schrödinger-*k.p* method described in Sec. A.1. Emerging differences between the *k.p*-results calculated using a 2D or 3D geometries will be commented. In the following, the cavity section is assumed to be pseudomorphically strained on the intermediate lattice constants acquired in the bottom-DBR in agreement with the discussion of Fig. 4.41. The variation of the strain state between 4 K and RT due to the different thermal expansion coefficients of AlGa_N and GaN will be neglected [300].

Figure 4.46(a) shows the computed energy and eigenfunction spectrum of a single 5 nm-thick *m*-plane GaN QW, that is sandwiched in between infinitely thick $\text{Al}_{0.13}\text{Ga}_{0.87}\text{N}$ barriers and strained on lattice constants corresponding to an AlGa_N alloy of $x_{\text{Al}} = 0.28$ (cf. Eq. (2.9)). Similarly to the idealized *c*-plane case of Fig. 2.7, the CB potential gives rise to two confined electron energy levels, whereas the VB trap allows a variety of sub-bands arising from the mixed three VBs of GaN in the vicinity of the Γ -point. Note however that due to the non-polar surface orientation the QW is free of built-in electric fields [75], which widely cancels optical transitions between CB and VB sub-bands with different quantum numbers $q_{e/h}$ due to symmetry conditions (cf. Eq. (2.42) and corresponding explanations). The optical response of the QW will thus be governed by A and B excitons related to the electron and hole sub-bands with $q_{e/h} = 1$, both being separated from the $q_{e/h} = 2$ transitions by about 110 meV. Based on these simulations, the energy splitting between X_A and X_B is expected to be 12 meV, i.e. a value in excellent agreement with experimental observations. Figure 4.46(b) shows the in-plane dispersion of the hole sub-bands. Due to the loss of symmetry, the in-plane directions \mathbf{k}_z and \mathbf{k}_x , being parallel to the crystal *c* and *a*-axes, respectively, exhibit different effective masses leading to various interactions in between the different sub-bands.

In analogy to the discussion of a strained *m*-plane bulk GaN layer reported in Sec. 2.2.1 (cf. Figs. 2.4(d-f)), the computed QW-transition energies and the respective f_{osc} -distribution as a function of the Al-content x_{Al} imprinting the in-plane lattice constants are shown in Fig. 4.47. The results of the bulk *k.p*-simulations from Ref. [169] are added in light colors for comparison. As in the bulk case, the transition energies in Fig. 4.47(a) increase with the value of

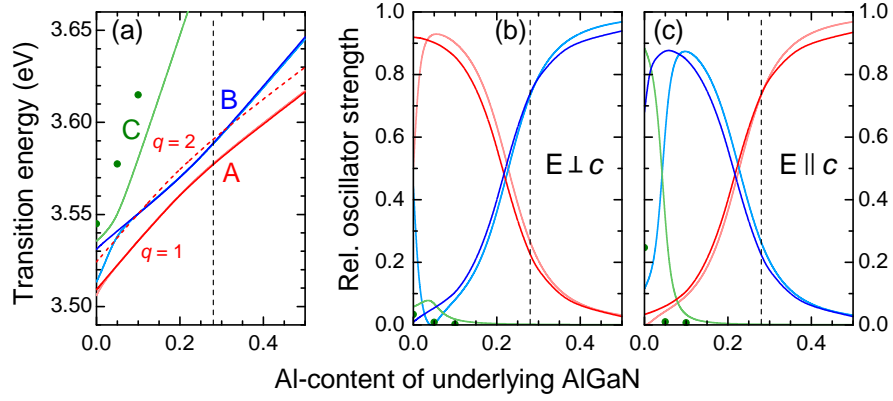


Figure 4.47: Results of Schrödinger- $k.p$ calculations performed for an m -plane 5 nm thick GaN/Al_{0.13}Ga_{0.87}N QW strained on AlGaN with an Al-content varying between 0 and 50%: (a) evolution of the transition energy for A (red), B (blue), and C (green) excitons at $\mathbf{k}_{\perp} = 0$. For C strong mixing with excited A and B-bands is observed. Green dots correspond to bands with high C-fractions emphasizing the trend. The red dashed line corresponds to the $q = 2$ -level of the A-VB. (b,c) Corresponding evolution of f_{osc} for (b) $E \perp c$ and (c) $E \parallel c$. The strain-state of the QWs in MC-2 as deduced from XRD is marked by the vertical dashed line. In all sub-figures, the computed results for pseudomorphically strained thick GaN layers are shown in light colored solid lines for comparison (taken from Ref. [169]).

the compressive strain. Different deformation potentials and strong p -orbital repulsion lead to an anticrossing between the fundamental A- and B-bands for $x_{Al} \approx 22\%$. This is accompanied by an exchange of oscillator strength between the polarization directions $E \perp c$ and $E \parallel c$ as displayed in Figs. 4.47(b,c). Indeed, for low compressive strain values and relaxed structures X_A is supposed to dominate the optical response for $E \perp c$, in a very similar fashion to the case of strain-free bulk GaN. In comparison, X_B is counter-polarized: in contrast to the bulk even for the strain-free case $x_{Al} = 0$. When the compressive strain exceeds the $x_{Al} = 22\%$ equivalent, both excitons exchange their roles: here, the lowest energy transition X_A dominates for $E \parallel c$, while X_B lying at higher energy gains importance along $E \perp c$. This is the situation observed in the experiments. According to the $k.p$ -simulations, the fundamental excitons X_A and X_B in the case $x_{Al} = 28\%$ are characterized by:

$$\begin{array}{llll}
 \mathbf{X}_A & E_A = 3.577 \text{ eV} & f_{osc,A}^{E \parallel c} : f_{osc,A}^{E \perp c} = 0.74 : 0.22 & \rho_A = 0.54 \\
 \mathbf{X}_B & E_B = 3.589 \text{ eV} & f_{osc,B}^{E \parallel c} : f_{osc,B}^{E \perp c} = 0.22 : 0.74 & \rho_B = -0.54
 \end{array} \quad (4.40)$$

Here, the sum rule for the relative oscillator strengths is not fulfilled owing to two different facts: (i) a potential contribution in the third polarization direction, where \mathbf{E} is oriented parallel to the growth axis, is not considered as it only becomes weakly effective for high angles of incidence, and (ii) the effective wave-function overlap in the QW is taken into account. Due to different penetration depths of electrons and holes into the barriers p_{QW} is reduced to about 0.98 for the present QW. The experimentally observed transition energies are slightly reduced with respect to the theoretical prediction owing to the influence of E_{loc} and the uncertainties in the modeling.

The differences between the $k.p$ -results for 2D and 3D geometries in Fig. 4.47 are fairly negligible for high compressive strain values, but significant for almost relaxed structures, i.e. $x_{Al} < 0.05$. Here, the discrepancy arises from two different effects: first, even in a relaxed QW-lattice the 2D-confinement breaks the electronic symmetry in the hexagonal basal plane, and second, the interactions occurring in between different sub-bands cause a significant redistribution of oscillator strength. The latter mechanism applies especially for the C-exciton, that couples and mixes with higher A- and B-bands but continuously shifts to higher energies in agreement with the predictions of the 3D-simulations.

In conclusion, the experienced lattice strain imprinted from the bottom-DBR leads to a redistribution of exciton oscillator strength in the m -plane GaN MQWs of the active region. The fundamental QW-excitons X_A and X_B are separated by about 12 meV and partially counter-polarized with a high degree of linear polarization $|\rho| \approx 0.5$. The experimental results agree accurately with the employed $k.p$ -method taking into account the 2D-confinement and the strain-state. Note that a strain variation of only 1% is necessary to explain the discrepancy between experimental and theoretical ρ -values. In view of the resonance conditions in the eventual MC structure, it is further worth mentioning that the overlap between the DBR stopband and the exciton is better for X_A along $\mathbf{E} \parallel c$ than for X_B in the ordinary direction.

Side-Glance: X-ray Diffraction of MC-2

For the purpose of drawing a complete analysis of the strain state in MC-2, the initial XRD studies that have been carried out externally and remained incomplete have been repeated in-house recently. Surprisingly, the results hint at a significantly modified strain state, indicating pseudomorphic strain along the c -direction and a partial stress relaxation along the in-plane a -direction. Thereby the experienced stress is generally lower than initially assumed. Owing to various transfers and low-temperature cooldowns MC-2 was subjected to a huge amount of mechanical and thermal stress during the past three years, which led to the formation of cracks parallel to the c -direction, that already broke the sample into multiple pieces. It is thus very likely that this sample is aging. Note however that $k.p$ -simulations for the new strain state yield almost identical optical selection rules and that the entirety of the findings about the anisotropic light-matter coupling reported in Refs. [169, 272] and in the upcoming analysis are solely based on optical measurements. They remain thus fully valid. Further information about this issue can be found in App. A.3.

4.7.3 Anisotropic Coupling Regime

The previous considerations provide the basis for understanding the anisotropic optical properties of the full MC-structure MC-2. The latter is completed by a dielectric top-DBR, which exhibits a purely isotropic response. Thus, the optical anisotropy arises exclusively from the III-nitride layer stack. Three sources of optical anisotropy have to be considered: the polarization-dependent energy shift of the bottom-DBR stopband as observed in Fig. 4.44, the exciton selection rules discussed above, and finally the anisotropy of the cavity mode [301]. In analogy to the discussion on the bottom-DBR, the latter depends on the birefringence according to the phase thickness in Eq. (4.4). The polarization-dependent energy shift is expected to be similar to the one of the bottom-DBR, amounting to about ~ 35 meV. The situation is summarized in Fig. 4.48.

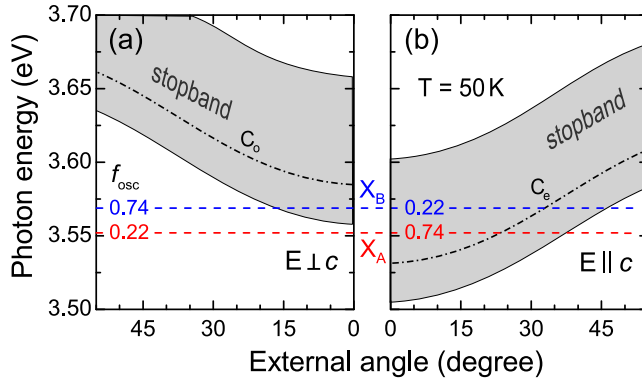
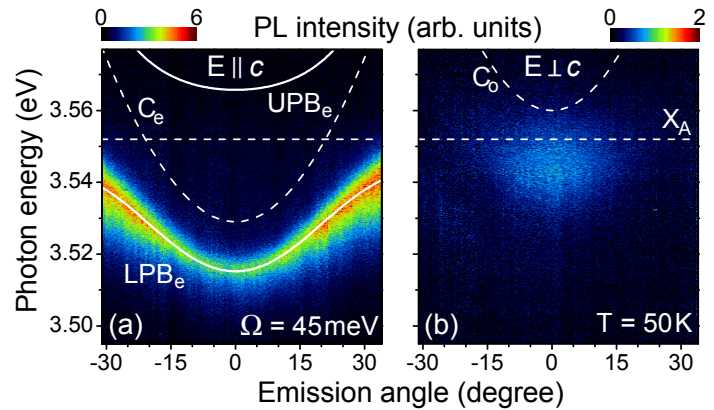


Figure 4.48: Schematic view of the optical response of the MC-2 III-nitride layer stack: (a) for $\mathbf{E} \perp c$ the bottom-DBR stopband (gray) hardly overlaps with X_A (red) and X_B (blue). On the contrary, for $\mathbf{E} \parallel c$, there is a perfect overlap between the excitonic resonances and the bottom-DBR. The respective cavity mode positions C_0 and C_e of the full-MC are given for comparison.

Experimental Results

Figure 4.49 shows polarization-resolved far-field PL-spectra of MC-2 recorded at 50 K under non-resonant pulsed excitation and a low-injection level at the same sample spot. Along the extraordinary polarization direction $\mathbf{E} \parallel c$, the emission is dominated by an intense dispersive mode that converges toward the X_A energy at high angles. It is attributed to the LPB emerging from the strong-coupling between the extraordinary cavity mode C_e and X_A , referred to as LPB_e in the following. The SCR arises in this polarization direction due to the high value of $f_{\text{osc},A}^{\mathbf{E} \parallel c}$ and the good matching between the exciton and the DBR at low temperatures according to Fig. 4.44(c). Reproducing the LPB_e dispersion with the COM yields a Rabi-splitting $\Omega = 45 \text{ meV}$ and a negative detuning $\delta = -23 \text{ meV}$. The linewidth amounts to about 10 meV at $\mathbf{k}_\perp = 0$ and increases continuously toward higher angles reaching 16 meV at $\Theta_{\text{ext}} = 30^\circ$. Considering an exciton linewidth $\gamma_X \approx 20 \text{ meV}$ at this temperature (cf. Fig. 4.42) and a photonic fraction of 70% at the bottom of the LPB_e , the Q -factor of MC-2 can be estimated to be around 500. The LPB_e occupancy appears highly non-thermal. This is caused by the high photon fraction in the center of the BZ and the low lattice temperature leading to the formation of a relaxation bottleneck according to Ref. [140]. By contrast, no trace of X_B or UPB_e can be identified in PL. In analogy to the discussion for MC-1, this is likely caused by an efficient carrier relaxation to the excitonic reservoir, low thermal occupation factors, the high excitonic fraction at small angles, and residual damping emerging from the barrier absorption tails.

Figure 4.49: Far-field PL-spectra of MC-2 obtained at 50 K for (a) $\mathbf{E} \parallel c$ and (b) $\mathbf{E} \perp c$. Uncoupled modes are shown with dashed lines. Solid lines in (a) mark the polariton branches fitted by the coupled-oscillator model. Taken from Ref. [169].



The existence of the SCR for X_A along $\mathbf{E} \parallel c$ is further confirmed by the reflectivity measurements and the high-angle Fourier-PL image displayed in Fig. 4.50. Both show a clear inflection point and the converging of LPB_e toward the free exciton energy at high in-plane momentum. As in Fig. 4.49, UPB_e could not be observed. At higher angles LPB_e crosses a BM, leading to a leakage of cavity polaritons and a restriction of the relaxation bottleneck to the vicinity of the inflection point. The absence of any signature of X_B can be explained by its low oscillator strength in this direction. Indeed, taking into account γ_X , Ω , and the observed Q -factor, the coupling strength g_0 of X_A with $f_{\text{osc},A}^{\mathbf{E} \parallel c} = 0.74$ can be estimated to 27 meV based on Eq. (4.26). When now assuming a simple scaling of g_0 with $f_{\text{osc},B}^{\mathbf{E} \parallel c} = 0.22$ according to Eq. (4.16), the resulting Rabi-splitting for X_B would be equal to zero, i.e. the light-matter coupling strength is not sufficient to exceed the excitonic and photonic damping rates giving rise to the WCR. Thus, even when ignoring that γ_X exceeds the X_A - X_B energy separation only a very weak optical signature may be expected from X_B along $\mathbf{E} \parallel c$.

This situation is reversed for the ordinary polarization direction. Here, X_B features a high $f_{\text{osc},B}^{\mathbf{E} \perp c}$ value, that should be sufficient to establish the SCR given that the overlap with the bottom-DBR stopband in Fig. 4.44(b) is adequate. On the contrary, X_A is expected to be only weakly coupled. Reflectivity measurements identical to that of Fig. 4.50(a) have also been carried out for $\mathbf{E} \perp c$ (not shown here), but revealed no evidence for a polariton or cavity dispersion. Similarly, in Fig. 4.49(b) only a very weak emission is detected in the ordinary direction. It is located slightly below X_A in energy, confined around zero in-plane momentum, and only weakly dispersive. At first sight, the origin of this mode is not clear.

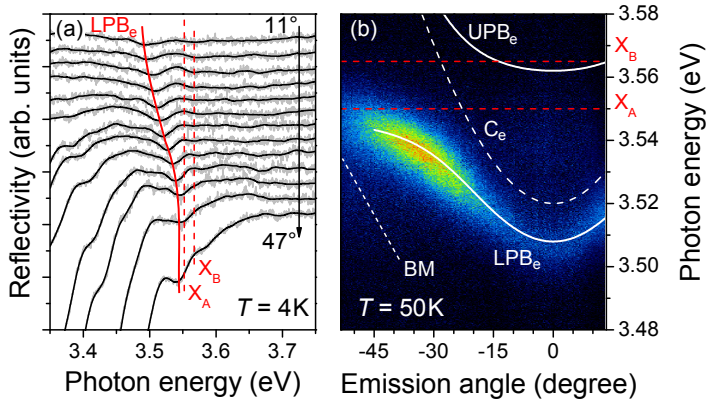


Figure 4.50: (a) Angle-resolved reflectivity spectra recorded at 4 K with $\mathbf{E} \parallel c$: the red solid line highlights the LPB_e dispersion converging toward X_A at high angles. (b) Fourier-PL image acquired below threshold for $\mathbf{E} \parallel c$ at 50 K showing a clear anticrossing between LPB_e and X_A , and a signature of the relaxation bottleneck. Taken from Ref. [272].

Transfer-Matrix Simulations

In order to gain a deeper insight into the complex light-matter coupling regime of MC-2, anisotropic TMS have been performed. The applied 4×4 -formalism is based on Ref. [302], and uses anisotropic optical constants of the AlGaIn alloy. These have been linearly interpolated using the analytic dispersion model of Ref. [303] and the experimental data available for GaN [59], and AlN [44, 60]. More details about the procedure can be found in Sec. A.2. All imaginary parts of the dielectric function have been neglected, except for the GaN MQWs, for which the applied complex refractive index is shown in Fig. 4.51(b). It is composed of a background refractive index dispersion, that is linked to the BB-absorption edge modeled by a Gaussian-broadened Heaviside-function, and the excitonic resonances. The latter are

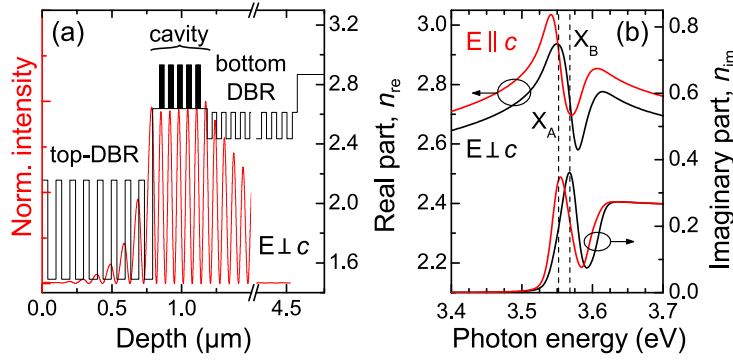


Figure 4.51: Optical properties of MC-2 [169]: (a) depth profile of the refractive index at the cavity mode energy for $E \parallel c$ (black) and corresponding intensity profile of the electric light-field (red). (b) Anisotropic complex refractive index of the GaN QWs used for TMS.

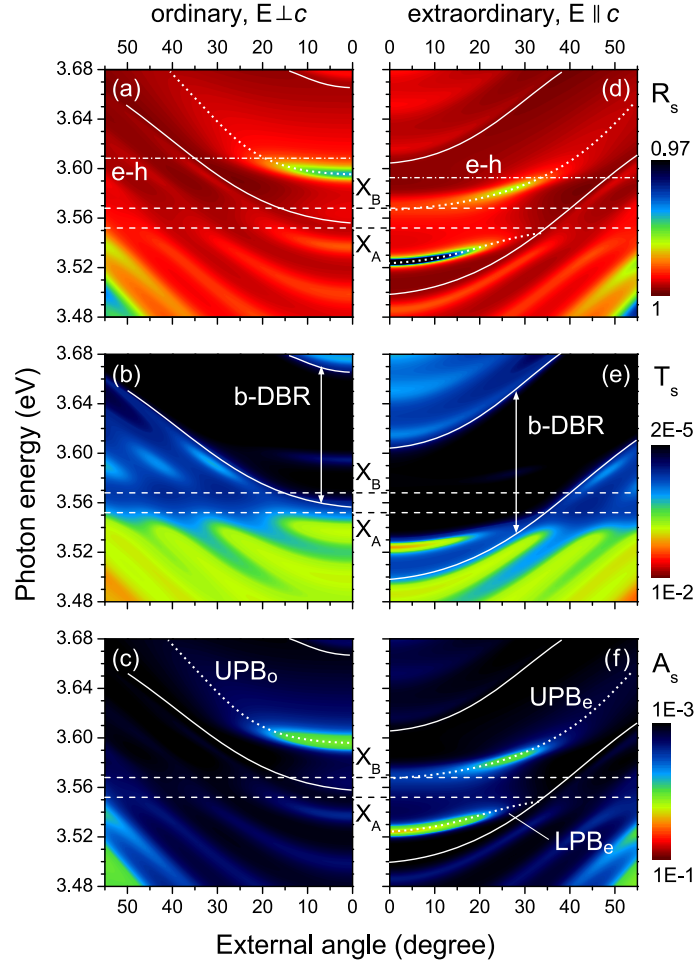
represented in the local approximation by Voigt-profiles with realistic homogeneous and inhomogeneous linewidth values equal to $\gamma_{\text{hom}} = 7 \text{ meV}$ and $\gamma_{\text{inh}} = 20 \text{ meV}$, respectively. They obey the oscillator strength distribution deduced from k - p -simulations, using for a certain polarization direction the relation $f_X = f_{\text{osc}} \cdot 2.5 \cdot 10^{13} \text{ cm}^{-2}$ [168],¹⁴ and considering an exciton binding energy $E_B = 41 \text{ meV}$ as deduced from envelope function calculations. Figure 4.51(a) compares the adopted refractive index profile with the calculated electric-field intensity profile of the cavity-mode for $E \perp c$. In the cavity section, the high refractive index of the five QW-sets situated at the field antinodes can be clearly resolved.

Figure 4.52 summarizes polarization-dependent TMS results for MC-2 in reflectivity R , transmission T and absorption A . All spectra have been calculated as a function of the external angle Θ_{ext} for s -polarization. The latter corresponds to the situation where the incoming light is unpolarized and the detector filters the component polarized perpendicular to the plane of incidence. The position of the bottom-DBR stopband is clearly revealed in the T -spectra of Figs. 4.52(b,e). It features a width of approximately 100 meV and a polarization-dependent energy shift of about 50 meV , i.e. slightly more than the experimentally observed shift reported in Fig. 4.44, indicating the uncertainty of the applied refractive indices.

Superimposed to the DBR-stopband dispersive modes emerge for both polarization directions. They shall first be discussed for $E \parallel c$. As expected from the previous analysis the high oscillator strength of X_A and the proper overlap with the bottom-DBR stopband lead to unambiguous signatures of the SCR. With a slight negative detuning, LPB_e converges toward X_A at high angles and leaves the photonic confinement of the bottom-DBR for $\Theta_{\text{ext}} > 35^\circ$. For even higher in-plane momentum weak anticrossings with the bottom-DBR Bragg modes (BMs) may occur. The computed Rabi-splitting agrees accurately with the experimental findings from Fig. 4.43(a). By contrast, due to its low oscillator strength and the small energy separation from X_A , being smaller than its actual linewidth, X_B remains widely absent. In the refractive index dispersion of Fig. 4.51(b) it only appears as a shoulder-like feature that causes the large smearing of UPB_e close to normal incidence in Figs. 4.52(d-f) and a strong damping of the latter in reflectivity. This effect is additionally intensified by the proximity of the BB-absorption edge. For illustration, the minimum of the UPB_e reflectivity occurring around 27° amounts to 0.985 , while the LPB_e signal drops down to 0.936 at zero in-plane momentum. This finding confirms the reflectivity results from Fig. 4.50(a), where no signature of the UPB_e dispersion could be

¹⁴The value $f_X = 5.1 \cdot 10^{13} \text{ cm}^{-2}$ given in Ref. [168] has been overestimated by about a factor of two.

Figure 4.52: Anisotropic TMS results for MC-2: (a-c) reflectivity R , transmission T , and absorption A spectra for the optical axis oriented parallel to the plane of incidence $\mathbf{E} \parallel c$, respectively, and (d)-(e) for $\mathbf{E} \perp c$. Horizontal dashed lines mark the energy position of the optically active excitons. In (a) and (d) the energy of the band-to-band absorption edges is also given (dash-dotted line, e-h). The dispersive edges of the bottom-DBR stopband are highlighted by continuous lines in the T -spectra (b-DBR). Dotted lines act as a guide to the eye for apparent eigenmodes. A and T -data are displayed in logarithmic scale. See text for details concerning method and interpretation. Taken from Ref. [169].



traced. It is further worth mentioning that the spot size used for reflectivity measurements, i.e. $\sim 100\mu\text{m}$, significantly exceeds the lateral scale of photonic disorder, which causes a reduced overall sensitivity to corresponding dips in reflectivity. Eventually, the strong damping of UPB_e close to $\Theta_{\text{ext}} = 0$ is a signature of the WCR for X_B along $\mathbf{E} \parallel c$.

In comparison, the situation in the ordinary polarization direction is far less obvious. Both excitons are located on the low-energy side of the bottom-DBR stopband preventing the formation of a potential LPB_o . However, it is worth noticing that according to the linear dispersion theory one of the two polariton branches might exist without the other, especially when the UPB is damped by the strong BB-absorption in bulk MCs based on wide-bandgap semiconductors [304]. Transferred to the present case, the absence of LPB_o due to a lossy optical confinement does not automatically prevent the formation of UPB_o . Thus the well-resolved mode located around 3.595 eV may be attributed to a UPB formed by X_B and C_e . This interpretation is confirmed when simulating the same structure with an artificially redshifted bottom-DBR stopband (not shown here): in this case, the good optical confinement gives rise to clear characteristics of the SCR similar to what is observed for $\mathbf{E} \parallel c$. Eventually, the question regarding the coupling regime of X_B cannot be clearly answered. Despite a potentially existing UPB_o , the absence of LPB_o will prevent the system to show any effect related to polariton condensation and the weak absorption signature simulated at the X_B -energy in Fig. 4.52(c)

suggests the presence of the WCR. Note in addition that this latter mode would progressively transform into LPB_0 when artificially redshifting the bottom-DBR. On the contrary, for X_A applies the same argumentation than that given for X_B along $\mathbf{E} \parallel c$: the low oscillator strength and the large linewidth promote the WCR. It additionally lies right on the edge of the bottom-DBR stopband, which gives rise to interpret the weak luminescence detected for $\mathbf{E} \perp c$ in Fig. 4.43(b) as originating from localized X_A -states. A modulation due to the first low-energy BM may explain the slight dispersive shape and the restriction around $\Theta_{\text{ext}} = 0$.

Side-Glance: Engineering the Coupling Regime

Before proceeding to the discussion of the non-linear emission properties of MC-2, an interesting potential of such non-polar MCs shall be briefly highlighted: the previous analysis emphasizes the strong impact of a certain strain-state on the anisotropic optical response of such non-polar III-nitride MC-structures. The design of the bottom-DBR, e.g. a variation of the AlGaN composition or even switching to AlInN or AlInGaN alloys, allows to directly tune the distribution of f_{osc} of the different excitons and thus to engineer the light-matter coupling regime. In doing so different excitons could be promoted to the strong- or weak coupling regime with the polarization-dependent cavity modes. Naturally, technological restrictions arising from the need for a high structural quality and a sufficiently high refractive index contrast have also to be considered. Ref. [169] details this capability and provides a first phase diagram for varying Al-contents of the bottom-DBR bilayers.

4.7.4 Non-linear Emission Properties

The major part of the aforementioned experimental results was recorded at $T = 50\text{ K}$. This temperature was not chosen randomly, but states the following compromise: at very low temperature excitation with the Nd:YAG laser leads directly to a non-linear emission even for the lowest adjustable power density, which prevents a comprehensive injection-dependent study. On the contrary, as for MC-1 the lasing regime could not be reached with the Ar^+ -laser. An upper limit for the temperature window is set by the overlap with the narrow stopband of the bottom-DBR. Indeed, X_A leaves the high optical confinement along $\mathbf{E} \parallel c$ at around 100 K switching the whole system to the WCR and preventing any study at higher temperatures as done for MC-1. All measurements presented hereafter have been performed under non-resonant pulsed excitation with the Nd:YAG laser using the Fourier-space PL-setup depicted in Fig. 4.16 with small spot diameters of $\sim 5\mu\text{m}$. The temperature was fixed to $T = 50\text{ K}$.

Polariton Lasing in an Anisotropic Coupling Regime

Figure 4.53 shows the evolution of the far-field emission spectra of MC-2 with increasing pump power density. No polarization selection was set in the collection line meaning that both polarization components $\mathbf{E} \parallel c$ and $\mathbf{E} \perp c$ were recorded simultaneously.

Under low injection conditions shown in Fig. 4.53(a) for an average power density $P = 7\text{ W/cm}^2$, the MC emission is dominated by a broad emission band centered around 3.535 eV. It is restricted to small in-plane momentum and exhibits a slightly dispersive shape. According to the discussion of Fig. 4.49, it is attributed to the recombination of localized X_A excitons that are in the WCR for $\mathbf{E} \parallel c$ and leak out at the low-energy edge of the bottom-DBR stopband. On the

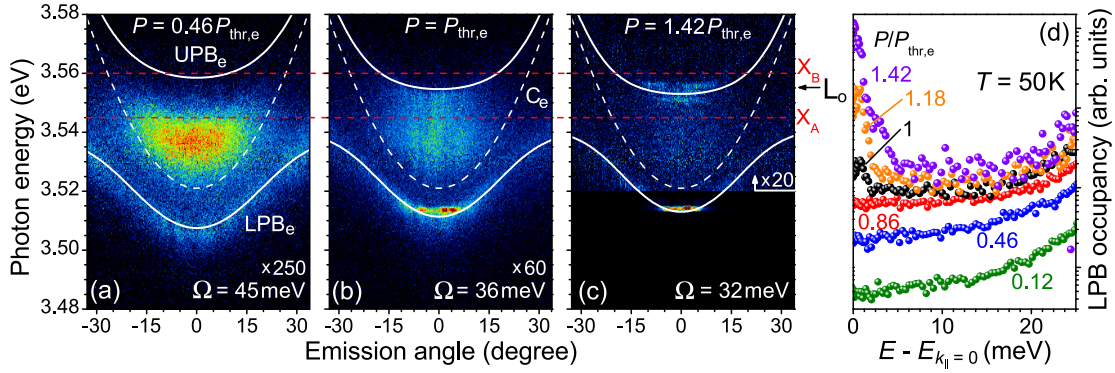


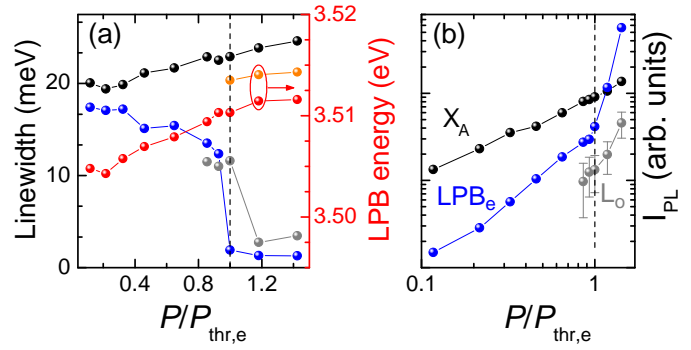
Figure 4.53: Fourier-space PL-images recorded at various excitation power densities below and above the polariton lasing threshold $P_{\text{thr},e}$ without polarization selection at $T = 50$ K. Fitted coupled modes (solid lines) are displayed for the extraordinary polarization direction only. The two free-exciton lines (red) are active in both directions. (d) Occupancy of LPB_e as a function of excitation power. Taken from Ref. [169].

low-energy side of this mode LPB_e emerges. It is much narrower, more dispersive and can be easily identified by comparison with Fig. 4.49(a). The mode dispersion has been reproduced with the COM yielding a Rabi-splitting $\Omega = 45$ meV in agreement with previous low-injection results. The detuning at this sample position amounts to about -25 meV.

Increasing the excitation power leads to a blueshift of LPB_e due to a saturation-induced reduction of the Rabi-splitting and eventually for $P_{\text{thr},e} = 15 \text{ W/cm}^2$ in Fig. 4.53(b) to a strong non-linear emission intensity rise slightly above the bottom of the branch (cf. Fig. 4.54(b)). Despite the injection-induced blueshift, the non-linear LPB_e emission occurs significantly below the modeled cavity mode energy indicating that the SCR is preserved across $P_{\text{thr},e}$. The analysis of the PL-bands at $\mathbf{k}_\perp = 0$ shown in Fig. 4.54(a) reveals further that the transition is also accompanied by a strong reduction of the linewidth. The latter decreases down to ~ 1 meV at threshold, i.e. well below the value given by the cavity Q -factor, implying high temporal coherence. On the basis of all these characteristics, the non-linear emission occurring in the extraordinary polarization direction is attributed to polariton lasing. Despite the rather small negative detuning value it emerges in the kinetically-driven condensation regime as evidenced by the non-thermal LPB_e occupancy displayed in Fig. 4.53(d). Apart from the high photonic fraction the relaxation efficiency is in this case further limited by the combination of a low local Q -factor of ≈ 350 and the low lattice temperature [25, 26]. The small blueshift of the condensed population with respect to the bottom of LPB_e can also be assigned to the strong non-equilibrium conditions and the influence of disorder.

At elevated carrier densities, the appearance of an additional mode can be noticed at higher energy $E_{L,o} = 3.552$ eV in Figs. 4.53(b,c). It is denoted as L_o in the following and also features a non-linear emission regime, that is reached for $P_{\text{thr},o} \approx 1.3 P_{\text{thr},e}$. Depending on the probed position on the sample, L_o can be more or less pronounced than the polariton lasing emission and the $P_{\text{thr},o}/P_{\text{thr},e}$ ratio may also vary. Indeed, partly issued from the surface morphology shown in Fig. 4.40(c), MC-2 is subject to strong excitonic and photonic disorder: the energy of X_A fluctuates around 3.55 eV with a standard deviation of about 5 meV and the region showing strong light-matter coupling spans a diameter of only $\sim 200 \mu\text{m}$. Note that the latter value

Figure 4.54: Analysis of the Fourier-PL power-series in Fig. 4.53 at $\mathbf{k}_\perp = 0$: (a) linewidth evolution of LPB_e (blue), X_A (black), and L_o (gray) and energy variation of the linear (red) and non-linear (orange) LPB_e emissions. (b) Respective integrated PL intensities as a function of P_{exc} . Adapted from Ref. [169].



is still much larger than the probed spot size. However, while the threshold is hardly visible in Fig. 4.54(b), the lasing feature for L_o is more obvious in the polarization-resolved power series presented in Fig. 4.55(b), that was measured around zero in-plane momentum. For $\mathbf{E} \perp c$ polarization, the low injection regime is dominated by emission of localized X_A states leaking out through the first low-energy BM. Increasing the excitation power induces a progressive blueshift of the emission band, which is accompanied by a rising L_o occupancy. This can either be caused by delocalization of X_A excitons or by population of potentially localized X_B states. Eventually the lasing emission of L_o emerges energetically between the X_A and X_B free exciton positions. The linewidth at threshold amounts to about 2.5 meV.

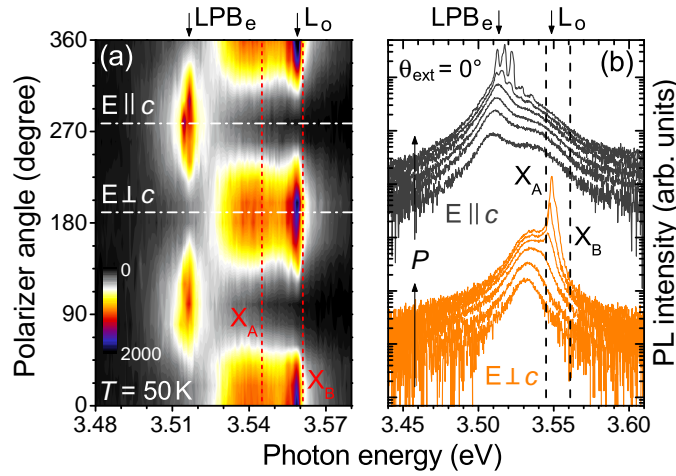


Figure 4.55: Polarization-resolved Fourier-space PL measurements performed at $T = 50$ K: (a) angle-integrated far-field emission spectra NA = 0.55 recorded above $P_{\text{thr},e}$ and $P_{\text{thr},o}$ as a function of the light-polarization, and (b) spectral profiles at $\mathbf{k}_\perp = 0$ as a function of the excitation power density P_{exc} ranging from 0.07 to $2.14P_{\text{thr},e}$ for $\mathbf{E} \parallel c$ (gray) and $\mathbf{E} \perp c$ (orange). The spectra taken along $\mathbf{E} \parallel c$ are vertically shifted.

Note once more that LPB_e is completely absent along $\mathbf{E} \perp c$ in Fig. 4.55(b), and that at the same time for the extraordinary polarization direction X_A appears only very weak (or even negligible depending on the sample spot, cf. Figs. 4.49 and 4.50(b)) although its oscillator strength is maximum.¹⁵ This counter-polarization of LPB_e with respect to X_A and L_o and the respective anisotropic light-matter coupling regime in MC-2 are further highlighted by the angle-integrated ($-33^\circ < \Theta_{\text{ext}} < 33^\circ$) polarization series presented in Fig. 4.55(a). It was recorded above the two lasing thresholds.

¹⁵Excitonic luminescence of X_A for $\mathbf{E} \parallel c$ despite the SCR may for instance be allowed due to disorder or partly uncoupled QWs situated slightly apart from the cavity light-field antinodes.

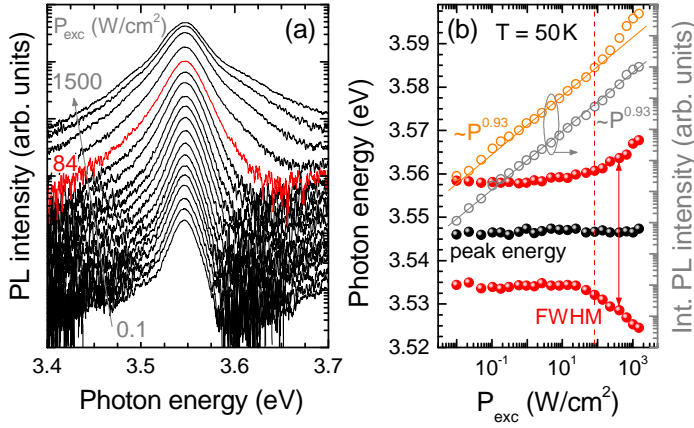


Figure 4.56: Excitation power dependent micro-PL recorded on MC-2 without top-DBR at $T = 50$ K (no polarization selection): (a) PL spectra, and (b) injection-dependent evolution of the QW peak energy (black), FWHM (red), and I_{PL} (gray), and the PL intensity integrated between 3.57 and 3.65 eV (orange). The vertical dashed line corresponds to the red spectrum in (a).

Examination of the Carrier-Injection Regime

While the non-linear emission along $\mathbf{E} \parallel c$ can be clearly attributed to polariton lasing, the mechanism of the lasing action along the ordinary polarization direction is less obvious. Here, no clear signature of any coupled or uncoupled modes could be tracked in optical experiments. In order to examine its potential origin, the carrier injection regime of the present measurements shall be investigated in more detail. Therefore, the high carrier-injection regime has been studied in the III-nitride layer stack of MC-2 in analogy to the procedure discussed for MQW-1 in Sec. 3.5. The corresponding PL-spectra recorded under pulsed non-resonant pumping at $T = 50$ K are shown in Fig. 4.56(a). In agreement with previous explanations concerning the MT in MQW-1, the injection regime and thus the collected signal in the present MQWs cannot be homogeneous, neither in depth due to the absorption profile nor in the time domain due to the pulsed excitation. Nevertheless, the detected PL is expected to be dominated by the QWs subjected to the highest injection, i.e. the four QWs the closest to the surface, giving access to certain characteristics of the exciton renormalization and the eventual MT. As expected for a field-free non-polar QW (cf. Sec. 2.3.4), the QCSE is absent and the carrier density has no influence on the peak energy of the emission in Fig. 4.56(b). By contrast, the MT appears in perfect agreement with the explanations in Ch. 3: it is accompanied by a strong increase in the PL linewidth and the rise of the electron-hole plasma emission on the high-energy side, emerging beyond $P_{\text{crit}} = 84 \text{ W/cm}^2$ in Fig. 4.56(a). This can also be followed when considering the super-linear increase of the integrated emission intensity in this energy window shown in Fig. 4.56(b).

In an oversimplified approach, this discussion can be transposed to the complete MC-2 structure by considering that the polariton lasing threshold $P_{\text{thr,e}}$ as well as $P_{\text{thr,o}}$ occur well below the value of P_{crit} . Apart from the uncertainty on the exact laser focus, it is worth clarifying that the carrier density in the bare III-nitride layer stack and in the full MC-structure being exposed to the same pumping power density may be significantly different. In the full-MC the different surface reflectivity, the transmission of the top-DBR at the laser wavelength ($\sim 65\%$) and the redistribution of the radiative excitons inside the cavity region have to be considered. Indeed, whereas in the bare III-nitride layer stack only the first set of four QWs is significantly populated due to the exponential absorption profile, the optical feedback in the

full-MC causes a fast redistribution of radiative carriers due to Rabi-oscillations. Conclusively, the values of $P_{\text{thr,e}}$ and $P_{\text{thr,o}}$ should rather be situated further below the MT than expected from a comparison with P_{crit} . This interpretation agrees well with the experiments shown in Fig. 4.55(b), where no significant changes in the emission characteristics of the QW-exciton in the full-MC can be traced, in particular with respect to the high-energy emission tail. Moreover, it is worth emphasizing that both non-linear emissions rely on the same carrier species: with regard to the proof of polariton lasing occurring for $\mathbf{E} \parallel c$, it has to be clearly excitonic.

Origin of the Lasing Action in the Ordinary Direction

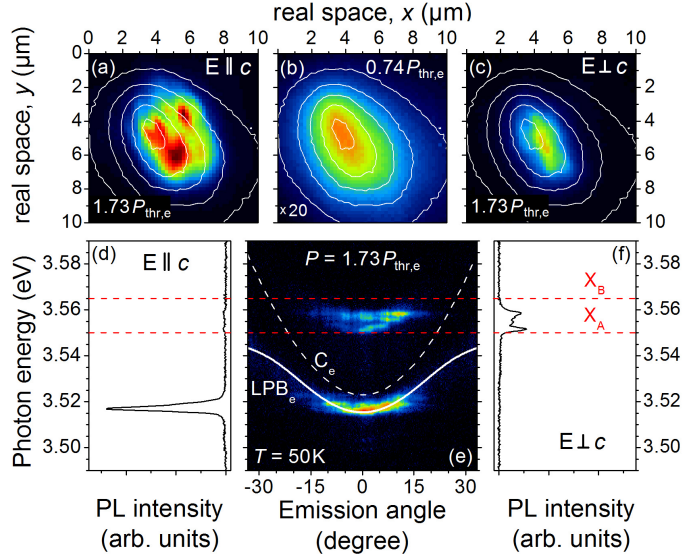
Following the previous analysis, MC-2 is operated in an injection regime where exciton saturation effects play a certain role, as evidenced by the power-dependent decrease of the light-matter coupling constant in Fig. 4.53, but well below the transparency limit. Conventional lasing based on a degenerate electron-hole population (cf. Sec. 3.3.1), i.e. at an injection level higher than the critical Mott-density, can thus be safely excluded as driving mechanism. However, in a system operated below the Bernard-Durauffourg limit a non-linear emission can still occur either based on the spontaneous decay of a coherent polariton condensate as evidenced for $\mathbf{E} \parallel c$ or alternatively due to so-called excitonic gain [111]. As an exciton represents a simple two-level system, excitonic gain requires an additional mechanism such as a biexcitonic [154, 305] or phonon-assisted transition [306], a potential BEC of excitons [307], an efficient intra-excitonic scattering channel [308, 309], or the introduction of a third energy level due to localized excitons [310]. Those mechanisms shall separately be evaluated hereafter.

Contrary to the c -plane case of MQW-1, no biexcitonic signature could be traced in the PL power-series displayed in Fig. 4.56 for these non-polar QWs. Indeed, based on Hayne's rule from Eq. (3.2) the biexciton binding energy should not exceed a value of 10 meV for the QWs of MC-2, which likely prevents any observation due to the comparably larger inhomogeneous linewidth.

Thus, biexcitonic gain as measured in Ref. [154] can be excluded for the present system. Moreover, lasing mechanisms relying on a phonon-assisted transition or an exciton-exciton scattering process following Ref. [309] can also be ruled out as gain source when taking into account that the L_0 lasing emission emerges between the X_A and X_B energy positions. Based on an LO-phonon energy of 92 meV and $E_B = 41$ meV the corresponding gain bands are supposed to emerge at considerably lower energy than the exciton resonances. As detailed in Sec. 4.1.3, BEC appears when the extent of the particle wave-function approaches the inter-particle distance. Taking into account the exciton effective mass, this is expected to occur well below 1 K for these QWs, being incompatible with the present observations at 50 K.

Despite the state of the art quality, even at $T = 50$ K the present MQW-system is clearly dominated by disorder, as evidenced by the predominantly inhomogeneous linewidth and a relatively large localization energy $E_{\text{loc}} \approx 15$ meV (cf. Fig 4.42). These conditions and the position of L_0 close to the energy of X_A and X_B seem to be compatible with a gain mechanism relying on localized exciton states [308, 310]. Given that at a sufficiently high carrier density the potential gain band would span the whole spectral range of localized X_A and X_B states due to the small energy separation and the comparably large linewidth, the non-linear emission would eventually occur at the energy position exhibiting the largest optical feedback. Taking

Figure 4.57: Polarization resolved real-space patterns of the lasing emissions in MC-2: (e) Fourier-PL image recorded above the two lasing thresholds without polarization selection (log-scaled, $T = 50\text{K}$). (d,f) Spectral profiles at $\mathbf{k}_\perp = 0$ as a function of polarization. (a,c) Corresponding real-space emission patterns along $\mathbf{E} \parallel c$ and $\mathbf{E} \perp c$, respectively. The superimposed white lines represent the near-field emission pattern recorded below threshold without polarization selection displayed in (b). Taken from Ref. [272].



into account the position of both excitons close to the low-energy edge of the bottom-DBR stopband, this condition would be in clear favor of localized X_B states located at higher energy, in agreement with the experimental observations.

Further details about the lasing mechanism can also be deduced from the polarization-dependent real space emission patterns shown in Figure 4.57. Indeed, whereas the emission pattern in the linear regime remains unstructured mainly contouring the pump spot (Fig. 4.57(b)), the different nature of the lasing mechanisms is revealed by the profiles recorded above both thresholds. Here, PL polarized along $\mathbf{E} \parallel c$ in Fig. 4.57(a), preferentially originating from the bottom of LPB_e , emerges from randomly-distributed emission hot spots, that may even be located a few microns apart from the center of the pump spot. These polariton traps are likely induced by photonic disorder and cause the finite beam divergence visible in the Fourier-PL images due to the uncertainty limit [25, 172]. By contrast, for $\mathbf{E} \perp c$ lasing exclusively arises from the vicinity of the maximum pump power density without any significant texture in Fig. 4.57(c). Both observations may be interpreted as characteristics of lasing action occurring in the WCR, where a non-linear emission is triggered when the gain exceeds the losses, i.e. in the vicinity of the maximum pumping power. Moreover, excitonic disorder is expected to emerge on a much smaller spatial scale than the photonic one, likely resulting in an unstructured emission pattern.

Note that despite their different characteristics both lasing emissions come from the same sample region and thus coexist sharing the same exciton reservoir. A lasing mechanism, where SCR and WCR coexist spatially separated due to an inhomogeneous pump spot as reported by Lagoudakis and co-workers can be discarded [311]. By contrast, on the basis of the real-space emission pattern polariton lasing cannot be completely ruled out as possible origin for the non-linear emission along $\mathbf{E} \perp c$ given that the bottom-DBR overlap with X_B is larger than expected from TMS in Sec. 4.7.3. Owing to the reduced coupling strength and the proximity to the exciton, polaritons would feature a very high excitonic fraction and thus be rather insensitive to the photonic disorder landscape. Hence, their motion would be limited by a

short exciton diffusion length in agreement with the recorded real space pattern in Fig. 4.57(c). However, in this case the high density of states and the shallow LPB trap would cause a drastically increased polariton lasing threshold [26], rather inconsistent with the observed behavior.

Whatever the assumed scenario for the lasing emission L_o , the proximity between both non-linear emission thresholds $P_{thr,e}$ and $P_{thr,o}$ may look surprising, as polariton lasers are ideally expected to exhibit an ultra-low threshold owing to the release of the Bernard-Duraffourg condition [11]. At this point it is worth recalling that the threshold of polariton lasing is intrinsically limited by the carrier relaxation efficiency usually leading to an increased threshold with respect to the optimum case set by the thermodynamics [26]. This interpretation is well supported by the non-thermal occupancy of LPB_e in Fig. 4.53(d). Another important effect, that could explain the proximity between both threshold values, concerns the nature of a potentially existing lasing mechanism via localized exciton states. The latter feature a much lower density of states, being rather 0D than 2D-like, compared to free excitons resulting in a significantly reduced threshold for reaching the transparency condition. The observation of a randomly-distributed $P_{thr,o}/P_{thr,e}$ ratio, ranging in between 0.8 and 5 all over the sample depending on the local excitonic and photonic disorder landscapes, hints also toward such an interpretation. Eventually, a quantitative comparison between both thresholds appears to be clearly beyond the scope of the present study and a conclusion on the present gain mechanism for L_o awaits further theoretical development and experimental examination. Possible future studies could involve optical gain measurements or the search for a second threshold that should be observed when the system transits toward a degenerate electron-hole plasma above the MT. Note however that the high exciton binding energy and the important disorder present in III-nitride compounds could strongly favor the existence of exciton lasing involving localized states. For instance, Kojima and co-workers reported on gain of two different origins in InGaN QW-based LDs [312]. Interestingly, within this study the device with the largest inhomogeneities featured a second gain peak that emerged on the low energy side of the main absorption. With increasing injection it was observed to rapidly saturate at the expense of the main transition peak, which appears consistent with the phase-space filling model of Ref. [310]. In 2007, Schwarz and co-workers could theoretically account for these results by considering the inhomogeneous broadening of the band edge [142].

5 Conclusion

Within the frame of this thesis the knowledge about planar GaN QW-based microcavities operating in the SCR has been deepened by examining the relaxation and renormalization characteristics of 2D cavity-polaritons right up to the condensation threshold and by investigating the linear and non-linear emission properties of intrinsically anisotropic non-polar III-nitride based microcavities. A comprehensive treatment of the polariton renormalization led additionally to the exploration of the optical characteristics of GaN/AlGaIn QWs in the high carrier-density regime up to the Mott-transition. Various optical spectroscopy techniques, such as time-resolved, time-integrated or Fourier-space PL measurements, served as experimental basis. For modelling and interpreting the experimental results a 1D Schrödinger- k , p Poisson-solver and an anisotropic 4×4 optical transfer matrix algorithm have been developed among others.

5.1 Summary and Classification of the Results

After a consolidated introduction to the structural and optical properties of III-nitride semiconductors and corresponding heterostructures, the first part of this thesis focused on the investigation of high-quality c -plane GaN/AlGaIn QWs that have preferentially been grown on free-standing GaN substrates. Following a thorough discussion of their low-density absorption characteristics based on combined PL and PLE measurements, their high-injection optical properties have been studied by non-resonant time-resolved and continuous-wave PL. A spot size of a few microns and a careful spatial filtering allowed to probe the emission properties of different high-quality SQW structures beyond the MT with a well-defined carrier density. The latter has been deduced from an appropriate lineshape modeling. When approaching the MT the QW emission spectrum undergoes a characteristic and continuous modification. Starting from about one order of magnitude below the Mott-density, the QW exciton is observed to slightly blueshift based solely on the QCSE, while the progressive saturation of its oscillator strength could only be shown qualitatively by power-dependent PLE measurements. In the critical density range, the exciton vanishes into the e-h continuum, the low-energy emission edge starts redshifting due to BGR, and Fermi-filling causes a strong extension of the high-energy tail and a plateau-like emission band. Due to the large binding energy of excitons in such QWs, their injection-induced dissociation could be studied over a wide range of temperatures, i.e. up to 150 K. Different criteria, that define the MT, have been analyzed without indicating any clear trend with temperature: the exciton to e-h plasma crossover

takes invariably place at carrier densities around 10^{12} cm^{-2} for the investigated heterostructures. Depending on the Al-content of the barrier and the QW-width, the QCSE influences the stability of biexcitons in GaN/AlGaIn QWs. When the biexciton comes additionally into play in optimized structures, the situation becomes even more complex. Despite its presumably lower stability, based on the binding energy, it seems that the biexcitonic complex is more robust against an increasing carrier density than the exciton itself. The typical biexciton recombination signature remains observable even beyond the density where the high-energy tail of the fundamental QW-emission turns mono-exponential and the e-h plasma emission clearly emerges from the biexciton peak.

While the MT has already been studied for GaN bulk systems in a rather qualitative manner [56, 124], the present results constitute the first thorough study for GaN-based QWs. Despite existing counter-examples, the observed second-order nature agrees well with most theories [117, 129] and findings obtained in a similar experimental scheme for a GaAs-based SQW [131]. As another novelty, the large exciton binding energy allowed to track the MT over a significant range of lattice temperatures. The observed constancy of the critical density with temperature contradicts the simple interpretation of exciton dissociation based on a static screening length [114, 123] and suggests the importance of dynamical screening effects [113, 313]. This fact may also favor a description of the MT via BGR [114]. However, it is worth pointing out that no evidence for BGR could be traced in the exciton-dominated injection regime below the critical density, in agreement with the findings of Ref. [131]. Taking further into account the surprising stability of biexcitons at high carrier density, the present results call for a coherent theory encompassing the full frame of many-body effects occurring between exciton, biexciton, and uncoupled e-h populations.

The extensive study of the MT in GaN/AlGaIn SQWs and the qualitative complement conducted on the bare active medium provided the basis for a comprehensive study of the polariton renormalization in a strongly-coupled *c*-plane MQW-based MC. In particular, it was evidenced that based on QCSE the QW exciton only marginally blueshifts when the carrier density approaches the Mott limit. An exciton blueshift in the order of its binding energy can thus be clearly ruled out. The blueshift of the LPB toward the condensation threshold seems to be rather caused by a decreasing light-matter coupling strength issued from the saturation of the exciton oscillator strength. This implies a general operation of this MC only one or at most two orders of magnitude below the critical density depending on the actual $\{\delta, T\}$ -combination. The universality of the Mott-transition observed in QWs of different material systems [131], and a number of observations reported in the literature [17, 238], suggest that contrary to the predominant habits saturation effects should readily be considered in other material systems, such as GaAs and CdTe.

Similarly to previous results in alternative material systems [182, 183, 262], a relaxation channel relying on the direct transition from the polariton reservoir to the LPB ground state via emission of an LO-phonon has been evidenced in the present GaN-based MC. However, the additional feeding of the ground state population by the radiative dissociation of biexcitons involving an LO-phonon as evidenced by time-resolved experiments appears more prominent. Both mechanisms have been shown to substantially enhance the relaxation efficiency and lower the condensation threshold for specific negative detuning conditions set by the LO-phonon energy. Such a biexciton-related mechanism has been observed for the first time in a strongly-coupled MC and emphasizes the high-quality of the studied structure and the strong role played by biexcitons in III-nitrides.

The last part of this thesis reports on the first realization of a non-polar III-nitride based MC that operates in the SCR and features polariton condensation related non-linear emission properties at temperatures up to 50 K. Such structures promise an increased optical efficiency based on the absence of the QCSE and the correspondingly increased exciton oscillator strength and stability. Moreover they give rise to a pronounced optical anisotropy of the light-matter coupling regime, involving the position of the DBR stopband and the cavity mode as well as the selection rules of the exciton resonances. In the present case, clear evidences of strong coupling and polariton lasing have been observed in the extraordinary polarization direction, for which the ground state exciton exhibits the highest oscillator strength owing to the experienced strain state and the corresponding valence-band mixing. By contrast, the ordinary polarization direction lacks a clear coupling regime definition due to the limited overlap with the bottom-DBR stopband. The still observed non-linear emission might hint at an exciton-related gain mechanism, but needs further examination.

5.2 Perspectives

Injection-dynamics and gain mechanisms occurring in conventional GaAs-based LDs at room temperature can accurately be described in a simple electron-hole picture omitting any excitonic influence, as done e.g. when using the ABC-model [314]. By contrast, InGaN-based LDs exhibit several characteristics that may require a modification of such an idealized framework: for instance the dominating impact of disorder and the presence of stable excitons at room temperature. This statement is closely linked to the final discussion of the lasing mechanism along the ordinary polarization direction in the non-polar MC in Sec 4.7 and the potential existence of an excitonic gain mechanism in III-nitride based LDs [231, 312]. In order to substantially address this topic, the MT occurring in GaN and InGaN-based QWs should be investigated on a broader scope.

The presently applied PL-method to study the MT occurring in III-nitride based QWs provides several advantages, such as the ease of carrier injection and the determination of an accurate carrier density above the critical limit. Complementary studies could for instance rely on pump-probe experiments that may help to find the exact correlation between carrier density and the exciton oscillator strength saturation when probing the transmission at the exciton energy. Low-temperature gain measurements on single QWs, potentially as a function of the disorder scale, could yield exciting insights on biexciton- or exciton-related amplification mechanisms such as seen e.g. in Ref. [154]. Alternatively, one might design a combined electro-optical setup scheme that could allow monitoring the QW-conductance in presence of optical pumping. Indeed, an exciton gas represents an insulator that transforms into a conductive e-h plasma across the MT. A measurement of the lateral conductivity in etched mesa-structures under cw-pumping should thus allow to address the exciton dissociation mechanisms in more detail.

Future studies regarding the MT in III-nitride based QWs should also concern the Auger-effect, which is controversially discussed to dramatically impact device performances already well below the Mott-density [6, 7]. No clear signature of Auger-recombination could be tracked in the present GaN QWs up to the highest densities. Nevertheless, it is certainly worth extending this study to InGaN QWs that may behave in a different manner, e.g. owing to the different scale of disorder. Eventually, the study of the MT in non-polar QWs would also be of key interest to eliminate the impact of QCSE and examine the interplay between an almost isotropic electron

band and strongly anisotropic valence-bands.

Section 4.6 provided only a brief glimpse to the properties of polariton condensates at elevated temperatures. These results are far from being fully comprehensive and conclusive, and call for supplementary studies including the investigation of spatial and temporal coherence by using the already assembled Michelson-interferometer. In doing so, deeper insights into the difference between polariton and photon lasing mechanisms could be gained and the interaction of localized condensates with a thermal phonon gas could be investigated over a wide range of temperatures. Indeed, the large disorder in GaN-based MCs likely prevents probing the properties of flowing polariton condensates as conducted in GaAs-based systems [19], but it could certainly allow tracking phenomena like pinned vortices and Josephson-junctions, such as done in CdTe-based structures [18, 20]. When probing condensates with relatively high-excitation power densities it is likely that the stability of the top-DBR of MC-1 will become an issue: it might be worth exchanging it with a $\text{SiO}_2/\text{ZrO}_2$ layer stack, that is widely transparent for the pump laser.

The different solutions for realizing a III-nitride based polariton laser diode have already been discussed in Sec. 4.2.3. It seems that the major advantage of InGaN/GaN over GaN/AlGaN QWs consists in the ease of the current injection and the availability of transparent conductive oxides for the top current-spreading layer. The latter usually requires an emission wavelength $> 400\text{ nm}$, for which the optical quality of the InGaN QWs in terms of oscillator strength and linewidth is already degraded compared to the GaN case. A solution to this issue may be given by GaN-based tunnel junctions that could facilitate the use of highly n -doped GaN as current-spreading layer. In such a scenario QWs with lower In-content could be used, i.e. 5-6%, optimizing the optical quality and potentially giving rise to the SCR.

Appendix

A.1 Band-Structure Calculations

This appendix provides further information about the formalism that was used for calculations of the band structure around the Γ -point in both two-dimensional and three-dimensional III-nitride layers. It is based on the semi-empirical $k.p$ -approach and obeys the quasi-cubic approximation. The latter relies on the similarity between a hexagonal crystal and a cubic one that is subject to uniaxial strain along the $[111]$ -direction.

A.1.1 The $k.p$ -Formalism

As already indicated the one-electron Schrödinger-equation of Eq. (2.11) can be further simplified by taking into account the translational invariance of the crystal and applying Bloch's theorem. For this purpose $\phi_q(\mathbf{r})$ in Eq. (2.11) is replaced by the Bloch-function:

$$\phi_{q\mathbf{k}}(\mathbf{r}) = e^{i\mathbf{k}\mathbf{r}} u_{q\mathbf{k}}(\mathbf{r}) . \quad (\text{A.1})$$

It is composed of a phase factor and a periodic part $u_{q\mathbf{k}}(\mathbf{r})$, that follows the symmetry of the lattice. The execution of the impulse operator $\hat{p} = -i\hbar\nabla$ transforms the one-electron Schrödinger-equation for $u_{q\mathbf{k}}(\mathbf{r})$ into:

$$\left[\frac{\hat{p}^2}{2m_0} + \frac{\hbar}{m_0} \mathbf{k} \cdot \hat{p} + \frac{\hbar^2 k^2}{2m_0} + V(\mathbf{r}) \right] u_{q\mathbf{k}}(\mathbf{r}) = E_q(\mathbf{k}) u_{q\mathbf{k}}(\mathbf{r}) . \quad (\text{A.2})$$

This is the basic equation of the $k.p$ -method. When the properties of a semiconductor are known at $\mathbf{k} = 0$, either due to measurements or *ab initio* calculations, this formalism yields a reasonable approximation of the band structure around the Γ -point by treating the second term in Eq. (A.2) using time-independent perturbation theory [315, 316]. Detailed information about this method can for example be found in Ref. [144]. This section will focus on the $k.p$ -method for wurtzite semiconductors mainly based on Ref. [40]. It relies on the orbital basis functions of Eq. (2.20) and additionally considers the spin-orbit interaction via:

$$\hat{H}_{\text{so}} = \frac{\hbar}{4m_0^2 c_0^2} [\nabla V(\mathbf{r}) \times \hat{p}] \cdot \boldsymbol{\sigma} = \hat{H}_{sx} \sigma_x + \hat{H}_{sy} \sigma_y + \hat{H}_{sz} \sigma_z , \quad (\text{A.3})$$

where the components of the tensor $\boldsymbol{\sigma}$ denote the Pauli-spin matrices. The band structure around the Γ -point in the orbital basis of Eq. (2.20) can then be described by a Hamiltonian of

the form:

$$\begin{pmatrix} \tilde{\mathbf{H}}_{\text{cc}} & \tilde{\mathbf{H}}_{\text{cv}} \\ \tilde{\mathbf{H}}_{\text{cv}}^* & \tilde{\mathbf{H}}_{\text{vv}} \end{pmatrix}. \quad (\text{A.4})$$

Here, $\tilde{\mathbf{H}}_{\text{cc}}$ and $\tilde{\mathbf{H}}_{\text{vv}}$ correspond to 2×2 and 6×6 matrices, respectively. They determine the curvature and interactions within the spin-degenerated CBs and VBs, respectively, while $\tilde{\mathbf{H}}_{\text{cv}}$ and its complex conjugate define the interaction between CBs and VBs across the bandgap. For wide-bandgap semiconductors, such as GaN, AlN, and Al-rich AlInN these interband interactions are marginal and can be neglected in good approximation [317]. This decouples CB and VB Hamiltonians and leads to the representation [40]:

$$\mathbf{H}_{\text{cc}} = \begin{pmatrix} E_{\text{c}} & 0 \\ 0 & E_{\text{c}} \end{pmatrix} \quad \text{and} \quad \mathbf{H}_{\text{vv}} = \begin{pmatrix} F & -K^* & -H^* & 0 & 0 & 0 \\ -K & G & H & 0 & 0 & \Delta \\ -H & H^* & \lambda & 0 & \Delta & 0 \\ 0 & 0 & 0 & F & -K & H \\ 0 & 0 & \Delta & -K^* & G & -H^* \\ 0 & \Delta & 0 & H^* & -H & \lambda \end{pmatrix}. \quad (\text{A.5})$$

Note that despite identical basis functions these matrices may be different from the elements in Eq. (A.4). The strain-dependent components of \mathbf{H}_{cc} and \mathbf{H}_{vv} are given by [40]:

$$\begin{aligned} E_{\text{c}} &= E_{\text{G}} + \Delta_1 + \Delta_2 + \frac{\hbar^2 k_z^2}{2m_{\parallel}^*} + \frac{\hbar^2 (k_x^2 + k_y^2)}{2m_{\perp}^*} + a_{\parallel}^{\text{c}} \epsilon_{zz} + a_{\perp}^{\text{c}} (\epsilon_{xx} + \epsilon_{yy}), \\ F &= \Delta_1 + \Delta_2 + \lambda + \Sigma, \\ G &= \Delta_1 - \Delta_2 + \lambda + \Sigma, \\ \lambda &= \frac{\hbar^2}{2m_0} \left[A_1 k_z^2 + A_2 (k_x^2 + k_y^2) \right] + D_1 \epsilon_{zz} + D_2 (\epsilon_{xx} + \epsilon_{yy}), \\ \Sigma &= \frac{\hbar^2}{2m_0} \left[A_3 k_z^2 + A_4 (k_x^2 + k_y^2) \right] + D_3 \epsilon_{zz} + D_4 (\epsilon_{xx} + \epsilon_{yy}), \\ K &= \frac{\hbar^2}{2m_0} A_5 (k_x + i k_y)^2 + D_5 (\epsilon_{xx} + 2i \epsilon_{xy} - \epsilon_{yy}), \\ H &= \frac{\hbar^2}{2m_0} A_6 (k_x + i k_y) k_z + D_6 (\epsilon_{zx} - i \epsilon_{yz}), \\ \Delta &= \sqrt{2} \Delta_3. \end{aligned} \quad (\text{A.6})$$

Here, m_{\parallel}^* and m_{\perp}^* denote the effective electron masses according to Eq. (2.12), while the effective masses of the VBs are described by the A_i -parameters. In the cubic approximation they follow:

$$A_1 - A_2 = -A_3 = 2A_4 \quad \text{and} \quad A_3 + 4A_5 = \sqrt{2}A_6. \quad (\text{A.7})$$

Equivalent symmetry relations exist also for the strain-related VB deformation potentials D_i :

$$D_1 - D_2 = -D_3 = 2D_4 \quad \text{and} \quad D_3 + 4D_5 = \sqrt{2}D_6. \quad (\text{A.8})$$

The deformation of the CB due to lattice strain is described by the values of a_{\parallel}^c and a_{\perp}^c . Finally, in Eq. (A.6) the spin-orbit interaction and the crystal-field splitting are considered via:

$$\begin{aligned}\Delta_{\text{cr}} &= \Delta_1 \\ \Delta_{\text{so}} &= 3\Delta_2 = 3\Delta_3 .\end{aligned}\tag{A.9}$$

It is worth emphasizing once more that the symmetry operations in Eqs. (A.7), (A.8), and (A.9) hold only in the cubic approximation and may be lifted partially when the latter is violated. Recent experimental reports indicate this situation in GaN [318]. However, such effects shall be neglected here in a first instance. All GaN-parameters used within this work were taken from Ref. [31]. The formalism presented above is applicable to thick bulk layers and was used to generate the data presented in Figs. 2.3 and 2.4.

A.1.2 Schrödinger- k,p Simulations for Quantum-Wells

In order to transpose the aforementioned bulk k,p -formalism to QWs, the confinement potential according to Eq. (2.40) has to be taken into account. This can be done in the envelope function approximation following Ref. [319] by substituting k_z in the Hamiltonian of Eq. (A.5) with the operator $i\frac{\partial}{\partial z}$. The separate solutions of the CB and VB sub-bands in the QW are then obtained by solving (cf. Fig. 2.7):

$$\begin{aligned}\left[\mathbf{H}_{\text{cc}} \left(k_x, k_y, \frac{\partial}{\partial z} \right) + V_{\text{QW}}^{\text{CB}}(z) \right] \Psi_{q_e}^{\text{CB}}(z) &= E_{q_e}^{\text{CB}} \Psi_{q_e}^{\text{CB}}(z) \\ \left[\mathbf{H}_{\text{vv}} \left(k_x, k_y, \frac{\partial}{\partial z} \right) + V_{\text{QW}}^{\text{VB}}(z) \right] \Psi_{q_h}^{\text{VB}}(z) &= E_{q_h}^{\text{VB}} \Psi_{q_h}^{\text{VB}}(z) .\end{aligned}\tag{A.10}$$

Here, $\Psi_{q_e}^{\text{CB}}(z)$ and $\Psi_{q_h}^{\text{VB}}(z)$ denote the wave-functions of the CB and VB sub-bands with indices n_e and n_h , respectively. They are composed of the orbital basis functions from Eq. (2.20): when assuming spin-degeneracy for the CB, $\Psi_{q_e}^{\text{CB}}(z)$ can be replaced by a scalar, while $\Psi_{q_h}^{\text{VB}}(z)$ is projected on the six p -orbital components. These differential equations can be transformed to a simple eigenvalue problem by applying the Fourier-expansion method introduced in Ref. [299]. This approach relies on solving Eq. (A.10) with periodic boundary conditions on a reference length L , that ideally amounts to a multiple of the QW-width L_{QW} and is chosen large enough to ensure a sufficiently low presence probability at the boundary, e.g. $L = 8L_{\text{QW}}$. For the VB, each sub-band envelope-function is represented by the following ansatz:

$$\Psi^{\text{VB}}(z) = \sum_{m=0}^N \frac{1}{\sqrt{L}} \mathbf{c}_m \exp(i\kappa_m z) ,\tag{A.11}$$

where N sets the even number of basis functions and κ_m corresponds to the wave-vector of the harmonic Fourier series: $\kappa_m = \pi(N - 2m)/L$. This approach is only exact when $N \rightarrow \infty$, but for the highly-confined levels an adequate compromise between accuracy and numerical effort is already achieved for $N \geq 50$ [299]. Inserting Eq. (A.11) into Eq. (A.10), multiplication by $\exp(i\kappa_l z)/\sqrt{L}$, and integration over the length interval L yields for the components of \mathbf{H}_{vv} ($i, j = 1..6$, using sum convention):

$$\left([\mathbf{H}_{\text{vv}}(k_x, k_y, \kappa_m)]_{ij} \delta_{lm} + V_{lm}^{\text{VB}} \delta_{ij} \right) c_j = E c_i .\tag{A.12}$$

Here, δ is the Kronecker-delta and c_{ilj} denote the components of the Fourier-coefficients $\mathbf{c}_{m/l}$ in Eq. (A.11), with $l, m = 1..N$. Due to the use of plane waves as basis functions in Eq. (A.11), the differential matrix operator $\mathbf{H}_{vv}(k_x, k_y, \frac{\partial}{\partial z})$ in Eq. (A.10) is traced back to a series of the bulk Hamiltonian with different values for q_m : $\mathbf{H}_{vv}(k_x, k_y, \kappa_m)$. V_{lm}^{VB} corresponds to the Fourier-transform of the QW-potential that is obtained via:

$$V_{lm}^{\text{VB}} = \frac{1}{L} \int_{-L/2}^{L/2} \exp[-i(\kappa_l - \kappa_m)z] V_{\text{QW}}^{\text{VB}}(z) dz. \quad (\text{A.13})$$

By means of the index transformation:

$$\alpha = 6m + j \quad \text{and} \quad \beta = 6l + i, \quad (\text{A.14})$$

leading to:

$$\mathbf{H}'_{\alpha\beta} = [\mathbf{H}_{vv}(k_x, k_y, \kappa_m)]_{ij} \delta_{lm} + V_{lm}^{\text{VB}} \delta_{ij}, \quad (\text{A.15})$$

Eq. (A.12) can be rewritten as a simple matrix eigenvalue problem:

$$\mathbf{H}'_{\alpha\beta} c_\beta = E c_\alpha. \quad (\text{A.16})$$

The latter can be solved numerically and yields eigenvalues and eigenvectors with $6N$ components as a function of the in-plane momentum (k_x, k_y) . They can be transferred to the m -th eigenenergy and wave-function when inverting the index transformation in Eq. (A.14). The same formalism is applied to the CB, where due to the scalar properties the index transformation can be omitted. Note that in this Fourier-expansion approximation the change in the effective masses across the QW-barrier interface is neglected, which decreases the accuracy for very thin QWs, i.e. $L_{\text{QW}} < 1$ nm. However, it is rather easily applicable and provides the advantage that the symmetries, selection rules, and effective masses of the different VBs are fully taken into account. For non c -plane structures the tilt of the crystal must be considered: coordinates, in-plane wave-vectors, and strain components have to be rotated by the matrix:

$$\mathbf{U} = \begin{pmatrix} \cos\Theta & 0 & \sin\Theta \\ 0 & 1 & 0 \\ -\sin\Theta & 0 & \cos\Theta \end{pmatrix}. \quad (\text{A.17})$$

Θ denotes the angle between the growth axis and the c -direction as introduced in Sec. 2.1.2.

A.1.3 Self-consistent Schrödinger-Poisson Solver

As already indicated in Sec. 2.3.4, the treatment of QCSE-screening due to a finite carrier density requires to solve the Schrödinger- $k.p$ formalism introduced above self-consistently with Eq. (2.53). Although this seems to be a rather straightforward task, it requires a careful choice of the iteration steps and the boundary conditions in order to reach a satisfactory convergence. In the following, the utilized algorithm shall be summarized for the simple case of an undoped c -plane QW with carrier density n_{QW} at $T = 0$ K, being free of external electric fields. Complementary information can for instance be found in Ref. [320].

- The procedure is initiated by solving the Schrödinger- $k.p$ formalism for zero carrier density, yielding the CB and VB energy levels and wave-functions.
- For zero temperature, only the CB and VB ground states are populated. Electrons and holes with density n_{QW} are distributed along the growth axis z according to the normalized presence probabilities $|\Psi_n(z)|^2$. The charge carrier distribution along the growth axis is obtained via:

$$\rho(z) = -e \cdot n_{QW} \cdot \left(|\Psi_1^{CB}(z)|^2 - |\Psi_1^{VB}(z)|^2 \right), \quad (A.18)$$

- The profile of the electric potential is calculated by integrating the Poisson-equation of Eq. (2.53). This step is more complex than it looks like: already the finite spatial resolution and/or the numerical precision may cause large convergence instabilities. The second derivative of an arbitrary 1D array can be obtained by multiplication with the matrix:

$$\mathbf{D} = \begin{pmatrix} 2 & -1 & 0 & 0 & 0 & \dots \\ -1 & 2 & -1 & 0 & 0 & \dots \\ 0 & -1 & 2 & -1 & 0 & \dots \\ \dots & \dots & \dots & \dots & \dots & \dots \end{pmatrix}. \quad (A.19)$$

It has the squared dimension of the array length and can be inverted to obtain the second integration. Respecting the spatial discretization Δz and the boundary condition of a minimum electric field at infinite distance from the QW, the electrical potential $\Phi(z)$ can be computed via:

$$\Phi(z) = \frac{\Delta z^2}{\epsilon_0 \epsilon_r} \cdot \mathbf{D}^{-1} \rho(z). \quad (A.20)$$

- The derived $\Phi(z)$ can then be added to the unperturbed QW-potential yielding the modified total potential $V'_{QW}(z)$. Note however that in view of the stability of the procedure it may be convenient to mix the electric potential of the m -th iteration with the previous one based on the variable parameter w [321], with $0 < w < 1$:

$$V'_{QW}(z) = V_{QW}(z) + w \cdot \Phi^{(m)}(z) + (1 - w) \cdot \Phi^{(m-1)}(z). \quad (A.21)$$

Good convergence is usually achieved with $w = 0.5$. Nevertheless, for very high carrier densities or when the procedure gets stuck in a local minimum, it is often useful to decrease the value of w .

- Subsequently, the next iteration is started by solving the Schrödinger- $k.p$ formalism in the modified QW-potential $V'_{QW}(z)$. The eventual convergence condition can be based on an arbitrary indicator: in the present case, the procedure was terminated when the normalized variation between $\Phi^{(m)}$ and $\Phi^{(m-1)}$ fell below 10^{-5} . It was found to be stable up to carrier concentrations of $\sim 10^{13} \text{ cm}^{-2}$ depending on the investigated structure.

In principle, the above-described procedure could be arbitrarily expanded, e.g. including background doping, an externally applied voltage, or a finite lattice temperature. In the latter case the thermal distribution of carriers across the different sub-bands according to the Fermi-distribution and the effective carrier masses has to be taken into account.

A.2 Optical Transfer-Matrix Simulations

The linear optical response of a planar multi-layer structure is determined by an infinite number of coherent internal reflections. With increasing number of layers a corresponding simulation following every single ray of light gets rapidly voluminous. For such a problem a much smarter solution is given by optical transfer-matrix simulations (TMS), where the wave propagation within the layer stack is traced back to the continuity conditions of the electric field \mathbf{E} across the layer interfaces based on Maxwell's equations. In the following external charges and currents are neglected. Furthermore, the thin-films shall be homogeneous and grown along the z -direction, which is pointing from the surface to the substrate.

A.2.1 Isotropic Media

In order to explain the TMS basics, we start considering optically isotropic media, which can be described by a scalar complex refractive index $n = n_{\text{re}} + i \cdot n_{\text{im}}$, consisting of the refractive index dispersion n_{re} and the extinction coefficient n_{im} . Both properties are related to the complex dielectric function ε via $\varepsilon = \varepsilon_1 + i\varepsilon_2 = n^2$. The translation of the electric field amplitudes E_i of a plane electro-magnetic wave at the interface between layers j and $j+1$ is given by the Fresnel-coefficients:

$$\begin{aligned} r_s^{j,j+1} &= \frac{E_{s,-}^j}{E_{s,+}^j} = \frac{n_j \cos \Theta_j - n_{j+1} \cos \Theta_{j+1}}{n_j \cos \Theta_j + n_{j+1} \cos \Theta_{j+1}} & t_s^{j,j+1} &= \frac{E_{s,+}^{j+1}}{E_{s,+}^j} = 1 + r_s^{j,j+1} \\ r_p^{j,j+1} &= \frac{E_{p,-}^j}{E_{p,+}^j} = \frac{n_j \cos \Theta_{j+1} - n_{j+1} \cos \Theta_j}{n_j \cos \Theta_{j+1} + n_{j+1} \cos \Theta_j} & t_p^{j,j+1} &= \frac{E_{p,+}^{j+1}}{E_{p,+}^j} = \frac{n_j}{n_{j+1}} (1 + r_p^{j,j+1}) \end{aligned} \quad (\text{A.22})$$

Here, subscripts s and p denote field components perpendicular and parallel to the plane of incidence, while $+$ and $-$ label waves propagating in positive and negative z -direction. The light propagation direction in the j -th layer and the z -axis comprise an angle Θ_j given by Snell's law: $n_j \cos \Theta_j = n_0 \cos \Theta_0$, where Θ_0 and n_0 denote the angle of incidence and the refractive index of the ambient medium, respectively. By using the identity $r_{s/p}^{j,j+1} = -r_{s/p}^{j+1,j}$, the Fresnel relations can be converted to [322]:

$$\begin{pmatrix} E_{s/p,+}^j \\ E_{s/p,-}^j \end{pmatrix} = \frac{1}{t_{s/p}^{j,j+1}} \begin{pmatrix} 1 & r_{s/p}^{j,j+1} \\ r_{s/p}^{j,j+1} & 1 \end{pmatrix} \begin{pmatrix} E_{s/p,+}^{j+1} \\ E_{s/p,-}^{j+1} \end{pmatrix} = \mathbf{I}_{s/p}^{j,j+1} \begin{pmatrix} E_{s/p,+}^{j+1} \\ E_{s/p,-}^{j+1} \end{pmatrix}, \quad (\text{A.23})$$

defining the interface transfer matrix $\mathbf{I}_{s/p}^{j,j+1}$. In addition to the modification at the layer interfaces the light field is also transformed when passing through a certain layer with thickness d according to the phase thickness β :

$$\beta = 2\pi \frac{d}{\lambda} n \cos \Theta. \quad (\text{A.24})$$

The electric field amplitudes at the upper and lower edge of the layer j are then connected via:

$$\begin{pmatrix} E_{s/p,+}^{z+d} \\ E_{s/p,-}^{z+d} \end{pmatrix} = \begin{pmatrix} \exp(i\beta_j) & 0 \\ 0 & \exp(-i\beta_j) \end{pmatrix} \begin{pmatrix} E_{s/p,+}^z \\ E_{s/p,-}^z \end{pmatrix} = \mathbf{L}^j \begin{pmatrix} E_{s/p,+}^z \\ E_{s/p,-}^z \end{pmatrix}, \quad (\text{A.25})$$

where \mathbf{L}^j denotes the layer transfer matrix.

For a thin-film structure consisting of N layers, the system transfer matrix \mathbf{M} is obtained by a subsequent multiplication of interface and layer transfer matrices. Thereby, the multiplication starts with $\mathbf{I}^{0,1}$, which describes the interface between the ambient medium and the uppermost layer, and ends with $\mathbf{I}^{N,S}$. The latter corresponds to the interface between the lowermost layer N and the substrate (n_S):

$$\begin{pmatrix} E_{s/p,+}^0 \\ E_{s/p,-}^0 \end{pmatrix} = \left[\prod_{j=1}^N \mathbf{I}_{s/p}^{j-1,j} \mathbf{L}^j \right] \mathbf{I}_{s/p}^{N,S} \begin{pmatrix} E_{s/p,+}^S \\ E_{s/p,-}^S \end{pmatrix} = \mathbf{M}_{s/p} \begin{pmatrix} E_{s/p,+}^S \\ E_{s/p,-}^S \end{pmatrix}. \quad (\text{A.26})$$

The normalization $E_{s/p,+}^0 = 1$ yields the total reflection and emission coefficients:

$$r_{s/p} = \frac{\mathbf{M}_{s/p}^{(2,1)}}{\mathbf{M}_{s/p}^{(1,1)}} \quad \text{and} \quad t_{s/p} = \frac{1}{\mathbf{M}_{s/p}^{(1,1)}}, \quad (\text{A.27})$$

where $\mathbf{M}^{(l,m)}$ denotes the elements of \mathbf{M} . Satisfying energy conservation for the field intensities, the total reflectance R , transmittance T and absorptance A are finally obtained via:

$$R_{s/p} = |r_{s/p}|^2, \quad T_{s/p} = \frac{n_0}{n_S} |t_{s/p}|^2, \quad \text{and} \quad 1 = R_{s/p} + T_{s/p} + A_{s/p}. \quad (\text{A.28})$$

For microcavities, the internal field distribution as a function of depth z might be of particular interest. It can be calculated within this model, but a corresponding explanation would go beyond the scope of this section and can for instance be found in Ref. [323].

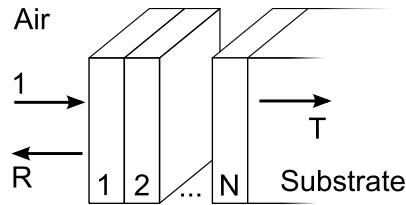


Figure A.1: Ideal planar multi-layer structure for TMS: the normalized incident field amplitude is transmitted through each layer j and transmitted or/and reflected at each layer interface $j/j+1$ giving rise to the total reflection R and transmission T of the system.

A.2.2 Anisotropic Media

In the most general case the complex refractive index or the dielectric function of a material are represented by a 3D tensor, that is aligned with the axes of the crystal (cf. Eq. (2.39)). In an isotropic medium all trace elements are identical and the tensor can be replaced by a scalar. By contrast, if these elements are different from each other, the material is optically anisotropic, two medium types can be distinguished: (i) in uniaxial crystals two trace elements are identical ($n_x = n_y \neq n_z$). They define the ordinary polarization direction. The optical axis of the crystal ($\parallel z$) marks the extraordinary polarization direction. III-nitrides are uniaxial materials with the optical axis oriented along [0001]. (ii) Biaxial media are characterized by $n_x \neq n_y \neq n_z$.

For anisotropic materials the diffraction at an interface is no longer exclusively determined by the polarization of light with respect to the plane of incidence but it also depends on

the polarization with respect to the orientation of the optical axes. In the same way light propagation and absorption inside the medium will be affected, resulting in birefringence and dichroism. In this case, the simple 2×2 -formalism presented above for isotropic crystals is not applicable anymore. An alternative approach for stratified anisotropic media was developed by Berreman [324]. His 4×4 TMS-method is directly based on Maxwell's equations, was refined by Schubert later on [302, 325], and shall be introduced in the following.

Within the 4×4 -matrix method the transformation of the electric light-field by a multi-layer structure is characterized by the transfer matrix \mathbf{T} :

$$\begin{pmatrix} E_{s,+}^0 \\ E_{s,-}^0 \\ E_{p,+}^0 \\ E_{p,-}^0 \end{pmatrix} = \mathbf{T} \begin{pmatrix} E_{s,+}^S \\ E_{s,-}^S \\ E_{p,+}^S \\ E_{p,-}^S \end{pmatrix} = \mathbf{I}_0^{-1} \left[\prod_{j=1}^N \mathbf{F}_j^{-1} \right] \mathbf{I}_S \begin{pmatrix} E_{s,+}^S \\ E_{s,-}^S \\ E_{p,+}^S \\ E_{p,-}^S \end{pmatrix}, \quad (\text{A.29})$$

where \mathbf{I}_0^{-1} and \mathbf{I}_S correspond to the input and output transfer matrices according to [325]:

$$\mathbf{I}_0^{-1} = \frac{1}{2} \begin{pmatrix} 0 & 1 & -1/n_0 \cos \Theta_0 & 0 \\ 0 & 1 & 1/n_0 \cos \Theta_0 & 0 \\ 1/\cos \Theta_0 & 0 & 0 & 1/n_0 \\ -1/\cos \Theta_0 & 0 & 0 & 1/n_0 \end{pmatrix} \quad \text{and} \quad (\text{A.30})$$

$$\mathbf{I}_S = \begin{pmatrix} 0 & 0 & \cos \Theta_z & -\cos \Theta_z \\ 1 & 1 & 0 & 0 \\ -n_y^S \cos \Theta_y & n_y^S \cos \Theta_y & 0 & 0 \\ 0 & 0 & n_x^S & n_x^S \end{pmatrix}. \quad (\text{A.31})$$

Here, the elements $n_{x/y}^S$ describe the refractive index of the potentially anisotropic substrate. The transmission angle in the latter is obtained via Snell's law:

$$\cos \Theta_{x/y} = \sqrt{1 - \left(n_0 / n_{x/y}^S \cdot \sin \Theta_0 \right)^2}. \quad (\text{A.32})$$

In Eq. (A.29) the inverse transfer matrix of the j -th layer \mathbf{F}_j^{-1} is defined as:

$$\mathbf{F}_j^{-1} = \exp \left(-i \frac{\omega}{c} \Delta_j d_j \right), \quad (\text{A.33})$$

where ω and c denote the angular frequency and the vacuum speed of light, and Δ_j is given for each layer by ($k_x = n_0 \sin \Theta_0$):

$$\Delta = \begin{pmatrix} -k_x \frac{\epsilon'^{(3,1)}}{\epsilon'^{(3,3)}} & -k_x \frac{\epsilon'^{(3,2)}}{\epsilon'^{(3,3)}} & 0 & 1 - \frac{k_x^2}{\epsilon'^{(3,3)}} \\ 0 & 0 & -1 & 0 \\ \epsilon'^{(2,3)} \frac{\epsilon'^{(3,1)}}{\epsilon'^{(3,3)}} - \epsilon'^{(2,1)} & k_x^2 - \epsilon'^{(2,2)} + \epsilon'^{(2,3)} \frac{\epsilon'^{(3,2)}}{\epsilon'^{(3,3)}} & 0 & k_x \frac{\epsilon'^{(2,3)}}{\epsilon'^{(3,3)}} \\ \epsilon'^{(1,1)} - \epsilon'^{(1,3)} \frac{\epsilon'^{(3,1)}}{\epsilon'^{(3,3)}} & \epsilon'^{(1,2)} - \epsilon'^{(1,3)} \frac{\epsilon'^{(3,2)}}{\epsilon'^{(3,3)}} & 0 & -k_x \frac{\epsilon'^{(1,3)}}{\epsilon'^{(3,3)}} \end{pmatrix}. \quad (\text{A.34})$$

The elements $\epsilon_j'^{(l,m)}$ of the dielectric function tensor ϵ_j' are obtained by rotating ϵ_j from Eq. (2.39) according to the Euler-angles $\boldsymbol{\phi} = (\phi_1, \phi_2, \phi_3)$ of the structure [322]:

$$\epsilon_j' = \mathbf{R} \epsilon_j \mathbf{R}^{-1}, \quad (\text{A.35})$$

using the unitary rotation matrix \mathbf{R} :

$$\begin{pmatrix} \cos \phi_1 \cos \phi_3 - \sin \phi_1 \cos \phi_2 \sin \phi_3 & -\cos \phi_1 \cos \phi_3 - \sin \phi_1 \cos \phi_2 \cos \phi_3 & \sin \phi_1 \sin \phi_2 \\ \sin \phi_1 \cos \phi_3 - \cos \phi_1 \cos \phi_2 \sin \phi_3 & -\sin \phi_1 \cos \phi_3 - \cos \phi_1 \cos \phi_2 \cos \phi_3 & -\cos \phi_1 \sin \phi_2 \\ \sin \phi_2 \sin \phi_3 & \sin \phi_2 \cos \phi_3 & \cos \phi_2 \end{pmatrix}.$$

The obvious difficulty, occurring when \mathbf{F}_j^{-1} from Eq. (A.33) shall be expressed in a simple matrix form, can be circumvented by adopting the finite expansion series introduced in Ref. [326]:

$$\mathbf{F}_j^{-1} = \alpha_0 \mathbf{E}_4 + \alpha_1 \boldsymbol{\Delta} + \alpha_2 \boldsymbol{\Delta}^2 + \alpha_3 \boldsymbol{\Delta}^3, \quad (\text{A.36})$$

where \mathbf{E}_4 is the 4-th order identity matrix, and the α -coefficients are defined as:

$$\begin{aligned} \alpha_0 &= \sum_{h=1}^4 q_k q_l q_m \frac{\exp(-i\omega q_h d_j / c)}{(q_h - q_k)(q_h - q_l)(q_h - q_m)}, \\ \alpha_1 &= \sum_{h=1}^4 (q_k q_l + q_k q_m + q_l q_m) \frac{\exp(-i\omega q_h d_j / c)}{(q_h - q_k)(q_h - q_l)(q_h - q_m)}, \\ \alpha_2 &= \sum_{h=1}^4 (q_k + q_l + q_m) \frac{\exp(-i\omega q_h d_j / c)}{(q_h - q_k)(q_h - q_l)(q_h - q_m)}, \\ \alpha_3 &= \sum_{h=1}^4 \frac{\exp(-i\omega q_h d_j / c)}{(q_h - q_k)(q_h - q_l)(q_h - q_m)}. \end{aligned} \quad (\text{A.37})$$

Here, q_h corresponds to the different eigenvalues of $\boldsymbol{\Delta}$, while the indices (k, l, m) have the values $(2, 3, 4)$ for $h = 1$, $(1, 3, 4)$ for $h = 2$, $(1, 2, 4)$ for $h = 3$, and $(1, 2, 3)$ for $h = 4$.

Finally, the complex reflection and transmission coefficients can be deduced from the elements of \mathbf{T} according to [327]:

$$\begin{aligned} r_{ss} &= \frac{\mathbf{T}^{(2,1)}\mathbf{T}^{(3,3)} - \mathbf{T}^{(2,3)}\mathbf{T}^{(3,1)}}{\mathbf{T}^{(1,1)}\mathbf{T}^{(3,3)} - \mathbf{T}^{(1,3)}\mathbf{T}^{(3,1)}}, & r_{sp} &= \frac{\mathbf{T}^{(4,1)}\mathbf{T}^{(3,3)} - \mathbf{T}^{(4,3)}\mathbf{T}^{(3,1)}}{\mathbf{T}^{(1,1)}\mathbf{T}^{(3,3)} - \mathbf{T}^{(1,3)}\mathbf{T}^{(3,1)}}, \\ r_{ps} &= \frac{\mathbf{T}^{(1,1)}\mathbf{T}^{(2,3)} - \mathbf{T}^{(2,1)}\mathbf{T}^{(1,3)}}{\mathbf{T}^{(1,1)}\mathbf{T}^{(3,3)} - \mathbf{T}^{(1,3)}\mathbf{T}^{(3,1)}}, & r_{pp} &= \frac{\mathbf{T}^{(1,1)}\mathbf{T}^{(4,3)} - \mathbf{T}^{(4,1)}\mathbf{T}^{(1,3)}}{\mathbf{T}^{(1,1)}\mathbf{T}^{(3,3)} - \mathbf{T}^{(1,3)}\mathbf{T}^{(3,1)}}, \\ t_{ss} &= \frac{\mathbf{T}^{(3,3)}}{\mathbf{T}^{(1,1)}\mathbf{T}^{(3,3)} - \mathbf{T}^{(1,3)}\mathbf{T}^{(3,1)}}, & t_{sp} &= \frac{-\mathbf{T}^{(3,1)}}{\mathbf{T}^{(1,1)}\mathbf{T}^{(3,3)} - \mathbf{T}^{(1,3)}\mathbf{T}^{(3,1)}}, \\ t_{ps} &= \frac{-\mathbf{T}^{(1,3)}}{\mathbf{T}^{(1,1)}\mathbf{T}^{(3,3)} - \mathbf{T}^{(1,3)}\mathbf{T}^{(3,1)}}, & t_{pp} &= \frac{\mathbf{T}^{(1,1)}}{\mathbf{T}^{(1,1)}\mathbf{T}^{(3,3)} - \mathbf{T}^{(1,3)}\mathbf{T}^{(3,1)}}. \end{aligned} \quad (\text{A.38})$$

Here, r_{ss} determines the fraction of an incoming s-polarized light beam that is reflected in s-polarization, while mixed indices determine the rotation of the polarization. The latter effect is forbidden in isotropic structures. The intensity coefficients are obtained equivalently to Eq. (A.28). Note however that when considering the incidence of unpolarized light, the

reflected intensities perpendicular and parallel to the plane of incidence are now given by:

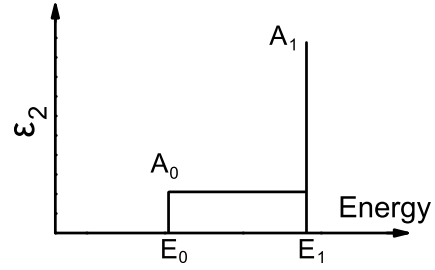
$$R_s = R_{ps} + R_{ss} \quad \text{and} \quad R_p = R_{sp} + R_{pp} . \quad (\text{A.39})$$

Equivalent relations hold for $T_{s/p}$ and $A_{s/p}$.

A.2.3 The Anisotropic Refractive Index of AlGa_N alloys

While the anisotropic refractive indices of GaN and AlN have already been measured over a wide spectral range with high accuracy (cf. Fig. 2.6), the quality of thick non- or semi-polar AlGa_N layers has not yet proven sufficient for a reliable examination of the variation of $\mathbf{n}(\hbar\omega)$ or $\epsilon(\hbar\omega)$ with alloy composition x . Literature values exist only for the ordinary polarization component, such as based on the transmission study of Brunner and co-workers in Ref. [328].

Figure A.2: Schematic representation of the analytical model of the dielectric function following Shokhovets and co-workers [303].



In order to model the optical response of the non-polar MC-2, another dataset had to be generated. Therefore, the optically anisotropic refractive indices of the binary alloys given in Fig. 2.6 have been approximated within the energy window between 1 and 7 eV using the analytic dispersion model introduced by Shokhovets and co-workers in Ref. [303]. The latter assumes the imaginary part of the dielectric function to be given by a step-like function for the band edge, that is characterized by an energy E_0 and an amplitude A_0 and that is terminated on the high-energy side by a Dirac-pole (cf. Fig. A.2). The latter is determined by an energy E_1 and an amplitude A_1 and accounts for the sum of the high-energy optical transitions. Based on the Kramers-Kronig relations from Eq. (2.38), the dispersion of the real part of the dielectric function is in this case given by:

$$\epsilon_1(E) = 1 + \frac{2}{\pi} \left[\frac{A_0}{2} \ln \left(\frac{E_1^2 - E^2}{E_0^2 - E^2} \right) + \frac{A_1 E_1}{E_1^2 - E^2} \right] . \quad (\text{A.40})$$

This model was initially proposed for the transparent region of GaN and AlN. However, using a complex energy representation for E_0 also a finite homogeneous linewidth can be considered that allows to model the near-band edge region with higher accuracy. The use of a large energy window was necessary to avoid strong correlation between E_0 and A_0 parameters for AlN. The fit results are summarized in Tab. A.1. Except for E_0 , all parameters were linearly interpolated to obtain the anisotropic dielectric function of an AlGa_N alloy with the desired composition x . For E_0 bowing values of 0.87 and 0.79 eV have been used in the ordinary and extraordinary polarization direction, respectively. These have been determined by anisotropic ellipsometry measurements of an Al_{0.12}Ga_{0.88}N layer. Table A.1 provides data for E_0 at $T = 0$ K: for a finite temperature, they have to be modified according to the temperature dependence of the bandgap discussed in Sec. 3.2.3.

Table A.1: Reproduction of the experimental anisotropic dielectric function of GaN and AlN with the model of Ref. [303] ($T = 4\text{K}$): comparison of the adjusted parameters that have, except for E_0 , been linearly interpolated to model the anisotropic optical response of an AlGaIn alloy.

	GaN		AlN	
	$E \perp c$	$E \parallel c$	$E \perp c$	$E \parallel c$
E_0 (eV)	3.511	3.536	6.272	6.052
A_0	1.525	1.691	2.136	2.332
E_1 (eV)	8.205	7.843	9.672	9.137
A_1	43.64	42.73	38.17	37.85

A.2.4 Refractive Index of a Quantum-Well

Semiconductor MQW structures represent an intrinsically uniaxial optical system. Owing to the finite extension of the exciton wave-function along the growth axis and the non-locality of the layered structure, the dielectric response can only be described in an accurate manner when considering a non-local approach, based on the in-plane wave-vector dispersion of the exciton [329]. Indeed, in extreme cases of very narrow exciton resonances, a local treatment of the QW dielectric function that assumes infinite exciton masses may lead to the appearance of unphysical standing waves in the QW. Nevertheless, it was shown that for sufficiently broadened resonances the local approach yields a reasonable approximation [62]. With linewidth values of $\sim 10\text{meV}$ and beyond this condition can be assumed to be commonly fulfilled for III-nitrides.

The dielectric response of a homogeneously broadened exciton with energy E_X and linewidth γ_{hom} in a QW of width L_{QW} is given by [108]:

$$\varepsilon_{\text{hom}}(\hbar\omega, E_X) = \varepsilon_B + \frac{1}{L_{\text{QW}}} \frac{f_X}{S} \frac{e^2 \hbar^2}{\varepsilon_0 m_0} \frac{1}{E_X^2 - (\hbar\omega)^2 + i\hbar\omega\gamma_{\text{hom}}}. \quad (\text{A.41})$$

Here, f_X/S marks the exciton oscillator strength per unit area provided by Eq. (2.46). The background refractive index represented by ε_B is derived using the method described in Sec. A.2.3 by setting $E_0 = E_X + E_B$. The band-to-band absorption can be taken into account by adding a broadened Heaviside-function in the imaginary part of ε_B .

In order to account for the impact of structural inhomogeneities the excitonic response can be additionally convoluted by a Gaussian profile with $\gamma_{\text{inh}} = 2\sigma\sqrt{2\ln 2}$:

$$\varepsilon(\hbar\omega, E_X) = \frac{1}{\sigma\sqrt{2\pi}} \int_{-\infty}^{\infty} \exp\left(-\frac{(\hbar\omega' - \hbar\omega)^2}{2\sigma^2}\right) \varepsilon_{\text{hom}}(\hbar\omega', E_X) d\omega'. \quad (\text{A.42})$$

The resulting lineshape is usually referred to as a Voigt-profile.

Finally, it is worth mentioning that this simplified model represents only a rather crude approximation, which however yields very convenient results. Nevertheless, depending on the specific demands of a future study it might be useful to rely on a more sophisticated approach, as e.g. introduced by Lefebvre and co-workers in Ref. [330] based on the fractional dimensionality.

A.3 Recent XRD results on MC-2

Unfortunately, the initial XRD-study on MC-2, which was conducted externally, remained incomplete: a potential tilt of the epitaxial structure was not taken into account and only a single asymmetric reflex along the c -axis was measured, i.e. (20 $\bar{2}$ 3). The results were similar to those of Fig. 4.41, but much noisier. For the purpose of drawing a comprehensive analysis in the present chapter, the XRD-study has been repeated in-house recently with a novel XRD-equipment. Figure A.3 shows RSMs of the asymmetric (20 $\bar{2}$ 3) and (3 $\bar{2}$ 13) reflexes of MC-2, giving access to the in-plane lattice parameters c and a , respectively. Here, the situation appears much more complex than initially assumed based on x_{geo} . Along the c -direction both AlGaIn alloys of the bottom-DBR adopt identical lattice constants at $q_z = 3.66 \text{ nm}^{-1}$, which corresponds to an effective Al-content of about 16% contrary to the conclusion drawn for Fig. 4.41. In the other in-plane direction shown in Fig. A.3(b), both bilayer components feature a broad double-peak signature. Based on an analysis of the symmetric reflex, this characteristic could be traced back to two different crystal domains that are tilted symmetrically by about 0.2° with respect to the GaN substrate reflex. This effect may be related to the sawtooth profile visible in the AFM-scan of Fig. 4.40. Figure A.3(b) shows the inverse lattice constants corrected for the tilt of the AlGaIn peaks at lower q_y . They emerge at different q_x values indicating plastic strain relaxation occurring along the in-plane a -direction. Conclusively, the epitaxial III-nitride layer stack appears to be elastically strained on x_{Al} lattice constants along the c -direction and partially relaxed along the a -direction. As expected, in both RSMs the out-of-plane lattice constants given by q_y are identical. Based on the unit cell volume and the elastic constants given by Tab. 2.2, the Al-contents of the DBR-bilayer components were estimated to 38 and 12%, i.e. quite close to the nominal values.

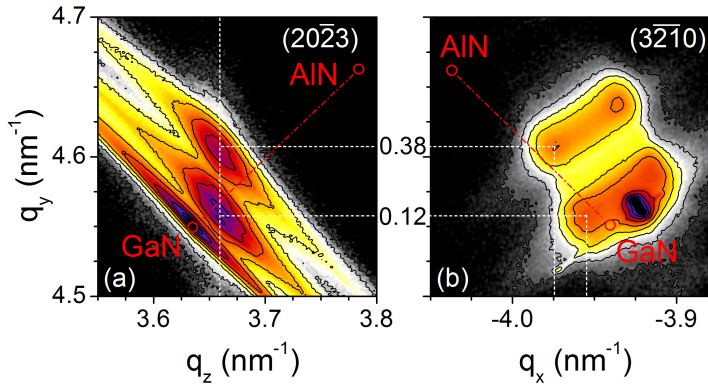
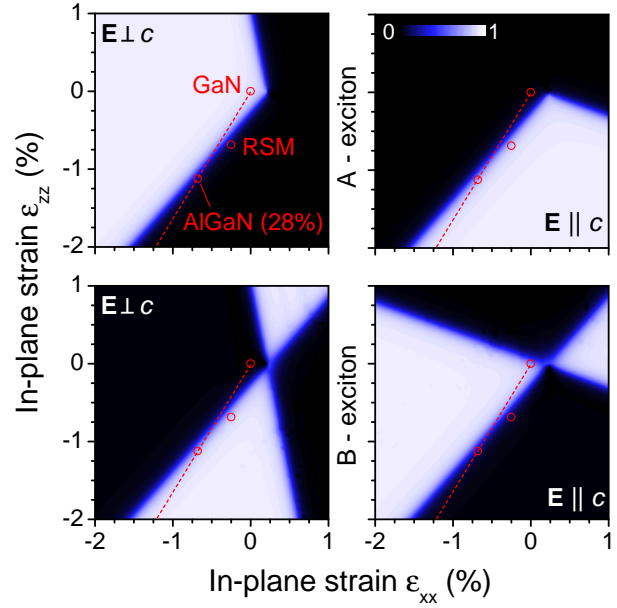


Figure A.3: Asymmetric XRD-RSMs of the reflexes (a) (20 $\bar{2}$ 3) and (b) (3 $\bar{2}$ 13) measured on MC-2. The white dashed lines mark the lattice parameters of the two bottom-DBR components. The red circles mark the equilibrium positions of GaN and AlN. See text for details.

Based on this analysis the actual strain state of the MQWs of MC-2 is different from that initially assumed Sec 4.7.2 and in Ref. [169]. Although it cannot be directly concluded from the XRD-measurements, it is very likely that along the c -direction the cavity region adopts the lattice constant of the quasi-pseudomorphic DBR layer stack. Due to the comparable Al-content and the moderate thickness the strain state along the a -direction should be very similar to that of the low Al-content DBR component. Figure A.4 shows the anisotropic relative oscillator strength of the QW ground states A and B as a function of the two in-plane strain components ϵ_{xx} and ϵ_{zz} (cf. Sec. 2.1.2). They have been calculated in the same way as the curves shown in Figs. 4.47(b,c) and contain the information of the latter: the variation of the strain components according to the c/a -ratio of the AlGaIn alloy are indicated by the red

Figure A.4: Anisotropic f_{osc} for an m -plane 5 nm thick GaN/Al_{0.12}Ga_{0.88}N QW as deduced from Schrödinger- $k.p$ simulations for the A and B ground state transitions (at the top and bottom, respectively) as a function of the in-plane strain components. Polarization directions $E \perp c$ and $E \parallel c$ are shown on the left- and right-hand sides, respectively. The trace along the red dashed line yields the curves displayed in Fig. 4.47. The red circles mark different strain states for the QW: strain-free, strained according to Fig. A.3, and pseudomorphically strained on Al_{0.28}Ga_{0.72}N lattice constants (in order of decreasing ϵ_{zz}).



dashed line in Fig. A.4. The strain position of the present RSM analysis is also marked. It corresponds to strongly asymmetric lattice stress perpendicular to the growth axis but features almost identical selection rules as for the scenario of $x_{\text{Al}} = 0.28$: $\rho_A = \rho_B = -0.58$. Due to the overall lower strain state the transition energy is expected to be shifted by about 25 meV down to lower energies compared to Eq. (4.40). These variations lie within the error margins of the modeling and do likewise fit the experimental results. According to Figure A.4 this agreement seems to be purely fortuitous, e.g. a small change in ϵ_{xx} could lead to a complete redistribution of f_{osc} .

Finally, it is worth wondering if the strain state of MC-2 changed over the past three years. Indeed, several evidences point toward an aging of the sample. The initial measurements indicated significantly higher strain values along ϵ_{zz} , comparable to the RSM shown in Fig. 4.41. Thus, a progressive degradation of the sample and thus a reduction of the experienced lattice strain state appears very likely, eventually making it invalid to draw a correction based on the recent XRD-results. Note however, that the revealed uncertainties concern exclusively the modeling of the f_{osc} redistribution within the $k.p$ -approach, whereas the whole results about the anisotropic light-matter coupling reported in Refs. [169, 272] are based exclusively on optical measurements. Therefore, they remain fully valid.

Bibliography

- [1] H. Amano, M. Kito, K. Hiramatsu, I. Akasaki, *P-type conduction in Mg-doped GaN treated with low-energy electron beam irradiation (LEEBI)*, Jpn. J. Appl. Phys. **28**, L2112 (1989)
- [2] S. Nakamura, M. Senoh, T. Mukai, *Highly p-typed Mg-doped GaN films grown with GaN buffer layers*, Jpn. J. Appl. Phys. **30**, L1708 (1991)
- [3] S. Nakamura, T. Mukai, M. Senoh, *High-power GaN p-n junction blue-light emitting diodes*, Jpn. J. Appl. Phys. **30**, L1998 (1991)
- [4] S. Nakamura, T. Mukai, M. Senoh, *Candela-class high brightness InGaN/AlGaIn double-heterostructure blue-light-emitting diodes*, Appl. Phys. Lett. **64**, 1687 (1994)
- [5] S. Nakamura, N. Iwasa, T. Yamada, T. Matsushita, H. Kiyoku, M. Senoh, S.-I. Nagahama, Y. Sugimoto, *InGaIn-based multi-quantum-well-structure laser diodes*, Jpn. J. Appl. Phys. **35**, L74 (1996)
- [6] M. H. Kim, M. F. Schubert, Q. Dai, J. K. Kim, E. F. Schubert, J. Piprek, Y. Park, *Origin of efficiency droop in GaN-based light-emitting diodes*, Appl. Phys. Lett. **91**, 183507 (2007)
- [7] E. Kioupakis, P. Rinke, K. T. Delaney, C. G. Van de Walle, *Indirect Auger recombination as a cause of efficiency droop in nitride light-emitting diodes*, Appl. Phys. Lett. **98**, 161107 (2011)
- [8] M. G. A. Bernard, G. Duraffourg, *Laser conditions in semiconductors*, Phys. Status Solidi **1**, 699 (1961)
- [9] N. F. Mott, *Conduction in polar crystals: II. The conduction band and ultra-violet absorption of alkali-halide crystals*, Trans. Faraday Soc. **34**, 500 (1938)
- [10] N. F. Mott, *Metal-Insulator Transition*, Rev. Mod. Phys. **40**, 677 (1968)
- [11] A. Imamoglu, R. J. Ram, S. Pau, Y. Yamamoto, *Nonequilibrium condensates and lasers without inversion: Exciton-polariton lasers*, Phys. Rev. A **53**, 4250 (1996)
- [12] C. Weisbuch, M. Nishioka, A. Ishikawa, Y. Arakawa, *Observation of the coupled exciton-photon mode splitting in a semiconductor quantum microcavity*, Phys. Rev. Lett. **69**, 3314 (1992)
- [13] S. N. Bose, *Plancks Gesetz und Lichtquantenhypothese*, Z. Phys **26**, 178 (1924)
- [14] A. Einstein, *Quantentheorie des einatomigen idealen Gases. Zweite Abhandlung.*, Sitzber. Preuss. Akad. **1**, 3 (1925)
- [15] A. Einstein, *Zur Quantentheorie des idealen Gases*, Sitzber. Preuss. Akad. **3**, 18 (1925)
- [16] Le Si Dang, D. Heger, R. André, F. Bœuf, R. Romestain, *Stimulation of polariton photoluminescence in semiconductor microcavity*, Phys. Rev. Lett. **81**, 3920 (1998)
- [17] J. Kasprzak, M. Richard, S. Kundermann, A. Baas, P. Jeambrun, J. M. J. Keeling, F. M. Marchetti, M. H. Szymanska, R. André, J. L. Staehli, V. Savona, P. B. Littlewood, B. Deveaud-Plédran, Le Si Dang, *Bose-Einstein condensation of exciton polaritons*, Nature (London) **443**, 409 (2006)
- [18] K. G. Lagoudakis, M. Wouters, M. Richard, A. Baas, I. Carusotto, R. André, Le Si Dang, B. Deveaud-Plédran, *Quantized vortices in an exciton-polariton condensate*, Nature Phys. **4**, 706 (2008)
- [19] A. Amo, J. Lefrère, S. Pigeon, C. Adrados, C. Ciuti, R. Houdré, I. Carusotto, E. Giacobino, A. Bramati, *Superfluidity of polaritons in semiconductor microcavities*, Nature Phys. **5**, 805 (2009)
- [20] K. G. Lagoudakis, B. Pietka, M. Wouters, R. André, B. Deveaud-Plédran, *Coherent oscillations in an exciton-polariton Josephson junction*, Phys. Rev. Lett. **105**, 120403 (2010)

- [21] M. Saba, C. Ciuti, J. Bloch, V. Thierry-Mieg, R. André, Le Si Dang, S. Kundermann, A. Mura, G. Bongiovanni, J. L. Staehli, B. Deveaud-Plédran, *High-temperature ultrafast polariton parametric amplification in semiconductor microcavities*, Nature (London) **414**, 731 (2001)
- [22] S. Christopoulos, G. Baldassarri Höger von Högersthal, A. J. D. Grundy, P. G. Lagoudakis, A. V. Kavokin, J. J. Baumberg, G. Christmann, R. Butté, E. Feltin, J.-F. Carlin, N. Grandjean, *Room-temperature polariton lasing in semiconductor microcavities*, Phys. Rev. Lett. **98**, 126405 (2007)
- [23] G. Christmann, R. Butté, E. Feltin, J.-F. Carlin, N. Grandjean, *Room temperature polariton lasing in a GaN/AlGaIn multiple quantum well microcavity*, Appl. Phys. Lett. **93**, 051102 (2008)
- [24] J. J. Baumberg, A. V. Kavokin, S. Christopoulos, A. J. D. Grundy, R. Butté, G. Christmann, D. D. Solnyshkov, G. Malpuech, G. Baldassarri Höger von Högersthal, E. Feltin, J.-F. Carlin, N. Grandjean, *Spontaneous polarization build-up in a room-temperature polariton laser*, Phys. Rev. Lett. **101**, 136409 (2008)
- [25] R. Butté, J. Levrat, G. Christmann, E. Feltin, J.-F. Carlin, N. Grandjean, *Phase diagram of a polariton laser from cryogenic to room temperature*, Phys. Rev. B **80**, 233301 (2009)
- [26] J. Levrat, R. Butté, E. Feltin, J.-F. Carlin, N. Grandjean, D. Solnyshkov, G. Malpuech, *Condensation phase diagram of cavity polaritons in GaN-based microcavities: Experiment and theory*, Phys. Rev. B **81**, 125305 (2010)
- [27] W. Paszkowicz, S. Podsiado, R. Minikayev, *Rietveld-refinement study of aluminium and gallium nitrides*, J. Alloys Compounds **382**, 100 (2004)
- [28] W. Paszkowicz, R. Cerny, S. Krukowski, *Rietveld refinement for indium nitride in the 105 – 295 K range*, Powder Diffr. **18**, 114 (2003)
- [29] L. Pauling, *The nature of the chemical bond and the structure of molecules and crystals* (Cornell University Press, New York, 1960)
- [30] L. Liu, J. H. Edgar, *Substrates for gallium nitride epitaxy*, Mat. Sci. Eng. R. **37**, 61 (2002)
- [31] I. Vurgaftman, J. R. Meyer, *Band parameters for nitrogen-containing semiconductors*, J. Appl. Phys. **94**, 3675 (2003)
- [32] S.-H. Park, S.-L. Chuang, *Crystal-orientation effects on the piezoelectric field and electronic properties of strained wurtzite semiconductors*, Phys. Rev. B **59**, 4725 (1999)
- [33] P. Y. Yu, M. Cardona, *Fundamentals of semiconductors: Physics and materials properties* (4th Edition, Springer, Heidelberg, 2010)
- [34] C. Kittel, *Introduction to solid state physics* (8th Edition, John Wiley & Sons, New York, 2005)
- [35] L.C. de Carvalho, A. Schleife, F. Bechstedt, *Influence of exchange and correlation on structural and electronic properties of AlN, GaN, and InN polytypes*, Phys. Rev. B **84**, 195105 (2011)
- [36] E.M. Purcell, *Spontaneous emission probabilities at radio frequencies*, Phys. Rev. **69**, 681 (1946)
- [37] A. Shikanai, T. Azuhata, T. Sota, S. Chichibu, A. Kuramata, K. Horino, S. Nakamura, *Biaxial strain dependence of exciton resonance energies in wurtzite GaN*, J. Appl. Phys. **81**, 417 (1997)
- [38] E.I. Rashba, *Properties of semiconductors with an extremum loop: 1. Cyclotron and combinational resonance in a magnetic field perpendicular to the plane of the loop*, Sov. Phys. Solid State **2**, 1109 (1960)
- [39] Yu. M. Sirenko, J. B. Jeon, B. C. Lee, K. W. Kim, M. A. Littlejohn, M. A. Stroscio, G. J. Iafrate, *Hole scattering and optical transitions in wide-band-gap nitrides: Wurtzite and zinc-blende structures*, Phys. Rev. B **55**, 4360 (1997)
- [40] S. L. Chuang, C. S. Chang, *k-p method for strained wurtzite semiconductors*, Phys. Rev. B **54**, 2491 (1996)
- [41] J. J. Hopfield, *Theory of the contribution of excitons to the complex dielectric constant of crystals*, Phys. Rev. **112**, 1555 (1958)
- [42] P. Rinke, M. Winkelnkemper, A. Qteish, D. Bimberg, J. Neugebauer, M. Scheffler, *Consistent set of band parameters for the group-III nitrides AlN, GaN, and InN*, Phys. Rev. B **77**, 075202 (2008)
- [43] E. Silveira, J. A. Freitas, M. Kneissl, D. W. Treat, N. M. Johnson, G. A. Slack, L. J. Schowalter,

- Near-bandedge cathodoluminescence of an AlN homoepitaxial film*, Appl. Phys. Lett. **84**, 3501 (2004)
- [44] G. Rossbach, M. Feneberg, M. Röppischer, C. Werner, N. Esser, C. Cobet, T. Meisch, K. Thonke, A. Dadgar, J. Bläsing, A. Krost, R. Goldhahn, *Influence of exciton-phonon coupling and strain on the anisotropic optical response of wurtzite AlN around the band edge*, Phys. Rev. B **83**, 195202 (2011)
- [45] W. M. Yim, E. J. Stofko, P. J. Zanzucchi, J. I. Pankove, M. Ettenberg, S. L. Gilbert, *Epitaxially grown AlN and its optical band gap*, J. Appl. Phys. **44**, 292 (1972)
- [46] V. Darakchieva, M.-Y. Xie, F. Tasnadi, I. A. Abrikosov, L. Hultman, B. Monemar, J. Kamimura, K. Kishino, *Lattice parameters, deviations from Vegard's rule, and E_2 phonons in InAlN*, Appl. Phys. Lett. **93**, 261908 (2008)
- [47] B. K. Meyer, G. Steude, A. Göldner, A. Hoffmann, H. Amano, I. Akasaki, *Photoluminescence investigations of AlGaIn on GaN epitaxial films*, Phys. Status Solidi B **216**, 187 (1999)
- [48] A. Riefer, F. Fuchs, C. Rödl, A. Schleife, F. Bechstedt, R. Goldhahn, *Interplay of excitonic effects and van Hove singularities in optical spectra: CaO and AlN polymorphs*, Phys. Rev. B **84**, 075218 (2011)
- [49] G. H. Wannier, *The structure and electronic excitation levels in insulating crystals*, Phys. Rev. **52**, 191 (1937)
- [50] T. Azuhata, T. Sota, K. Suzuki, S. Nakamura, *Polarized Raman spectra in GaN*, J. Phys.: Condens. Matter **7**, L129 (1995)
- [51] W. J. Moore, J. A. Freitas, R.T. Holm, O. Kovalenkov, V. Dmitriev, *Infrared dielectric function of wurtzite aluminum nitride*, J. Appl. Phys. **86** (2005)
- [52] V. Y. Davydov, V. V. Emtsev, I. N. Goncharuk, A. N. Smirnov, V. D. Petrikov, V. V. Mamutin, V. A. Vekshin, S. V. Ivanov, M. B. Smirnov, T. Inushima, *Experimental and theoretical studies of phonons in hexagonal InN*, Appl. Phys. Lett. **75**, 3297 (1999)
- [53] K. Kornitzer, T. Ebner, K. Thonke, R. Sauer, C. Kirchner, V. Schwegler, M. Kamp, M. Leszczynski, I. Grzegory, S. Porowski, *Photoluminescence and reflectance spectroscopy of excitonic transitions in high-quality homoepitaxial GaN films*, Phys. Rev. B **60**, 1471 (1999)
- [54] B. Gil, O. Briot, *Internal structure and oscillator strengths of excitons in strained α -GaN*, Phys. Rev. B **55**, 2530 (1997)
- [55] B. Deveaud, F. Clérot, N. Roy, K. Satzke, B. Sermage, D. S. Katzer, *Enhanced radiative recombination of free excitons in GaAs quantum wells*, Phys. Rev. Lett. **67**, 2355 (1991)
- [56] F. Binet, J. Y. Duboz, J. Off, F. Scholz, *High-excitation photoluminescence in GaN: Hot-carrier effects and the Mott transition*, Phys. Rev. B **60**, 4715 (1999)
- [57] S. Rudin, T. L. Reinecke, B. Segall, *Temperature-dependent exciton linewidths in semiconductors*, Phys. Rev. B **42**, 11218 (1990)
- [58] J. H. Edgar, S. Strite, I. Akasaki, H. Amano, C. Wetzel, *Gallium nitride and related semiconductors* (Inspec, London, 1999)
- [59] C. Buchheim, M. Röppischer, R. Goldhahn, G. Gobsch, C. Cobet, C. Werner, N. Esser, A. Dadgar, M. Wieneke, J. Bläsing, A. Krost, *Influence of anisotropic strain on excitonic transitions in a-plane GaN films*, Microelectron. J. **40**, 322 (2009)
- [60] G. Rossbach, M. Röppischer, P. Schley, G. Gobsch, C. Werner, C. Cobet, N. Esser, A. Dadgar, M. Wieneke, A. Krost, R. Goldhahn, *Valence-band splitting and optical anisotropy of AlN*, Phys. Status Solidi B **247**, 1679 (2010)
- [61] C. Weisbuch, B. Vinter, *Quantum semiconductor structures: Fundamentals and applications* (Academic Press Inc., San Diego, 1991)
- [62] L. C. Andreani, *Radiative lifetime of free excitons in quantum wells*, Solid State Commun. **77**, 641 (1991)
- [63] A. V. Kavokin, J. J. Baumberg, G. Malpuech, F. P. Laussy, *Microcavities* (Oxford University Press, Oxford, 2007)

- [64] R. P. Leavitt, J. W. Little, *Simple method for calculating exciton binding energies in quantum-confined semiconductor structures*, Phys. Rev. B **42**, 11774 (1990)
- [65] X. F. He, *Excitons in anisotropic solids: The model of fractional-dimensional space*, Phys. Rev. B **43**, 2063 (1991)
- [66] H. Mathieu, P. Lefebvre, P. Christol, *Simple analytical method for calculating exciton binding energies in semiconductor quantum wells*, Phys. Rev. B **46**, 4092 (1992)
- [67] C. Weisbuch, R. C. Miller, R. Dingle, A. C. Gossard, W. Wiegman, *Intrinsic radiative recombination from quantum states in GaAs-Al_xGa_{1-x}As multi-quantum well structures*, Solid State Commun. **37**, 219 (1981)
- [68] V. Savona, L. C. Andreani, P. Schwendimann, A. Quattropani, *Unified treatment of weak and strong coupling regimes*, Solid State Commun. **93**, 773 (1995)
- [69] P. Corfdir, J. Levrat, G. Rossbach, R. Butté, E. Feltin, J.-F. Carlin, G. Christmann, P. Lefebvre, J.-D. Ganière, N. Grandjean, B. Deveaud-Plédran, *Impact of biexcitons on the relaxation mechanisms of polaritons in III-nitride based multiple quantum well microcavities*, Phys. Rev. B **85**, 245308 (2012)
- [70] F. Bernardini, V. Fiorentini, *Nonlinear macroscopic polarization in III-V nitride alloys*, Phys. Rev. B **64**, 085207 (2001)
- [71] M. A. Khan, A. Bhattarai, J. N. Kuznia, D. T. Olson, *High electron mobility transistor based on a GaN-Al_xGa_{1-x}N heterojunction*, Appl. Phys. Lett. **63**, 1214 (1993)
- [72] M. Gonschorek, J.-F. Carlin, E. Feltin, M. A. Py, N. Grandjean, *High electron mobility lattice-matched AlInN/GaN field-effect transistor heterostructures*, Appl. Phys. Lett. **89**, 062106 (2006)
- [73] J. Schalwig, G. Müller, M. Eickhoff, O. Ambacher, M. Stutzmann, *Gas sensitive GaN/AlGaN heterostructures*, Sens. Actuators B **87**, 425 (2002)
- [74] R. Butté, J.-F. Carlin, E. Feltin, M. Gonschorek, S. Nicolay, G. Christmann, D. Simeonov, A. Castiglia, J. Dorsaz, H. J. Buehlmann, S. Christopoulos, G. Baldassarri Höger von Högersthal, A. J. D. Grundy, M. Mosca, C. Pinquier, M. A. Py, F. Demangeot, J. Frandon, P. G. Lagoudakis, J. J. Baumberg, N. Grandjean, *Current status of AlInN layers lattice-matched to GaN for photonics and electronics*, J. Phys. D: Appl. Phys. **40**, 6328 (2007)
- [75] P. Waltereit, O. Brandt, A. Trampert, H. T. Grahn, J. Menniger, M. Ramsteiner, M. Reiche, K. H. Ploog, *Nitride semiconductors free of electrostatic fields for efficient white light-emitting diodes*, Nature (London) **406**, 865 (2000)
- [76] O. Ambacher, J. Majewski, C. Miskys, A. Link, M. Hermann, M. Eickhoff, M. Stutzmann, F. Bernardini, V. Fiorentini, V. Tilak, B. Shaff, L. F. Eastman, *Pyroelectric properties of Al(In)GaN/GaN hetero- and quantum well structures*, J. Phys.: Condens. Matter **14**, 3399 (2002)
- [77] G. Cosendey, J.-F. Carlin, N. A. K. Kaufmann, R. Butté, N. Grandjean, *Strain compensation in AlInN/GaN multilayers on GaN substrates: Application to the realization of defect-free Bragg reflectors*, Appl. Phys. Lett. **98**, 181111 (2011)
- [78] A. E. Romanov, T. J. Baker, S. Nakamura, J. S. Speck, ERATO/JST UCSB Group, *Strain-induced polarization in wurtzite III-nitride semipolar layers*, J. Appl. Phys. **100**, 023522 (2006)
- [79] K. Nishizuka, M. Funato, Y. Kawakami, S. Fujita, Y. Narukawa, T. Mukai, *Efficient radiative recombination from <11-22>-oriented In_xGa_{1-x}N multiple quantum wells fabricated by the regrowth technique*, Appl. Phys. Lett. **85**, 3122 (2004)
- [80] M. Leroux, N. Grandjean, M. Laugt, J. Massies, B. Gil, P. Lefebvre, P. Bigenwald, *Quantum confined Stark effect due to built-in internal polarization fields in (Al,Ga)N/GaN quantum wells*, Phys. Rev. B **58**, R13371 (1998)
- [81] N. Grandjean, B. Damilano, S. Dalmaso, M. Leroux, M. Laügt, J. Massies, *Built-in electric-field effects in wurtzite AlGaN/GaN quantum wells*, J. Appl. Phys. **86**, 3714 (1999)
- [82] M. Leroux, N. Grandjean, J. Massies, B. Gil, P. Lefebvre, P. Bigenwald, *Barrier-width dependence of group-III nitrides quantum-well transition energies*, Phys. Rev. B **60**, 1496 (1999)

- [83] R. Sharma, P. M. Pattison, H. Masui, R. M. Farrell, T. J. Baker, B. A. Haskell, F. Wu, S. P. DenBaars, J. S. Speck, S. Nakamura, *Demonstration of a semipolar (10-1-3) InGaN/GaN green light emitting diode*, Appl. Phys. Lett. **87**, 231110 (2005)
- [84] Y. Yoshizumi, M. Adachi, Y. Enya, T. Kyono, S. Tokuyama, T. Sumitomo, K. Akita, T. Ikegami, M. Ueno, K. Katayama, T. Nakamura, *Continuous-wave operation of 520 nm green InGaN-based laser diodes on semi-polar {20 $\bar{2}$ 1} GaN substrates*, Appl. Phys. Express **2**, 092101 (2009)
- [85] T. Miyoshi, S. Masui, T. Okada, T. Yanamoto, T. Kozaki, S.-I. Nagahama, T. Mukai, *510-515 nm InGaN-based green laser diodes on c-plane GaN substrate*, Appl. Phys. Express **2**, 062201 (2009)
- [86] S. Kalliakos, P. Lefebvre, T. Taliercio, *Nonlinear behavior of photoabsorption in hexagonal nitride quantum wells due to free carrier screening of the internal fields*, Phys. Rev. B **67**, 205307 (2003)
- [87] G. Rossbach, J. Levrat, G. Jacopin, M. Shahmohammadi, J.-F. Carlin, J.-D. Ganière, R. Butté, B. Deveaud, N. Grandjean, *High-temperature Mott-transition in wide band-gap semiconductor quantum wells* (submitted)
- [88] F. Stokker-Cheregi, A. Vinattieri, E. Feltin, D. Simeonov, J.-F. Carlin, R. Butté, N. Grandjean, M. Gurioli, *Biexciton kinetics in GaN quantum wells: Time-resolved and time-integrated photoluminescence measurements*, Phys. Rev. B **77**, 125342 (2008)
- [89] F. Stokker-Cheregi, A. Vinattieri, E. Feltin, D. Simeonov, J. Levrat, J.-F. Carlin, R. Butté, N. Grandjean, M. Gurioli, *Impact of confinement and quantum confined Stark effect on biexciton binding energy in GaN/AlGaIn quantum wells*, Appl. Phys. Lett. **93**, 152105 (2008)
- [90] S. Shokhovets, O. Ambacher, B. K. Meyer, G. Gobsch, *Anisotropy of the momentum matrix element, dichroism, and conduction-band dispersion relation of wurtzite semiconductors*, Phys. Rev. B **78**, 035207 (2008)
- [91] E. Feltin, D. Simeonov, J.-F. Carlin, R. Butté, N. Grandjean, *Narrow UV emission from homogeneous GaN/AlGaIn quantum wells*, Appl. Phys. Lett. **90**, 021905 (2007)
- [92] K. Okada, Y. Yamada, T. Taguchi, F. Sasaki, S. Kobayashi, T. Tani, S. Nakamura, G. Shinomiya, *Biexciton luminescence from GaN epitaxial layers*, Jpn. J. Appl. Phys. **35**, L787 (1996)
- [93] M. Feneberg, R. A. R. Leute, B. Neuschl, K. Thonke, M. Bickermann, *High-excitation and high-resolution photoluminescence spectra of bulk AlN*, Phys. Rev. B **82**, 075208 (2010)
- [94] S. Kako, K. Hoshino, S. Iwamoto, S. Ishida, Y. Arakawa, *Exciton and biexciton luminescence from single hexagonal GaN/AlN self-assembled quantum dots*, Appl. Phys. Lett. **85**, 64 (2004)
- [95] D. Simeonov, A. Dussaigne, R. Butté, N. Grandjean, *Complex behavior of biexcitons in GaN quantum dots due to a giant built-in polarization field*, Phys. Rev. B **77**, 075306 (2008)
- [96] D. A. Kleinman, *Binding energy of biexciton and bound excitons in quantum wells*, Phys. Rev. B **28**, 871 (1983)
- [97] J. Usukura, Y. Suzuki, K. Varga, *Stability of two- and three-dimensional excitonic complexes*, Phys. Rev. B **59**, 5652 (1999)
- [98] T. F. Rønnow, T. G. Pedersen, B. Partoens, *Biexciton binding energy in fractional dimensional semiconductors*, Phys. Rev. B **85**, 045412 (2012)
- [99] J. R. Haynes, *Experimental proof of the existence of a new electronic complex in silicon*, Phys. Rev. Lett. **4**, 361 (1960)
- [100] W. Langbein, J. M. Hvam, *Localization-enhanced biexciton binding in semiconductors*, Phys. Rev. B **59**, 15405 (1999)
- [101] Y. Yamada, Y. Ueki, K. Nakamura, T. Taguchi, Y. Kawaguchi, A. Ishibashi, T. Yokogawa, *Biexciton luminescence from Al_xGa_{1-x}N epitaxial layers*, Appl. Phys. Lett. **84**, 12 (2004)
- [102] R. T. Phillips, D. J. Lovering, G. J. Denton, G. W. Smith, *Biexciton creation and recombination in a GaAs quantum well*, Phys. Rev. B **45**, 4308 (1992)
- [103] J. Levrat, R. Butté, T. Christian, M. Glauser, E. Feltin, J.-F. Carlin, N. Grandjean, D. Read, A. V. Kavokin, Y. G. Rubo, *Pinning and depinning of the polarization of exciton-polariton condensates at room temperature*, Phys. Rev. Lett. **104**, 166402 (2010)

- [104] G. Rossbach, J. Levrat, E. Feltn, J.-F. Carlin, R. Butté, N. Grandjean, *Impact of saturation on the polariton renormalization in III-nitride based planar microcavities*, Phys. Rev. B **88**, 165312 (2013)
- [105] L. Viña, S. Logothetidis, M. Cardona, *Temperature dependence of the dielectric function of germanium*, Phys. Rev. B **30**, 1979 (1984)
- [106] M. Feneberg, M. Fatima-Romero, M. Röppischer, C. Cobet, N. Esser, B. Neuschl, K. Thonke, M. Bickermann, R. Goldhahn, *Anisotropic absorption and emission of bulk (1-100) AlN*, Phys. Rev. B **87**, 235209 (2013)
- [107] M. Gurioli, A. Vinattieri, M. Colocci, *Temperature dependence of the radiative and nonradiative recombination time in GaAs/Al_xGa_{1-x}As quantum-well structures*, Phys. Rev. B **44**, 3115 (1991)
- [108] J. Levrat, *Physics of Polariton Condensates in GaN-based Planar Microcavities* (Thesis No. 5449, EPF Lausanne, 2012)
- [109] N. F. Mott, *The transition to the metallic state*, Philos. Mag. **6**, 287 (1961)
- [110] S. A. Moskalenko, *Reversible optico-hydrodynamic phenomena in a non ideal exciton gas*, Sov. Phys. Solid State **4**, 199 (1962)
- [111] H. Hanamura, H. Haug, *Condensation effects of excitons*, Phys. Rep. **33**, 209 (1977)
- [112] M. Kira, F. Jahnke, S. W. Koch, J. D. Berger, D. V. Wick, T. R. Nelson Jr., G. Khitrova, H. M. Gibbs, *Quantum theory of nonlinear semiconductor microcavity luminescence explaining "Boser" experiments*, Phys. Rev. Lett. **79**, 5170 (1997)
- [113] S. Schmitt-Rink, D. S. Chemla, D. A. B. Miller, *Theory of transient excitonic optical nonlinearities in semiconductor quantum-well structures*, Phys. Rev. B **32**, 6601 (1985)
- [114] C. Klingshirn, R. Hauschild, J. Fallert, H. Kalt, *Room-temperature stimulated emission of ZnO: Alternatives to excitonic lasing*, Phys. Rev. B **75**, 115203 (2007)
- [115] R. Houdré, J. L. Gibernon, P. Pellandini, R. P. Stanley, U. Oesterle, C. Weisbuch, J. O'Gorman, B. Roycroft, M. Ilegems, *Saturation of the strong coupling regime in a semiconductor microcavity: Free-carrier bleaching of cavity polaritons*, Phys. Rev. B **52**, 7810 (1995)
- [116] W. H. Knox, R. L. Fork, M. C. Downer, D. A. B. Miller, D. S. Chemla, C. V. Shank, A. C. Gossard, W. Wiegman, *Femtosecond dynamics of resonantly excited excitons in room-temperature GaAs quantum wells*, Phys. Rev. Lett. **54**, 1306 (1985)
- [117] R. Zimmermann, *Nonlinear optics and the Mott transition in semiconductors*, Phys. Status Solidi B **146**, 371 (1988)
- [118] D. W. Snoke, J. D. Crawford, *Hysteresis in the Mott-transition between plasma and insulating gas*, Phys. Rev. E **52**, 5796 (1995)
- [119] L. M. Sander, D. K. Fairbent, *Mott transition of the electron-hole liquid in Ge*, Solid State Commun. **20**, 631 (1976)
- [120] L. J. Schowalter, F. M. Steranka, M. B. Salamon, J. P. Wolfe, *Evidence for separate Mott and liquid-gas transitions in photoexcited, strained germanium*, Phys. Rev. B **29**, 2970 (1984)
- [121] R. Zimmermann, *Many particle theory of highly excited semiconductors* (Teubner Verlag, Leipzig, 1988)
- [122] J. Shah, M. Combescot, A. H. Dayem, *Investigation of exciton-plasma Mott transition in Si*, Phys. Rev. Lett. **38**, 1497 (1977)
- [123] H. Schweizer, A. Forchel, A. Hangleiter, S. Schmitt-Rink, J. P. Lövenau, H. Haug, *Ionization of the direct-gap exciton in photoexcited germanium*, Phys. Rev. Lett. **51**, 698 (1983)
- [124] T. Nagai, A. Yamamoto, Y. Kanemitsu, *Photoluminescence dynamics of GaN under intense band-to-band and exciton resonant excitation*, Phys. Rev. B **71**, 121201(R) (2005)
- [125] T. Ando, A. B. Fowler, F. Stern, *Electronic-properties of two-dimensional systems*, Rev. Mod. Phys. **54**, 437 (1982)
- [126] G. Tränkle, E. Lach, M. Walther, A. Forchel, *Optical Investigation of 2D Mott transitions in GaAs/-GaAlAs quantum well structures*, Surface Science **196**, 584 (1988)

- [127] H. Reinholz, *Mott effect for an electron-hole plasma in a two-dimensional structure*, Solid State Commun. **123**, 489 (2002)
- [128] Y. E. Lozovik, O. L. Berman, *The excitonic superfluid liquid in the system of spatially separated electrons and holes*, Phys. Scripta **55**, 491 (1997)
- [129] G. Manzke, D. Semkat, H. Stolz, *Mott transition of excitons in GaAs-GaAlAs quantum wells*, New J. Phys. **14**, 095002 (2012)
- [130] H. W. Yoon, M. D. Sturge, L. N. Pfeiffer, *Magnetic field induced Mott transition of a one-component electron plasma in GaAs quantum wells*, Solid State Commun. **104**, 287 (1997)
- [131] L. Kappei, J. Szczytko, F. Morier-Genoud, B. Deveaud-Plédran, *Direct observation of the Mott transition in an optically excited semiconductor quantum well*, Phys. Rev. Lett. **94**, 147403 (2005)
- [132] C. K. Choi, Y. H. Kwon, J. S. Krasinski, G. H. Park, G. Setlur, J. J. Son, Y. C. Chang, *Ultrafast carrier dynamics in a highly excited GaN epilayer*, Phys. Rev. B **63**, 115315 (2001)
- [133] S. P. Lepkowski, T. Suski, P. Perlin, V. Yu. Ivanov, M. Godlewski, *Study of light emission from GaN/AlGaIn quantum wells under power-dependent excitation*, J. Appl. Phys. **91**, 9622 (2002)
- [134] P. Lefebvre, S. Kalliakos, T. Bretagnon, P. Valvin, T. Taliercio, B. Gil, N. Grandjean, J. Massies, *Observation and modeling of the time-dependent descreening of internal electric field in a wurtzite GaN/Al_{0.15}Ga_{0.85}N quantum well after high photoexcitation*, Phys. Rev. B **69**, 035307 (2004)
- [135] S. Schmitt-Rink, C. Ell, S. W. Koch, H. E. Schmidt, H. Haug, *Subband-level renormalization and absorptive optical bistability in semiconductor multiple quantum well structures*, Solid State Commun. **52**, 123 (1984)
- [136] D. A. Kleinman, R. C. Miller, *Band-gap renormalization in semiconductor quantum-wells containing carriers*, Phys. Rev. B **32**, 2266 (1985)
- [137] C. Ciuti, V. Savona, C. Piermarocchi, A. Quattropani, P. Schwendimann, *Role of the exchange of carriers in elastic exciton-exciton scattering in quantum wells*, Phys. Rev. B **58**, 7926 (1998)
- [138] S. Utsunomiya, L. Tian, G. Roumpos, C. W. Lai, N. Kumada, T. Fujisawa, M. Kuwata-Gonokami, A. Löffler, S. Höfling, A. Forchel, Y. Yamamoto, *Observation of Bogoliubov excitations in exciton-polariton condensates*, Nature Phys. **4**, 700 (2008)
- [139] S. Wachter, M. Maute, H. Kalt, I. Galbraith, *Coherent exciton interactions: Dependence on excitation fluence and polarization*, Phys. Rev. B **65**, 205314 (2002)
- [140] F. Tassone, Y. Yamamoto, *Exciton-exciton scattering dynamics in a semiconductor microcavity and stimulated scattering into polaritons*, Phys. Rev. B **59**, 10830 (1999)
- [141] K. Litvinenko, D. Birkedal, V. G. Lyssenko, J. M. Hvam, *Exciton dynamics in GaAs/Al_xGa_{1-x}As quantum wells*, Phys. Rev. B **59**, 10255 (1999)
- [142] U. T. Schwarz, H. Braun, K. Kojima, M. Funato, Y. Kawakami, S. Nagahama, T. Mukai, *Investigation and comparison of optical gain spectra of (Al,In)GaIn laser diodes emitting in the 375 nm to 470 nm spectral range*, Proc. SPIE **6485**, 648506 (2007)
- [143] J. Szczytko, L. Kappei, J. Berney, F. Morier-Genoud, M. T. Portella-Oberli, B. Deveaud-Plédran, *Determination of the exciton formation in quantum wells from time-resolved interband luminescence*, Phys. Rev. Lett. **93**, 137401 (2004)
- [144] S. L. Chuang, *Physics of optoelectronic devices* (Wiley, New York, 1995)
- [145] M. Tchernycheva, L. Nevou, L. Doyennette, F. H. Julien, E. Warde, F. Guillot, E. Monroy, E. Bellet-Amalric, T. Remmele, M. Albrecht, *Systematic experimental and theoretical investigation of intersubband absorption in GaN/AlN quantum wells*, Phys. Rev. B **73**, 125347 (2006)
- [146] P. T. Landsberg, *Electron interaction effects on recombination spectra*, Phys. Status Solidi **15**, 623 (1966)
- [147] P. Corfdir, A. Dussaigne, H. Teisseyre, T. Suski, I. Grzegory, P. Lefebvre, E. Giraud, J.-D. Ganière, N. Grandjean, B. Deveaud-Plédran, *Thermal carrier emission and nonradiative recombinations in nonpolar (Al,Ga)N/GaN quantum wells grown on bulk GaN*, J. Appl. Phys. **111**, 033517 (2012)
- [148] J.-N. Fehr, M.-A. Dupertuis, T. P. Hessler, L. Kappei, D. Marti, F. Salleras, M. S. Nomura, B. Deveaud,

- J.-Y. Emery, B. Dagens, *Hot-phonons and Auger-related carrier heating in semiconductor optical amplifiers*, IEEE J. Quantum Electron. **38**, 674 (2002)
- [149] N. Peyghambarian, H. M. Gibbs, J. L. Jewell, A. Antonetti, A. Migus, D. Hulin, A. Mysyrowicz, *Blue shift of the exciton resonance due to exciton-exciton interactions in a multiple-quantum-well structure*, Phys. Rev. Lett. **53**, 2433 (1984)
- [150] T. Amand, X. Marie, B. Baylac, B. Dareys, J. Barrau, M. Brousseau, R. Planel, D. J. Dunstan, *Enhanced exciton blue shift in spin polarized dense exciton system in quantum wells*, Phys. Lett. A **193**, 105 (1994)
- [151] P. Corfdir, B. Van Hattem, E. Uccelli, A. Fontcuberta i Morral, R. T. Phillips, *Charge carrier generation, relaxation, and recombination in polytypic GaAs nanowires studied by photoluminescence excitation spectroscopy*, Appl. Phys. Lett. **103**, 133109 (2013)
- [152] S. Schmitt-Rink, C. Ell, *Excitons and electron-hole plasma in quasi-two-dimensional systems*, J. Lumin. **30**, 585 (1985)
- [153] J. Singh, D. Birkedal, V. G. Lyssenko, J. M. Hvam, *Binding energy of two-dimensional biexcitons*, Phys. Rev. B **53**, 15909 (1995)
- [154] Y. Hayamizu, M. Yoshita, Y. Takahashi, H. Akiyama, C. Z. Ning, L. N. Pfeiffer, K. W. West, *Biexciton gain and the Mott-transition in GaAs quantum wires*, Phys. Rev. Lett. **99**, 167403 (2007)
- [155] P. Bigenwald, A. V. Kavokin, B. Gil, P. Lefebvre, *Exclusion principle and screening of excitons in GaN/Al_xGa_{1-x}N quantum wells*, Phys. Rev. B **63**, 035315 (2001)
- [156] E. Yablonoitch, *Inhibited spontaneous emission in solid-state physics and electronics*, Phys. Rev. Lett. **58**, 2059 (1987)
- [157] S. John, *Strong localization of photons in certain disordered dielectric superlattices*, Phys. Rev. Lett. **58**, 2486 (1987)
- [158] N. Vico Triviño, G. Rossbach, U. Dharanipathy, J. Levrat, A. Castiglia, J.-F. Carlin, K. A. Atlasov, R. Butté, R. Houdré, N. Grandjean, *High quality factor two dimensional GaN photonic crystal cavity membranes grown on silicon substrate*, Appl. Phys. Lett. **100**, 071103 (2012)
- [159] K. J. Vahala, *Optical microcavities*, Nature (London) **424**, 839 (2003)
- [160] H. Benisty, H. De Neve, C. Weisbuch, *Impact of planar microcavity effects on light extraction - Part I: basic concepts and analytical trends*, IEEE J. Quantum Electron. **34**, 1612 (1998)
- [161] G. Cosendey, A. Castiglia, G. Rossbach, J.-F. Carlin, N. Grandjean, *Blue monolithic AlInN-based vertical cavity surface emitting laser diode on free-standing GaN substrate*, Appl. Phys. Lett. **101**, 151113 (2012)
- [162] Y. Kaluzny, P. Goy, M. Gross, J. M. Raimond, S. Haroche, *Observation of self-induced Rabi-oscillations in two-level atoms excited inside a resonant cavity: the ringing regime of superradiance*, Phys. Rev. Lett. **51**, 1175 (1983)
- [163] S. Pau, G. Björk, J. Jacobson, H. Cao, Y. Yamamoto, *Microcavity exciton-polariton splitting in the linear regime*, Phys. Rev. B **51**, 14437 (1995)
- [164] T. B. Norris, J.-K. Rhee, C.-Y. Sung, Y. Arakawa, M. Nishioka, C. Weisbuch, *Time-resolved vacuum Rabi oscillations in a semiconductor quantum microcavity*, Phys. Rev. B **50**, 14663 (1994)
- [165] V. Savona, C. Weisbuch, *Theory of time-resolved light emission from polaritons in a semiconductor microcavity under resonant excitation*, Phys. Rev. B **54**, 10835 (1996)
- [166] R. Houdré, R. P. Stanley, M. Ilegems, *Vacuum-field Rabi splitting in the presence of inhomogeneous broadening: Resolution of a homogeneous linewidth in an inhomogeneously broadened system*, Phys. Rev. A **53**, 2711 (1996)
- [167] G. Christmann, R. Butté, E. Feltin, J.-F. Carlin, N. Grandjean, *Impact of inhomogeneous broadening on the strong exciton-phonon coupling in quantum well nitride cavities*, Phys. Rev. B **73**, 153305 (2006)
- [168] G. Christmann, R. Butté, E. Feltin, A. Mouti, P. A. Stadelmann, A. Castiglia, J.-F. Carlin, N. Grandjean, *Large vacuum Rabi splitting in a multiple quantum well GaN-based microcavity in the*

- strong-coupling regime*, Phys. Rev. B **77**, 085310 (2008)
- [169] G. Rossbach, J. Levrat, A. Dussaigne, G. Cosendey, M. Glauser, M. Cobet, R. Butté, N. Grandjean, H. Teisseyre, M. Bockowski, I. Grzegory, T. Suski, *Tailoring the light-matter coupling in anisotropic microcavities: Redistribution of oscillator strength in strained m-plane GaN/AlGaIn quantum wells*, Phys. Rev. B **84**, 115315 (2011)
 - [170] M. Glauser, G. Rossbach, G. Cosendey, J. Levrat, M. Cobet, J.-F. Carlin, J. Besbas, M. Gallart, P. Gilliot, R. Butté, N. Grandjean, *Investigation of InGaIn/GaN quantum wells for polariton laser diodes*, Phys. Status Solidi C **9**, 1325 (2012)
 - [171] I. Iorsh, M. Glauser, G. Rossbach, J. Levrat, M. Cobet, R. Butté, N. Grandjean, M. A. Kaliteevski, R. A. Abram, A. V. Kavokin, *Generic picture of the emission properties of III-nitride polariton laser diodes: Steady state and current modulation response*, Phys. Rev. B **86**, 125308 (2012)
 - [172] G. Björk, H. Heitmann, Y. Yamamoto, *Spontaneous-emission coupling factor and mode characteristics of planar dielectric microcavity lasers*, Phys. Rev. A **47**, 4451 (1993)
 - [173] M. H. Anderson, J. R. Ensher, M. R. Matthews, C. E. Wieman, E. A. Cornell, *Observation of Bose-Einstein condensation in a dilute atomic vapor*, Science **269**, 198 (1995)
 - [174] K. B. Davis, M. O. Mewes, M. R. Andrews, N. J. van Druten, D. S. Durfee, D. M. Kurn, W. Ketterle, *Bose-Einstein condensation in a gas of sodium atoms*, Phys. Rev. Lett. **75**, 3969 (1995)
 - [175] L. V. Butov, A. Zrenner, G. Abstreiter, G. Böhm, G. Weimann, *Condensation of indirect excitons in coupled AlAs/GaAs quantum wells*, Phys. Rev. Lett. **73**, 304 (1994)
 - [176] T. Nikuni, M. Oshikawa, A. Oosawa, H. Tanaka, *Bose-Einstein condensation of dilute magnons in TlCuCl₃*, Phys. Rev. Lett. **84**, 5868 (2000)
 - [177] J. Klaers, J. Schmitt, F. Vewinger, M. Weitz, *Bose-Einstein condensation of photons in an optical microcavity*, Nature (London) **468**, 545 (2010)
 - [178] H. Morkoç, *Handbook of nitride semiconductors and devices* (Vol.3, John Wiley & Sons, New York, 2009)
 - [179] E. Tassone, C. Piermarocchi, V. Savona, A. Quattropani, P. Schwendimann, *Bottleneck effects in the relaxation and photoluminescence of microcavity polaritons*, Phys. Rev. B **56**, 7554 (1997)
 - [180] G. Malpuech, A. V. Kavokin, A. Di Carlo, J. J. Baumberg, *Polariton lasing by exciton-electron scattering in semiconductor microcavities*, Phys. Rev. B **65**, 153310 (2002)
 - [181] D. Porras, C. Ciuti, J. J. Baumberg, C. Tejedor, *Polariton dynamics and Bose-Einstein condensation in semiconductor microcavities*, Phys. Rev. B **66**, 085304 (2002)
 - [182] F. Bœuf, R. André, R. Romestain, Le Si Dang, E. Péronne, J. F. Lampin, D. Hulin, A. Alexandrou, *Evidence of polariton stimulation in semiconductor microcavities*, Phys. Rev. B **62**, R2279 (2000)
 - [183] M. Maragkou, A. J. D. Grundy, T. Ostatnický, P. G. Lagoudakis, *Longitudinal optical phonon assisted polariton laser*, Appl. Phys. Lett. **97**, 111110 (2010)
 - [184] P. G. Savvidis, J. J. Baumberg, R. M. Stevenson, M. S. Skolnick, D. M. Whittaker, J. S. Roberts, *Angle-resonant stimulated polariton amplifier*, Phys. Rev. Lett. **84**, 1547 (2000)
 - [185] J.-K. Rhee, D. S. Citrin, T. B. Norris, Y. Arakawa, M. Nishioka, *Femtosecond dynamics of semiconductor-microcavity polaritons in the nonlinear regime*, Solid State Commun. **97**, 941 (1996)
 - [186] R. Butté, G. Delalleau, A. I. Tartakovskii, M. S. Skolnick, V. N. Astratov, J. J. Baumberg, G. Malpuech, A. Di Carlo, A. V. Kavokin, J. S. Roberts, *Transition from strong to weak coupling and the onset of lasing in semiconductor microcavities*, Phys. Rev. B **65**, 205310 (2002)
 - [187] A. I. Tartakovskii, M. Emam-Ismaïl, R. M. Stevenson, M. S. Skolnick, V. N. Astratov, D. M. Whittaker, J. J. Baumberg, J. S. Roberts, *Relaxation bottleneck and its suppression in semiconductor microcavities*, Phys. Rev. B **62**, R2283 (2000)
 - [188] J. Bloch, T. Freixanet, J. Y. Marzin, V. Thierry-Mieg, R. Planel, *Giant Rabi splitting in a microcavity containing distributed quantum wells*, Appl. Phys. Lett. **73**, 1694 (1996)
 - [189] E. Wertz, L. Ferrier, D. D. Solnyshkov, P. Senellart, D. Bajoni, A. Miard, A. Lemaître, G. Malpuech,

- J. Bloch, *Spontaneous formation of a polariton condensate in a planar GaAs microcavity*, Appl. Phys. Lett. **95**, 051108 (2009)
- [190] H. Deng, G. Weihs, D. Snoke, J. Bloch, Y. Yamamoto, *Polariton lasing vs. photon lasing in a semiconductor microcavity*, P. Natl. Acad. Sci. USA **100**, 15318 (2003)
- [191] K. G. Lagoudakis, T. Ostatnický, A. V. Kavokin, Y. G. Rubo, R. André, B. Deveaud-Plédran, *Observation of half-quantum vortices in an exciton-polariton condensate*, Science **326**, 5955 (2009)
- [192] A. Amo, D. Sanvitto, F. P. Laussy, D. Ballarini, E. del Valle, M. D. Martin, A. Lemaître, J. Bloch, D. N. Krizhanovskii, M. S. Skolnick, C. Tejedor, L. Viña, *Collective fluid dynamics of a polariton condensate in a semiconductor microcavity*, Nature (London) **457**, 291 (2008)
- [193] A. Amo, S. Pigeon, D. Sanvitto, V. G. Sala, R. Hivet, I. Carusotto, F. Pisanello, G. Leménager, R. Houdré, E. Giacobino, C. Ciuti, A. Bramati, *Polariton superfluids reveal quantum hydrodynamic solitons*, Science **332**, 1167 (2011)
- [194] H. Oka, H. Ishihara, *Highly efficient generation of entangled photons by controlling cavity bipolariton states*, Phys. Rev. Lett. **100**, 170505 (2008)
- [195] A. V. Kavokin, G. Malpuech, M. Glazov, *Optical spin Hall effect*, Phys. Rev. Lett. **95**, 136601 (2005)
- [196] C. Leyder, M. Romanelli, J.-Ph. Karr, E. Giacobino, T. C. H. Liew, M. M. Glazov, A. V. Kavokin, G. Malpuech, A. Bramati, *Observation of the optical spin Hall effect*, Nature Phys. **3**, 628 (2007)
- [197] R. M. Stevenson, V. N. Astratov, M. S. Skolnick, D. M. Whittaker, E. Emam-Ismaïl, A. I. Tartakovskii, P. G. Savvidis, J. J. Baumberg, J. S. Roberts, *Continuous wave observation of massive polariton redistribution by stimulated scattering in semiconductor microcavities*, Phys. Rev. Lett. **85**, 3680 (2000)
- [198] I. A. Shelykh, G. Pavlovic, D. D. Solnyshkov, G. Malpuech, *Proposal for a mesoscopic optical Berry-phase interferometer*, Phys. Rev. Lett. **102**, 046407 (2009)
- [199] L. Gu, H. Huang, Z. Gan, *Sagnac effect of excitonic polaritons*, Phys. Rev. B **84**, 075402 (2011)
- [200] I. A. Shelykh, A. V. Kavokin, Y. G. Rubo, T. C. H. Liew, G. Malpuech, *Polariton polarization-sensitive phenomena in planar semiconductor microcavities*, Semicond. Sci. Technol. **25**, 013001 (2009)
- [201] T. K. Paraïso, M. Wouters, Y. Léger, F. Morier-Genoud, B. Deveaud-Plédran, *Multistability of a coherent spin ensemble in a semiconductor microcavity*, Nature Mat. **9**, 655 (2010)
- [202] A. Amo, T. C. H. Liew, C. Adrados, R. Houdré, E. Giacobino, A. V. Kavokin, A. Bramati, *Exciton-polariton spin switches*, Nature Phot. **4**, 361 (2010)
- [203] F. P. Laussy, A. V. Kavokin, I. A. Shelykh, *Exciton-polariton mediated superconductivity*, Phys. Rev. Lett. **104**, 106402 (2010)
- [204] R. Balili, V. Hartwell, D. Snoke, L. Pfeiffer, K. West, *Bose-Einstein condensation of microcavity polaritons in a trap*, Science **316**, 1007 (2007)
- [205] S. Kéna-Cohen, S. R. Forrest, *Room-temperature polariton lasing in an organic single-crystal microcavity*, Nature Phot. **4**, 371 (2010)
- [206] K. S. Daskalakis, S. A. Maier, R. Murray, S. Kéna-Cohen, *Nonlinear interactions in an organic polariton condensate*, Nature Mat. **13**, 271 (2014)
- [207] T. Guillet, M. Mexis, J. Levrat, G. Rossbach, C. Brimont, T. Bretagnon, B. Gil, , R. Butté, N. Grandjean, L. Orosz, F. Réveret, J. Leymarie, J. Zúñiga-Pérez, M. Leroux, F. Semon, S. Bouchoule, *Polariton lasing in a hybrid bulk ZnO microcavity*, Appl. Phys. Lett. **99**, 161104 (2011)
- [208] H. Franke, C. Sturm, R. Schmidt-Grund, G. Wagner, M. Grundmann, *Ballistic propagation of exciton-polariton condensates in a ZnO-based microcavity*, New J. Phys. **14**, 013037 (2012)
- [209] S. I. Tsintzos, N. T. Pelekanos, G. Konstantinidis, Z. Hatzopoulos, P. G. Savvidis, *A GaAs polariton light-emitting diode operating near room temperature*, Nature (London) **453**, 372 (2008)
- [210] P. Bhattacharya, B. Xiao, A. Das, S. Bhowmick, J. Heo, *Solid-state electrically-injected exciton-polariton laser*, Phys. Rev. Lett. **110**, 206403 (2013)
- [211] C. Schneider, A. Rahimi-Iman, N. Y. Kim, J. Fischer, I. G. Savenko, M. Amthor, M. Lermer, A. Wolf, L. Worschech, V. D. Kulakovskii, I. A. Shelykh, M. Kamp, S. Reitzenstein, A. Forchel, Y. Yamamoto,

- S. Höfling, *An electrically pumped polariton laser*, Nature (London) **497**, 348 (2013)
- [212] M. Wouters, I. Carusotto, *Excitations in a nonequilibrium Bose-Einstein condensate of exciton polaritons*, Phys. Rev. Lett. **99**, 140402 (2007)
- [213] N. Antoine-Vincent, F. Natali, D. Byrne, A. Vasson, P. Disseix, J. Leymarie, M. Leroux, F. Semond, J. Massies, *Observation of Rabi splitting in a bulk GaN microcavity grown on silicon*, Phys. Rev. B **68**, 153313 (2003)
- [214] J.-F. Carlin, M. Ilegems, *High-quality AlInN for high index contrast Bragg mirrors lattice matched to GaN*, Appl. Phys. Lett. **83**, 668 (2003)
- [215] J.-F. Carlin, C. Zellweger, J. Dorsaz, S. Nicolay, G. Christmann, E. Feltin, R. Butté, N. Grandjean, *Progresses in III-nitride distributed Bragg reflectors and microcavities using AlInN/GaN materials*, Phys. Status Solidi B **242**, 2326 (2005)
- [216] J.-F. Carlin, J. Dorsaz, E. Feltin, R. Butté, N. Grandjean, M. Ilegems, M. Laügt, *Crackfree fully epitaxial nitride microcavity using highly reflective AlInN/GaN Bragg mirrors*, Appl. Phys. Lett. **86**, 031107 (2005)
- [217] E. Feltin, G. Christmann, J. Dorsaz, A. Castiglia, J.-F. Carlin, R. Butté, N. Grandjean, S. Christopoulos, G. B. H. von Högersthal, A. J. D. Grundy, P. G. Lagoudakis, J. J. Baumberg, *Blue lasing at room temperature in an optically pumped lattice-matched AlInN/GaN VCSEL structure*, Electron. Lett. **43**, 924 (2007)
- [218] G. Christmann, D. Simeonov, R. Butté, E. Feltin, J.-F. Carlin, N. Grandjean, *Impact of disorder on high quality factor III-V nitride microcavities*, Appl. Phys. Lett. **89**, 261101 (2006)
- [219] R. Butté, G. Christmann, E. Feltin, J.-F. Carlin, M. Mosca, M. Ilegems, N. Grandjean, *Room-temperature polariton luminescence from a bulk GaN microcavity*, Phys. Rev. B **73**, 033315 (2006)
- [220] E. Feltin, G. Christmann, R. Butté, J.-F. Carlin, M. Mosca, N. Grandjean, *Room temperature polariton luminescence from a GaN/AlGaIn quantum well microcavity*, Appl. Phys. Lett. **89**, 071107 (2006)
- [221] Y. G. Rubo, *Kinetics of the polariton condensate formation in a microcavity*, Phys. Status Solidi A **201**, 641 (2003)
- [222] D. Read, T. C. H. Liew, Y. G. Rubo, A. V. Kavokin, *Stochastic polarization formation in exciton-polariton Bose-Einstein condensates*, Phys. Rev. B **80**, 195309 (2009)
- [223] J. Levrat, R. Butté, G. Christmann, E. Feltin, J.-F. Carlin, N. Grandjean, *Tailoring the strong coupling regime in III-nitride based microcavities for room temperature polariton laser applications*, Phys. Status Solidi C **6**, 2820 (2009)
- [224] M. D. Martín, D. Ballarini, A. Amo, L. Klopotoski, L. Viña, A. V. Kavokin, R. André, *Striking dynamics of II-VI microcavity polaritons after linearly polarized excitation*, Phys. Stat. Solidi C **2**, 3880 (2005)
- [225] M. Vladimirova, S. Cronenberger, D. Scalbert, K. V. Kavokin, A. Miard, A. Lemaître, J. Bloch, D. D. Solnyshkov, G. Malpuech, A. V. Kavokin, *Polariton-polariton interaction constants in microcavities*, Phys. Rev. B **82**, 075301 (2010)
- [226] F. Stokker-Cheregi, A. Vinattieri, F. Semond, M. Leroux, R. Sellers, J. Massies, D. Solnyshkov, G. Malpuech, M. Colocci, M. Gurioli, *Polariton relaxation bottleneck and its thermal suppression in bulk GaN microcavities*, Appl. Phys. Lett. **92**, 042119 (2008)
- [227] J. Kasprzak, D. D. Solnyshkov, R. André, Le Si Dang, G. Malpuech, *Formation of exciton polariton condensate: thermodynamic versus kinetic regimes*, Phys. Rev. Lett. **101**, 146404 (2008)
- [228] A. V. Kavokin, I. A. Shelykh, T. Taylor, M. M. Glazov, *Vertical cavity surface emitting terahertz laser*, Phys. Rev. Lett. **108**, 197401 (2012)
- [229] T.-C. Lu, C.-C. Kao, H.-C. Kuo, G.-S. Huang, S.-C. Wang, *CW lasing of current injection blue GaN-based vertical cavity surface emitting laser*, Appl. Phys. Lett. **92**, 141102 (2008)
- [230] C. Berger, A. Dadgar, J. Bläsing, A. Franke, T. Hempel, R. Goldhahn, J. Christen, A. Krost, *Growth of AlInN/AlGaIn distributed Bragg reflectors for high quality microcavities*, Phys. Status Solidi C **9**,

- 1253 (2012)
- [231] S. Chichibu, T. Azuhata, T. Sota, S. Nakamura, *Spontaneous emission of localized excitons in InGaN single and multi-quantum well structures*, Appl. Phys. Lett. **69**, 4188 (1996)
 - [232] S. F. Chichibu, A. Uedono, T. Onuma, B. A. Haskell, A. Chakraborty, T. Koyama, P. T. Fini, S. Keller, S. P. Denbaars, J. S. Speck, U. K. Mishra, S. Nakamura, S. Yamaguchi, S. Kamiyama, H. Amano, I. Akasaki, J. Han, T. Sota, *Origin of defect-insensitive emission probability in In-containing (Al,In,Ga)N alloy semiconductors*, Nature Mat. **5**, 810 (2006)
 - [233] D. M. Graham, A. Soltani-Vala, P. Dawson, M. J. Godfrey, T. M. Smeeton, J. S. Barnard, M. J. Kappers, C. J. Humphreys, E. J. Thrush, *Optical and microstructural studies of InGaN/GaN single-quantum-well structures*, J. Appl. Phys. **97**, 103508 (2005)
 - [234] N. A. K. Kaufmann, *Investigation of indium-rich InGaN alloys and kinetic growth regime of GaN* (Thesis No. 5776, EPF Lausanne, 2013)
 - [235] G. Malpuech, D. Solnyshkov, A. Di Carlo, E. Petrolati (Bull. Officiel Propriété Industrielle 10/19 - 132, Institut National de la Propriété Industrielle, France, 2010)
 - [236] D. Bajoni, A. Miard, A. Lemaître, S. Bouchoule, J. Bloch, J. Tignon, *Nonresonant electrical injection of excitons in an InGaAs quantum well*, Appl. Phys. Lett. **90**, 121114 (2007)
 - [237] S. I. Tsintzos, P. G. Savvidis, G. Deligeorgis, Z. Hatzopoulos, N. T. Pelekanos, *Room temperature GaAs exciton-polariton light emitting diode*, Appl. Phys. Lett. **94**, 071109 (2009)
 - [238] D. Bajoni, P. Senellart, E. Wertz, I. Sagnes, A. Miard, A. Lemaître, J. Bloch, *Polariton laser using single micropillar GaAs-AlAs semiconductor cavities*, Phys. Rev. Lett. **100**, 047401 (2008)
 - [239] E. O. Kane, *Pollmann-Büttner variational method for excitonic polarons*, Phys. Rev. B **18**, 6849 (1978)
 - [240] J. Schmutzler, F. Veit, M. Aßmann, J.-S. Tempel, S. Höfling, M. Kamp, A. Forchel, M. Bayer, *Determination of operating parameters for a GaAs-based polariton laser*, Appl. Phys. Lett. **102**, 081115 (2013)
 - [241] Feng Li, L. Orosz, O. Kamoun, S. Bouchoule, C. Brimont, P. Disseix, T. Guillet, X. Lafosse, M. Leroux, J. Leymarie, M. Mexis, M. Mihailovic, G. Patriarche, F. Réveret, D. Solnyshkov, J. Zuniga-Perez, G. Malpuech, *From excitonic to photonic polariton condensate in a ZnO-based microcavity*, Phys. Rev. Lett. **110**, 196406 (2013)
 - [242] M. Zamfirescu, A. Kavokin, B. Gil, G. Malpuech, M. Kaliteevski, *ZnO as a material mostly adapted for the realization of room-temperature polariton lasers*, Phys. Rev. B **65**, 161205 (2002)
 - [243] R. Schmidt-Grund, B. Rheinländer, C. Czekalla, G. Benndorf, H. Hochmuth, M. Lorenz, M. Grundmann, *Exciton-polariton formation at room temperature in a planar ZnO resonator structure*, Appl. Phys. B **93**, 331 (2008)
 - [244] M. Nakayama, S. Komura, T. Kawase, D. Kim, *Observation of exciton polaritons in a ZnO microcavity with HfO₂/SiO₂ distributed Bragg reflectors*, J. Phys. Soc. Jpn. **77**, 093705 (2008)
 - [245] R. Shimada, J. Xie, Ü. Özgür V. Avrutin, H. Morkoç, *Cavity polaritons in ZnO-based hybrid microcavities*, Appl. Phys. Lett. **92**, 011127 (2008)
 - [246] J. R. Chen, T. C. Lu, Y. C. Wu, S. C. Lin, W. R. Liu, W. F. Hsieh, C. C. Kuo, C. C. Lee, *Cavity polaritons in ZnO-based hybrid microcavities*, Appl. Phys. Lett. **94**, 061103 (2009)
 - [247] S. Halm, S. Kalusniak, S. Sadofev, H.-J. Wünsche, F. Henneberger, *Strong exciton-photon coupling in a monolithic ZnO/(Zn,Mg)O multiple quantum well microcavity*, Appl. Phys. Lett. **99**, 181121 (2011)
 - [248] A. Trichet, L. Sun, G. Pavlovic, N. A. Gippius, G. Malpuech, W. Xie, Z. Chen, M. Richard, L. S. Dang, *One-dimensional ZnO exciton polaritons with negligible thermal broadening at room temperature*, Phys. Rev. B **83**, 041302(R) (2011)
 - [249] C. Sturm, H. Hilmer, R. Schmidt-Grund, M. Grundmann, *Observation of strong exciton-photon coupling at temperatures up to 410 K*, New J. Phys. **11**, 073044 (2009)
 - [250] T.-C. Lu, Y.-Y. Lai, Y.-P. Lan, S.-W. Huang, J.-R. Chen, Y.-C. Wu, W.-F. Hsieh, H. Deng, *Room*

- temperature polariton lasing vs. photon lasing in a ZnO-based hybrid microcavity*, Opt. Express **20**, 5530 (2012)
- [251] J. Frenkel, *On the transformation of light into heat in solids. I*, Phys. Rev. **37**, 17 (1931)
- [252] D. G. Lidzey, D. D. C. Bradley, M. S. Skolnick, T. Virgili, S. Walker, D. M. Whittaker, *Strong exciton-photon coupling in an organic semiconductor microcavity*, Nature (London) **395**, 53 (1998)
- [253] P. A. Hobson, W. L. Barnes, D. G. Lidzey, G. A. Gehring, D. M. Whittaker, M. S. Skolnick, S. Walker, *Strong exciton-photon coupling in a low-Q all-metal mirror microcavity*, Appl. Phys. Lett. **81**, 3519 (2002)
- [254] L. G. Connolly, D. G. Lidzey, R. Butté, A. M. Adawi, D. M. Whittaker, M. S. Skolnick, R. Airey, *Strong coupling in high-finesse organic semiconductor microcavities*, Appl. Phys. Lett. **83**, 5377 (2003)
- [255] R. J. Holmes, S. R. Forrest, *Exciton-photon coupling in organic materials with large intersystem crossing rates and strong excited-state molecular relaxation*, Phys. Rev. B **71**, 235203 (2005)
- [256] J. Wenus, R. Parashkov, S. Ceccarelli, A. Brehier, J.-S. Lauret, M. S. Skolnick, E. Deleporte, D. G. Lidzey, *Hybrid organic-inorganic exciton-polaritons in a strongly coupled microcavity*, Phys. Rev. B **74**, 235212 (2006)
- [257] S. Kéna-Cohen, S. R. Forrest, *Giant Davydov splitting of the lower polariton branch in a polycrystalline tetracene microcavity*, Phys. Rev. B **77**, 073205 (2008)
- [258] R. Brückner, M. Sudzius, S. I. Hintschich, H. Fröb, V. G. Lyssenko, K. Leo, *Hybrid optical Tamm states in a planar dielectric microcavity*, Phys. Rev. B **83**, 033405 (2011)
- [259] K. Sebald, M. Seyfried, S. Klemmt, S. Bley, A. Rosenauer, D. Hommel, C. Kruse, *Strong coupling in monolithic microcavities with ZnSe quantum wells*, Appl. Phys. Lett. **100**, 161104 (2012)
- [260] C. Ciuti, P. Schwendimann, B. Deveaud-Plédran, A. Quattropani, *Theory of the angle-resonant polariton amplifier*, Phys. Rev. B **62**, R4825 (2000)
- [261] Y. G. Rubo, G. Malpuech, A. V. Kavokin, P. Bigenwald, *Dynamical theory of polariton amplifiers*, Phys. Rev. Lett. **91**, 156403 (2003)
- [262] L. Orosz, F. Réveret, F. Médard, P. Disseix, J. Leymarie, M. Mihailovic, D. Solnyshkov, G. Malpuech, J. Zuniga-Pérez, F. Semon, M. Leroux, S. Bouchoule, X. Lafosse, M. Mexis, C. Brimont, T. Guillet, *LO-phonon-assisted polariton lasing in a ZnO-based microcavity*, Phys. Rev. B **85**, 121201 (2012)
- [263] D. Birkedal, J. Singh, V. G. Lyssenko, J. Erland, J. M. Hvam, *Binding of quasi-two-dimensional biexcitons*, Phys. Rev. Lett. **76**, 672 (1996)
- [264] Y. Yamada, Y. Ueki, K. Nakamura, T. Taguchi, A. Ishibashi, Y. Kawaguchi, T. Yokogawa, *Stokes shift of biexcitons in $Al_xGa_{1-x}N$ epitaxial layers*, Phys. Rev. B **70**, 195210 (2004)
- [265] G. C. La Rocca, F. Bassani, V. M. Agranovich, *Biexcitons and dark states in semiconductor microcavities*, J. Opt. Soc. Am. B **15**, 652 (1998)
- [266] M. Saba, F. Quochi, C. Ciuti, U. Oesterle, J. L. Staehli, B. Deveaud-Plédran, G. Bongiovanni, A. Mura, *Crossover from exciton to biexciton polaritons in semiconductor microcavities*, Phys. Rev. Lett. **85**, 385 (2000)
- [267] M. Wouters, *Resonant polariton-polariton scattering in semiconductor microcavities*, Phys. Rev. B **76**, 045319 (2007)
- [268] M. Richard, J. Kasprzak, R. André, R. Romestain, Le Si Dang, G. Malpuech, A. V. Kavokin, *Experimental evidence for nonequilibrium Bose condensation of exciton polaritons*, Phys. Rev. B **72**, 201301 (2005)
- [269] L. Ferrier, E. Wertz, R. Johne, D. D. Solnyshkov, P. Senellart, I. Sagnes, A. Lemaître, G. Malpuech, J. Bloch, *Interactions in confined polariton condensates*, Phys. Rev. Lett. **106**, 126401 (2011)
- [270] E. Wertz, L. Ferrier, D. D. Solnyshkov, R. Johne, D. Sanvitto, A. Lemaître, I. Sagnes, R. Grousson, A. V. Kavokin, P. Senellart, G. Malpuech, J. Bloch, *Spontaneous formation and optical manipulation of extended polariton condensates*, Nature Phys. **6**, 860 (2010)
- [271] C. Antón, T. C. H. Liew, G. Tosi, M. D. Martín, T. Gao, Z. Hatzopolous, P. S. Eldridge, P. G. Savvidis, L. Viña, *Energy relaxation of exciton-polariton condensates in quasi-one-dimensional microcavi-*

- ties, Phys. Rev. B **88**, 035313 (2013)
- [272] J. Levrat, G. Rossbach, A. Dussaigne, G. Cosendey, M. Glauser, M. Cobet, R. Butté, N. Grandjean, H. Teisseyre, M. Bockowski, I. Grzegory, T. Suski, *Nonlinear emission properties of an optically anisotropic GaN-based microcavity*, Phys. Rev. B **86**, 165321 (2012)
 - [273] A. Huynh, J. Tignon, Ph. Roussignol, C. Delalande, *Experimental determination of intrinsic nonlinearities in semiconductor microcavities*, Phys. Rev. B **66**, 113301 (2002)
 - [274] M. Sliotsky, Y. Zhang, S. R. Forrest, *Temperature dependence of polariton lasing in a crystalline anthracene microcavity*, Phys. Rev. B **86**, 045312 (2012)
 - [275] G. Roumpos, W. H. Nitsche, S. Höfling, A. Forchel, Y. Yamamoto, *Gain-induced trapping of microcavity exciton polariton condensates*, Phys. Rev. Lett. **104**, 126403 (2010)
 - [276] G. Malpuech, D. D. Solnyshkov, H. Ouerdane, M. M. Glazov, I. Shelykh, *Bose glass and superfluid phases of cavity polaritons*, Phys. Rev. Lett. **98**, 206402 (2007)
 - [277] A. Baas, K. G. Lagoudakis, M. Richard, R. André, Le Si Dang, B. Deveaud-Plédran, *Synchronized and desynchronized phases of exciton-polariton condensates in the presence of disorder*, Phys. Rev. Lett. **100**, 170401 (2008)
 - [278] J. Kasprzak, R. André, Le Si Dang, I. A. Shelykh, A. V. Kavokin, Y. G. Rubo, K. V. Kavokin, G. Malpuech, *Build up and pinning of linear polarization in the Bose condensates of exciton polaritons*, Phys. Rev. B **75**, 045326 (2007)
 - [279] P. Corfdir, P. Lefebvre, L. Balet, S. Sonderegger, A. Dussaigne, T. Zhu, D. Martin, J.-D. Ganière, N. Grandjean, B. Deveaud-Plédran, *Exciton recombination dynamics in a-plane (Al,Ga)N/GaN quantum wells probed by picosecond photo and cathodoluminescence*, J. Appl. Phys. **107**, 043524 (2010)
 - [280] M. Wouters, I. Carusotto, C. Ciuti, *Spatial and spectral shape of inhomogeneous nonequilibrium exciton-polariton condensates*, Phys. Rev. B **77**, 115340 (2008)
 - [281] G. Christmann, G. Tosi, N. G. Berloff, P. Tsotsis, P. S. Eldridge, Z. Hatzopoulos, P. G. Savvidis, J. J. Baumberg, *Polariton ring condensates and sunflower ripples in an expanding quantum liquid*, Phys. Rev. B **85**, 235303 (2012)
 - [282] B. Nelsen, G. Liu, M. Steger, D. W. Snoke, R. Balili, K. West, L. Pfeiffer, *Dissipationless flow and sharp threshold of a polariton condensate with long lifetime*, Phys. Rev. X **3**, 041015 (2013)
 - [283] D. Porras, C. Tejedor, *Linewidth of a polariton laser: theoretical analysis of self-interaction effects*, Phys. Rev. B **67**, 161310(R) (2003)
 - [284] Y.-L. Huang, C.-K. Sun, J.-C. Liang, S. Keller, M. P. Mack, U. K. Mishra, S. P. DenBaars, *Femtosecond Z-scan measurement of GaN*, Appl. Phys. Lett. **75**, 3524 (1999)
 - [285] Y. Yamamoto, S. Machida, G. Björk, *Microcavity semiconductor laser with enhanced spontaneous emission*, Phys. Rev. A **44**, 657 (1991)
 - [286] H. Yokoyama, *Physics and device applications of optical microcavities*, Science **256**, 66 (1992)
 - [287] H. Yokoyama, M. Suzuki, Y. Nambu, *Spontaneous emission and laser oscillation properties of microcavities containing a dye solution*, Appl. Phys. Lett. **58**, 2598 (1991)
 - [288] J. J. Baumberg, P. G. Savvidis, R. M. Stevenson, A. I. Tartakovskii, M. S. Skolnick, D. M. Whittaker, J. S. Roberts, *Parametric oscillation in a vertical microcavity: A polariton condensate or micro-optical parametric oscillation*, Phys. Rev. B **62**, R16247 (2000)
 - [289] G. Malpuech, A. Di Carlo, A. V. Kavokin, J. J. Baumberg, P. Lugli, *Room-temperature polariton lasers based on GaN microcavities*, Appl. Phys. Lett. **81**, 412 (2002)
 - [290] G. Björk, Y. Yamamoto, *Analysis of semiconductor microcavity lasers using rate equations*, IEEE J. Quantum Electron. **27**, 2386 (1991)
 - [291] J. Cuadra, D. Sarkar, L. Viña, J. M. Hvam, A. Nalitov, D. Solnyshkov, G. Malpuech, *Polarized emission in polariton condensates: Switching in a one-dimensional natural trap versus inversion in two dimensions*, Phys. Rev. B **88**, 235312 (2013)
 - [292] Y. Enya, Y. Yoshizumi, T. Kyono, K. Akita, M. Ueno, M. Adachi, T. Sumitomo, S. Tokuyama,

- T. Ikegami, K. Katayama, T. Nakamura, *531 nm green lasing of InGaN based laser diodes on semi-polar 2021 free-standing GaN substrates*, Appl. Phys. Express **2**, 082101 (2009)
- [293] H. Teisseyre, J. Z. Domagala, B. Lucznik, A. Reszka, B. J. Kowalski, M. Bockowski, G. Kamler, I. Grzegory, *Characterization of the nonpolar GaN substrate obtained by multistep regrowth by hydride vapor phase epitaxy*, Appl. Phys. Express **5**, 011001 (2011)
- [294] L. Lymperakis, J. Neugebauer, *Large anisotropic adatom kinetics on nonpolar GaN surfaces: Consequences for surface morphologies and nanowire growth*, Phys. Rev. B **79**, 241308(R) (2009)
- [295] P. Corfdir, P. Lefebvre, J. Levrat, J.-D. Ganière, D. Martin, J. Ristić, T. Zhu, N. Grandjean, B. Deveaud-Plédran, *Exciton localization on basal stacking faults in a-plane epitaxial lateral overgrown GaN grown by hydride vapor phase epitaxy*, J. Appl. Phys. **105**, 043102 (2009)
- [296] Y. J. Sun, O. Brandt, M. Ramsteiner, H. T. Grahn, K. H. Ploog, *Polarization anisotropy of the photoluminescence of m-plane (In,Ga)N/GaN multiple quantum wells*, Appl. Phys. Lett. **82**, 3850 (2003)
- [297] D. M. Schaadt, O. Brandt, S. Ghosh, T. Flissikowski, U. Jahn, H. T. Grahn, *Polarization-dependent beam switch based on an m-plane GaN/AlN distributed Bragg reflector*, Appl. Phys. Lett. **90**, 231117 (2007)
- [298] P. Misra, O. Brandt, H. T. Grahn, H. Teisseyre, M. Siekacz, C. Skierbiszewski, B. Lucznik, *Complete in-plane polarization anisotropy of the A exciton in unstrained A-plane GaN films*, Appl. Phys. Lett. **91**, 141903 (2007)
- [299] W. G. Scheibenzuber, U. T. Schwarz, R. G. Veprek, B. Witzigmann, A. Hangleiter, *Calculation of optical eigenmodes and gain in semipolar and nonpolar InGaN/GaN laser diodes*, Phys. Rev. B **80**, 115320 (2009)
- [300] H. Iwanaga, A. Kunishige, S. Takeuchi, *Anisotropic thermal expansion in wurtzite-type crystals*, J. Mater. Sci. **35**, 2451 (2000)
- [301] T. Zhu, A. Dussaigne, G. Christmann, C. Piquier, E. Feltin, D. Martin, R. Butté, N. Grandjean, *Nonpolar GaN-based microcavity using AlN/GaN distributed Bragg reflector*, Appl. Phys. Lett. **92**, 061114 (2008)
- [302] M. Schubert, *Polarization-dependent optical parameters of arbitrarily anisotropic homogeneous layered systems*, Phys. Rev. B **53**, 4265 (1996)
- [303] S. Shokhovets, R. Goldhahn, G. Gobsch, S. Piekh, R. Lantier, A. Rizzi, V. Lebedev, W. Richter, *Determination of the anisotropic dielectric function for wurtzite AlN and GaN by spectroscopic ellipsometry*, J. Appl. Phys. **94**, 307 (2003)
- [304] S. Faure, P. Lefebvre, T. Guillet, T. Bretagnon, B. Gil, *Comparison of strong coupling regimes in bulk GaAs, GaN, and ZnO semiconductor microcavities*, Phys. Rev. B **78**, 235323 (2008)
- [305] F. Kreller, M. Lowisch, J. Puls, F. Henneberger, *Role of biexcitons in the stimulated emission of wide-gap II-VI quantum wells*, Phys. Rev. Lett. **75**, 2420 (1995)
- [306] Y. Kawakami, I. Hauksson, J. Simpson, H. Stewart, I. Galbraith, K. A. Prior, B. C. Cavenett, *Photoluminescence excitation spectroscopy of the lasing transition in ZnSe-(Zn,Cd)Se quantum wells*, J. Cryst. Growth **138**, 759 (1994)
- [307] L. V. Butov, C. W. Lai, A. L. Ivanov, A. C. Gossard, D. S. Chemla, *Towards Bose-Einstein condensation of excitons in potential traps*, Nature (London) **417**, 47 (2002)
- [308] J. Y. Jen, T. Tsutsumi, I. Souma, Y. Oka, H. Fujiyasu, *Stimulated emission processes in $Zn_{1-x}Cd_xSe/ZnSe$ multiquantum wells*, Jpn. J. Appl. Phys. **32**, L1542 (1993)
- [309] J. M. Hvam, *Exciton-exciton interaction and laser emission in high-purity ZnO*, Solid State Commun. **12**, 95 (1973)
- [310] J. Ding, T. Ishihara, M. Hagerott, A. V. Nurmikko, H. Luo, N. Samarth, J. Furdyna, *Excitonic gain and laser emission in ZnSe-based quantum wells*, Phys. Rev. Lett. **69**, 1707 (1992)
- [311] P. G. Lagoudakis, M. D. Martin, J. J. Baumberg, G. Malpuech, A. Kavokin, *Coexistence of low threshold lasing and strong coupling in microcavities*, J. Appl. Phys. **95**, 2487 (2004)

Bibliography

- [312] K. Kojima, M. Funato, K. Kawakami, S. Nagahama, T. Mukai, H. Braun, U. T. Schwarz, *Gain suppression phenomena observed in $\text{In}_x\text{Ga}_{1-x}\text{N}$ quantum well laser diodes emitting at 470 nm*, Appl. Phys. Lett. **89**, 241127 (2006)
- [313] S. Ben-Tabou de-Leon, B. Laikhtman, *Mott transition, biexciton crossover, and spin ordering in the exciton gas in quantum wells*, Phys. Rev. B **67**, 235315 (2003)
- [314] E. Rosencher, B. Vinter, *Optoélectronique* (Dunod, Paris, 2002)
- [315] E. O. Kane, *Band structure of indium antimonide*, J. Phys. Chem. Solids **1**, 249 (1957)
- [316] G. L. Bir, G. E. Pikus, *Symmetry and strain induced effects in semiconductors* (Wiley, New York, 1974)
- [317] M. Suzuki, T. Uenoyama, A. Yanase, *First-principle calculations of effective-mass parameters of AlN and GaN*, Phys. Rev. B **52**, 8132 (1995)
- [318] R. Ishii, A. Kaneta, M. Funato, Y. Kawakami, *All deformation potentials in GaN determined by reflectance spectroscopy under uniaxial stress: Definite breakdown of the quasicubic approximation*, Phys. Rev. B **81**, 155202 (2010)
- [319] W. W. Chow, S. W. Koch, *Semiconductor-laser fundamentals: Physics of gain materials* (Springer, Heidelberg, 1999)
- [320] S. Datta, *Quantum transport: atom to transistor* (Cambridge University Press, Cambridge, 2005)
- [321] E. J. Roan, S. L. Chuang, *Linear and nonlinear intersubband electroabsorptions in a modulation-doped quantum well*, J. Appl. Phys. **69**, 3249 (1991)
- [322] H. G. Tompkins, E. A. Irene, *Handbook of ellipsometry* (Springer, Heidelberg, 2005)
- [323] J. S. C. Prentice, *Coherent, partially coherent and incoherent light absorption in thin-film multi-layer structures*, J. Phys. D: Appl. Phys. **33**, 3139 (2000)
- [324] D. W. Berreman, *Optics in stratified and anisotropic media: 4×4 -matrix formulation*, J. Opt. Soc. Am. **62**, 502 (1972)
- [325] M. Schubert, *Infrared ellipsometry on semiconductor layer structures - Phonons, plasmons and polaritons* (Springer, Berlin, 2004)
- [326] H. Wöhler, G. Haas, M. Fritsch, D. A. Mlynski, *Faster 4×4 matrix method for uniaxial inhomogeneous media*, J. Opt. Soc. Am. A **5**, 1554 (1988)
- [327] P. Yeh, *Optics of anisotropic layered media: a new 4×4 matrix algebra*, Surface Science **96**, 41 (1980)
- [328] D. Brunner, H. Angerer, E. Bustarret, F. Freudenberger, R. Höpler, R. Dimitrov, O. Ambacher, M. Stutzmann, *Optical constants of epitaxial AlGaIn films and their temperature dependence*, J. Appl. Phys. **82**, 5090 (1997)
- [329] L. C. Andreani, *Exciton-polaritons in superlattices*, Phys. Lett. A **192**, 99 (1994)
- [330] P. Lefebvre, P. Christol, H. Mathieu, *Unified formulation of excitonic absorption spectra of semiconductor quantum wells, superlattices, and quantum wires*, Phys. Rev. B **48**, 17308 (1993)

List of Acronyms

0..3D	zero..three-dimensional	LPB	lower polariton branch
AFM	atomic force microscopy	MBE	molecular beam epitaxy
BB	band-to-band	MC	microcavity
BEC	Bose-Einstein condensate	MOVPE	metal-organic vapor phase epitaxy
BGR	bandgap renormalization	MQW	multiple quantum wells
BM	Bragg-mode	MT	Mott-transition
BS	beam splitter	NA	numerical aperture
BZ	first Brillouin-zone	OPO	optical parametric oscillator
CB	conduction band	PL	photoluminescence
CCD	charge-coupled device	PLD	polariton laser diode
COM	coupled-oscillator model	PLE	PL excitation spectroscopy
cw	continuous wave	PSF	phase-space filling
DBR	distributed Bragg-reflector	QCSE	quantum-confined Stark-effect
e-h	electron-hole	QW	quantum well
EPC	exciton-phonon complex	RSM	reciprocal space map
FWHM	full width at half maximum	RT	room temperature
HEMT	high-electron mobility transistor	SCR	strong-coupling regime
hh	heavy-hole	SEM	scanning electron microscopy
HVPE	hydride vapor phase epitaxy	so	spin-orbit split-off
IQE	internal quantum efficiency	SP	Schrödinger-Poisson
IR	infra-red	SQW	single quantum well
JDOS	joint density of states	TEM	transmission electron microscopy
LED	light-emitting diode	TMS	transfer-matrix simulations
LD	laser diode	tr	time-resolved
lh	light-hole	UP	upper polariton
LO	longitudinal-optical	UPB	upper polariton branch
LP	lower polariton	UHV	ultra-high vacuum

List of Acronyms

UV	ultra-violet	X	exciton
VB	valence band	XX	biexciton
VCSEL	vertical cavity surface emitting laser	XRD	X-ray diffraction
WCR	weak coupling regime	YAG	yttrium aluminium garnet

Acknowledgements

Even if it is only my name that is written in bold on the front cover, this work and the four years I have spent with it would have never been such a success without the input of a few kind characters. This section is dedicated to them.

In the first instance, I would like to thank my supervisor Nicolas Grandjean for having offered me this great job in an exceptional and innovative environment. I sincerely appreciated your soft guidance, our scientific discussions, the variety of international conferences that I was allowed to attend, and last but not least your continuous support for my career.

Directly after, I want to express my gratitude to Raphaël Butté. He has been the machine that keeps the lab running, a very helpful troubleshooter, always available for discussion or coffee, and the hardest referee for paper writing, being feared in the corridor because of his uncompromising red pen. Thank you for all this Raphaël, and in addition for the relaxed restaurant and bar moments in SAT or during our conferences.

It was a pleasure and honour for me to have Luis Viña, Pierre Lefebvre, Vincenzo Savona, and Olivier Martin as referees and examiners in my thesis jury. I really appreciated your interest and your constructive feedback.

During the past four years I enjoyed the opportunity to participate in a couple of fruitful collaborations: I would like to thank Benoit Deveaud from EPFL and his group members Pierre Corfdir, Mehran Shahmohammadi, Gwénolé Jacopin, and Jean-Daniel Ganière for the numerous scientific discussions and the great experimental support. I am also very grateful to Tadek Suski and Henryk Teisseyre from the Institute of High Pressure Physics in Warsaw for our joint excursion to the fascinating field of non-polar microcavities. Furthermore, I appreciated interesting and rewarding collaborations with Thierry Guillet and Meletis Mexis from the University of Montpellier, and Christophe Durand from the University of Grenoble.

With the next few lines I want to direct my gratitude to all the people that shared my daily routines and made my life in Switzerland an unforgettable experience.

Directly from the start I had the great pleasure to meet Jacques Levrat. It would take multiple pages to detail my thankfulness for all these hours spent in the lab and in the office, so that I will simply skip it and focus on the really important things: *Merci pour tout mon ami, pour le sympathique échange culturel Suisse-Allemagne, de m'avoir montré les cols suisse avec la moto, pour tout les photos compromettantes de moi, d'avoir mis toujours la bonne musique au bureau, et pour nos innombrables soirées de shisha et youtube, au bord du lac, au centre ville, en conférence,...* Something very similar also applies to Pierre Corfdir: *Merci pour toutes les discussions scientifiques et non-scientifiques, pour notre échange musical, en particulier*

Acknowledgements

pour partager ta passion de Claude François avec moi, pour nos soirées au XIIIe siècle, et pour me montrer l'art de préparer une véritable fondue suisse. Further on, I would like to thank my friends and office mates Gatien, with whom I might start a promising popstar career some day, and Nils, who frequently spoiled me with his delicious *Braten*. I appreciated the excellent working atmosphere in our office, the breaks in SAT, and all the other nice moments that we shared and that made these years passing way too fast. I am also grateful to my brave combatants in the fight against the InGaN misery: Marlene, Munise, and Christian. The whole piece of work would have never been possible without the fantastic work of our growth team: Merci Amélie, Etienne, Jean-François, Eric, and with a tiny wink Lise, to whom I am also grateful for the numerous French lessons ;). Finally, and no less than before, I also want to thank the rest of the LASPE team for their great support and the likeable atmosphere: Lorenzo, Marco, Luca, Julien, Noelia, Nino, Marcus, Marco, Marcel, Jean-Michel, Guillaume, Nicola, Yoshi, Jérôme, Aline, Roger, Nadja, and Denis.

Not part of the lab, but nonetheless related to all this, it is my pleasure to also thank my friends bases in Ilmenau, Dresden, and Aachen for the unabated support, and Anja, Kim, Marc, Patrick, Anna ($\times 2$), and in particular Bruna for upgrading my Switzerland experience.

An letzter Stelle und dafür mit umso mehr Nachdruck, danke ich meiner Familie, allen voran meinen Eltern, meinen Großeltern und meinen Brüdern, für ihre fortwährende und in allen Belangen großzügige Unterstützung. Was wäre eine Gleichung ohne Konstanten...

Lausanne, den 3. Juli 2014

Georg Roßbach

Georg Roßbach (Dipl.-Ing.)

address Avenue d'Echallens 8
1004 Lausanne, Switzerland
mobile +41 76 7402229
e-mail georg.rossbach@gmail.com
date of birth 2nd May 1985
nationality German
marital status single



curriculum vitae

Working Experience

- April 2010 - present** **Research Assistant at the École Polytechnique Fédérale de Lausanne**
Experimental research in the field of GaN-based quantum-wells and semiconductor microcavities by means of optical spectroscopy techniques
PhD-thesis: *High-density excitonic effects in GaN: Mott-Transition and Polariton Lasing* (submitted 1st May 2014)
- April 2008 - September 2008** **Internship as Research Engineer at Q-Cells SE (Thalheim, Germany)**
Optical, electrical and structural characterization and optimization of silicon and thin-film based solar cells (a-Si, μ -Si, CIGS, CdTe)

Education

- 2004 - 2009** **Studies of Technical Physics at the University of Technology Ilmenau**
Focus on solid-state and semiconductor physics, optics, photonics, laser physics, and micro- and nanotechnology
19th November 2009
Engineer Diploma in Technical Physics (final mark: 1.1 - excellent)
Experimental research in the field of III-nitride material properties
Diploma-thesis: *Optical properties of hexagonal aluminium nitride*
28th September 2006
Intermediate examination in Technical Physics (final mark: 1.4 - very good)
- 1995 - 2004** Grammar School, Novalis Gymnasium Hettstedt
26th June 2004
Abitur (A-Levels, final mark: 1.0 - excellent)
Focus on mathematics and natural sciences

Languages

German - native speaker | **English** - fluent | **French** - good knowledge | **Russian** - basics

Personal Profile & Skills

- Computer** **Scientific Programs** - Matlab, Labview, Origin, C
Others - MS Office, LaTeX, Inkscape, Adobe Photoshop
- Scientific Background** Advanced competences in optics and semiconductor physics
Optical spectroscopy (various techniques, setup design)
Vacuum and cryogenic setup design
Various scientific simulations
- Supervision** Master-students and undergraduates
Assistant of laboratory assignments for physics students
- Personal Interests** Travelling, Volleyball, Snowboarding, Hiking, Photography

Theses

PhD Thesis submitted by 1 st May, 2014	High-density excitonic effects in GaN: Mott-transition and polariton lasing École Polytechnique Fédérale de Lausanne (Switzerland) LASPE - directed by Nicolas Grandjean and Raphaël Butté
Diploma Thesis 19 th November 2009	Optical properties of hexagonal aluminium nitride University of Technology Ilmenau (Germany) - directed by Rüdiger Goldhahn

Book Chapter

J. Levrat, G. Roßbach, R. Butté, and N. Grandjean, *Toward quantum fluids at room temperature: polariton condensation in III-nitride based microcavities*, pages 201-230,
in *Physics of Quantum Fluids*, edited by A. Bramati and M. Modugno, Springer Heidelberg (2013)

Selected Publications

- C. Durand, C. Bougerol, J.-F. Carlin, G. Roßbach, F. Godel, J. Eymery, P.-H. Jouneau, A. Mukhtarova, R. Butté, and N. Grandjean, *M-plane GaN/InAlN multiple quantum wells in core-shell wire structure for UV emission*, ACS Photonics **1**, 38 (2014)
- G. Roßbach, J. Levrat, E. Feltn, J.-F. Carlin, R. Butté, and N. Grandjean, *Impact of saturation on the polariton renormalization in III-nitride based microcavities*, Phys. Rev. B **88**, 165312 (2013)
- J. Levrat, G. Roßbach, A. Dussaigne, H. Teisseyre, G. Cosendey, M. Glauser, M. Cobet, M. Bockowski, I. Grzegory, T. Suski, R. Butté, and N. Grandjean, *On the nature of the nonlinear emission properties of an optically anisotropic GaN-based microcavity*, Phys. Rev. B **86**, 165321 (2012)
- G. Cosendey, A. Castiglia, G. Roßbach, J.-F. Carlin, and N. Grandjean, *Lasing in a blue monolithic AlInN-based vertical cavity surface emitting laser diode on free-standing GaN substrate*, Appl. Phys. Lett. **101**, 151113 (2012)
- N. Vico Triviño, G. Roßbach, U. Dharanipathy, J. Levrat, A. Castiglia, J.-F. Carlin, K. A. Atlasov, R. Butté, R. Houdré, and N. Grandjean, *High quality factor two dimensional GaN photonic crystal cavity membranes grown on silicon substrate*, Appl. Phys. Lett. **100**, 071103 (2012)
- G. Roßbach, J. Levrat, A. Dussaigne, H. Teisseyre, G. Cosendey, M. Glauser, M. Cobet, M. Bockowski, I. Grzegory, T. Suski, R. Butté, and N. Grandjean, *Tailoring the light-matter coupling in anisotropic microcavities: Redistribution of oscillator strength in strained m-plane GaN/AlGaIn quantum wells*, Phys. Rev. B **84**, 115315 (2011)
- G. Roßbach, M. Feneberg, M. Röppischer, C. Werner, N. Esser, C. Cobet, T. Meisch, K. Thonke, A. Dadgar, J. Bläsing, A. Krost, and R. Goldhahn, *Influence of exciton-phonon coupling and strain on the anisotropic optical response of wurtzite AlN around the band edge*, Phys. Rev. B **83**, 195202 (2011)
- G. Roßbach, M. Röppischer, P. Schley, G. Gobsch, C. Werner, C. Cobet, N. Esser, A. Dadgar, M. Wieneke, A. Krost, and R. Goldhahn, *Valence-band splitting and optical anisotropy of AlN*, Phys. Status Solidi B **247**, 1679 (2010)
- M. Röppischer, R. Goldhahn, G. Roßbach, P. Schley, C. Cobet, N. Esser, T. Schupp, K. Lischka, and D. J. As, *Dielectric function of zinc-blende AlN from 1 to 20 eV: Band gap and van Hove singularities*, J. Appl. Phys. **107**, 076104 (2009)

+ 8 others and 2 submitted

Presentations

Orals	invited - 2 presentations contributed - 7 presentations at 7 international conferences
Poster	11 first-authored presentations at 10 international conferences
Awards	Best Student Paper Award - 38th International Symposium on Compound Semiconductors (ISCS-38), Berlin (Germany), May 2011 (Talk)
192	Best Poster Award - International Summer-School on Nanophotonics and Photovoltaics, Phuket (Thailand), April 2012 (Poster)